

Connected array antennas : analysis and design

Citation for published version (APA):

Cavallo, D. (2011). *Connected array antennas : analysis and design*. [Phd Thesis 1 (Research TU/e / Graduation TU/e), Electrical Engineering]. Technische Universiteit Eindhoven. <https://doi.org/10.6100/IR719461>

DOI:

[10.6100/IR719461](https://doi.org/10.6100/IR719461)

Document status and date:

Published: 01/01/2011

Document Version:

Publisher's PDF, also known as Version of Record (includes final page, issue and volume numbers)

Please check the document version of this publication:

- A submitted manuscript is the version of the article upon submission and before peer-review. There can be important differences between the submitted version and the official published version of record. People interested in the research are advised to contact the author for the final version of the publication, or visit the DOI to the publisher's website.
- The final author version and the galley proof are versions of the publication after peer review.
- The final published version features the final layout of the paper including the volume, issue and page numbers.

[Link to publication](#)

General rights

Copyright and moral rights for the publications made accessible in the public portal are retained by the authors and/or other copyright owners and it is a condition of accessing publications that users recognise and abide by the legal requirements associated with these rights.

- Users may download and print one copy of any publication from the public portal for the purpose of private study or research.
- You may not further distribute the material or use it for any profit-making activity or commercial gain
- You may freely distribute the URL identifying the publication in the public portal.

If the publication is distributed under the terms of Article 25fa of the Dutch Copyright Act, indicated by the "Taverne" license above, please follow below link for the End User Agreement:

www.tue.nl/taverne

Take down policy

If you believe that this document breaches copyright please contact us at:

openaccess@tue.nl

providing details and we will investigate your claim.

Connected Array Antennas

Analysis and Design

Connected Array Antennas

Analysis and Design

PROEFSCHRIFT

ter verkrijging van de graad van doctor aan de
Technische Universiteit Eindhoven, op gezag van de
rector magnificus, prof.dr.ir. C.J. van Duijn, voor een
commissie aangewezen door het College voor
Promoties in het openbaar te verdedigen
op maandag 7 november 2011 om 16.00 uur

door

Daniele Cavallo

geboren te Benevento, Italië

Dit proefschrift is goedgekeurd door de promotoren:

prof.dr.ir. G. Gerini

en

prof.dr.ir. A. Neto

Copromotor:

prof.dr. A.G. Tjhuis

A catalogue record is available from Eindhoven University of Technology Library

Cavallo, Daniele

Connected Array Antennas: Analysis and Design/ by Daniele Cavallo. - Eindhoven :
Technische Universiteit Eindhoven, 2011.

Proefschrift. - ISBN 978-94-6191-035-6

NUR 959

Trefwoorden: antennestelsels / fasegestuurde stelsels / kruispolarisatie /
Greense functie methoden/ breedband antennes.

Subject headings: antenna arrays / phased arrays / cross polarization /
Green's function methods/ broadband antennas.

Copyright ©2011 by D. Cavallo, TNO, The Hague, The Netherlands

Cover design: Daniele Cavallo

Press: Ipskamp Drukkers B.V., Enschede, The Netherlands

The work presented in this thesis has been performed at TNO and financed by TNO with support of the Dutch Ministry of Defense.

To my family

Contents

1	Introduction	1
1.1	The Need for Wideband Wide-Scan Phased Arrays	2
1.1.1	In-Flight Entertainment: ACTiFE	2
1.1.2	Wideband and Multi-Band Radars	3
1.1.3	Radio Astronomy: the Square Kilometer Array	3
1.2	State of the Art: Limitations of Present Solutions	4
1.3	Connected Arrays	8
1.3.1	Historical Context	9
1.4	Novel Contributions in This Thesis	9
1.5	Outline of the Thesis	10
2	Spectral Green's Functions of Connected Arrays	13
2.1	Green's Functions of an Infinite Dipole or Slot	13
2.1.1	Current Solution for an Infinite Dipole	17
2.1.2	Current Solution for an Infinite Slot in Free Space and with Backing Reflector	19
2.2	Green's Function of 2-D Periodic Connected Arrays	21
2.2.1	Active Impedance of a Unit Cell for Connected Arrays of Dipoles	24
2.2.2	Active Impedance of a Unit Cell for Connected Arrays of Slots	27
3	Scanning Behavior of Backed Connected Arrays	31
3.1	Impedance of Connected Arrays when Scanning	31
3.1.1	Dominant Floquet Wave	32
3.2	Analysis of Polar Singularities of the Longitudinal Spectra	35
3.2.1	Leaky Wave Poles in Connected Slots	35
3.2.2	TEM Poles in Connected Dipoles	37
3.3	Bandwidth Dependence on the Gap Width	40

3.3.1	Slot Case: Lumped Inductance	40
3.3.2	Dipole Case: Lumped Capacitance	41
3.4	Double Feed for the Dipoles	42
3.4.1	Active Admittance for Multiple Feeds per Unit Cell	45
3.5	Active Array Far-Field Patterns	47
3.5.1	Transverse Windowing Approximation	48
3.5.2	Longitudinal Windowing Approximation	49
3.5.3	Longitudinal Green's Function	50
3.5.4	Pattern Quality	51
3.6	Conclusions	53
4	Equivalent Circuit Representation of Connected Arrays	55
4.1	Limitations of Equivalent Norton or Thévenin Circuits	56
4.2	Integral Equation for Connected Array of Loaded Dipoles	56
4.2.1	Separation of Variables	58
4.2.2	One-Dimensional Equation	59
4.2.3	Total Currents on the Gaps	60
4.2.4	Spectral Integral Equation	60
4.3	Solution for Periodic Arrays and Thévenin Circuits	61
4.3.1	Transmit Case	62
4.3.2	Receive Case	62
4.4	Expansion of the Thévenin Circuits in Equivalent Networks	63
4.4.1	Equivalent Circuit Representation of the Fundamental Floquet Mode	65
4.5	The Equivalent Circuit in Reception	67
4.5.1	Numerical Validation of the Equivalent Circuit in Reception	69
4.5.2	Power Absorbed and Scattered by Connected Arrays	69
4.6	Consequence: RCS of Antennas as Measure of TX Matching	72
4.7	Conclusions	74
5	Finite Connected Arrays	79
5.1	Set Up of the Spectral Equation: The Finite \times Infinite Array Case	81
5.2	Numerical Solution	83
5.2.1	Receive Mode	85
5.2.2	Results of the Numerical Solution	86
5.3	Efficiency of Finite Connected Arrays	86
5.4	Spectral Integral Approximation	90

5.4.1	Simple Case: Low Frequency and Generator Distributed over the Entire Cell	91
5.4.2	Extrapolation of the Simple Case Solution	93
5.5	Free Space Case: Uniform Asymptotic Evaluation of the Integral Approximation	95
5.5.1	Contributions from the Two Edges	95
5.5.2	Comments on the Analytical Solution	97
5.6	Conclusions	98
6	Practical Implementation of Feed Networks in Connected Arrays	101
6.1	Resonances Typical of Connected Arrays	103
6.1.1	Common-Mode Resonances	104
6.2	Design of PCB Slot-Based Transformers	106
6.2.1	CPS/GCPS Transformer	107
6.2.2	CPS/MS Balun	110
6.3	Performance of the Feed Network: Array Design	110
6.3.1	Finite Ground Planes	112
6.3.2	Backed Array	113
6.3.3	Limitations of Over-Sampling the Unit Cell	114
6.4	Common-Mode Rejection Loop Design	114
6.4.1	Performance of the Loop-Shaped Feed Structure	116
6.4.2	Single-Polarization Array Design	118
6.4.3	Dual-Polarization Array Design	119
6.5	Conclusions	120
7	Experimental Validation	123
7.1	A 3 to 5 GHz Singly-Polarized Connected Array	123
7.1.1	Design Strategy	123
7.2	Prototype Array: Simulations	127
7.3	Prototype Array: Measurements	130
7.3.1	Practical Implementation of the Backing Reflector	132
7.3.2	Measured Results	132
7.4	Conclusions	138
8	Conclusions and Recommendations	141
8.1	Analytical Description of Connected Arrays	141

8.2	Connected Dipoles Versus Connected Slots	142
8.3	Equivalent Circuit Representation	142
8.4	Finite Connected Arrays	143
8.5	Practical Design of a Connected Array	144
8.6	Outlook	145
8.7	Impact of the Research	146
A	Spectral Green's Functions of Plane-Stratified Media	147
A.1	Electromagnetic Field in Terms of z -Directed Vector Potentials	147
A.2	TE-TM Transmission Lines in Unbounded (x, y) -Domains	149
A.3	Spectral Green's Function for Electric Source	152
A.3.1	(x, y) -Oriented Electric Source	152
A.3.2	z -Oriented Electric Source	155
A.3.3	Dyadic Spectral GF of an Arbitrarily Oriented Electric Source	158
A.4	Spectral Green's Function for Magnetic Source	158
A.4.1	(x, y) -Oriented Magnetic Source	158
A.4.2	z -Oriented Magnetic Source	161
A.4.3	Dyadic Spectral GF of an Arbitrarily Oriented Magnetic Source	163
A.5	Evaluation of G_{xx}^{EJ} for a Dipole in Free Space and with Backing Reflector	164
A.5.1	Free Space	164
A.5.2	Backing Reflector	164
B	Radiation Patterns from Connected Arrays	167
B.1	Plane-Wave Spectrum Approximation of the Far Field	167
B.2	Radiation Pattern from a Finite Connected Array	169
B.2.1	Longitudinal Windowing Approximation	170
B.2.2	Longitudinal Green's Function	171
B.2.3	Far-Fields Expressions from the Vector Potential	172
C	Admittance Matrix Evaluation: IEMEN Approach	173
C.1	Integral Equation	173
C.2	Closed-Form Evaluation of the Admittance Matrix	176
C.2.1	Analytical Solution for the Current Spectrum	177
C.2.2	Analytical Solution for the Admittance Matrix	178
C.2.3	Circuit Steps to Validate the Equivalent Circuit in Reception	179

D Asymptotic Evaluation of Edge-Current Integrals	181
D.1 Analysis of the Singularities	182
D.1.1 Load Dependent Pole	183
D.2 Asymptotic Evaluation in Terms of Fresnel Functions	184
D.3 On the Evaluation of the Integral $\int_{-\infty}^{\infty} \frac{\sqrt{k_0 - k_x}}{k_x - k_{xp}} e^{-jk_x x} dk_x$	187
D.3.1 Steepest Descent Path	191
D.3.2 Fresnel Integral	193
 List of Publications	 209
 Summary	 215
 About the Author	 217
 Acknowledgements	 219

Chapter 1

Introduction

The rapid advancement in telecommunication and radar technology is placing increasing demands on wireless system performance and functionality. In particular, many of today's satellite communication and radar systems necessitate phased array antennas that are capable of wideband/multi-band operation and good polarization purity over a wide scan volume.

Wideband and multi-band arrays are receiving growing attention for both military and commercial applications, since they can provide multi-function capability with a single aperture. In environments where multiple sensors are competing for the same physical space, the possibility to concurrently support communications, electronic warfare and radar functions with a single phased array would result in size, weight and cost advantages.

However, the need to maintain the antenna performance stable over a very large frequency band (in terms of polarization, radiation pattern quality, efficiency and matching) sets very demanding requirements on the antenna system and poses several technological challenges. Particularly important is the aspect of polarization purity, since most of these applications require antennas that can provide dual-linear and circular polarization.

Nevertheless, as it will be subsequently pointed out in this chapter, the antenna solutions typically used for wideband wide-scan applications trade off matching performance against polarization efficiency. Thus, to fulfill the above mentioned system and technology challenges, new advanced array architectures, new design guidelines and new accurate theoretical formulations have to be developed. Within this dissertation, all these aspects will be addressed, focusing in particular on the concept of "connected arrays": this antenna solution represents one of the most promising concepts in the field of wideband arrays, for being able to achieve both broad bandwidth and low cross polarization.

1.1 The Need for Wideband Wide-Scan Phased Arrays

Wideband, wide-scan phased arrays are attractive for their potential to enable new system functionality and increased integration. For example, the development of such antenna arrays responds to the trend in advanced naval and airborne military environments toward combining multiple functions on the same radiating apertures. Besides multi-function radars in X-band and lower, other applications can benefit from antenna arrays with such characteristics: these range from communication applications in Ku-bands [1] to earth-based deep space investigation (e.g. Square Kilometer Array [2]) or satellite based sub-mm wave instruments (e.g. SPICA [3]).

This section gives an overview of the main specific applications on which the research of this thesis focuses.

1.1.1 In-Flight Entertainment: ACTiFE

In satellite communications, a single wideband feed antenna can strongly reduce space and weight when supporting many communication channels. An important commercial application that demands an advanced solution for satellite-to-aircraft communication is the in-flight entertainment. An activity has been recently proposed by the European Space Agency, which requires the development of advanced antenna concepts for aircraft in-flight entertainment (ACTiFE) [1]. Funding from this project supported part of the research on connected arrays presented in this dissertation.

For such application, the use of wide-scan angle arrays with extreme polarization requirements is necessary. The beam of the array antenna is required to be electronically steerable. The antenna should be integrated in the aircraft fuselage and be able to cover the full hemisphere ($\pm 90^\circ$ in elevation and 360° in azimuth). This allows the system to maintain a good pointing and a good signal reception under all possible flight operations, including high-latitude air routes.

For the in-flight entertainment application, the antenna is required to support two orthogonal polarizations, characterized by isolation between the channels better than 15 dB over the entire hemisphere. Moreover, to minimize the impact of the antenna on the aircrafts, a single antenna for both the uplink and the downlink bands is preferred, with a wide bandwidth (about 30%, from 10.7 to 14.5 GHz) to operate on both transmit (Tx) and receive (Rx) bands. The antenna could be constituted by a unique conformal or multi-faceted solution that minimizes the dimension of the aperture for any given desired gain in all

directions. However, such a solution does not lend itself to a simple implementation with Printed Circuit Board (PCB) technology. A small number of flat panels, or even a single panel with very wide-angle beam steering in combination with minor mechanical scanning, could be adopted as an alternative solution. In this case, it is crucial that the array can maintain stable matching and polarization performance over a very wide scan volume (up to $45^\circ - 60^\circ$ in elevation).

1.1.2 Wideband and Multi-Band Radars

Also in radar applications, the need for specialized multi-function operations (e.g., simultaneous surveillance, discrimination, tracking), the use of high data rates, and the ability to withstand adverse environmental conditions have stimulated considerable research activity in the area of wideband phased arrays.

The proliferation of advanced sensor and communication systems aboard military platforms (ships, aircraft, land vehicles, etc.) has led to an increasingly large number of associated antenna systems. Since space, weight, and antenna siting for optimal coverage are at a premium on these platforms, it is desirable to reduce the number of antennas by consolidating the functionality of several systems into a single shared aperture. As this system integration increases, a single antenna is often required to support multiple services across ultra-wideband (UWB) frequency ranges. Moreover, if a wideband aperture is shared between radar and communication systems, multiple polarizations have to be guaranteed, setting the necessity for good polarization purity of the radiators.

The development of connected arrays for multi-function radars has been one of the focuses at The Netherlands Organization for Applied Scientific Research (TNO) in the last years. Part of the work described in this thesis was supported by the TNO Radar Program [4].

1.1.3 Radio Astronomy: the Square Kilometer Array

Another important application for wideband wide-scan arrays is radio astronomy, for which phased arrays can be used by themselves or as feeds of large reflector antennas. An ongoing project that may use phased arrays in both these configurations is the Square Kilometer Array (SKA) [2, 5, 6]. The SKA is an international project aimed at building a huge radio telescope that will provide an increase in sensitivity of two orders of magnitude over existing telescopes. The SKA is planned to operate over an extremely wide frequency range, from 70 MHz to 25 GHz. Although there have been different suggestions for antennas, nowadays it is likely that the final array design for SKA will utilize Vivaldi antennas for the individual

elements [7]. However, these antennas have some limitations, as pointed out in the next section.

Connected arrays are recently attracting growing interest as a valid option for radio astronomy applications. For instance, the Commonwealth Scientific and Industrial Research Organization (CSIRO), which is the Australian national science agency, is investigating the capability of wideband connected array antennas for the Australian Square Kilometer Array Pathfinder (ASKAP) radio telescope [8].

1.2 State of the Art: Limitations of Present Solutions

The solutions typically used for wideband wide-scan applications trade off matching performance against polarization purity. Before presenting an overview of the most typically adopted antennas and their performance, let us introduce the definitions of bandwidth and cross polarization which we will refer to within this dissertation.

Definition of Bandwidth

The bandwidth of an antenna does not have a unique definition. Depending on the operational requirements of the application for which the antenna is to be used, the functional bandwidth of an antenna might be limited by any one or several of the following factors: change of pattern shape or pattern direction, increase in side-lobe level, loss in gain, change of polarization characteristics, or deterioration of the impedance response. For the sake of fair comparison with the literature and previous works, it is important to specify the definition of bandwidth that will be used in this thesis, as of course much larger bandwidths can be obtained with more relaxed requirements.

Unless differently specified, the definition for bandwidth used within this dissertation is that *band within which the array shows an active S_{11} lower than -10 dB when pointing at broadside and at 45° on the E - and H -planes*. In other words, the bandwidth is given by the overlap between the -10 dB bands for broadside, 45° E -plane scan and 45° H -plane scan.

For bandwidths that are less than one octave, we will use the percent bandwidth, defined as $(f_H - f_L)/f_c$ %, where f_c is the center frequency, and f_L , f_H are the lower and upper cut-off frequencies, respectively. For wider bandwidths we will instead refer to the fractional or ratio bandwidth, defined as $f_H : f_L$.

Definition of Cross Polarization

The cross-polarization (X-pol) level is herein defined as the ratio between co-polarized and cross-polarized fields, determined according to the third definition from Ludwig [9]. The co-polar and the cross-polar unit vectors for an electric current directed along x are given by

$$\hat{\mathbf{i}}_{co} = \cos \varphi \hat{\boldsymbol{\theta}} - \sin \varphi \hat{\boldsymbol{\varphi}} \quad (1.1)$$

$$\hat{\mathbf{i}}_{cross} = \sin \varphi \hat{\boldsymbol{\theta}} + \cos \varphi \hat{\boldsymbol{\varphi}} \quad (1.2)$$

referring to the coordinate system defined in Fig. 1.1. According to this definition, a short electric dipole does not radiate any cross-polarized field in the E - and H -plane, as rigorously proved in [10]. However, cross polarization appears on all other planes, for which $\varphi \neq 0^\circ$ and $\varphi \neq 90^\circ$. By using the well known expression of the far-field radiation from a short electric dipole, one can easily show that, once fixed the elevation angle θ , the highest X-pol level is observed in the diagonal plane (D -plane), for which $\varphi = 45^\circ$. This is evident from Fig. 1.2, where the X-pol level relative to a short dipole placed along the x -axis is shown in terms of the observation angles θ and φ . If we focus on a volume of $\pm 45^\circ$ in elevation, the worst case occurs for $\theta = 45^\circ$ and $\varphi = 45^\circ$, when the X-pol reaches the value of -15 dB.

Similarly to a short dipole, the X-pol level of well sampled linearly polarized array is ideally zero when observing in the main planes, while is higher in the D -plane. For this reason, we characterize the polarization performance on the D -plane for maximum elevation angle, which is considered as the worst case. When scanning up to 45° , the X-pol levels are given for $\theta = 45^\circ$ and $\varphi = 45^\circ$, as depicted in Fig. 1.1.

An overview of some typical array elements for wideband wide-scan applications is reported in Table 1.1. The elements are compared in terms of bandwidth and X-pol level, according to the afore-given definitions.

Although tapered slot (or Vivaldi) antennas are characterized by very large impedance matching bandwidths [11, 12], they exhibit relatively poor performance in terms of polarization purity, especially when large scan angles are required. In particular, high X-pol levels are observed when scanning in the diagonal plane [10, 13–15]. The high X-pol is

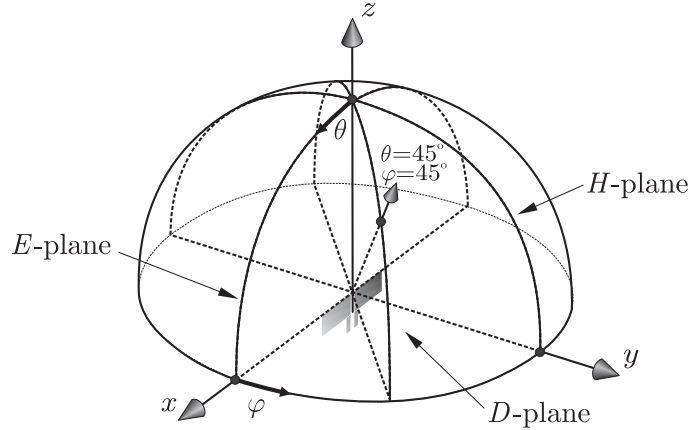


Figure 1.1: Reference coordinate system and definition of E - H - and D -plane for a dipole; X-pol is characterized for observations at $\theta = 45^\circ$ and $\varphi = 45^\circ$.

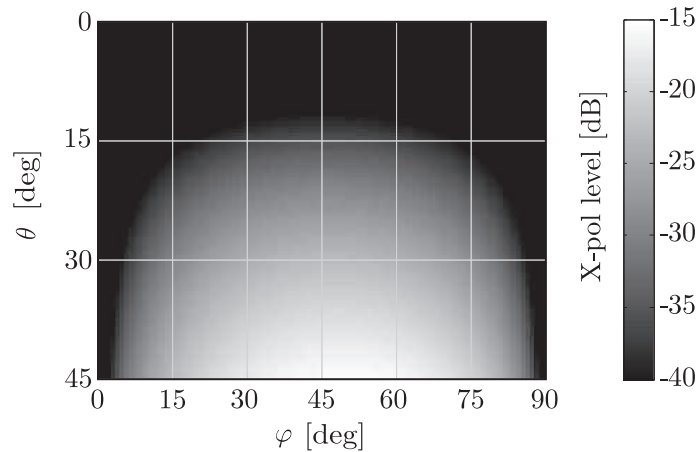


Figure 1.2: X-pol level radiated by a short electric dipole along x toward the direction defined by θ and φ , according to the reference coordinate system in Fig. 1.1.

attributed to the non-linearly polarized nature of the radiating currents in Vivaldi antennas. In fact, due to the flare of the metallization, the current distribution along the element inherently comprises a vertical component (orthogonal to the aperture plane), which increases the cross-polar radiation.

A better polarization performance can be achieved by exploiting a denser sampling of the array, with array periods that are smaller than a quarter wavelength. However, such a configuration would increase the number of required Transmit/Receive (T/R) modules, which poses significant challenges in cost and construction of the array. The arrangement of Vivaldi antennas in an “egg-crate” configuration [16,17] is necessary to improve polarization

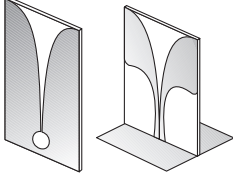
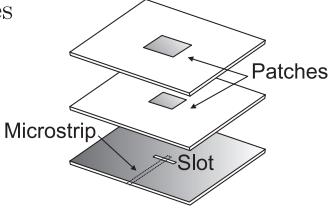
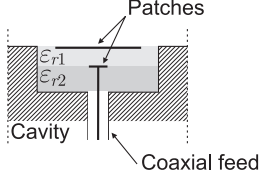
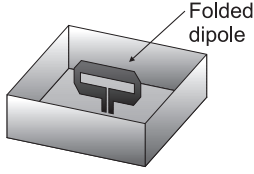
Antenna Element		Performance
Tapered Slot Antennas		<ul style="list-style-type: none"> • Bandwidth 4:1 • X-pol at $\theta=45^\circ, \varphi=45^\circ$ -10 dB
Stacked Patches		<ul style="list-style-type: none"> • Bandwidth 25% • X-pol at $\theta=45^\circ, \varphi=45^\circ$ -15 dB
Cavity Backed Patches		<ul style="list-style-type: none"> • Bandwidth 30% • X-pol at $\theta=45^\circ, \varphi=45^\circ$ -11 dB
Cavity Backed Folded Dipoles		<ul style="list-style-type: none"> • Bandwidth 16% • X-pol at $\theta=45^\circ, \varphi=45^\circ$ -15 dB

Table 1.1: Comparison of antenna elements for wide-scan angle phased arrays in terms of bandwidth ($S_{11} < -10$ dB within a 45° scan volume) and X-pol levels (for scanning to 45° in the D -plane).

performance in dual-polarization application.

On the other hand, phased arrays based on resonant elements that resort to completely planar feeds can achieve better polarization purity, but only moderate bandwidths ($\sim 25\%$). Some examples are given by stacked patches [18–20], cavity-backed patches [21] or cavity-backed folded dipoles [22].

To overcome the limitations stated above, there is a recent trend aiming at reducing X-pol by making arrays of long slots or dipoles periodically fed: these arrays are indicated as connected arrays of slot or dipoles. Connected arrays offer wide bandwidth, while maintaining low X-pol levels.

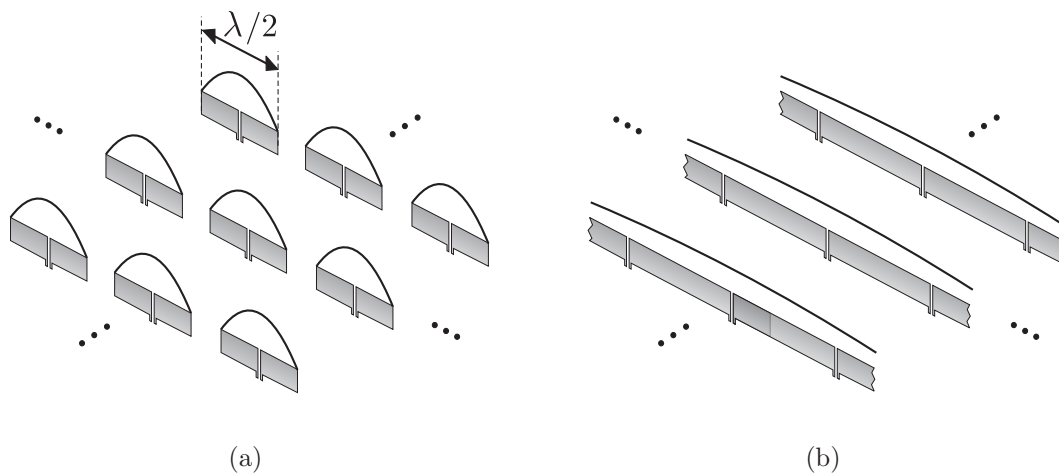


Figure 1.3: Current distribution on dipole elements in array configuration: (a) resonant unconnected dipoles; (b) connected dipoles.

1.3 Connected Arrays

In standard narrow-band array designs, the objective is to keep low mutual coupling between the radiating elements not to alter too much the performance of each isolated element.

In recent years, a new approach has arisen for the design of broadband arrays in which mutual coupling is intentionally introduced between the array elements. A simple way to enhance the coupling between neighboring elements is to electrically connect them one to another. A *connected array* can be briefly described as an array of slots or dipoles which are electrically connected to each other. In this way, the array is no longer composed of separated resonant elements, but can be considered as a single antenna periodically fed. The current distribution on resonant narrow-band dipoles is sinusoidal and frequency dependent, as shown in Fig. 1.3(a). Contrarily, connected arrays achieve wideband performance, due to the fact that the connections between neighboring elements allow currents to remain nearly constant with frequency (see Fig. 1.3(b)).

Another attractive feature of connected arrays is their capability to achieve good polarization purity, in virtue of the planarity of the radiating currents. For this reason, in about the last ten years, connected arrays have emerged as one of the most valid alternatives to the aforementioned solutions (Sec. 1.2), as they can guarantee both the broad band and the low cross polarization.

1.3.1 Historical Context

While the origin of connected arrays stems from the concept of self complementarity [23,24], recently it was R. C. Hansen [25] who brought the concept of connected arrays of dipoles to the attention of the antenna community. The design strategy for arrays of disconnected dipoles presented in [26], while appearing different because it is based on capacitively-coupled dipoles, presents some similarities as the one based on connected arrays. Indeed, the purpose and effect of the capacitive loading in [26] is to obtain almost continuous currents among the different dipole elements, thus realizing the continuous current sheet proposed by Wheeler [27,28]. This is the same scope of the connected-dipole arrays.

In [29] the connected-dipole concept was extended to the dual structure, based on slots. In [30] and [31] the Green's functions (GF) of such long slot arrays were derived and presented in analytical form, starting from a spectral representation of the field in each slot [32]. This work demonstrated that the bandwidth achievable with connected arrays in free space is theoretically infinite, for infinitely long slots or dipoles. In practical designs, the bandwidth is not infinite, but it is limited only by the finite dimensions of the array. The low frequency limit occurs when the array length is roughly $\lambda/4$. A very wideband (10:1) long slot array, operating in the frequency range 200-2000 MHz, was reported in [33]. The true limiting factor on connected array bandwidth is the metallic back plane that is needed to ensure unidirectional radiation [34]. However, thanks to the availability of the analytical GF that greatly facilitates the design, a broad band (4:1) was achieved with a connected array demonstrator with backing reflector in [35]. This consisted of a 4×8 backed connected array of slots radiating at broadside with good efficiency ($VSWR < 2$) on a bandwidth that spanned from 150 MHz to 600 MHz.

1.4 Novel Contributions in This Thesis

Starting from the theoretical formulation available at the beginning of the study, this dissertation, on the one hand, further develops the theory of connected arrays, based on a spectral GF formalism. On the other hand, the study addresses and proposes solutions to the issues associated with the practical design of such arrays.

The main novel aspects that have been investigated can be summarized as follows:

- An extension of the GF formalism to the cases of receiving arrays and arrays that include load impedances at the feed points.

- An investigation on the scan performance of connected array of dipoles and slots, based on the analysis of the singularities of the pertinent GFs.
- A rigorous equivalent circuit for the array unit cell, whose components are expressed in analytical form. This circuit representation constitutes a powerful design tool and provides gain in physical insight on both local and global behaviors of the array.
- A rigorous study on finiteness effects, which can be dominant in connected arrays, due to the high inter-element mutual coupling. Both numerical and analytical methods are presented. The link with the load impedance of the array elements is also pointed out, giving useful guidelines for the design of the array element to minimize edge effects.
- The design of practical feed structures for these arrays, aiming at reducing common-mode propagation into the feed lines. The problem of common mode is extensively addressed and explained in this thesis and it is believed to be the major practical issue for all very wideband arrays. A solution is proposed and experimentally validated by a prototype demonstrator.

1.5 Outline of the Thesis

This thesis is structured in two main parts. In the first part, which includes Chapters 2 to 5, the focus is on the theoretical analysis and the derivation of closed-form analytical formulas for the modelling of connected arrays. The second part, which comprises Chapters 6 and 7, reports on the practical design, the implementation of feed structures and the experimental verification. More in detail, the dissertation is organized as follows.

In Chapter 2, the theoretical formulation for the analysis of connected array is presented, as it constitutes the mathematical basis for the subsequent chapters. The derivation of the GF of a single infinite dipole is reported, as well as its generalization to a infinite periodic array of connected dipoles. Finally, analytical formulas for the active input impedance are given, for connected arrays of slots and dipoles with or without backing reflector. These expressions are remarkably useful for the design of a connected array, since they set a one-to-one correspondence between geometrical parameters and antenna parameters, thus constituting a faster alternative to numerical methods.

In Chapter 3¹, the scanning performance of connected arrays is investigated, with emphasis

¹This chapter is an extended version of the article [J1] (a list of the author's publications is included at the end of this dissertation, p. 209)

on the comparison between slot and dipole elements when the arrays are backed by a metallic plane. Based on this study, a connected-dipole design with a bandwidth in the order of 40% and wide sampling periods ($d_x = d_y \approx 0.5 \lambda_0$ at the highest useful frequency) is presented and discussed, showing its full functionality even when scanning up to $\pm 45^\circ$. In Chapter 4², an equivalent circuit representation of the array unit cell is derived. The analytical expression of the element input impedance can be expanded in different terms, each representable in circuit form. The circuit is a very powerful design tool, as all its components can be analytically derived from the geometrical parameters of the element. The equivalent circuit is used to interpret the experimental results from a dual-band connected array demonstrator, based on passive Radar Cross Section (RCS) measurements.

Chapter 5 presents a GF-based procedure to assess edge effects in finite connected arrays. First, the electric current distribution on the array is rigorously derived. Later on, the introduction of a few simplifying assumptions allows the derivation of an analytical approximation for the current distribution. This formalism provides meaningful insights in the induced dominant edge-wave mechanism.

Starting from the ideal design, in Chapter 6, the practical implementation of the feed structure is addressed. Two novel solutions are presented to avoid common-mode current propagation on the vertical feed lines. Simulation results obtained via commercial electromagnetic tools are presented.

Based on the common-mode rejection circuit described in Chapter 6, a wideband, wide-scan phased array of 7×7 connected dipoles has been designed and fabricated for 3 to 5 GHz operation. The measured results from the prototype demonstrator are presented in Chapter 7 for experimental validation.

Chapter 8 concludes with a review of the most significant results presented in this thesis and an outlook on possible future developments.

²This chapter is an extended version of the article [J3] (a list of the author's publications is included at the end of this dissertation, p. 209)

Chapter 2

Spectral Green's Functions of Connected Arrays

This chapter presents the theoretical formulation adopted for the analysis of connected arrays. The formulation is explained in detail for connected dipoles, whereas only final results are given for connected slots, as the extension is a straightforward application of the Babinet's principle. First, the problem of a single infinite dipole is considered and formalized in terms of a spectral domain integral equation. The spectral solution to this problem can be found in a closed form, therefore no discretization method (e.g. moment method) is necessary. The generalization of the procedure to an infinite periodic array of connected dipoles via Floquet's theorem is then described and leads to analytical formulas for the active input impedance of an array element. These formulas constitute, on the one hand, a very useful tool for the design of connected arrays; on the other hand, they can be expanded in constitutive terms or analyzed in terms of singularities to gain a deep physical insight into both the localized and the global behaviors of these arrays.

2.1 Green's Functions of an Infinite Dipole or Slot

The derivation of the spectral Green's Function (GF) for a single infinite slot excited by a delta-gap source was reported in [32, 36, 37]. In this section, a simple extension of the formulation is described in detail, for the case of a single infinite dipole. Similar final expressions can be derived for the case of an infinite slot and are also reported, without detailed proof, for the sake of completeness.

The geometry under analysis is depicted in Fig. 2.1(a) and consists of an infinitely long dipole oriented along x . The width w_d is assumed to be uniform along x and small compared

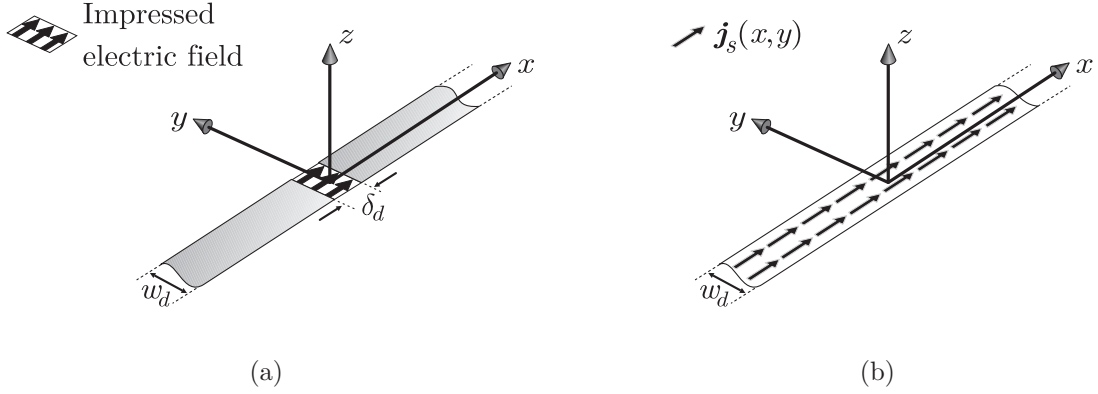


Figure 2.1: (a) Infinite dipole in free space excited by a δ -gap source; (b) equivalent unknown surface current distribution $\mathbf{j}_s(x, y)$.

to the wavelength. The dipole is excited by an electric field oriented along x , applied across a gap of dimension δ_d , and uniformly distributed over the width w_d . It should be noted that such a field is an idealized model (δ -gap source) and it is here considered for the sake of simplicity. More realistic feed structures will be widely described in Chapter 6. This initial problem can be simplified by applying an equivalence theorem. Equivalent magnetic and electric currents can be defined on the surface coinciding with the (x, y) plane, so that the boundary conditions for the tangential components of the electromagnetic field are satisfied:

$$\hat{\mathbf{z}} \times (\mathbf{h}_+ - \mathbf{h}_-) = \mathbf{j}_s(x, y) \quad \hat{\mathbf{z}} \times (\mathbf{e}_+ - \mathbf{e}_-) = -\mathbf{m}_s(x, y) \quad (2.1)$$

where the subscripts $+$ and $-$ refer to the electric and magnetic field at $z > 0$ and $z < 0$, respectively. The tangential electric field vanishes on the conductive part of the dipole; thus, from the (2.1), only the surface electric currents can be different from zero. Also in the gap region the magnetic current vanishes from the second equation in (2.1), since the tangential components of the electric field are continuous ($\hat{\mathbf{z}} \times \mathbf{e}_+ = \hat{\mathbf{z}} \times \mathbf{e}_-$ for $z \rightarrow 0$). Hence, the equivalent problem becomes the one in Fig. 2.1(b), where only electric surface currents $\mathbf{j}_s(x, y)$ are distributed over the region occupied by the dipole.

If the dipole width is assumed to be small with respect to the wavelength, the unknown currents can be considered as oriented along x only, i.e. $\mathbf{j}_s(x, y) = j_x(x, y)\hat{\mathbf{x}}$. By imposing the continuity of the total electric field along the dipole axis ($y = 0$), the following integral equation is obtained:

$$\int_{-\infty}^{\infty} \int_{-w_d/2}^{w_d/2} g_{xx}^{EJ}(x-x', -y') j_x(x', y') dx' dy' = -e_x^i(x, 0) \quad (2.2)$$

where $e_x^i(x, y)$ is the x -oriented impressed electric field. The integral at the left hand side (LHS) is the secondary field radiated by the electric current on the strip. g_{xx}^{EJ} represents the spatial scalar GF associated with the electric field radiated by an electric current, and its expression is derived in the spectral domain in Appendix A.

Equation (2.2) is a two-dimensional convolution integral in the two spatial variables x' and y' . However, under the assumption of small width of the dipole with respect to the wavelength, a separable space dependence of the unknown current can be assumed: $j_x(x', y') = i(x') j_t(y')$. The transverse y -dependence is chosen to satisfy the edge singularity condition:

$$j_t(y') = \frac{2}{w_d \pi} \frac{1}{\sqrt{1 - \left(\frac{2y'}{w_d}\right)^2}} \quad (2.3)$$

where the normalization constant $2/(w_d \pi)$ is such that $i(x')$ represents a net current flow along the dipole at any point $x = x'$.

In a similar way, the x -component of the impressed electric field can also be expressed as the product between two functions of the longitudinal (x) and transverse (y) variables; that is, in the transmission case, $e_x^i(x, y) = (V_0/\delta_d) \text{rect}_{\delta_d}(x) \text{rect}_{w_d}(y)$, where V_0 is the amplitude of the excitation voltage and the rectangular function $\text{rect}_T(x)$ is equal to 1 if $x \in [-T/2, T/2]$ and 0 otherwise.

With this separable functional dependence, the integral equation (2.2) can be written as

$$\int_{-\infty}^{\infty} \underbrace{\left(\int_{-w_d/2}^{w_d/2} g_{xx}^{EJ}(x-x', -y') j_t(y') dy' \right)}_{d(x-x')} i(x') dx' = -\frac{V_0}{\delta_d} \text{rect}_{\delta_d}(x). \quad (2.4)$$

By grouping the terms depending on y' together, a function $d(x-x')$ can be defined as the space-convolution integral in the transverse variable y' . Since the GFs of stratified media are known in closed form in the spectral domain, it is convenient to express the integral

equation (2.4) in the same domain. The spatial convolution $\int_{-\infty}^{\infty} d(x-x')i(x')dx'$ is Fourier transformed into the product of the spectra:

$$\frac{1}{2\pi} \int_{-\infty}^{\infty} D(k_x)I(k_x)e^{-jk_x x} dk_x = -\frac{1}{2\pi} V_0 \int_{-\infty}^{\infty} \text{sinc}\left(\frac{k_x \delta_d}{2}\right) e^{-jk_x x} dk_x. \quad (2.5)$$

$D(k_x)$, $I(k_x)$ and $\text{sinc}(\frac{k_x \delta_d}{2})$ are the Fourier transforms of the spatial functions $d(x)$, $i(x)$ and $\frac{1}{\delta_d} \text{rect}_{\delta_d}(x)$, respectively. We assume a time (t) dependence of the fields according to the exponential function $e^{j\omega t}$, where ω is the radian frequency. Since Eq. (2.5) is valid for any x , one can equate the integrands at the right- and left-hand side, which leads to

$$I(k_x) = \frac{-V_0 \text{sinc}\left(\frac{k_x \delta_d}{2}\right)}{D(k_x)}. \quad (2.6)$$

The current along the entire dipole axis can be expressed at any position x as an inverse Fourier transform:

$$i(x) = \frac{1}{2\pi} \int_{-\infty}^{\infty} \frac{-V_0 \text{sinc}(k_x)}{D(k_x)} e^{-jk_x x} dk_x. \quad (2.7)$$

Recalling the definition of the function $d(x)$ in Eq. (2.4), the denominator $D(k_x)$ can be written as

$$D(k_x) = \frac{1}{2\pi} \int_{-\infty}^{\infty} \tilde{G}_{xx}^{EJ}(k_x, -y') j_t(y') dy' \quad (2.8)$$

where $\tilde{G}_{xx}^{EJ}(k_x, y)$ is the Fourier transform, with respect to the longitudinal spatial variable (x) only, of the spatial GF $g_{xx}^{EJ}(x, y)$. Using Parseval's theorem, Eq. (2.8) can be also expressed as

$$D(k_x) = \frac{1}{2\pi} \int_{-\infty}^{\infty} G_{xx}^{EJ}(k_x, k_y) J_t(k_y) dk_y. \quad (2.9)$$

J_t is the Fourier transform of the transverse electric current distribution in (2.3) and it can be easily proved to be equal to $J_0(k_y w_d/2)$, with J_0 being the Bessel function of the first

kind and of zeroth order. The expression for the xx component of the dyadic GF $\underline{\underline{G}}^{EJ}$ is given in Appendix A (Eq. (A.29)) and can be substituted in (2.9), which leads to

$$D(k_x) = \frac{1}{2\pi} \int_{-\infty}^{\infty} -\frac{v_{TM}k_x^2 + v_{TE}k_y^2}{k_\rho^2} J_0\left(\frac{k_y w_d}{2}\right) dk_y \quad (2.10)$$

with $k_\rho = \sqrt{k_x^2 + k_y^2}$. The values of the voltages v_{TM} and v_{TE} depend on the specific stratification along the z axis. In the next sections, the integral in Eq. (2.10) will be evaluated for the two specific cases: a dipole in free space and in the presence of a backing reflector.

2.1.1 Current Solution for an Infinite Dipole

Free Space

Equation (2.10) contains a generic expression of the scalar electric field GF, valid for general stratification along z . The explicit expression of the GF, for the specific case of a dipole in free space, is derived in Appendix A, and given by the expression (A.67). By substituting (A.67) for $z = 0$ in (2.10), one obtains

$$D_{fs}(k_x) = -\frac{\zeta_0}{2k_0} \frac{1}{2\pi} \int_{-\infty}^{\infty} \frac{k_0^2 - k_x^2}{\sqrt{k_0^2 - k_x^2 - k_y^2}} J_0\left(\frac{k_y w_d}{2}\right) dk_y \quad (2.11)$$

where k_0 is the wave number in free space and ζ_0 is the free space characteristic impedance. This spectral integration can be performed in analytical form by resorting to the following identity [38]:

$$\int_{-\infty}^{\infty} \frac{J_0\left(\frac{k_y w_d}{2}\right)}{\sqrt{k_0^2 - k_x^2 - k_y^2}} dk_y = \pi J_0\left(\frac{w_d}{4} \sqrt{k_0^2 - k_x^2}\right) H_0^{(2)}\left(\frac{w_d}{4} \sqrt{k_0^2 - k_x^2}\right) \quad (2.12)$$

where $H_0^{(2)}$ is the Hankel function of the second type and zeroth order. The longitudinal spectral GF becomes

$$D_{fs}(k_x) = -\frac{\zeta_0}{4k_0} (k_0^2 - k_x^2) J_0\left(\frac{w_d}{4} \sqrt{k_0^2 - k_x^2}\right) H_0^{(2)}\left(\frac{w_d}{4} \sqrt{k_0^2 - k_x^2}\right). \quad (2.13)$$

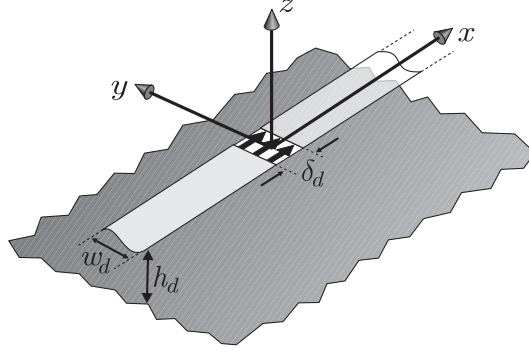


Figure 2.2: Infinite dipole in the presence of a backing reflector at distance h_d .

One can note that, to obtain the same result, an equivalent approach can be adopted, which starts from the GF of an infinite filament current and proceeds with the integration over the finite width of the dipole.

Backing Reflector

Let us now consider the inclusion of an infinite backing reflector located at $z = -h_d$, as shown in Fig. 2.2. In this case, by using the expression of the scalar GF given in Eq. (A.72), Eq. (2.10) can be written as follows:

$$D_{br}(k_x) = -\frac{\zeta_0}{2k_0} \frac{1}{2\pi} \int_{-\infty}^{\infty} \frac{k_0^2 - k_x^2}{\sqrt{k_0^2 - k_x^2 - k_y^2}} J_0\left(\frac{k_y w_d}{2}\right) (1 - e^{-j2k_z h_d}) dk_y. \quad (2.14)$$

The integral can be then split into two terms:

$$D_{br}(k_x) = D_{fs}(k_x) + D_{refl}(k_x) = -\frac{\zeta_0}{2k_0} \frac{1}{2\pi} (k_0^2 - k_x^2) \left(\int_{-\infty}^{\infty} \frac{J_0\left(\frac{k_y w_d}{2}\right)}{\sqrt{k_0^2 - k_x^2 - k_y^2}} dk_y - \int_{-\infty}^{\infty} \frac{J_0\left(\frac{k_y w_d}{2}\right)}{\sqrt{k_0^2 - k_x^2 - k_y^2}} e^{-j2k_z h_d} dk_y \right) \quad (2.15)$$

where $D_{fs}(k_x)$ has already been evaluated in Eq. (2.13), while the reflected contribution, assuming a small width of the dipole compared to the wavelength ($J_0(k_y w_d/2) \approx 1$), is given by

$$D_{refl}(k_x) \approx \frac{\zeta_0}{2k_0} (k_0^2 - k_x^2) \frac{1}{2\pi} \int_{-\infty}^{\infty} \frac{e^{-j2k_z h_d}}{\sqrt{k_0^2 - k_x^2 - k_y^2}} dk_y. \quad (2.16)$$

The integral in the last equation can be expressed in closed form [39] in terms of Hankel function, which results in the following total expression:

$$D_{br}(k_x) \approx \frac{\zeta_0(k_0^2 - k_x^2)}{4k_0} \left(H_0^{(2)} \left(2h_d \sqrt{k_0^2 - k_x^2} \right) - J_0 \left(\frac{w_d}{4} \sqrt{k_0^2 - k_x^2} \right) H_0^{(2)} \left(\frac{w_d}{4} \sqrt{k_0^2 - k_x^2} \right) \right). \quad (2.17)$$

Once analytical expressions have been derived for the function $D(k_x)$, the current spectrum can be evaluated by using Eq. (2.6), while the spatial current distribution can be numerically calculated from the inverse Fourier integral in Eq. (2.7).

2.1.2 Current Solution for an Infinite Slot in Free Space and with Backing Reflector

A very similar procedure can be followed for an infinite slot, to find the longitudinal voltage distribution along its axis. The geometry in this case would be the one in Fig. 2.3(a). An equivalent problem is shown in Fig. 2.3(b), where the slot region is replaced with an equivalent magnetic current distribution $\mathbf{m}_s(x, y)$ over an infinitely thin and perfectly conducting surface.

Assuming a functional separability of the equivalent surface current between transverse and longitudinal dependence ($\mathbf{m}_s(x, y) = v(x)m_t(y)\hat{\mathbf{x}}$), and following the same steps as for the dipole case, we can write the voltage distribution along the x axis as

$$v(x) = \frac{1}{2\pi} \int_{-\infty}^{\infty} \frac{I_0 \operatorname{sinc} \left(\frac{k_x \delta_s}{2} \right)}{D^{slot}(k_x)} e^{-jk_x x} dk_x \quad (2.18)$$

where I_0 is the current amplitude of the excitation. The spectral function $D^{slot}(k_x)$ assumes different forms in the free space case and in the presence of a backing reflector. For free space, it is given by

$$D_{fs}^{slot} = \frac{1}{\zeta_0 k_0} (k_0^2 - k_x^2) J_0 \left(\frac{w_s}{4} \sqrt{k_0^2 - k_x^2} \right) H_0^{(2)} \left(\frac{w_s}{4} \sqrt{k_0^2 - k_x^2} \right) \quad (2.19)$$

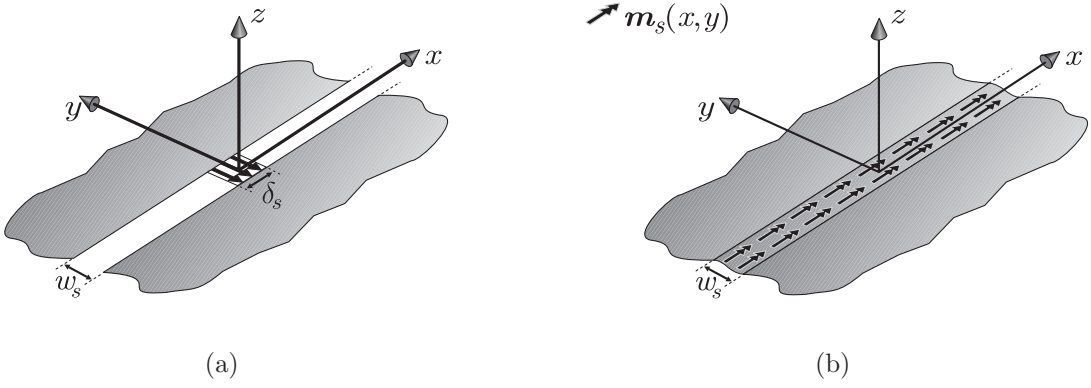


Figure 2.3: (a) Infinite slot in free space excited by a δ -gap source; (b) equivalent unknown surface current distribution $\mathbf{m}_s(x, y)$.

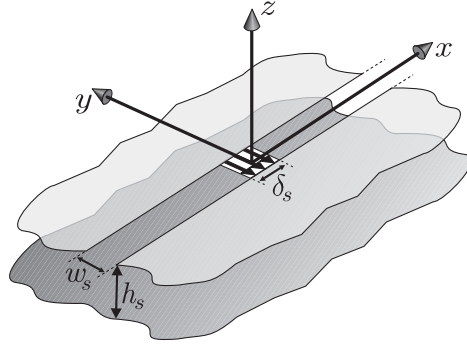


Figure 2.4: Infinite slot in the presence of a backing reflector at distance h_s .

while, in the case of a metallic reflector at distance h_s from the plane of the slot, as depicted in Fig. 2.4, it is given by

$$D_{br}^{slot}(k_x) = -\frac{1}{\zeta_0 k_0} (k_0^2 - k_x^2) \cdot \left(H_0^{(2)} \left(2h_s \sqrt{k_0^2 - k_x^2} \right) - J_0 \left(\frac{w_s}{4} \sqrt{k_0^2 - k_x^2} \right) H_0^{(2)} \left(\frac{w_s}{4} \sqrt{k_0^2 - k_x^2} \right) \right). \quad (2.20)$$

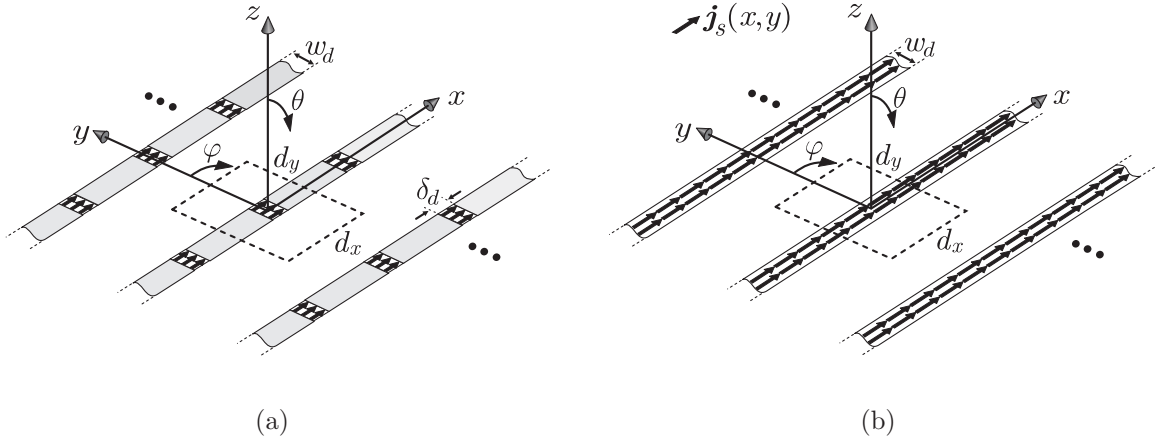


Figure 2.5: (a) Infinite periodic array of dipoles in free space excited by δ -gap sources; (b) equivalent unknown current distribution $\mathbf{j}_s(x, y)$.

2.2 Green's Function of 2-D Periodic Connected Arrays

The theoretical formulation described for a single infinite dipole can be generalized to the case of an infinite periodic array of dipoles. The initial problem is shown in Fig. 2.5(a). It consists of a periodic array of x -oriented dipoles at distance d_y , each one excited at an infinite number of gaps, with period d_x . The cross section w_d of the dipole is uniform in x and electrically small. Figure 2.5(b) represents a simpler problem obtained by applying the equivalence principle.

By enforcing the continuity of the tangential electric field along the x axis ($y = 0$), as it was done for the single dipole in Eq. (2.2), one can write

$$\int_{-\infty}^{\infty} \int_{-\infty}^{\infty} g_{xx}^{EJ}(x - x', -y') j_x(x', y') dx' dy' = -e_x^i(x, 0). \quad (2.21)$$

For a transmitting array, the impressed field is given by an infinite sum of rectangular functions centered in the feeding points:

$$e_x^i(x, 0) = \sum_{n_x=-\infty}^{\infty} \frac{V_0}{\delta_d} \text{rect}_{\delta_d}(x - n_x d_x) e^{-jk_{z0} n_x d_x} \quad (2.22)$$

where $k_{x0} = k_0 \sin \theta_0 \cos \varphi_0$ is the longitudinal excitation law when the array is scanning toward the direction (θ_0, φ_0) . In the transverse direction we define $k_{y0} = k_0 \sin \theta_0 \sin \varphi_0$. The spatial integral in (2.21), whose domain is the entire surface represented by the plane (x', y') , can be expressed as the sum of an infinite number of integrals over the array periodic cells:

$$\sum_{n_x=-\infty}^{\infty} \sum_{n_y=-\infty}^{\infty} \int_{n_x d_x - \frac{d_x}{2}}^{n_x d_x + \frac{d_x}{2}} \int_{n_y d_y - \frac{d_y}{2}}^{n_y d_y + \frac{d_y}{2}} g_{xx}^{EJ}(x - x', -y') i(x') j_t(y') dx' dy' = -e_x^i(x, 0). \quad (2.23)$$

By resorting to the variable substitutions $x' = x' - n_x d_x$, $y' = y' - n_y d_y$ and writing the GF in the spectral domain, one obtains

$$\frac{1}{4\pi^2} \int_{-\infty}^{+\infty} \int_{-\infty}^{+\infty} \sum_{n_x=-\infty}^{\infty} \sum_{n_y=-\infty}^{\infty} \int_{-\frac{d_x}{2}}^{\frac{d_x}{2}} \int_{-\frac{d_y}{2}}^{\frac{d_y}{2}} i(x' - n_x d_x) j_t(y' - n_y d_y) G_{xx}^{EJ}(k_x, k_y) e^{jk_x n_x d_x} e^{jk_y n_y d_y} e^{-jk_x x'} e^{jk_y y'} dk_x dk_y dx' dy' = -e_x^i(x, 0). \quad (2.24)$$

Due to periodicity along the x - and y -directions, one can write $i(x' - n_x d_x) = i(x') e^{-jk_{x0} n_x d_x}$ and $j_t(y' - n_y d_y) = j_t(y') e^{-jk_{y0} n_y d_y}$. Hence, by grouping the terms depending on x' and y' , one can identify two Fourier transforms (between parentheses):

$$\frac{1}{4\pi^2} \int_{-\infty}^{+\infty} \int_{-\infty}^{+\infty} \sum_{n_x=-\infty}^{\infty} \sum_{n_y=-\infty}^{\infty} \left(\int_{-\frac{d_x}{2}}^{\frac{d_x}{2}} i(x') e^{jk_x x'} dx' \right) \left(\int_{-\frac{d_y}{2}}^{\frac{d_y}{2}} j_t(y') e^{jk_y y'} dy' \right) G_{xx}^{EJ}(k_x, k_y) e^{j(k_x - k_{x0}) n_x d_x} e^{j(k_y - k_{y0}) n_y d_y} e^{-jk_x x} dk_x dk_y = -e_x^i(x, 0). \quad (2.25)$$

Therefore, by writing also the impressed field at the right hand side (RHS), defined by Eq. (2.22), as an inverse Fourier transform, the integral equation becomes

$$\frac{1}{4\pi^2} \int_{-\infty}^{+\infty} \int_{-\infty}^{+\infty} \sum_{n_x=-\infty}^{\infty} \sum_{n_y=-\infty}^{\infty} I(k_x) J_0\left(\frac{k_y w_d}{2}\right) G_{xx}^{EJ}(k_x, k_y) e^{j(k_x - k_{x0}) n_x d_x} e^{j(k_y - k_{y0}) n_y d_y} e^{-jk_x x} dk_x dk_y = -\frac{1}{2\pi} \int_{-\infty}^{+\infty} V_0 \operatorname{sinc}\left(\frac{k_x \delta_d}{2}\right) \sum_{n_x=-\infty}^{\infty} e^{j(k_x - k_{x0}) n_x d_x} e^{-jk_x x} dk_x. \quad (2.26)$$

We can now resort to Poisson's summation formula [40], which relates the Fourier series coefficients of the periodic summation of a function f to values of the function's continuous Fourier transform:

$$\sum_{n=-\infty}^{\infty} f(n) = \sum_{m=-\infty}^{\infty} \int_{-\infty}^{\infty} f(\nu) e^{-j2\pi m\nu} d\nu. \quad (2.27)$$

By applying Poisson's sum formula to the infinite sums in Eq. (2.26), after a few algebraic steps, we obtain the following expressions:

$$\begin{aligned} \sum_{n_x=-\infty}^{\infty} e^{j(k_x-k_{x0})n_x d_x} &= \frac{2\pi}{d_x} \sum_{m_x=-\infty}^{\infty} \delta(k_x - k_{xm}) \\ \sum_{n_y=-\infty}^{\infty} e^{j(k_y-k_{y0})n_y d_y} &= \frac{2\pi}{d_y} \sum_{m_y=-\infty}^{\infty} \delta(k_y - k_{ym}) \end{aligned} \quad (2.28)$$

where $k_{xm} = k_{x0} - \frac{2\pi m_x}{d_x}$, $k_{ym} = k_{y0} - \frac{2\pi m_y}{d_y}$ are referred to as the Floquet wave numbers, and δ represents the Dirac distribution. Equation (2.26) then becomes

$$\begin{aligned} \frac{1}{d_x d_y} \int_{-\infty}^{+\infty} \int_{-\infty}^{+\infty} I(k_x) J_0\left(\frac{k_y w_d}{2}\right) G_{xx}^{EJ}(k_x, k_y) \sum_{m_x=-\infty}^{\infty} \delta(k_x - k_{xm}) \sum_{m_y=-\infty}^{\infty} \delta(k_y - k_{ym}) e^{-jk_x x} dk_x dk_y = \\ - \frac{1}{d_x} \int_{-\infty}^{+\infty} V_0 \operatorname{sinc}\left(\frac{k_x \delta_d}{2}\right) \sum_{m_x=-\infty}^{\infty} \delta(k_x - k_{xm}) e^{-jk_x x} dk_x. \end{aligned} \quad (2.29)$$

From the property of the Dirac δ -distribution, the integration over a continuous spectral variable becomes a summation over the discrete Floquet wave numbers k_{xm} , k_{ym} :

$$\begin{aligned} \frac{1}{d_x d_y} \sum_{m_x=-\infty}^{\infty} \sum_{m_y=-\infty}^{\infty} I(k_{xm}) J_0\left(\frac{k_{ym} w_d}{2}\right) G_{xx}^{EJ}(k_{xm}, k_{ym}) e^{-jk_{xm} x} = \\ - \frac{V_0}{d_x} \sum_{m_x=-\infty}^{\infty} \operatorname{sinc}\left(\frac{k_{xm} \delta_d}{2}\right) e^{-jk_{xm} x}. \end{aligned} \quad (2.30)$$

Defining

$$D_\infty(k_x) = \frac{1}{d_y} \sum_{m_y=-\infty}^{\infty} J_0\left(\frac{k_{ym}w_d}{2}\right) G_{xx}^{EJ}(k_x, k_{ym}) \quad (2.31)$$

leads to

$$\frac{1}{d_x} \sum_{m_x=-\infty}^{\infty} I(k_{xm}) D_\infty(k_{xm}) e^{-jk_{xm}x} = -\frac{V_0}{d_x} \sum_{m_x=-\infty}^{\infty} \text{sinc}\left(\frac{k_{xm}\delta_d}{2}\right) e^{-jk_{xm}x}. \quad (2.32)$$

Since the previous identity holds for any x , one can equate the respective spectra for each plane wave ($e^{-jk_{xm}x}$), thus obtaining the discrete current spectrum:

$$I(k_{xm}) = \frac{-V_0 \text{sinc}\left(\frac{k_{xm}\delta_d}{2}\right)}{D_\infty(k_{xm})}. \quad (2.33)$$

2.2.1 Active Impedance of a Unit Cell for Connected Arrays of Dipoles

The spectrum in Eq. (2.33) can be inversely Fourier transformed, which leads to an explicit spatial expression of the current:

$$i(x) = \frac{1}{d_x} \sum_{m_x=-\infty}^{\infty} \frac{-V_0 \text{sinc}\left(\frac{k_{xm}\delta_d}{2}\right)}{D_\infty(k_{xm})} e^{-jk_{xm}x}. \quad (2.34)$$

The active input admittance can be calculated at any feed point in an infinite periodic array, for instance for the array element in the origin ($n_x = n_y = 0$). In this case, the active input impedance is

$$y = \frac{1}{\delta_d} \int_{-\frac{\delta_d}{2}}^{\frac{\delta_d}{2}} i(x) dx = \frac{1}{d_x} \sum_{m_x=-\infty}^{\infty} \frac{-V_0 \text{sinc}^2\left(\frac{k_{xm}\delta_d}{2}\right)}{D_\infty(k_{xm})} \quad (2.35)$$

where we used the identity $\frac{1}{\delta_d} \int_{-\delta_d/2}^{\delta_d/2} e^{-jk_{xm}x} dx = \text{sinc}(k_{xm}\delta_d/2)$.

By substituting Eq. (2.31) in Eq. (2.35), with the explicit expression of the scalar spectral GF for free space (Eq. (A.67)), leads to

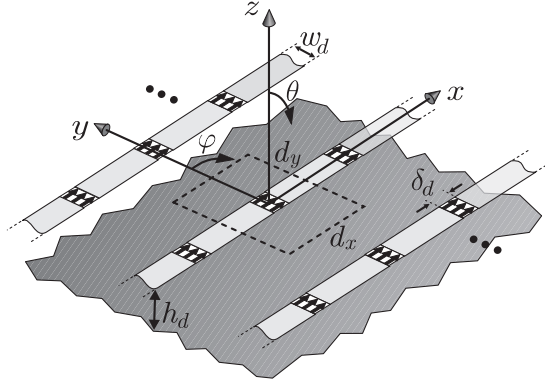


Figure 2.6: Infinite periodic array of dipoles in the presence of a backing reflector located at $z = -h_d$.

$$y_{dipole}^{fs} = \frac{2k_0 d_y}{\zeta_0 d_x} \sum_{m_x=-\infty}^{\infty} \frac{\text{sinc}^2(k_{xm} \delta_d / 2)}{(k_0^2 - k_{xm}^2) \sum_{m_y=-\infty}^{\infty} \frac{J_0(k_{ym} \frac{w_d}{2})}{k_{zm}}} \quad (2.36)$$

where $k_{zm} = \sqrt{k_0^2 - k_{xm}^2 - k_{ym}^2}$ and we assumed a unit voltage excitation ($V_0 = 1$).

If a backing reflector is included, as shown in Fig. 2.6, the expression (2.35) is still valid, but the pertinent expression of the GF is the one in Eq. (A.70). The input admittance in this case is given by

$$y_{dipole}^{br} = \frac{k_0 d_y}{\zeta_0 d_x} \sum_{m_x=-\infty}^{\infty} \frac{\text{sinc}^2(k_{xm} \delta_d / 2)}{(k_0^2 - k_{xm}^2) \sum_{m_y=-\infty}^{\infty} \frac{J_0(k_{ym} \frac{w_d}{2})}{k_{zm}(1-j \cot(k_{zm} h_d))}}. \quad (2.37)$$

The evaluation of the admittance in (2.36) and (2.37) involves infinite series of Floquet modes. However, the spectral sums can be truncated to a finite number of terms. The convergence rate of the series depends on the geometry of the unit cell. To highlight this aspect, Figs. 2.7(a) and 2.7(b) show the active impedances z_{dipole}^{fs} and z_{dipole}^{br} , which are the reciprocals of the admittances defined by Eqs. (2.36) and (2.37), as a function of the number of Floquet modes considered in the spectral sums in m_x and m_y . Three cases are considered: $w_d = \delta_d = 0.1 \lambda_0$; $w_d = 0.1 \lambda_0, \delta_d = 0.01 \lambda_0$; and $w_d = 0.01 \lambda_0, \delta_d = 0.1 \lambda_0$. The remaining geometrical parameters are set to $d_x = d_y = 0.5 \lambda_0$, $h_d = 0.25 \lambda_0$, with λ_0 being the wavelength at the frequency f_0 . The calculation frequency is equal to $0.6 f_0$ and the array is scanned to broadside. It can be noted that a slower convergence of the spectral sums occurs for either a small gap or a small width of the dipole. In fact, an higher number of modes is required to model the reactive energy associated with small

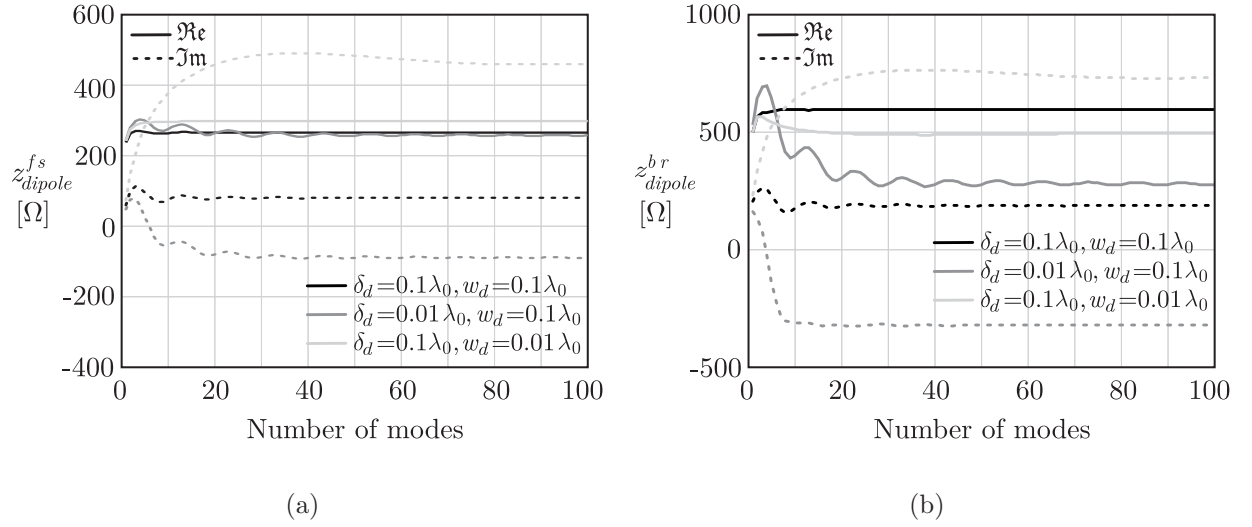


Figure 2.7: Analytical expression of the active impedance for a connected array of dipoles as a function of the number of Floquet modes in the spectral sums in Eqs. (2.36) and (2.37): (a) free space; (b) backing reflector. The dimensions are $d_x = d_y = 0.5 \lambda_0$, $h_d = 0.25 \lambda_0$, with λ_0 being the wavelength at the frequency f_0 . Three cases are considered: 1) $w_d = \delta_d = 0.1 \lambda_0$; 2) $w_d = 0.1 \lambda_0, \delta_d = 0.01 \lambda_0$; 3) $w_d = 0.01 \lambda_0, \delta_d = 0.1 \lambda_0$. The calculation frequency is $0.6 f_0$ and a broadside scanning is considered.

dimensions of the dipole gap (capacitive) or the dipole width (inductive) in the expression of the input admittance.

Figure 2.8 shows the active impedances z_{dipole}^{fs} and z_{dipole}^{br} as a function of the frequency for a connected array of dipoles in free space and with backing reflector, respectively. For validation of the GF-based procedure, the results of the analytical expressions are compared with full-wave simulations obtained via Ansoft HFSS [41]. The curves refer to $d_x = d_y = 0.5 \lambda_0$, $w_d = \delta_d = 0.1 \lambda_0$, $h_d = 0.25 \lambda_0$, with λ_0 being the wavelength at the frequency f_0 . The Floquet sums in Eqs. (2.36) and (2.37) have been truncated at $m_x = \pm 20$ and $m_y = \pm 20$, as higher order modes are negligible for this choice of the geometrical parameters, as shown in Fig. 2.7. A good agreement can be observed when comparing the analytical expressions with HFSS results. Although the results are not reported here for the sake of brevity, the same accuracy was observed for scanning angles, and for different geometrical parameters.

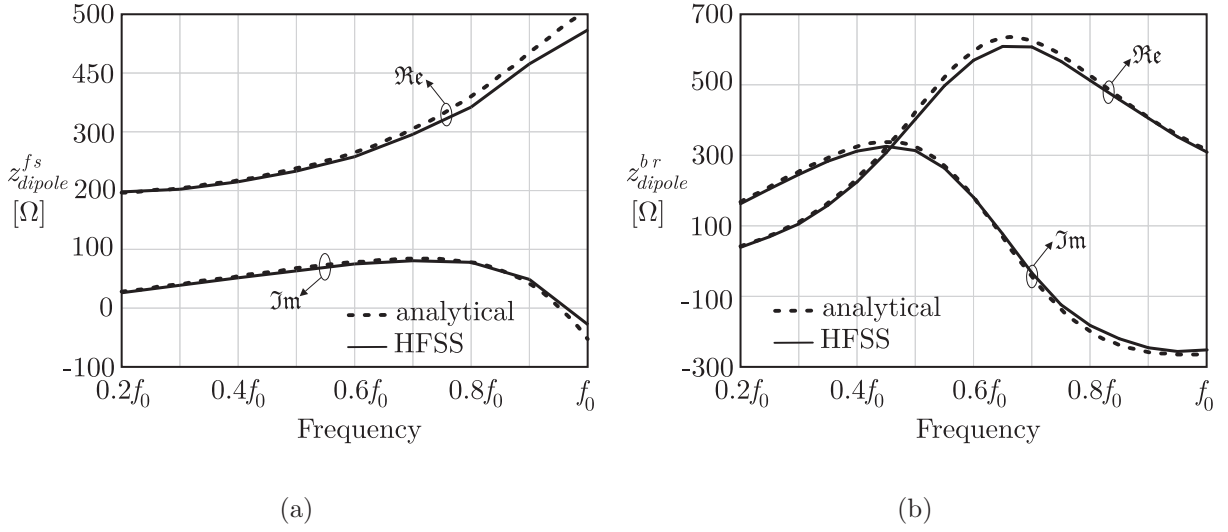


Figure 2.8: Analytical expression of the active impedance for a connected array of dipoles, compared with HFSS: (a) free space; (b) backing reflector. The dimensions are $d_x = d_y = 0.5 \lambda_0$, $w_d = \delta_d = 0.1 \lambda_0$, $h_d = 0.25 \lambda_0$, with λ_0 being the wavelength at the frequency f_0 , and a broadside scanning is assumed.

2.2.2 Active Impedance of a Unit Cell for Connected Arrays of Slots

Similar expressions can be obtained for the active input impedance of the unit cell of an infinite array of slots, with or without backing reflector (Fig. 2.9). The pertinent expressions are given by

$$z_{slot}^{fs} = \frac{k_0 \zeta_0 d_y}{2d_x} \sum_{m_x=-\infty}^{\infty} \frac{\text{sinc}^2(k_{xm} \delta_s / 2)}{(k_0^2 - k_{xm}^2) \sum_{m_y=-\infty}^{\infty} \frac{J_0(k_{ym} \frac{w_s}{2})}{k_{zm}}} \quad (2.38)$$

for free space and

$$z_{slot}^{br} = \frac{k_0 \zeta_0 d_y}{d_x} \sum_{m_x=-\infty}^{\infty} \frac{\text{sinc}^2(k_{xm} \delta_s / 2)}{(k_0^2 - k_{xm}^2) \sum_{m_y=-\infty}^{\infty} \frac{J_0(k_{ym} \frac{w_s}{2}) (1 - j \cot(k_{zm} h_s))}{k_{zm}}} \quad (2.39)$$

for a backed array.

Figures 2.10(a) and (b) show the active impedances given by Eqs. (2.38) and (2.39), respectively. The considered geometrical parameters are $d_x = d_y = 0.5 \lambda_0$, $w_s = \delta_s = 0.1 \lambda_0$, $h_s = 0.25 \lambda_0$, where λ_0 is the wavelength at the frequency f_0 . Comparisons with HFSS

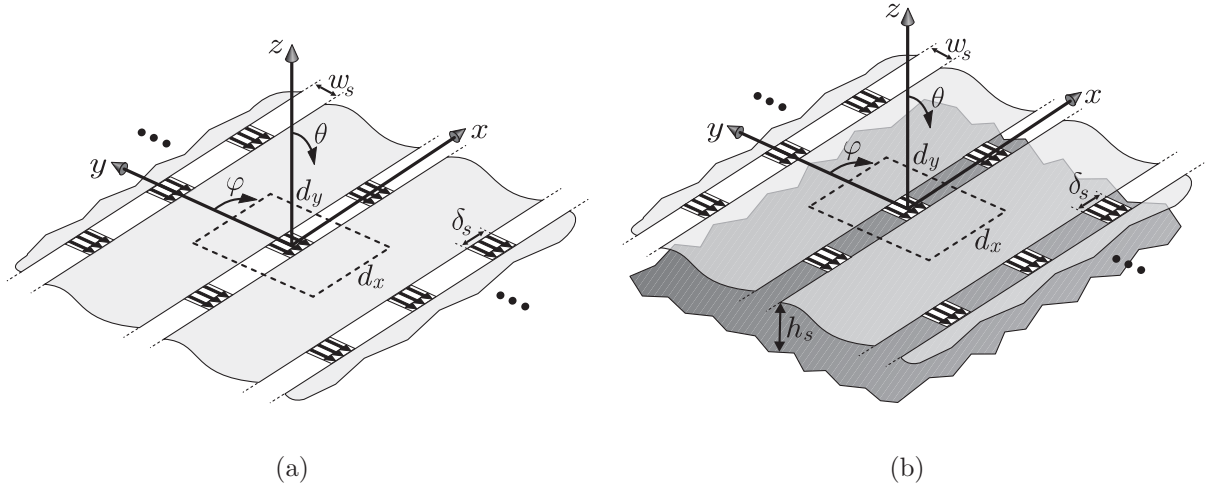


Figure 2.9: Infinite periodic array of slots (a) in free space and (b) with backing reflector at distance h_s .

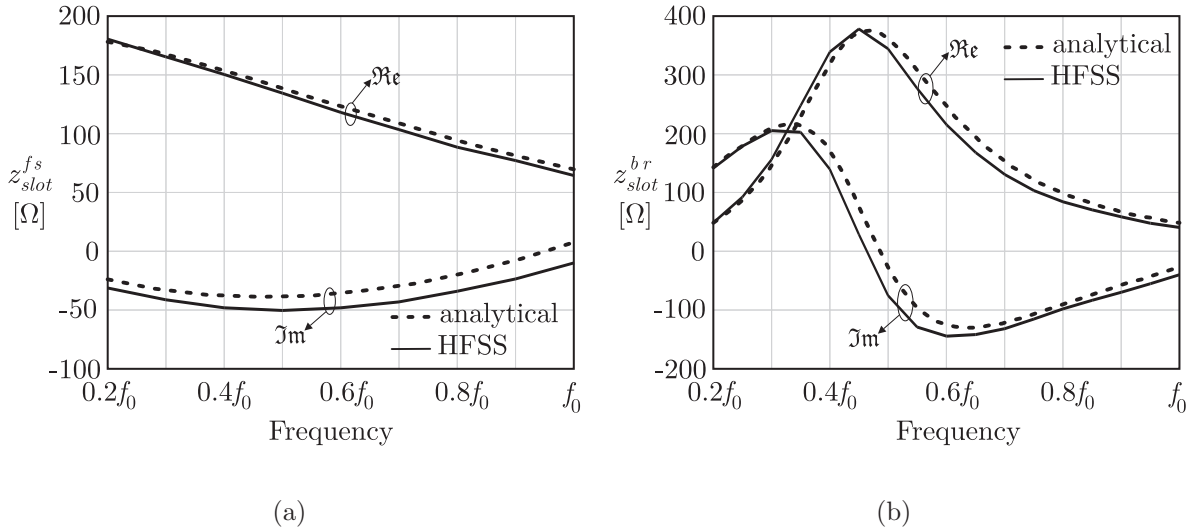


Figure 2.10: Analytical expression of the active impedance for a connected array of dipoles, compared with HFSS: (a) free space; (b) backing reflector. The dimensions are $d_x = d_y = 0.5 \lambda_0$, $w_s = \delta_s = 0.1 \lambda_0$, $h_s = 0.25 \lambda_0$, with λ_0 being the wavelength at the frequency f_0 .

show a similar accuracy in the dipole case, reported in Fig. 2.8.

The analytical expressions for the active impedance given in Eqs. (2.36), (2.37), (2.38) and (2.39) represent a very powerful tool for the design of connected arrays. As demonstrated in [30, 31], for both the cases of array of connected dipoles and slots in free space, the

bandwidth is theoretically unlimited in the sense that, although there is an upper cut-off frequency, there is practically no cut-off at the low end of the band. Indeed, for the static case at zero frequency, the array in free-space can be interpreted as an infinite current sheet whose impedance tends to the parallel of two free-space impedances ($\zeta_0/2$). This is true for an infinite array without a back plane, since the reflector would short-circuit the current sheet in the static case. The low-frequency characteristics of the array can be obtained by retaining only the lowest-order terms ($m_x = 0, m_y = 0$) in Eqs. (2.36) and (2.38). The resulting expression of the impedance is frequency independent, as it was shown in [31]. The presence of a back plane introduces a dependence on the frequency, thus reducing the bandwidth of the connected array. A study of the array performance, for the case where a backing plane is included, is reported in Chapter 3.

Chapter 3

Scanning Behavior of Backed Connected Arrays

In this chapter, the scanning properties of connected array are investigated, with focus on the comparison between slots and dipoles. The scan performance of this type of arrays is governed by a number of factors, such as the array sampling, the distance from the ground plane and the reactive energy associated with the feed points. In particular, it is shown how the capacitive energy stored in the feed gaps of connected dipoles can be used to match the array for wide-scan angles. This observation sets a preference for connected dipoles over connected slots. A design with a bandwidth in the order of 40% and wide sampling periods ($d_x = d_y \approx 0.5 \lambda_0$ at the highest useful frequency) is presented and discussed. The designed array keeps its full functionality even when scanning up to $\pm 45^\circ$.

3.1 Impedance of Connected Arrays when Scanning

The slot and dipole arrays under consideration are shown in Fig. 3.1(a) and (b), respectively, together with the pertinent reference system and characterizing parameters. The derivation of the Green's Function (GF) for connected arrays of slots and dipoles was described in Chapter 2 and led to analytical expressions for the input impedance/admittance in the case of backed arrays (Eqs. (2.39) and (2.37)). For the slot case in Fig. 3.1(a), the active input impedance of an array element can be expressed as follows:

$$z_{slot}^{br} = \frac{k_0 \zeta_0 d_y}{d_x} \sum_{m_x=-\infty}^{\infty} \frac{\text{sinc}^2(k_{xm} \delta_s / 2)}{(k_0^2 - k_{xm}^2)} \sum_{m_y=-\infty}^{\infty} \frac{J_0(k_{ym} \frac{w_s}{2}) (1 - j \cot(k_{zm} h_s))}{k_{zm}} \quad (3.1)$$

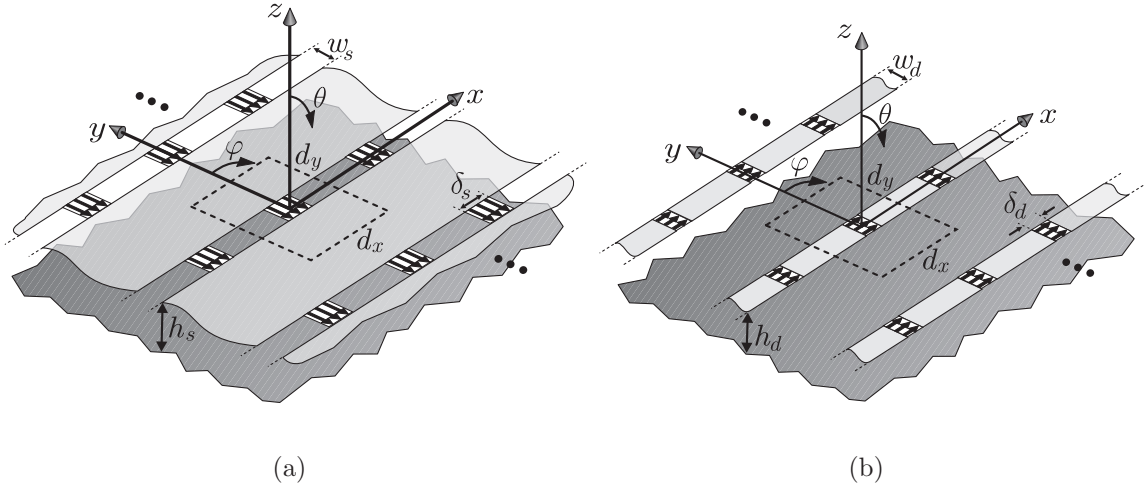


Figure 3.1: Two-dimensional periodic connected arrays of (a) slots and (b) dipoles with backing reflector.

where J_0 is the Bessel function of zeroth order of the first kind, k_0 is the free-space propagation constant, $k_{xm} = k_0 \sin \theta_0 \cos \varphi_0 - \frac{2\pi m_x}{d_x}$, $k_{ym} = k_0 \sin \theta_0 \sin \varphi_0 - \frac{2\pi m_y}{d_y}$, and $k_{zm} = \sqrt{k_0^2 - k_{xm}^2 - k_{ym}^2}$. The array is pointing toward the direction defined by the angles $\theta = \theta_0$ and $\varphi = \varphi_0$.

For the dipole structure with backing reflector depicted in Fig. 3.1(b), the active input admittance at each feed can be written as

$$y_{dipole}^{br} = \frac{1}{z_{dipole}^{br}} = \frac{k_0 d_y}{\zeta_0 d_x} \sum_{m_x=-\infty}^{\infty} \frac{\text{sinc}^2(k_{xm} \delta_d / 2)}{(k_0^2 - k_{xm}^2) \sum_{m_y=-\infty}^{\infty} \frac{J_0(k_{ym} \frac{w_d}{2})}{k_{zm}(1-j \cot(k_{zm} h_d))}}. \quad (3.2)$$

Note that here it is assumed that both slots and dipoles in Fig. 3.1 are oriented along x . This implies that the connected array of dipoles operates in a polarization orthogonal to the one associated with the connected array of slots.

3.1.1 Dominant Floquet Wave

Both expressions (3.1) and (3.2) present a clear resonance condition. The condition can be gathered by considering only the first mode ($m_x = m_y = 0$) in the double Floquet summations. Note that the dominant mode representation is a realistic hypothesis only when the array is extremely well sampled (low frequency). Under this approximation, the slot array impedance becomes

$$\tilde{z}_{slot}^{br} = z_{slot}^{br} \Big|_{m_x=m_y=0} = \frac{\zeta_0 d_y}{d_x} \frac{\cos \theta}{(1 - \sin^2 \theta \cos^2 \varphi)(1 - j \cot(k_0 h_s \cos \theta))}. \quad (3.3)$$

For the dipole case, retaining only the dominant mode, one obtains a similar expression:

$$\tilde{z}_{dipole}^{br} = z_{dipole}^{br} \Big|_{m_x=m_y=0} = \frac{\zeta_0 d_x}{d_y} \frac{1 - \sin^2 \theta \cos^2 \varphi}{\cos \theta (1 - j \cot(k_0 h_d \cos \theta))}. \quad (3.4)$$

The only difference with respect to Eq. (3.3) resides in the changed φ -dependence, consistently with the fact that the E - and H -planes are inverted in the dipole configuration with respect to the slots. The similarity between Eqs. (3.3) and (3.4) implies that there are no major differences in bandwidth between slots and dipoles, if only the fundamental Floquet mode is considered.

The resonance of the impedance is clearly given by the condition $k_0 h_{s,d} \cos \theta = \pi/2$, which implies $h_{s,d} = \lambda_0/4$ for broadside radiation. When this condition occurs, and if we assume a square periodic cell ($d_x = d_y$), it is easy to see from Eqs. (3.3) and (3.4) that $\tilde{z}_{slot}^{br} = \tilde{z}_{dipole}^{br} = \zeta_0$. Such value of the active impedance is twice as large as the asymptotic value for low frequency of a connected array of slots or dipoles without backing reflector ($\zeta_0/2$). The factor 2 derives from the fact that an array in free space radiates equally in the upper and lower half spaces. On the contrary, with a backing reflector, all the power provided to the radiating aperture is radiated in the upper half space.

If the array is pointing broadside only, the low-frequency approximations of the input impedance in Eqs. (3.3) and (3.4) state that the array can be matched with a real transmission line to present a reflection coefficient lower than -10 dB over about a 75% relative bandwidth. This can be observed from the continuous curves in Fig. 3.2, pertaining to a connected-dipole array. The height from the ground plane is $h_d = 0.25 \lambda_0$, where $\lambda_0 = \frac{c_0}{f_0}$ and c_0 is the free-space velocity. The curves are plotted as a function of the frequency, normalized with respect to f_0 . The transmission-line characteristic impedance that guarantees the widest frequency bandwidth is the one that matches the free-space impedance (377Ω). Figure 3.2 also shows the effects of scanning on the fundamental mode of the input impedance and the corresponding reflection coefficient, assuming a 377Ω feeding line. The array scanning produces two important effects.

- The input resistance is lowered by a factor of $\cos \theta$ when scanning in the E -plane and increased by a factor of $\sec \theta$ when scanning in the H -plane. This effect is readily apparent from Eqs. (3.3) and (3.4).

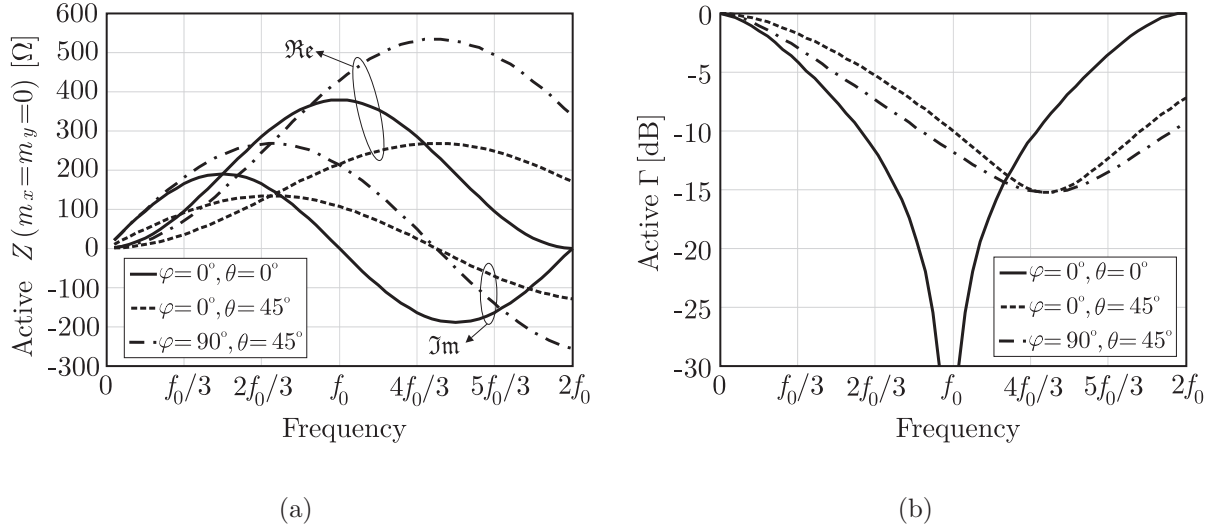


Figure 3.2: Scanning behavior of a connected array of dipoles, considering only the fundamental Floquet mode ($m_x = m_y = 0$): (a) active impedance and (b) reflection coefficient, assuming a 377Ω feeding line.

- Another important impact on the matching of the arrays as a function of the scanning results from the shift of the resonance frequency. As the scan angle grows, for example to 45° , the electrical length ($k_0 h_s \cos \theta$) becomes smaller. This implies that the resonance condition is achieved for a frequency that is 40% higher with respect to broadside (Fig. 3.2(b)).

If the low-frequency approximation is dropped, the full expression in (3.1) and (3.2) have to be considered. A parametric analysis has been performed for a connected array of slots, implementing Eq. (3.1). The maximum possible overlap between the matching bandwidth achieved at broadside and at 45° scan, on both planes, is about 30%. An example of this behavior is shown in Fig. 3.3, which reports the reflection coefficient of a well sampled array, with respect to a 400Ω transmission line. The periods of the array are $d_x = d_y = 0.4 \lambda_0$ and the curves are plotted as a function of the frequency, normalized with respect to f_0 . The results are shown for the cases of scanning at broadside and toward $\theta = 45^\circ$, in the two main planes.

The curves in Fig. 3.3 highlight two drawbacks. The first is that only a moderate bandwidth is achieved (28%). The second is that the array is highly sampled at the highest frequency of operation, which would imply the need for a very large number of Transmit/Receive (T/R) modules in a large array. The aim of this study is to identify a structure that, while maximizing the bandwidth (aiming at 40%) for wide scanning, also minimizes

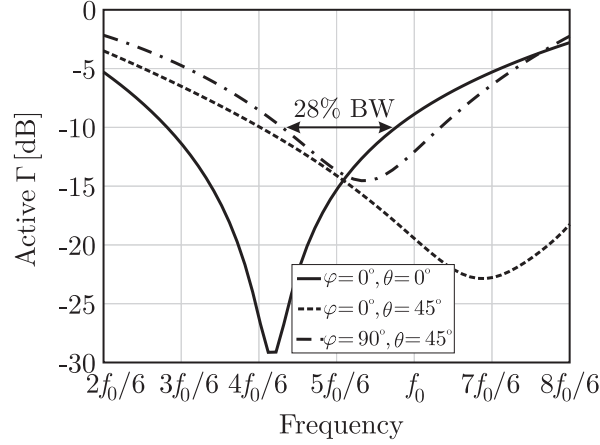


Figure 3.3: Active reflection coefficient, with respect to a 400Ω feeding line, of a connected array of slots with $d_x = d_y = 0.4 \lambda_0$, $w_s = \delta_s = 0.2 \lambda_0$, $h_s = 0.31 \lambda_0$. Curves are shown for broadside scan and for beam scan toward $\theta = 45^\circ$ in the two main planes.

the number of T/R modules.

3.2 Analysis of Polar Singularities of the Longitudinal Spectra

In this section, we discuss the feasibility of reducing the distance between the radiating elements and the backing reflector, h_s or h_d , to shift the operational bandwidth of the array at higher frequency, while maintaining the same sampling period. The distance from the back plane influences the position and the nature of the poles arising from the longitudinal dispersion equation. These poles are associated with waves that can propagate along the array. In fact, the connection between the different feeds in connected arrays implies the propagation of waves along the longitudinal direction of the slots or dipoles. Here we will discuss the nature of these propagations, highlighting the main differences between connected slots and dipoles.

3.2.1 Leaky Wave Poles in Connected Slots

Connected arrays of slots backed by a ground plane (Fig. 3.1(a)) can support leaky waves. To investigate the properties of such leaky waves, one must study their propagation along the slots. To this aim, it is necessary to do one step back and consider each of the slots in the array, as if it was excited by only one feed. In that case, the representation of the

voltage along each slot would be obtained as an inverse integral in k_x , similar to Eq. (2.18), but with a periodic GF that accounts for the periodicity along the transverse direction (y). Let us concentrate the attention to the case in which the array is phased to radiate in the plane $\varphi = 0$ (so that $k_{y0} = k_0 \sin \theta \sin \varphi = 0$) and investigate the spectrum in k_x . Expected branch point singularities appear in $\pm k_0$. However, also polar singularities emerge as solutions of the dispersion equation that is obtained by looking for the zeros of the denominator in Eq. (3.1):

$$(k_0^2 - k_x^2) \sum_{m_y=-\infty}^{\infty} \frac{J_0(k_{ym} \frac{w_s}{2}) (1 - j \cot(k_{zm} h_s))}{k_{zm}} = 0 \quad (3.5)$$

where $k_{zm} = \sqrt{k_0^2 - k_x^2 - k_{ym}^2}$. The discrete wave number k_{xm} is replaced with the continuous spectral variable k_x , because we are assuming that there is no periodicity along x , but only one feed is present in each slot.

The dispersion equation can be solved numerically with the aid of a first order Newton method [42], which is a simple descent along the gradient following an accurate starting point. Figure 3.4 shows the results of the dispersion analysis in the portion of the complex plane for which $-k_0 < \Re\{k_x\} < k_0$ and $-k_0 < \Im\{k_x\} < k_0$. The dashed curves indicate the location of pole singularities k_{xp}^{sl} of the GF, as a function of the slots widths (w_s) and parameterized for different heights (h_s) of the antenna from the backing reflector. The array is characterized by $d_x = d_y = 0.5 \lambda_0$, with $\lambda_0 = 2\pi/k_0$.

The poles represented in Fig. 3.4 are of the leaky wave type, in the sense that they are characterized by a propagation constant $\Re\{k_{xp}^{sl}\}$ and by an attenuation constant $\Im\{k_{xp}^{sl}\}$, the latter associated with radiation losses.

When the backing reflector is farther away from the radiating slots, the propagating mode of the slot k_{xp}^{sl} is quasi-TEM, travelling almost parallel to the slot direction. As h_s becomes smaller, the mode field distributions are increasingly affected by the presence of the backing reflector. As a consequence, the poles present an increasingly larger imaginary part. Most importantly, they present a smaller real part, meaning that they might be relevant also for arrays scanning in directions closer to broadside, since the condition $\sin \theta = \Re\{k_{xp}^{sl}/k_0\}$ may occur. An increasing width of the slots is also associated with an increased dispersion. In fact, the field is less tightly bound to the slots when their width is larger, so the impact of the ground plane becomes significant.

Curves similar to those in Fig. 3.4 have been obtained also for $\varphi \neq 0$, i.e. for scanning in planes different from the H -plane. However, since equivalent qualitative conclusions were

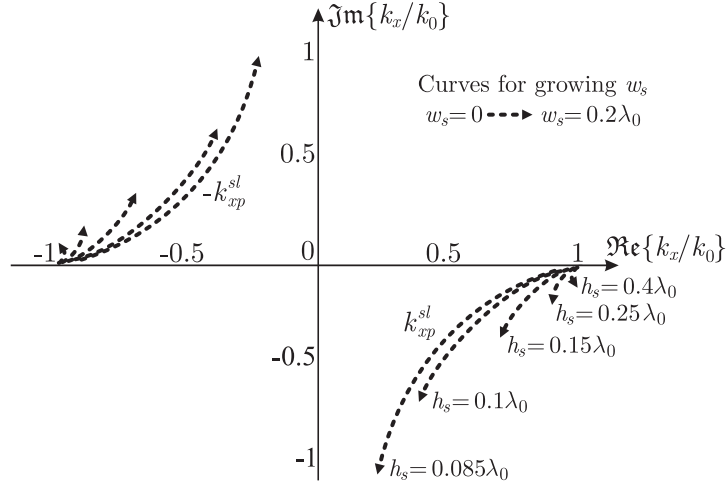


Figure 3.4: Polar singularities in the complex k_x/k_0 plane when the array is pointing broadside. The dimensions are $d_x = d_y = 0.5 \lambda_0$, $\delta_s = 0.1 \lambda_0$, while w_s and h_s are varying.

obtained, they are not reported here. Lower values of h_s imply poles in the visible region of the k_x spectrum.

To highlight the negative effect due to the compatibility of connected-slot arrays with leaky wave poles, Fig. 3.5 shows the real parts of the input impedance of a connected-slot array, over a broad frequency range. Indicating with λ_c the wavelength at the desired maximum operating frequency, the curves are given for $h_s = 0.1 \lambda_c$ and $h_s = 0.4 \lambda_c$. The remaining array parameters are fixed at $w_s = 0.2 \lambda_c$, $d_x = d_y = 0.5 \lambda_c$ and $\delta_s = 0.05 \lambda_c$. The curves are also given for different scan directions (broadside and 45° in the E - and H -planes). It is clear that, for smaller heights, the resonances are indeed shifted toward higher frequencies. However, smaller heights imply the drastic narrowing of the useful band when scanning in the E -plane.

Given these findings, it is clear that reducing h_s to achieve matching at higher frequencies, and accordingly to reduce the number of T/R modules, it is not a viable solution since the scan performance is seriously degraded.

3.2.2 TEM Poles in Connected Dipoles

If a similar dispersion analysis is performed for the connected-dipole array, in the presence of a backing reflector, no leaky wave poles are found when h_d is relatively small. This can be shown fairly easily. In the case of dipoles, one needs to find the solutions of the following dispersion equation, which is obtained by searching the zeros of the denominator

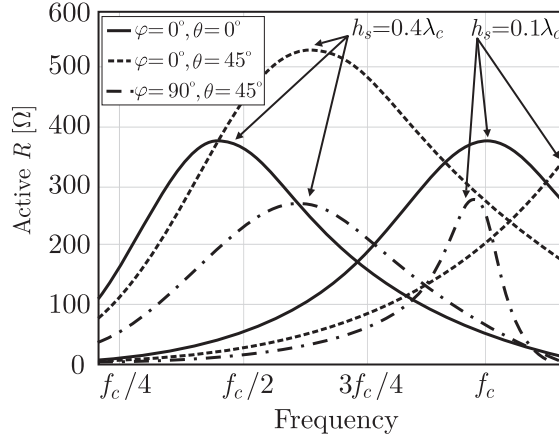


Figure 3.5: Active resistance of a connected-slot array as a function of the frequency for two values of the height from the backing reflector.

of the expression in Eq. (3.2):

$$(k_0^2 - k_x^2) \sum_{m_y=-\infty}^{\infty} \frac{J_0(k_{ym} \frac{w_d}{2})}{k_{zm}(1 - j \cot(k_{zm} h_d))} = 0. \quad (3.6)$$

Despite the similarity with Eq. (3.5), the analytic solutions of Eq. (3.6) are simpler to characterize. Solutions are found explicitly, for arbitrary values of frequency, azimuthal angle φ , and distance from the ground plane h_d , in correspondence of $k_x = \pm k_0$. They are associated with guided micro-strip like (TEM) modes. Other poles emerge at higher frequencies. In fact, they arise from the reduced dispersion equation

$$\sum_{m_y=-\infty}^{\infty} \frac{J_0(k_{ym} \frac{w_d}{2})}{k_{zm}(1 - j \cot(k_{zm} h_d))} = 0. \quad (3.7)$$

The possible solutions of this reduced dispersion equation are found by observing that

- $1 - j \cot(k_{zm} h_d) = 2/(1 - e^{-jk_{zm} 2h_d})$, as proved in Eq. (A.71);
- for a well sampled radiating array, k_{zm} is always purely imaginary except when $m_y = 0$, in which case $k_{z0} = k_0 \cos \theta$;
- both real and imaginary parts of Eq. (3.7) must be zero to have a solution of the dispersion equation.

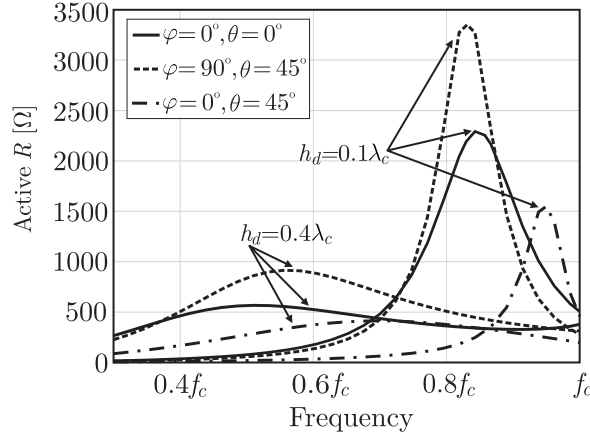


Figure 3.6: Active resistance of a connected-dipole array as a function of the frequency for two values of the height from the backing reflector.

From the last two conditions it follows that the contribution to the summation associated with the mode of index $m_y = 0$ must present a zero by itself. This is only possible when $(1 - e^{-jk_0 \cos \theta 2h_d}) = 0$, which leads to $h_d = \frac{n\lambda_0}{2\cos \theta}$, where n is integer. Thus, the distance between the ground plane and the dipoles should be at least larger than half wavelength to have another pole, different from the micro-strip TEM mode ($k_x = \pm k_0$), to be compatible with the structure. However, this can be easily avoided in practical designs.

The micro-strip modes are important since they guide power from one feed to the next, but they do not cause important degradation of the main focused radiation, since they contribute to radiation toward $\theta \approx 90^\circ$. Accordingly, the reduction of the height (h_d) does not present drawbacks specifically associated with scanning. However, a dipole array, whether connected or not, has a significantly reduced radiation bandwidth when h_d is small with respect to the wavelength. This can be observed in Fig. 3.6, which compares the real part of the impedances associated with two arrays of different heights, but identical sampling. The other dimensions are $w_d = \delta_d = 0.05 \lambda_c$ and $d_x = d_y = 0.5 \lambda_c$. Differently from the slot case, for the dipoles we observe not only a shift of the resonance when varying the distance h_d from the ground plane, but also much higher impedance values for lower h_d .

Overall, one can conclude that the nature of the dominant waves in connected arrays of dipoles is much simpler (pure TEM) than the one (leaky) of connected arrays of slots. However, for both structures, a lower height does not bring significant advantages.

3.3 Bandwidth Dependence on the Gap Width

So far it has been established that the impedances of backed connected dipoles and slots exhibit a similar dependence on the periodicity and the distance from the ground plane. The aspect in which they truly differ is the reactive energy stored in the feeds, associated with the size of the feed gap. In the connected-slot case this reactive energy plays only a marginal role, while in the case of connected dipoles it can be used to effectively achieve wider matching bandwidths.

The reactance of the feed is mathematically represented by the higher order Floquet modes in the admittance of the connected dipoles in Eq. (3.2) or in the impedance of the connected slots in Eq. (3.1). This energy is localized in the proximity of each gap. Thus, for instance in a connected-slot array, one can assume that the concentrated inductance in each of the δ -gaps in every slot is the same as that localized in a single δ -gap of a unique infinitely extended slot in absence of the backing reflector. Analogously, one can assume that the concentrated capacitance associated with the δ -gaps in a connected-dipole array is the same as that of a single feed of an infinite dipole in free space. For the interested reader, these lumped equivalent impedances were provided in [43].

3.3.1 Slot Case: Lumped Inductance

In the connected-slot array case, the reactive energy localized at the feeding points is modelled by an inductance. This lumped inductance is in series with respect to an equivalent circuit representing the input impedance. That is because, in a well sampled array, the real part of the impedance is only associated with the term $m_x = 0$ of the Floquet mode summation in Eq. (3.1). The imaginary part depends also on all the other additive modes in m_x . Figure 3.7(a) shows the equivalent circuit for the active impedance of a connected-slot array. The dynamic portion of the impedance Z_{slot}^{dyn} can be introduced as the difference between the input impedance and the concentrated inductive reactance associated with the gap. To highlight the effects of this inductance, Fig. 3.8 shows a parametric investigation of the input impedance, as a function of the frequency, for increasing dimension of the gap (δ_s). It can be noted that the real part of the impedance is indeed not dependent from the dimension of the gap. At the lower frequencies, for all values of δ_s , the imaginary part of the impedance is inductive (positive). That is because the slots are operating in the close vicinity of the backing reflector, which acts as a short circuit. Then, as the frequency grows, the waves reflected from the ground plane tend to add less destructively to the ones directly radiated toward free space, until a resonance condition is achieved. Eventually,

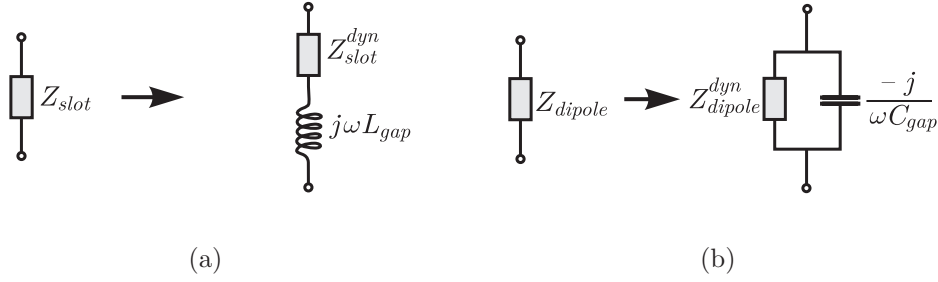


Figure 3.7: Equivalent circuit representing the active impedance at each feed in (a) connected arrays of slots, with inductive gap feed, and (b) connected arrays of dipoles, with capacitive gap feed.

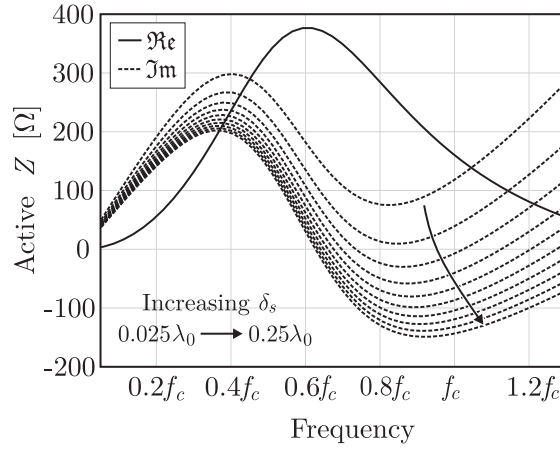


Figure 3.8: Active impedance of a connected-slot array as a function of the frequency for different gap widths, given $h_s = 0.3 \lambda_c$, $w_s = 0.2 \lambda_c$, $d_x = d_y = 0.5 \lambda_c$.

the resonance condition, when the imaginary part of the input impedance is equal to zero, depends on the specific width of the δ -gap. It is apparent that for larger (less inductive) gaps the condition of zero reactance occurs at slightly higher frequencies.

3.3.2 Dipole Case: Lumped Capacitance

In the case of connected dipoles, the gaps can instead be truly used as a design parameter to enlarge the bandwidth. Here a lumped capacitance representing the stored energy is in parallel with respect to the equivalent circuit of the input impedance, as in Fig. 3.7(b). That is because the capacitance is associated with the summation of the higher order contributions to the input admittance. Note that, in this case, in the equivalent circuit

the dynamic impedance Z_{dipole}^{dyn} is equal to $\frac{1}{Y_{dipole}^{dyn}}$, where the dynamic admittance Y_{dipole}^{dyn} is the difference between the input admittance and the capacitive susceptance. If the array is densely sampled, the real part of the admittance is associated with the $m_x = 0$ mode only, while the imaginary part depends also on contributions from higher order modes. Parametric curves of the input admittance as a function of the frequency are shown in Fig. 3.9(a), for increasing dimension of the gap (δ_d). The susceptance is inductive (< 0) for all the values of δ_d at the lower frequencies, when the dipoles are very close to the ground plane (short circuit). For higher frequencies, resonant conditions are achieved in different frequency points, depending on the specific width of the δ -gap. Let us observe the corresponding input impedance curves, shown in Fig. 3.9(b): when the gaps are small and the stored capacitive energy is high, the real part of the impedance defines a relatively narrow bell as in the connected-slot array case (Fig. 3.8). However, when the dimension of the gap increases, and accordingly the gaps store less capacitive energy, the overall impedance bell appears lower, much wider, and shifted toward higher frequencies. Also the imaginary part of the input impedance is less variable for larger sizes of the feeding gap. The same effect is not present in the slot case, where the series inductance would not affect the real part of the impedance. Thus, we can state that the gap's capacitance is a key design parameter that can be tuned to obtain a wider matching bandwidth of the connected-dipole array.

The most attractive aspect about this design parameter is that it allows to enlarge the impedance bells independently of the scanning angle to which the array is pointing. It is thus apparent that, if one is interested in broad bandwidth and wide-angle scanning, one should aim at a configuration that implements this controlled capacity condition.

3.4 Double Feed for the Dipoles

From the curves in Fig. 3.9, it appears that the best matching would be achieved for $\delta_d = 0.15 \lambda_0$. However, the practical realization of such large gaps is not simple, since it would require feeding lines (for instance coplanar strip lines) with inter-conductor distances so large that they would radiate and consequently worsen the polarization performance. The solution that we envisage is to excite a connected array of dipoles with a double feed in each periodic cell. The schematic view of the feeding arrangement is shown in Fig. 3.10. In this case, the effective capacitance at each cell is essentially divided by two, since the two feeds are connected in series. It is clear that, due to the logarithmic dependence of the capacitance from the gap width [43], much narrower gaps can be used

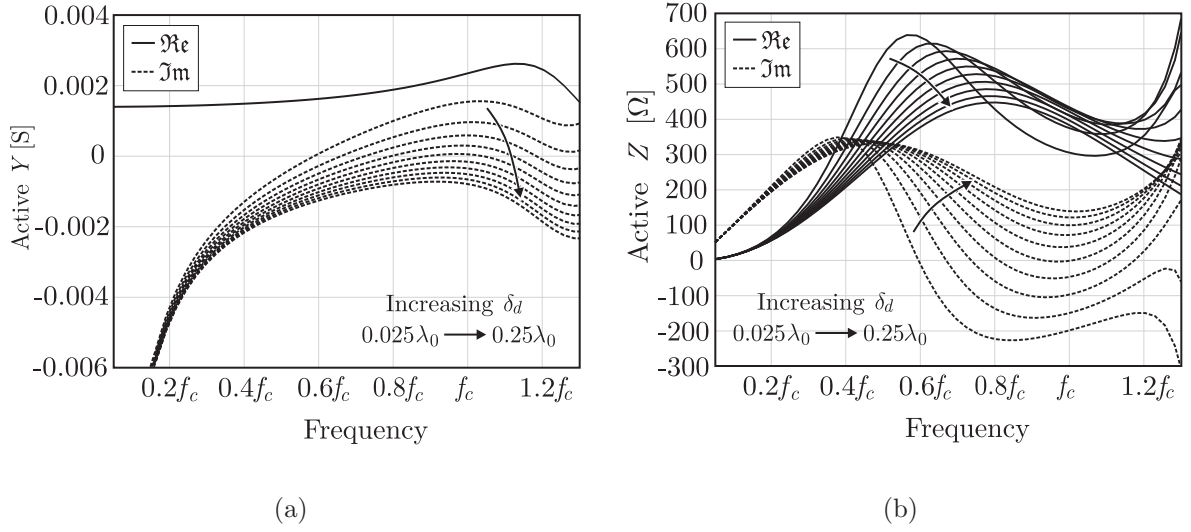


Figure 3.9: Active (a) admittance and (b) impedance of a connected-dipole array as a function of the frequency, for different gap-widths, given $h_d = 0.3 \lambda_c$, $w_d = 0.05 \lambda_c$, $d_x = d_y = 0.5 \lambda_c$.

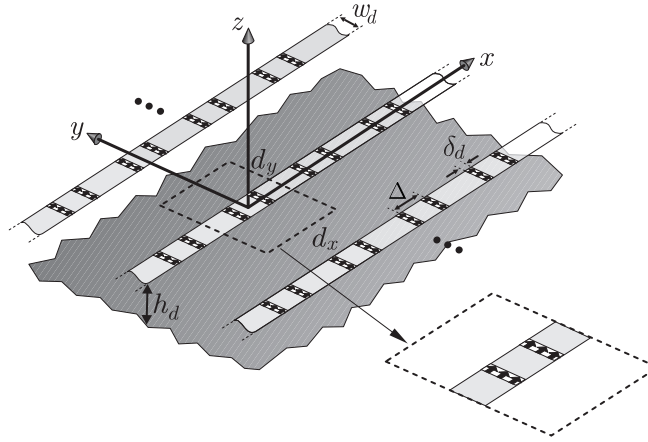


Figure 3.10: Schematic geometry of a double-feed configuration that guarantees low equivalent feed capacitance, while the width each of the gap is maintained small.

in the double feed case to obtain similar impedance curves, with respect to the single feed configuration. With such small gaps, the dipoles can be fed by transmission lines with negligible losses for cross-polar radiation. Figure 3.11 shows the comparison between the input impedances in the two cases of single feed with $\delta_d = 0.125 \lambda_0$, and double feed with $\delta_d = 0.01 \lambda_0$. An optimized array configuration based on a double feed per each unit cell was found to have 40% relative bandwidth, scanning up to 45° , as shown in Fig. 3.12.

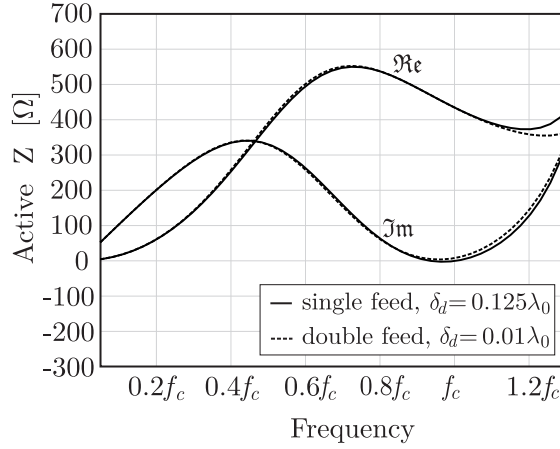


Figure 3.11: Real and imaginary part of the active impedance of a connected dipole with single feed ($\delta_d = 0.125 \lambda_0$), and with double feed ($\Delta = 0.29 \lambda_0$, $\delta_d = 0.01 \lambda_0$).

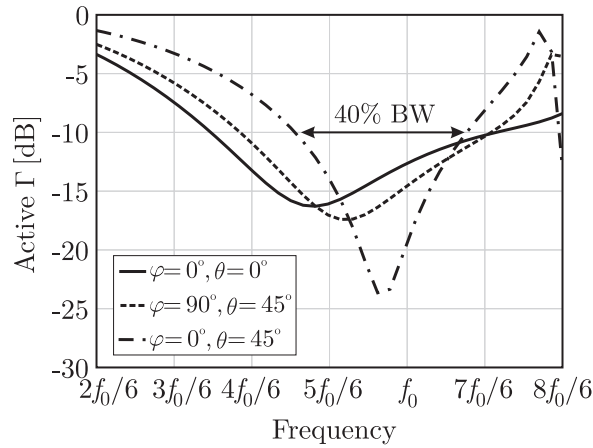


Figure 3.12: Active reflection coefficients, with respect to a 350Ω feeding line, of a dipole array with $d_x = d_y = 0.45 \lambda_0$, $w_d = 0.05 \lambda_0$, $\delta_d = 0.01 \lambda_0$, $\Delta = 0.29 \lambda_0$ and $h_d = 0.31 \lambda_0$. Curves are shown for scanning at broadside and toward $\theta = 45^\circ$ in the two main planes.

The feeds are at a distance $\Delta = 0.29 \lambda_0$, the gap size δ_d is chosen equal to $0.01 \lambda_0$, the dipole width is $w_d = 0.05 \lambda_0$, and the height from the ground plane is $h_d = 0.31 \lambda_0$. Note that $d_x = d_y = 0.45 \lambda_0 = 0.5 \lambda_{max}$, with λ_{max} being the wavelength at the maximal useful operational frequency.

To simplify the analysis with only minimal loss of generality, the double-feed curves in Fig. 3.11 and in Fig. 3.12 have been obtained representing the double-feed configuration by two delta-gap generators in each cell. Then the cell input impedance is the sum of two equal feed impedances, each of them defined as the inverse of the average active admittance observed

at the two ports. The description, the meaning and the mathematical representation of this implementation are discussed in the next section.

3.4.1 Active Admittance for Multiple Feeds per Unit Cell

The excitation at two feed points can be modelled as two impressed electric fields $e_{1,2}(x)$, such to create a voltage drop of 1 Volt at each feed. Assuming that the separation between the two feed points inside the same cell is Δ , the x -dependence of the electric field can be expressed as

$$e_{1,2}(x) = \frac{1}{\delta_d} \Pi_{\delta_d} \left(x \pm \frac{\Delta}{2} \right), \text{ where } \Pi_{\delta_d}(x) = \begin{cases} 1 & \text{if } x \in [-\frac{\delta_d}{2}, \frac{\delta_d}{2}] \\ 0 & \text{otherwise} \end{cases}. \quad (3.8)$$

Accordingly, the Fourier transform (FT) of the entire impressed electric field on the cell is

$$E(k_x) = \int_{-\frac{\delta_d}{2} - \frac{\Delta}{2}}^{\frac{\delta_d}{2} - \frac{\Delta}{2}} e_1(x') e^{jk_x x'} dx' + \int_{-\frac{\delta_d}{2} + \frac{\Delta}{2}}^{\frac{\delta_d}{2} + \frac{\Delta}{2}} e_2(x') e^{jk_x x'} dx' = 2 \cos \left(k_x \frac{\Delta}{2} \right) \text{sinc} \left(k_x \frac{\delta_d}{2} \right). \quad (3.9)$$

In a two-dimensional periodic array, following the same procedure as in Sec. 2.2, the current distribution along the dipole associated with the excitation in Eq. (3.8) can be written as

$$i(x) = \frac{k_0 d_y}{\zeta_0 d_x} \sum_{m_x=-\infty}^{\infty} \frac{2 \cos \left(\frac{k_{xm} \Delta}{2} \right) \text{sinc} \left(\frac{k_{xm} \delta_d}{2} \right) e^{-jk_{xm} x}}{(k_0^2 - k_{xm}^2) \sum_{m_y=-\infty}^{\infty} \frac{J_0 \left(k_{ym} \frac{w_d}{2} \right)}{k_{zm} (1 - j \cot(k_{zm} h_d))}}. \quad (3.10)$$

By proceeding as in Eq. (2.35), we can calculate the admittance in a gap feed of a dipole excited by unitary impressed voltage drop as the average electric current flowing in the gap. Accordingly, the active admittance in each of the two feeds can be expressed as

$$y_{1,2} = \frac{1}{\delta_d} \int_{-\frac{\delta_d}{2} \mp \frac{\Delta}{2}}^{\frac{\delta_d}{2} \mp \frac{\Delta}{2}} i(x') dx'. \quad (3.11)$$

By substituting Eq. (3.10) in Eq. (3.11), and by performing the integration in the x' -variable, we obtain

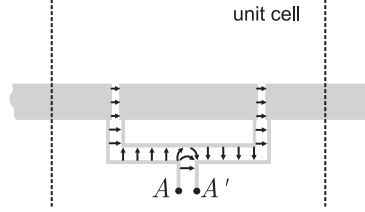


Figure 3.13: Schematic representation of the double feed excitation in a unit cell and related electric field vector lines.

$$y_{1,2} = \frac{k_0 d_y}{\zeta_0 d_x} \sum_{m_x=-\infty}^{\infty} \frac{2 \cos\left(\frac{k_{xm}\Delta}{2}\right) \operatorname{sinc}^2\left(\frac{k_{xm}\delta_d}{2}\right) e^{\pm j k_{xm} \frac{\Delta}{2}}}{(k_0^2 - k_{xm}^2) \sum_{m_y=-\infty}^{\infty} \frac{J_0\left(k_{ym} \frac{w_d}{2}\right)}{k_{zm}(1-j \cot(k_{zm} h_d))}}. \quad (3.12)$$

By comparing Eq. (3.12) with Eq. (3.2), it is apparent that, for a well sampled array in which only the $m_x = m_y = 0$ mode is dominant, the admittance at each feed point, in this double feed configuration, is twice as large as the admittance of the same array with a single feed per cell. As a result, within this approximation, the input impedance at each of the two feeds roughly becomes half the single-feed value. Only when the two ports are connected in series, is the single-feed value approximately recovered.

In practice, when the cell is fed at two points which are physically separated, the maintenance of a voltage excitation at the same amplitude and phase for the two ports can be achieved by means transmission lines that implement a series feeding scheme, as shown in Fig. 3.13. In that case, the active input admittance at the section AA' cannot be evaluated without introducing an explicit phase shift.

However, it might be convenient and useful to refer to the concept of the average input admittance y_{in}^{av} for each feed, which is defined as

$$y_{in}^{av} = \frac{y_1 + y_2}{2} = \frac{k_0 d_y}{\zeta_0 d_x} \sum_{m_x=-\infty}^{\infty} \frac{2 \cos^2\left(\frac{k_{xm}\Delta}{2}\right) \operatorname{sinc}^2\left(\frac{k_{xm}\delta_d}{2}\right)}{(k_0^2 - k_{xm}^2) \sum_{m_y=-\infty}^{\infty} \frac{J_0\left(k_{ym} \frac{w_d}{2}\right)}{k_{zm}(1-j \cot(k_{zm} h_d))}}. \quad (3.13)$$

As a consequence, the average input impedance of each feed in a double cell is $z_{in}^{av} = \frac{1}{y_{in}^{av}}$. Finally, the cell input impedance is $z_{cell} = 2z_{in}^{av}$. This is the impedance plotted in dashed lines in Fig. 3.11 and to which Fig. 3.12 refers.

Since, for broadside radiation, the double feed structure is actually a practical implementation of a feed sampling twice as dense, one might think that it is simply the effect of the

denser sampling that helps the matching. However, this is only partly true. In fact, when the array is phased to scan, the two feed points are associated with the same phase. The practical realization of such a double feed [44, 45] requires the connection of the two feeds via an appropriate transmission line, as shown in Fig. 3.13.

This final configuration that includes the double feed represents a schematic design, without explicit feeding network, that will be chosen as the basis for the development of a prototype demonstrator that will be presented in Chapter 6.

3.5 Active Array Far-Field Patterns

The radiation patterns of an 8×8 finite array are investigated with the aid of the appropriate analytical expressions for the far-field co- and cross-polarized directivities. These expressions can be evaluated using a windowing approximation, which is accurate only for very large arrays, or they can be derived directly from the GF and thus remain valid even for a small connected array. By finite array we indicate an array where a finite number of excitations are considered along the longitudinal direction, while the metallization is still infinitely extended.

The very widely used approximations based on infinite array theory [46, 47] and subsequent windowing [48], although very efficient from the computational point of view, would fail in equivalently small array cases. This is because of the intrinsic nature of connected arrays: they are characterized by a strong mutual coupling, which implies that global array effects need to be accounted for. Finally, the low cross-polarization level when scanning in the diagonal plane is highlighted as the main characterizing feature of these broadband arrays. The single most important reason for developing phased arrays based on connected dipoles or slots is the possibility to obtain radiation patterns of the highest polarization purity for wide scan angles and over large frequency bands. The present Green's function formalism enables the analytical evaluation of the radiation patterns. This not only saves computation time during the design process, but eventually rigorously demonstrates the properties of polarization purity of these arrays.

Before proceeding with the derivation of the radiated fields, it is worth noting that in this section we will focus on *active far fields* radiated by *active currents*. This means that, as typically done in large phased arrays, the radiating currents are those present when all feeds are excited with an ideal, uniform-amplitude, impressed voltages (electric field). In reality, one can only use real generators. Thus, a feed network that implements such uniform voltage generators independently of the scan angle and the frequency must be

properly designed and could turn out to be very challenging. This is particularly true in the present case of connected arrays, for which the mutual coupling between the elements is very high. The practical realization of a connected-dipole array prototype will be the subject of Chapter 6. For the present time we will make use of the *active current* ideal model.

The electric far field can be simply obtained from the expression of the magnetic potential, as demonstrated in Appendix B (Sec. B.2.3), and in particular:

$$\begin{aligned} E_\theta &\simeq -j\omega \cos \theta \cos \varphi A_x \\ E_\varphi &\simeq j\omega \sin \varphi A_x. \end{aligned} \quad (3.14)$$

It is also useful to remind that, according to the third Ludwig definition [9], the co- and cross-polarized directivities radiated by an array of dipoles oriented along x are given by

$$\begin{aligned} D_{co} &= \frac{4\pi |E_\theta \cos \varphi - E_\varphi \sin \varphi|^2}{2\zeta_0 P_r} \\ D_{cross} &= \frac{4\pi |E_\theta \sin \varphi + E_\varphi \cos \varphi|^2}{2\zeta_0 P_r} \end{aligned} \quad (3.15)$$

where P_r is the power radiated by the complete array.

The magnetic vector potential \mathbf{A} is oriented along the dipoles $\mathbf{A} = A_x \hat{\mathbf{x}}$ and its approximation for observation points \mathbf{r} in the far-field region is derived in Appendix B (Eq. (B.5)):

$$A_x(\mathbf{r}) \approx J_x(k_0 \sin \theta \cos \varphi, k_0 \sin \theta \sin \varphi) \frac{\mu e^{-jk_0 r}}{4\pi r} (1 - e^{-jk_0 2h_d \cos \theta}) \quad (3.16)$$

where $J_x(k_x, k_y)$ is the Fourier transform of the electric current distribution on the array. For the present structure, $J_x(k_x, k_y)$ can be expressed as the product of two separate variables: i.e. $J_x(k_x, k_y) = J_x^y(k_y) I(k_x)$. The key step in the evaluation of the far field is the approximation of the equivalent currents on the finite array.

3.5.1 Transverse Windowing Approximation

The so called windowing approach [48] can be used in approximating the current distribution transverse to the array, $J_x^y(k_y)$. Initially, the array is considered to be infinite, with currents on each element presenting the same amplitude but different phases. The phase

shift is dictated by the direction in which the array is focusing its radiation. In a second stage, the finiteness of the structure is accounted for by considering the total field as radiated by only a finite number of contributions. Indicating with N_y the number of elements along y and remembering that in each dipole the distribution satisfies the edge-singular condition, it results:

$$J_x^y(k_y) \approx AF(k_y - k_{y0}, N_y, d_y) J_0 \left(\frac{1}{2} w_d k_y \right) \quad (3.17)$$

where we introduced the array factor

$$AF(k_y - k_{y0}, N_y, d_y) = \sum_{n_x=-N_x/2}^{N_x/2} e^{j(k_y - k_{y0})n_y d_y}. \quad (3.18)$$

3.5.2 Longitudinal Windowing Approximation

A windowing approach, based on infinite array theory, can be used also to approximate the longitudinal current distribution. The derivation of an analytical expression that implements the windowing can be obtained with a few algebraic manipulations, reported in Sec. B.2.1. The procedure consists in evaluating the current on a single periodic cell in infinite array environment. The spectrum is then calculated by integration over an aperture composed of a finite number of these cells, which leads to:

$$I_w(k_x) = -V_0 AF(k_x - k_{x0}, N_x, d_x) \sum_{m_x=-\infty}^{\infty} \frac{\text{sinc} \left(\frac{k_{xm} d_d}{2} \right) \text{sinc} \left(\frac{(k_x - k_{xm}) d_x}{2} \right)}{D_\infty(k_{xm})}. \quad (3.19)$$

The use of (3.17) and (3.19) inside (3.16) and then in (3.15) provides the same directivity patterns as common commercial software tools also based on infinite array theory and windowing. A validation is presented in Fig. 3.14, where the active single element pattern in the E - and the H -plane is shown and compared with equivalent results obtained with the commercial software Ansoft Designer [49]. The array taken as reference for this figure, and also for the following ones, is the array characterized by the double feed configuration that was introduced in Sec. 3.4. The elementary cell dimensions, the dipole geometrical details and the height of the ground plane are the same as the ones to which Fig. 3.12 refers.

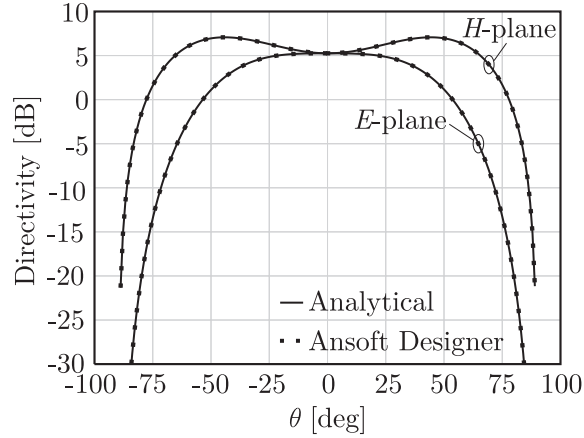


Figure 3.14: Directivity of the active element pattern in the E - and the H -plane, for broadside radiation. The comparison is with the results provided by the commercial tool Ansoft Designer resorting to the same type of approximation. The elementary cell dimensions in terms of the wavelength are the same as in Fig. 3.12.

Despite the agreement between our calculations and the results of the commercial software, the accuracy of the results obtained by using the longitudinal windowing approach is openly questionable, as will be discussed in the next section.

3.5.3 Longitudinal Green's Function

The difference between the current distributions of two elements of a finite array might be non negligible. In fact, in Sec. 3.2, we have demonstrated analytically that in any connected array, slots or dipoles, a dominant propagating mode is supported by the structure with backing reflector, even at low frequencies. This mode is a leaky wave in the slot case or a bounded micro-strip type of mode in a connected-dipole array. In particular, in the dipole case, the waves travelling from the edges in the longitudinal direction are not attenuated if no source impedance is included in the model of the feed. This suggests that an infinite array approximation could be inadequate, as it completely neglects longitudinal standing waves and associated strong current tapering, that could exist even in the presence of uniform excitations.

The expression of the current spectrum in the case of a finite number of δ -gap sources can be derived from Eq. (B.9) as

$$I(k_x) = V_0 A F(k_x - k_{x0}, N_x, d_x) \frac{\text{sinc}(k_x \delta_d / 2)}{D_\infty(k_x)} \quad (3.20)$$

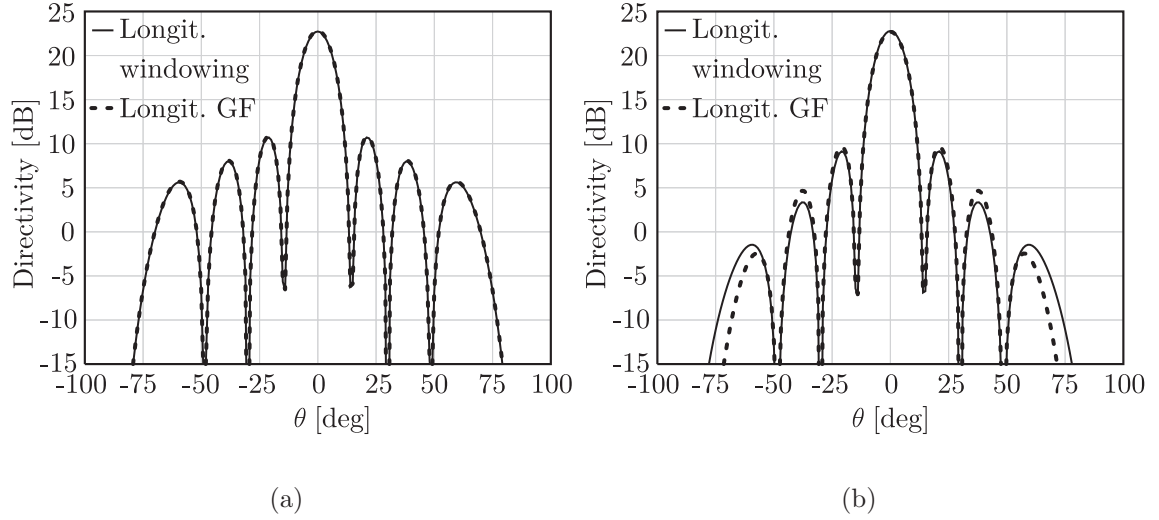


Figure 3.15: Broadside active array pattern from an 8×8 connected-dipole array with the same parameters as in Fig. 3.12. Comparison between longitudinal windowing and longitudinal GF approach: (a) H -plane and (b) E -plane.

This expression is based on the exact GF and is more accurate than Eq. (3.19). Moreover, its evaluation implies reduced computational costs, since it does not involve a spectral sum in m_x .

3.5.4 Pattern Quality

Let us now investigate the far-field co-polar directivity patterns radiated by an array of 8 dipoles, each of them fed by 8 δ -gap feeds. The calculation frequency is $f_0 = c_0/\lambda_0$, where c_0 is the free space speed of light. The array dimensions in terms of the wavelength are $d_x = d_y = 0.5 \lambda_0$, $\delta_d = w_d = 0.05 \lambda_0$, $h_d = 0.31 \lambda_0$.

For all radiation patterns presented in this section, we used the windowing approximation for the electric current distribution in the transverse direction, introduced in Sec. 3.5.1. For the longitudinal electric current distribution, two different expressions have been used: the windowing approximation (Sec. 3.5.2) and the exact Green's function (Sec. 3.5.3). Figures 3.15 and 3.16 show a comparison between the results achieved with these two expressions. It is apparent that for scanning and observations in the H -plane (Fig. 3.15(a) for broadside pointing and Fig. 3.16(a) for 45° scanning), the results are hardly influenced by the approximation used in the longitudinal plane. On the contrary, for E -plane scanning (Figs. 3.15(b) and 3.16(b)), the use of the complete GF shows higher side lobe levels

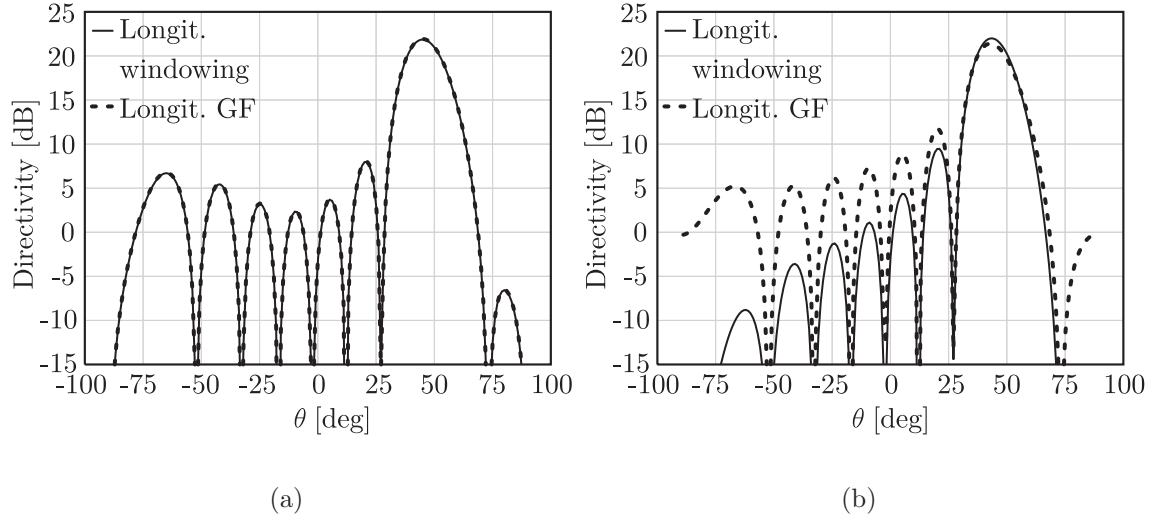


Figure 3.16: Active array patterns, scanning at elevations of 45° , from an 8×8 connected-dipole array with the same parameters as in Fig. 3.12. Comparison between longitudinal windowing and longitudinal GF approach: (a) H -plane and (b) E -plane.

and also broader beams at 45° . The difference can be explained from the fact that the windowing approximation assumes that the currents on each element are identical, except for weighting coefficients. The same assumption is not made in the second approach, which is more accurate. The use of the GF predicts also higher radiation at grazing angles. The actual values of grazing radiation are not very significant, since they will be affected as well by the finite length of the dipoles. However, their visibility suggests the necessity to control end-point longitudinal radiation when dealing with connected arrays of small dimension.

Finally, Fig. 3.17 presents a comparison between the co-polar and the cross-polar directivity obtained when the array is scanned to $\theta = 45^\circ$ in the diagonal plane ($\varphi = 45^\circ$). The cross-polarized field is at least 15 dB lower than the co-polarized field. This level of low cross polarization is the same as that of a single elementary dipole operating in free space (Sec. 1.2). Thus, it represents the lowest value theoretically achievable by planar array of linearly polarized dipoles [10].

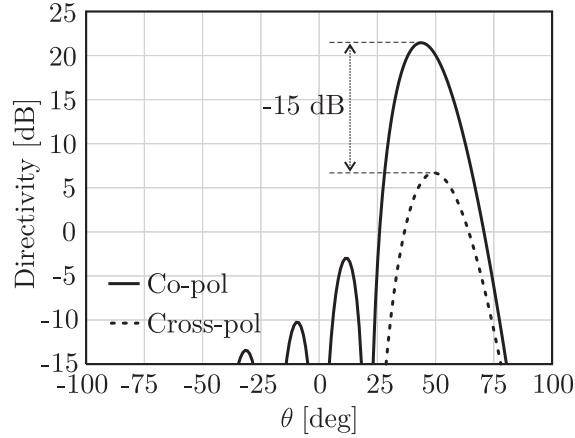


Figure 3.17: Co- and cross-polarized directivities in the diagonal plane ($\varphi = 45^\circ$), as a function of the elevation angle θ . The fields are again those radiated from an 8×8 connected-dipole array with dimensions as in Fig. 3.12.

3.6 Conclusions

A comparison between the scan performance of connected arrays of dipoles and slots in the presence of a backing reflector was shown. The comparison was based on a rigorous Green's function formulation. The investigation revealed that broad band matching can be obtained by tuning the reactive energy contained in the feeds of the connected dipoles, independently from the scan angle. Last but not least, we presented a planar connected array of dipoles with 40% bandwidth, even when scanning in elevation to 45° . The array was shown to radiate with the lowest theoretical cross-polarization levels for a planar singly polarized array. The number of required T/R modules remains limited, with $0.5 \lambda_0$ sampling at the highest operational frequency. The use of the rigorous GF in the prediction of the far fields in the E -plane provides more accurate results with respect to a standard windowing technique and is even less computationally intensive.

Chapter 4

Equivalent Circuit Representation of Connected Arrays

The spectral Green's Functions (GFs) of connected arrays were derived analytically in Chapter 2, for slots and dipoles, with and without backing reflector. All these GFs considered arrays operating in transmission (Tx). In this chapter, the formalism is extended to receiving arrays, including the presence of loads. When the arrays are assumed to be infinitely extended and periodically excited, the extension to reception (Rx) allows the derivation of a rigorous equivalent circuit for the array unit cell. This equivalent circuit is based on GFs, thus each component can be associated with a specific physical wave mechanism. Moreover, all components are evaluated analytically. The equivalent network can be used to represent the electromagnetic field distribution in transmission and/or reception.

This chapter is structured as follows: the first part is theoretical and presents the derivation of the spectral distribution of the electric currents on the array, as a function of the incident electric field and the load impedance. In the second part, the equivalent circuit is presented and its applicability to evaluate the power absorbed by the arrays is demonstrated. Based on the equivalent circuit representation of the array, we will discuss the amount of power transmitted, received and/or scattered by a connected array, for different antenna configurations. The full efficiency of an array with backing reflector is demonstrated and explained. Finally, in the third part, measured results from a dual-band connected array demonstrator are used to validate the equivalent circuit.

4.1 Limitations of Equivalent Norton or Thévenin Circuits

The use of the equivalent Norton or Thévenin circuits for antennas in reception [50,51], [52, p. 85] can lead to improper physical interpretation, as pointed out in [53,54]. In fact, it is erroneous to associate the equivalent Thévenin impedance with scattered or reradiated power. This would imply that, under conjugate matching condition, only half of the incoming power can be received by an antenna. This issue has been more recently discussed in [55–61]. In particular, [61] was the first to demonstrate analytically that all the power incident on an antenna array can be received if the antenna is supported by a backing reflector. An alternative equivalent circuit for phased arrays in reception has been proposed in [26]. However, although retaining deep physical insight, that circuit was not rigorously derived, accounting only for the energy included in the fundamental propagating Floquet wave.

Here, a rigorous equivalent circuit for planar connected phased arrays is provided. Unlike the Thévenin or Norton equivalence, the circuit here proposed can be used to quantify the scattered fields as well as the currents flowing into the loads. The representation is based on a GF formulation and, as a consequence, it accounts for all Floquet modes, including those associated with reactive energy. The circuit can be easily used for all types of planar stratifications such as dielectric layers, backing reflectors and also integrated Frequency Selective Surfaces (FSSs) [62].

The extension includes, on the one hand, the introduction of generators directly proportional to the amplitude of the incoming plane waves rather than the voltage induced in open circuit condition and, on the other hand, an expansion of the antenna impedance in different components, each with a well defined physical meaning.

4.2 Integral Equation for Connected Array of Loaded Dipoles

The connected array of dipoles under analysis is shown in Figure 4.1. It is assumed to be composed of an infinite number of x -oriented dipoles of width w , periodically spaced by d_y along y , in free space. The dipoles are fed at periodic locations, spaced by d_x , by a transmission line of characteristic impedance Z_l . In the transmit case, the incident field propagates toward the array along the mentioned transmission lines ($\mathbf{e}_{tl}^+ \propto V_{tl}^+$). In the reception case, the incident field is associated with an incoming plane wave \mathbf{e}_{pw}^+ . In both

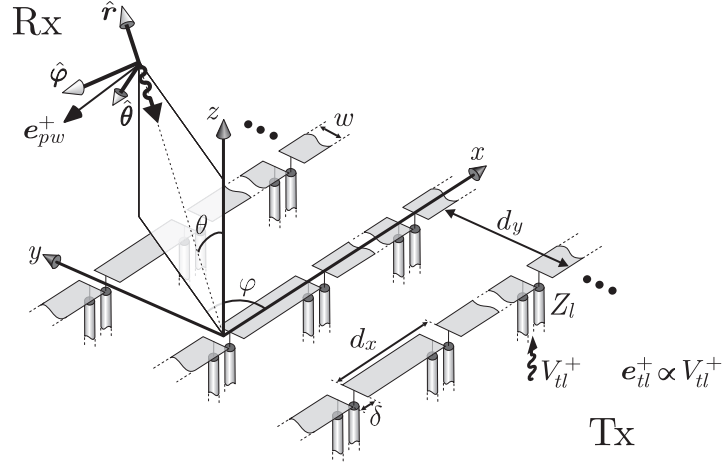


Figure 4.1: Two-dimensional connected array of dipoles in transmit or receive mode.

cases, on each n -th feeding point the incident fields $\mathbf{e}_i^{Tx/Rx}$ are equal in amplitude and with progressive phase to account for scanning or different directions of incidence. Note that a generic plane wave can be represented as superposition of transverse electric (TE) and transverse magnetic (TM) components (transverse with respect to the plane of incidence): $\mathbf{e}_{pw}^+ = \mathbf{e}_{TE}^+ + \mathbf{e}_{TM}^+$. The TE and TM unit vectors are parallel to $\hat{\boldsymbol{\varphi}}$ and $\hat{\boldsymbol{\theta}}$, respectively. This starting problem will be transformed into an equivalent completely planar one, to deal with planar boundary conditions. The equivalent problem is obtained by substituting the feeding transmission line with a distributed surface impedance that fills the gap region, as depicted in Fig. 4.2. Accordingly, boundary conditions are imposed on the total fields $\mathbf{e}_{tot}, \mathbf{h}_{tot}$ as follows:

$$\mathbf{e}_{tot} = Z_{surf} \hat{\mathbf{z}} \times (\mathbf{h}_{tot}^{(1)} - \mathbf{h}_{tot}^{(2)}) \quad (4.1)$$

where $\mathbf{h}_{tot}^{(1)}$ and $\mathbf{h}_{tot}^{(2)}$ represent the total magnetic field for $z > 0$ and $z < 0$, respectively. This equation is valid on the entire array surface $\Sigma_c \cup \Sigma_g$, if we assume that the surface impedance $Z_{surf}(x, y)$ is a discontinuous function that is equal to zero on the conductive part of the dipoles (Σ_c), and different from zero on the gaps (Σ_g).

The total electric field can be expressed as $\mathbf{e}_{tot} = \mathbf{e}_i + \mathbf{e}_s$, i.e. the superposition of the incident and the scattered field. The latter is the electric field radiated by equivalent electric currents $\mathbf{j} = \hat{\mathbf{z}} \times (\mathbf{h}_{tot}^{(1)} - \mathbf{h}_{tot}^{(2)})$ distributed on the surface $\Sigma_g \cup \Sigma_c$. Focusing only on the longitudinal (x) component of the electric field and the electric currents, we can express Eq. (4.1) in integral form as

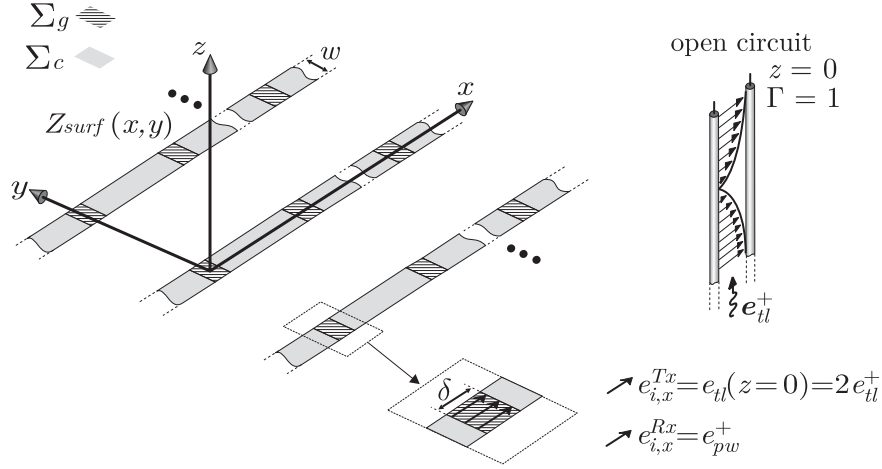


Figure 4.2: Definition of gap region Σ_g and conductive region Σ_c in the array plane and equivalent planar problem.

$$\int_{\Sigma_c \cup \Sigma_g} j_x(\boldsymbol{\rho}') g_{xx}(\boldsymbol{\rho}, \boldsymbol{\rho}') d\boldsymbol{\rho}' = -e_x^i(\boldsymbol{\rho}) + Z_{surf}(\boldsymbol{\rho}) j_x(\boldsymbol{\rho}) \quad (4.2)$$

where g_{xx} is the free-space GF, $\boldsymbol{\rho} \equiv (x, y)$, and e_x^i, j_x are the x -components of the incident field and the equivalent electric surface current density, respectively.

The incident electric field is the total electric field on the array in absence of the dipoles. It assumes different forms in the transmit and receive cases. In the transmit case, the absence of the dipoles implies an array of transmission lines terminated in open circuit. Thus for each feeding point $e_{i,x}^{Tx} = e_{tl}(z=0) = 2e_{tl}^+$ (see inset of Fig. 4.2). In the reception case, the presence of the feed lines should be considered as well. However, if only differential currents are allowed to propagate along these lines, the incident field is unperturbed and can be assumed to coincide with the incoming plane wave, $e_{i,x}^{Rx} = e_{pw}^+$. Common-mode currents on the feed lines and their impact on the array performance will be discussed in Chapter 6 and are neglected in the present investigation.

4.2.1 Separation of Variables

With little loss of generality, the incident electric field along x can be assumed to be expressed as the product of two functions of the longitudinal (x) and transverse (y) variables, i.e. $e_x^i(\boldsymbol{\rho}) = e_x^i(x) f_t(y)$, with $f_t(y=0) = 1$. Also the electric current on each dipole, when the dipole width is small in terms of wavelength, can be assumed to be characterized

by a separable functional dependence from the transverse and longitudinal dimensions, $j_x(\boldsymbol{\rho}) = \sum_{n_y=-\infty}^{\infty} i_{n_y}(x)j_t(y)$. In the following we will assume that the electric current on different dipoles are related by $i_{n_y}(x) = i_{n_y=0}(x)e^{-jk_{y0}n_yd_y}$, where $k_{y0} = k_0 \sin \theta \sin \varphi$ is the transverse excitation law when the array is scanning toward or receiving from the direction given by (θ, φ) , defined as in Fig. 4.1. The transverse y -dependence of the electric current in each dipole is assumed to comply with the quasi-static edge singularity, i.e. $j_t(y) = 2/(w\pi)(1 - (2y/w)^2)^{-1/2}$. This choice suggests to assume a surface impedance distribution as follows:

$$Z_{surf}(x, y) = \begin{cases} Z_l \frac{w\pi}{\delta} \sqrt{1 - \left(\frac{2y}{w}\right)^2} & \forall (x, y) \in \Sigma_g \\ 0 & \forall (x, y) \in \Sigma_c \end{cases} \quad (4.3)$$

so that, for every n_y , we can write

$$Z_{surf}(x, y = n_y d_y) j_x(x, y = n_y d_y) = \frac{Z_l}{\delta} \chi_g(x) i_{n_y}(x) \quad (4.4)$$

with $\chi_g(x) = \begin{cases} 1 & \forall x \in \Sigma_g \\ 0 & \forall x \in \Sigma_c \end{cases}$.

4.2.2 One-Dimensional Equation

When Eq. (4.2) is enforced on the axis of the zeroth dipole ($n_y = 0$), it can be compactly expressed as a one dimensional integral equation in the space domain:

$$\int_{-\infty}^{\infty} i(x') d_l(x, x') dx' = -e_x^i(x) + \frac{Z_l}{\delta} \chi_g(x) i(x) \quad (4.5)$$

where we used the notation $i(x) = i_{n_y=0}(x)$, and

$$d_l(x, x') = \sum_{n_y=-\infty}^{\infty} \int_{-\infty}^{\infty} j_t(y' - n_y d_y) g_{xx}(x, x', y=0, y') dy' e^{-jk_{y0}n_yd_y} \quad (4.6)$$

is the spatial expression of the longitudinal (x) dependence on the GF, once the dependence from the transverse dimension (y) is accounted for.

4.2.3 Total Currents on the Gaps

Equation (4.5) is a Fredholm integral equation of the second kind for the unknown spatial current distribution $i(x)$. To simplify the solution, it is convenient to assume that the gaps are small in terms of wavelength (δ -gap generator/load). Thus, the current in the gaps can be approximated with its total value:

$$\chi_g(x)i(x) \approx \sum_{n_x=-\infty}^{\infty} i_{n_x}^{tot} \Pi_\delta(x - n_x d_x) \quad (4.7)$$

with $\Pi_\delta(x) = \begin{cases} 1 & \text{for } x \in (-\frac{\delta}{2}, \frac{\delta}{2}) \\ 0 & \text{elsewhere} \end{cases}$

and

$$i_{n_x}^{tot} = \frac{1}{\delta} \int_{n_x d_x - \delta/2}^{n_x d_x + \delta/2} i(x) dx. \quad (4.8)$$

4.2.4 Spectral Integral Equation

Upon substituting (4.7) in (4.5) and expressing the equation in the spectral domain, the spatial convolution in the left hand side (LHS) becomes a spectral product, so that we obtain

$$\int_{-\infty}^{\infty} I(k_x) D_l(k_x) e^{-jk_x x} dk_x = \int_{-\infty}^{\infty} \left(-E_x^i(k_x) + Z_l \sum_{n_x=-\infty}^{\infty} i_{n_x}^{tot} \text{sinc}\left(\frac{k_x \delta}{2}\right) e^{jk_x n_x d_x} \right) e^{-jk_x x} dk_x \quad (4.9)$$

with

$$D_l(k_x) = \frac{1}{d_y} \sum_{m_y=-\infty}^{\infty} J_0\left(\frac{k_{ym} w}{2}\right) G_{xx}(k_x, k_{ym}). \quad (4.10)$$

In the last equation, D_l is expressed as an infinite summation over the transverse Floquet wavenumbers $k_{ym} = k_{y0} - 2\pi m_y/d_y$, due to periodicity in the transverse direction. G_{xx} is the spectral domain representation of the electric field GF of an electric source, in absence of the dipoles. J_0 is the zeroth order Bessel function of the first kind, corresponding to the Fourier transform (FT) of the transverse current distribution $j_t(y)$.

4.3 Solution for Periodic Arrays and Thévenin Circuits

Equation (4.9) is characterized by a continuous spectral integration and remains valid also for a finite number of feeds along the longitudinal direction. In that case, the infinite summation in n_x is truncated after a finite number of terms. However, when the array is assumed to be periodically excited by an infinite number of feeds, the currents in the gaps are related by $i_{n_x}^{tot} = i_0^{tot} e^{-jk_{x0}n_x d_x}$, with $k_{x0} = k_0 \sin \theta \cos \varphi$. Accordingly, the spectral integration in k_x can be expressed as spectral summation in $k_{xm} = k_{x0} - 2\pi m_x/d_x$. The solution for the current spectrum is then obtained by equating each spectral component with a procedure similar to the one presented in Sec. 2.2, and the result is

$$I(k_{xm}) = \frac{-E_x^i(k_{xm}) + Z_l i_0^{tot} \operatorname{sinc}\left(\frac{k_{xm}\delta}{2}\right)}{D_l(k_{xm})}. \quad (4.11)$$

The spatial current distribution on the zeroth dipole ($n_y = 0$) is then derived by performing a discrete inverse Fourier transform (FT):

$$i(x) = \frac{1}{d_x} \sum_{m_x=-\infty}^{\infty} I(k_{xm}) e^{-jk_{xm}x}. \quad (4.12)$$

It can be noted that the last two equations are not written in explicit form yet, as they depend on the unknown term i_0^{tot} . The explicit expressions can be obtained by substituting Eq. (4.12) in (4.8) to evaluate the total current on the gap with $n_x = 0$. This calculation, after simple but tedious algebraic manipulations, leads to

$$i_0^{tot} = \frac{Z_a}{Z_a + Z_l} \frac{1}{d_x} \sum_{m_x=-\infty}^{\infty} \frac{-E_x^i(k_{xm}) \operatorname{sinc}\left(\frac{k_{xm}\delta}{2}\right)}{D_l(k_{xm})} \quad (4.13)$$

where we introduced the infinite array antenna impedance $Z_a = 1/Y_a$. The antenna admittance Y_a can be defined from Eq. (2.35), assuming an array in transmission with unitary voltage excitations:

$$Y_a = \frac{1}{Z_a} = \frac{1}{d_x} \sum_{m_x=-\infty}^{\infty} \frac{-\operatorname{sinc}^2\left(\frac{k_{xm}\delta}{2}\right)}{D_l(k_{xm})}. \quad (4.14)$$

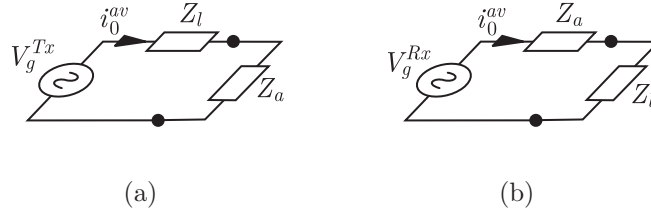


Figure 4.3: Equivalent Thévenin circuit of the 0-th element of the array in transmit mode (a) and receive mode (b).

4.3.1 Transmit Case

When the array is studied in transmission, the incident field can be assumed to be concentrated in the dipole gaps and uniformly distributed. The spectral expression for a δ -gap excitation can be written as

$$E_x^i(k_{xm}) = V_g^{Tx} \operatorname{sinc}\left(\frac{k_{xm}\delta}{2}\right) \quad (4.15)$$

where $V_g^{Tx} = 2e_{tl}^+/\delta = 2V_{tl}^+$.

When this expression is substituted in Eq. (4.13), the electric current i_0^{tot} becomes

$$i_0^{tot} = \frac{V_g^{Tx}}{Z_l + Z_a}. \quad (4.16)$$

Thus, a typical Thévenin-like equivalent circuit as the one in Fig. 4.3(a) can be used to describe the current in the feeding gaps of a transmitting connected array. As pointed out in Sec. 4.1, Z_l and V_g^{Tx} are Thévenin equivalent impedance and the voltage generator, just mathematical representations; thus, these components should not be interpreted with a physical mechanism. For instance, let us consider a lossless transmission line as in Fig. 4.4(a). The line can be replaced by a Thévenin generator as in Fig. 4.4(b). This latter is equivalent if one is interested to know the current that is flowing into the load Z_a . However, in the condition of conjugate matching, there would be no real power dissipation in the impedance Z_l , as no power is lost in the feeding transmission line.

4.3.2 Receive Case

When the array is analyzed in reception, a plane-wave excitation can be assumed. Since the x -component of the incident field is periodic, with constant amplitude and linear phase

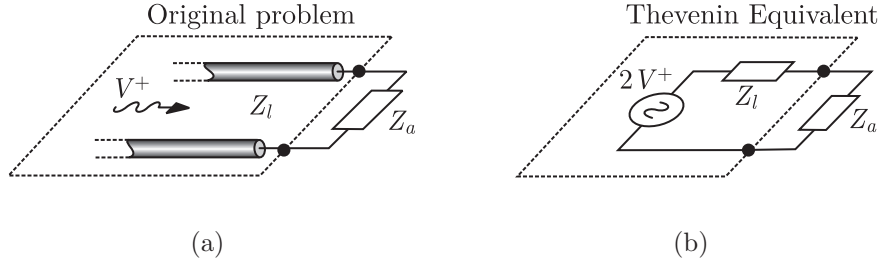


Figure 4.4: Equivalent Thévenin circuit of the 0-th element of the array in transmit mode (a) and receive mode (b).

(proportional to k_{x0}) over a unit cell, in the spectral domain it can be expressed as

$$E_x^i(k_{xm}) = e_{pw}^+ d_x \delta_{m_x} \quad (4.17)$$

where e_{pw}^+ is the amplitude of the incident electric field and δ_{m_x} is the Kronecker delta, which is 1 for $m_x = 0$ and 0 otherwise. By substituting this expression of the incident field in Eq. (4.13), one obtains

$$i_0^{tot} = \frac{V_g^{Rx}}{Z_a + Z_l} \quad (4.18)$$

where

$$V_g^{Rx} = Z_a \frac{-e_{pw}^+ \text{sinc}\left(\frac{k_{x0}\delta}{2}\right)}{D_l(k_{x0})}. \quad (4.19)$$

Thus, also in the receiving case, the equivalent circuit for the current in the feeding gaps can be recognized to be the one, Thévenin-like, in Fig. 4.3(b). This circuit is derived by directly solving the integral equation for the unknown current. In this case, Z_a is the Thévenin equivalent impedance, which should not be blindly associated with scattered power (see Sec. 4.1).

4.4 Expansion of the Thévenin Circuits in Equivalent Networks

The equivalent circuits in Fig. 4.3 give an accurate description of the power that is absorbed by the loads (receive case) or the power that is radiated in free space (transmit

case). However, these two circuits do not explicitly describe the interactions between the capacitive energy in the feed gaps, the inductive energy surrounding the dipoles, and the propagating fields associated with the lower order Floquet waves. A particularly interesting case from an application point of view is the one in which only the fundamental Floquet mode ($m_x = 0, m_y = 0$) is in propagation. This is a low-frequency approximation and is valid as long as the array is well sampled. In this case, an expanded rigorous circuit representation that accounts for all the above mentioned interactions can be derived. This circuit representation can be obtained expanding the antenna admittance and isolating different terms with a well defined physical meaning. It is evident from Eq. (4.14) that the antenna admittance is expressed as a double summation in m_x and, implicitly via D_l , in m_y (see Eq. (4.10)). Let us introduce a notation that implies summation over unspecified scripts, i.e. $Y_a = Y_{m_x}^{m_y}$. The starting point to obtain the expanded equivalent circuit representation is the isolation in Y_a of the term associated with $m_x = 0$:

$$Y_a = Y_{m_x}^{m_y} = Y_{m_x=0}^{m_y} + Y_{m_x \neq 0}^{m_y} = \frac{1}{d_x} \frac{-\text{sinc}^2(\frac{k_{x0}\delta}{2})}{D_l(k_{x0})} + \frac{1}{d_x} \sum_{m_x \neq 0} \frac{-\text{sinc}^2(\frac{k_{xm}\delta}{2})}{D_l(k_{xm})}. \quad (4.20)$$

$Z_{m_x=0}^{m_y} = 1/Y_{m_x=0}^{m_y}$ can be further expressed as the series of two impedances by expanding the explicit expression of D_l in two terms associated with $m_y = 0$ and $m_y \neq 0$, respectively:

$$Z_{m_x=0}^{m_y} = Z_{m_x=0}^{m_y=0} + Z_{m_x=0}^{m_y \neq 0} = \frac{-J_0(\frac{k_{y0}w}{2})G_{xx}(k_{x0}, k_{y0})}{\frac{d_y}{d_x} \text{sinc}^2(\frac{k_{x0}\delta}{2})} + \frac{-\sum_{m_y \neq 0} J_0(\frac{k_{ym}w}{2})G_{xx}(k_{x0}, k_{ym})}{\frac{d_y}{d_x} \text{sinc}^2(\frac{k_{x0}\delta}{2})}. \quad (4.21)$$

Finally, the input impedance of the antenna can be represented via three separate components, $Z_{m_x=0}^{m_y=0}$, $Z_{m_x=0}^{m_y \neq 0}$ and $Z_{m_x \neq 0}^{m_y}$, arranged as in the circuit in Fig. 4.5. Each of these components has the following physical interpretation:

1. $Z_{m_x=0}^{m_y=0}$ is the portion of the input impedance associated with the fundamental Floquet mode ($m_x = 0, m_y = 0$); thus, it accounts for the only field that can propagate away or toward the array surface.
2. $Z_{m_x=0}^{m_y \neq 0}$ is a term that accounts for the reactive energy (inductance) localized in the surrounding of the dipole, mostly depending on the dipole width (w); this term is in series with the fundamental-mode impedance.
3. $Z_{m_x \neq 0}^{m_y}$ accounts for the reactive energy (capacitance) stored in the feed gap, mostly depending on the gap width (δ); it is in parallel with the previous two components. This term has been previously introduced in Sec. 3.3.2.

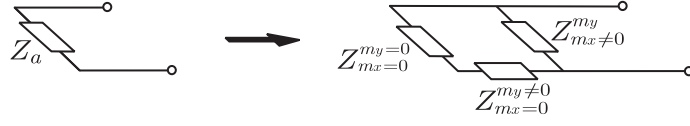


Figure 4.5: Circuit representation of the constitutive terms composing the antenna impedance.

Note that the contributions from higher-order Floquet modes are purely imaginary and sum up as positive reactance (inductive) in the second term and positive susceptance (capacitive) in the third term.

4.4.1 Equivalent Circuit Representation of the Fundamental Floquet Mode

The fundamental-mode component of the antenna impedance ($Z_{m_x=0}^{m_y=0}$) can be further expanded to account for the polarization and the direction of propagation of the radiated/received plane wave. Different components arise from the TE - TM decomposition of Maxwell's equations [39], as well as from the separation between the upper and lower half spaces defined by the array plane ($z = 0$). The spectral GF can be represented as superposition of TE and TM contributions, as shown in Appendix A (which leads to Eq. (A.65)):

$$G_{xx}(k_x, k_y, z = 0) = -\frac{v_{TM}k_x^2 + v_{TE}k_y^2}{k_x^2 + k_y^2} \quad (4.22)$$

where v_{TE} and v_{TM} are the voltage solutions, for unit shunt current generator, of the TE and TM transmission lines. These lines are characterized by propagation constant $k_{z0} = k_0 \cos \theta$ and characteristic impedances $Z_0^{TE} = \zeta_0 / \cos \theta$ and $Z_0^{TM} = \zeta_0 \cos \theta$, respectively (ζ_0 is the free-space characteristic impedance). Since the array is radiating in free space, the voltages v_{TE} , v_{TM} are equal to the impedances seen at the section of the generator. These are obtained as two impedances in parallel, representing the upper and lower media for the TE and TM modes, respectively:

$$Z_{00}^{Ti} = \frac{Z_{00}^{up,Ti} Z_{00}^{down,Ti}}{Z_{00}^{up,Ti} + Z_{00}^{down,Ti}} \quad (4.23)$$

where the superscript Ti can refer to TE or TM . Thus, from Eqs. (4.21) and (4.22), the fundamental component of the input impedance becomes

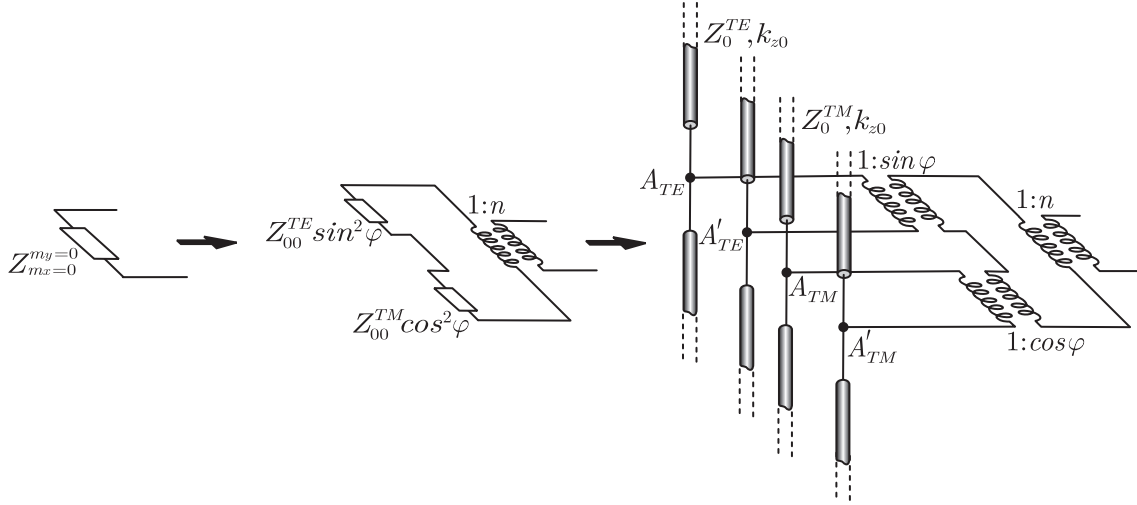


Figure 4.6: Circuit interpretation of the term of the antenna impedance associated with the fundamental Floquet mode ($Z_{m_x=0}^{m_y=0}$).

$$Z_{m_x=0}^{m_y=0} = \frac{-d_x J_0\left(\frac{k_{y0}w}{2}\right) G_{xx}(k_{x0}, k_{y0})}{d_y \operatorname{sinc}^2\left(\frac{k_{x0}\delta}{2}\right)} = n^2 (Z_{00}^{TE} \sin^2 \varphi + Z_{00}^{TM} \cos^2 \varphi) \quad (4.24)$$

with

$$n = \sqrt{\frac{d_x J_0\left(\frac{k_{y0}w}{2}\right)}{d_y \operatorname{sinc}^2\left(\frac{k_{x0}\delta}{2}\right)}}. \quad (4.25)$$

This component of the input impedance can be represented in circuit form as illustrated in Fig. 4.6, where the transformer $1:n$ has been included, accounting for the geometrical parameters of the dipole and the cell. A further expanded representation that includes the transmission lines is also depicted in Fig. 4.6. Two more transformers, $1:\sin\varphi$ and $1:\cos\varphi$, are included to account for the TE and TM portion of the field radiated by an electric current oriented along x , respectively. When the array is radiating in free space, $Z_{00}^{down, Ti} = Z_{00}^{up, Ti} = Z_0^{Ti}$. Different planar stratifications, dielectric or metallic, only alter the portion of the equivalent circuit following the sections $A_{TE}-A'_{TE}$ and $A_{TM}-A'_{TM}$. For instance, when a backing reflector at a distance h is included in the antenna geometry, the transmission line representing the lower half space becomes a short circuit stub, thus $Z_{00}^{down, Ti} = jZ_0^{Ti} \tan(k_{z0}h)$ (see Fig. 4.7).

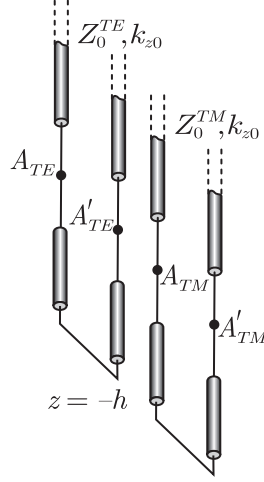


Figure 4.7: Transmission-line model for the propagating part of the fundamental-mode component of the input impedance. The connected array includes a backing reflector at distance h .

4.5 The Equivalent Circuit in Reception

The explicit circuit in Fig. 4.6 has been obtained by expanding the analytical expression of the antenna impedance, which has a physical meaning only in transmission. In reception it is just a Thévenin equivalent impedance. However, the same circuit expansion can also be used in reception as indicated in Fig. 4.8. This is explicitly shown in the Appendix C, where the admittance matrix characterizing the array as a transition at $z = 0$ (see Fig. 4.9) is evaluated analytically and proved to be equivalent to the circuit in Fig. 4.8. The formulation adopted is the one developed in [63, 64]. The analytical expression of the admittance matrix is given in Eqs. (C.28) and (C.29) of Appendix C:

$$\underline{\underline{Y}} = \begin{bmatrix} y_{TETE} & y_{TETM} \\ y_{TMTE} & y_{TM TM} \end{bmatrix} = \begin{bmatrix} \sin^2 \varphi & \sin \varphi \cos \varphi \\ \sin \varphi \cos \varphi & \cos^2 \varphi \end{bmatrix} \cdot \tilde{Y}_l. \quad (4.26)$$

\tilde{Y}_l is a simple function of the load $Y_l = 1/Z_l$ and the higher modal ($m_x \neq 0, m_y \neq 0$) components of Z_a :

$$\tilde{Y}_l = n^2 \frac{(Y_l + Y_{m_x \neq 0}^{m_y}) Y_{m_x=0}^{m_y \neq 0}}{(Y_l + Y_{m_x \neq 0}^{m_y}) + Y_{m_x=0}^{m_y \neq 0}}. \quad (4.27)$$

Since all plane waves can be expressed as a superposition of TE and TM waves, the circuit in Fig. 4.8 can be used to evaluate the reflection, the absorption, the transmission, as well

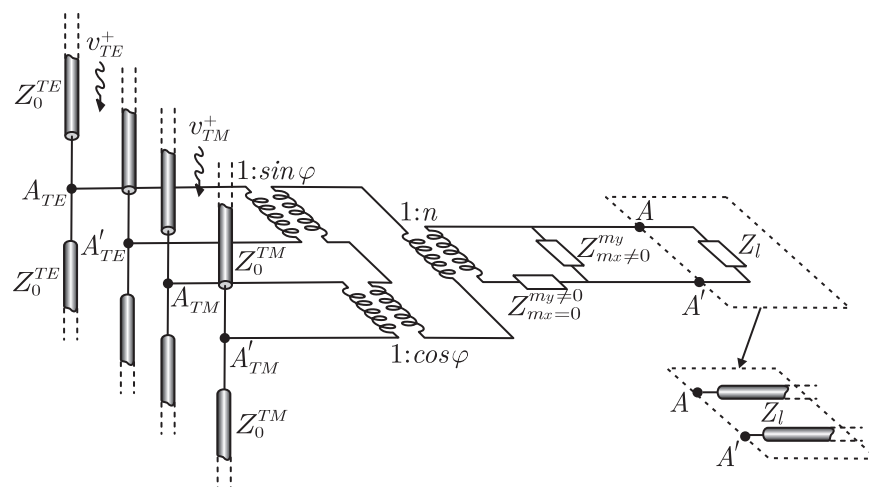


Figure 4.8: Explicit equivalent circuit of the unit cell of a receiving connected array.

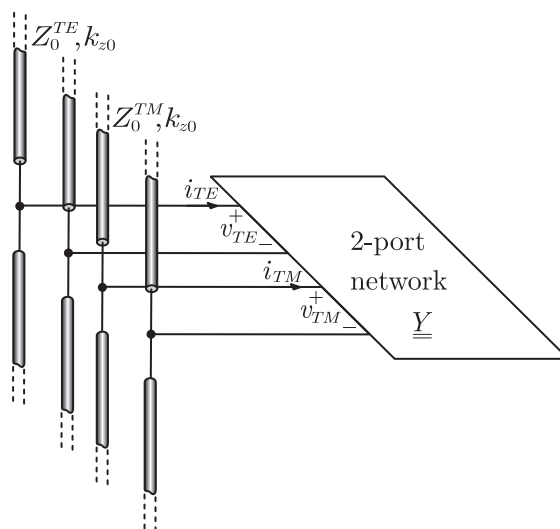


Figure 4.9: Multimode equivalent network representing a well-sampled connected array in free space.

as the induced cross polarization of the array under plane wave incidence. Note also that the load Z_l can be expanded as a feed transmission line, as in the inset, if needed.

4.5.1 Numerical Validation of the Equivalent Circuit in Reception

We now compare the admittance matrix elements (Fig. 4.9), obtained using our analytical circuit representation, with results from full-wave simulations performed with Ansoft HFSS [41]. Figure 4.10(a) shows this comparison for normal incidence, while Fig. 4.10(b) refers to $\theta = 45^\circ, \varphi = 45^\circ$. The cell dimensions are $d_x = d_y = 0.5 \lambda_0$, with λ_0 being the wavelength in free space at 10 GHz. The dipole width w and the gap δ are both $0.1 \lambda_0$. The plots show stable curves over a frequency bandwidth of two decades (1:100), highlighting once again the very broadband characteristic of a connected array structure. Very good agreement can be observed between the analytical and simulated results over most of the band. The discrepancy at the lowest frequencies is due to the lack of convergence of the HFSS solution when dealing with very small electrical dimensions of both the simulation domain and the absorbing boundary volume [65]. Our analytical procedure maintains full accuracy also in the low-frequency regime. To avoid this low-frequency breakdown in HFSS, a larger periodic domain has to be defined, meshed at lower frequency and including more unit cells. Eventually, also HFSS converged to our solution (Fig. 4.11).

4.5.2 Power Absorbed and Scattered by Connected Arrays

The equivalent circuit in Fig. 4.8 is particularly convenient if one is interested in estimating the amount of power that is received or scattered by the array. Figure 4.12(a) shows the power absorbed and backscattered by a connected array in free space, evaluated using the present formulation. The cell dimensions are $d_x = d_y = 0.5 \lambda_0$, and the dipole width w and the gap size δ are both $0.1 \lambda_0$ large. The load is assumed to be $Z_l = 188\Omega$, which would match the array in transmission over an infinite relative bandwidth [30]. It is apparent that an array in free space can only receive half of the incident power, as the level of absorption in the load is about -3 dB. The remaining half of the power is scattered equally to the lower and upper half spaces, resulting in a reflected power of -6 dB. Even if not reported in the graph, the transmitted power is equal to the reflected power ($P_{transm,FS} = P_{refl,FS}$). When the same array is operating in the presence of a backing reflector at a distance $h = 0.25 \lambda_0$, the best matching load in transmission is $Z_l = 377\Omega$, as pointed out in Chapter 3. At the frequencies for which the distance from the ground plane is about a quarter wavelength, the power absorption is almost total (≈ 0 dB) and a reflection lower than -10 dB is observed in Fig. 4.12(b).

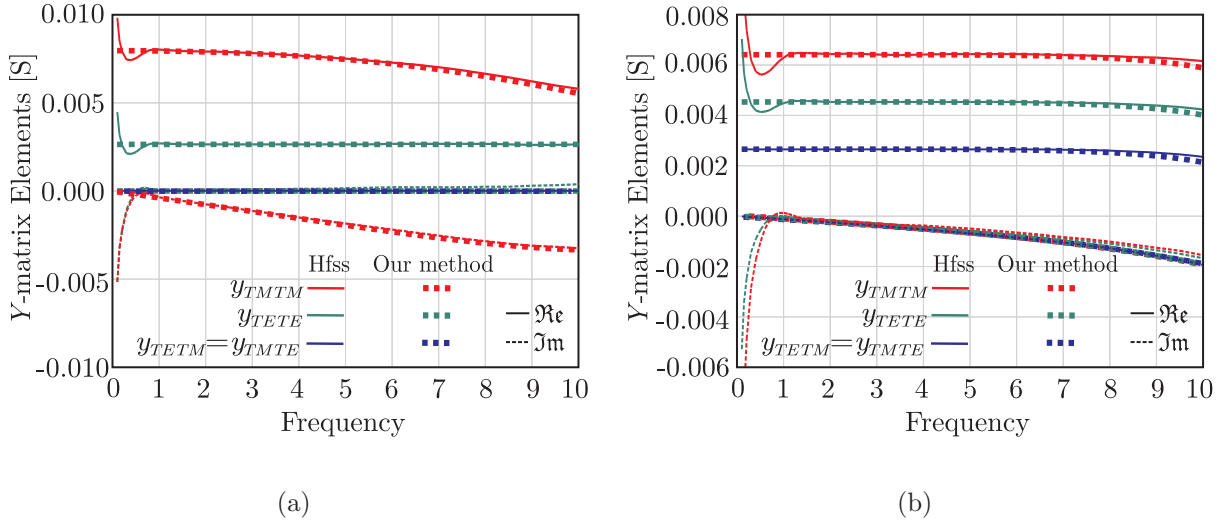


Figure 4.10: Elements of the admittance matrix calculated with the equivalent circuit and HFSS for (a) broadside and (b) for incidence at $\varphi = 45^\circ$ and $\theta = 45^\circ$.

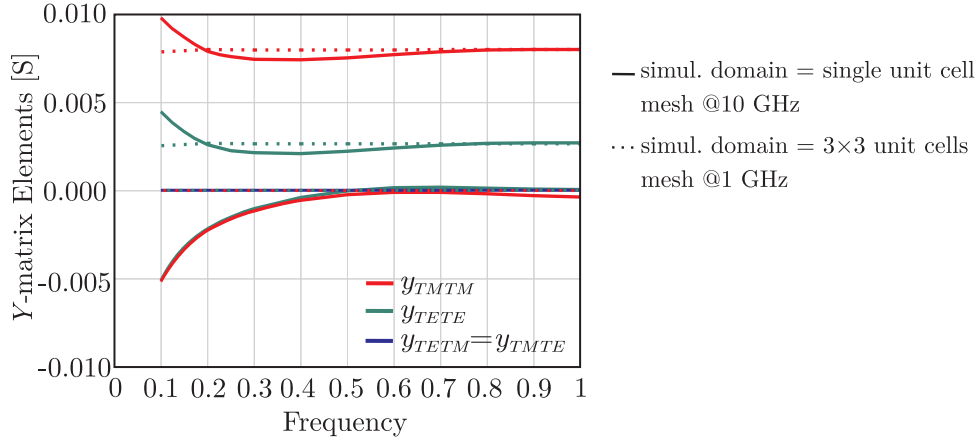


Figure 4.11: Elements of the admittance matrix for broadside incidence calculated via HFSS, with two different sizes of the simulation domain and two different meshes.

Main-Planes Incidence

One can further observe that, in some cases, and only for backed connected arrays, the self-scattering coefficients of the incoming plane wave can be equal to the reflection coefficient of the array analyzed in transmission. This is easy to verify for observation in the main planes. In fact, when $\varphi = 0^\circ$ or $\varphi = 90^\circ$, one of the two transformer $\sin \varphi$ and $\cos \varphi$ in Fig. 4.8 is equal to zero, so the circuit becomes the 2-port network in Fig. 4.13.

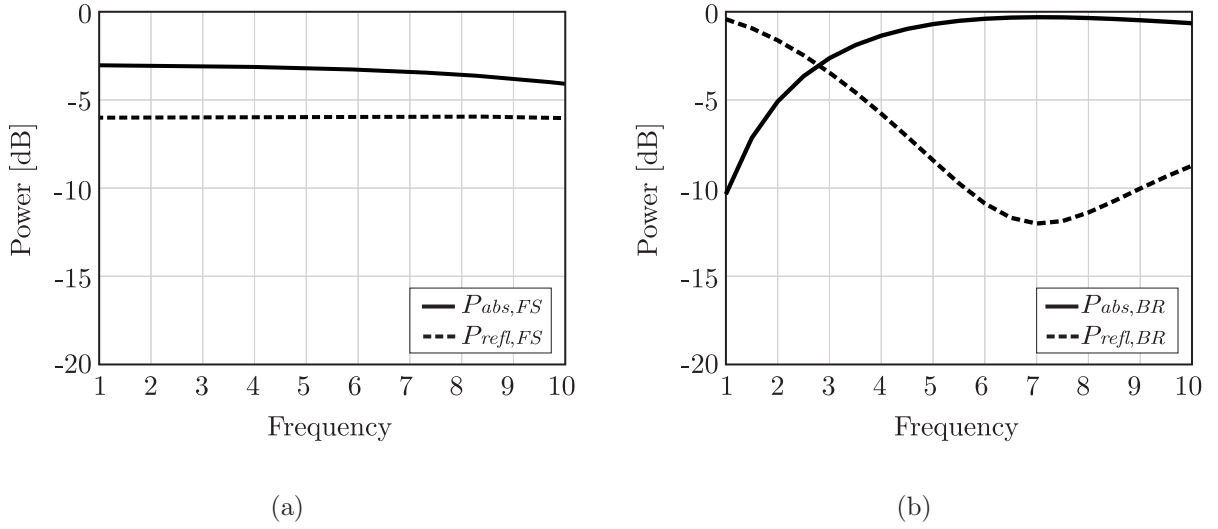


Figure 4.12: Absorbed and reflected power in the case of a connected array (a) in free space receiving from broadside ($Z_l = 188\Omega$) and (b) with backing reflector, receiving from broadside ($Z_l = 377\Omega$).

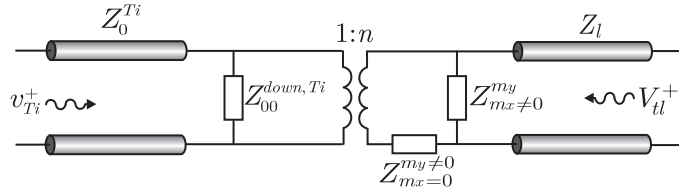


Figure 4.13: Equivalent circuit for plane wave incidence (Rx) or transmission (Tx) in the main planes.

In this circuit, the impedances $Z_{m_x \neq 0}^{m_y \neq 0}$ and $Z_{m_x \neq 0}^{m_y}$ are purely reactive, thus they do not dissipate power. The impedance $Z_{00}^{down,Ti}$ is also a pure reactance only when a backing structure is included. Thus, in this case, the circuit is a lossless two-port network, for which $|S_{11}| = |S_{22}|$.

Oblique Incidence: Polarization

For any other value of φ , the power backscattered by the array in Rx is equal to the reflection coefficient in Tx only if the polarization of the incoming plane wave maximally couples with the dipoles.

The field radiated by a transmitting connected array of dipoles oriented along x , for generic oblique direction, is polarized as specified in Fig. 4.14. The radiated electric field is parallel to the co-polar component, accordingly to the second definition of cross polarization (L2)

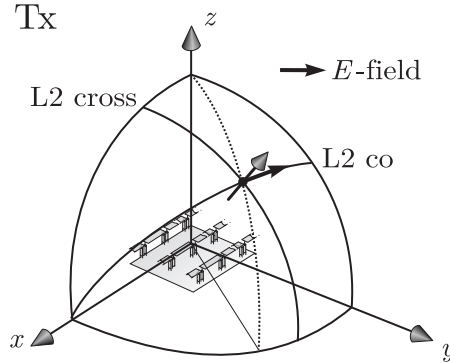


Figure 4.14: Radiation from a transmitting array of dipoles oriented along x : the radiation is polarized as the co-polar component according to the second definition of Ludwig [9].

from Ludwig [9]. If the same array operates in receive mode, its scattered power equals the Tx reflection coefficient only if the incident plane wave is also polarized according to L2.

To understand this aspect, let us consider two incident plane waves perfectly polarized according to the second and third (L3) definition by Ludwig, respectively, as shown in Figs. 4.15(a) and (b). Figure 4.16 compares the scattered power in receive mode for these two cases with the matching of the array operating in transmit mode. The plane wave impinges from $\varphi = 45^\circ$ and $\theta = 45^\circ$, and the geometrical parameters are the same as in Fig. 4.12. Let us remind the reader that a dipole produces no cross polarization for any θ , φ according to L2, while it has a cross-polarization level equal to about -15 dB according to L3, when it is observed at $\varphi = 45^\circ$ and $\theta = 45^\circ$. Accordingly, from Fig. 4.16 it is apparent that, if the incident plane wave is directed along the co-polar component defined by L2, the power reflected by the array is equal to the matching in transmission. Instead, the incident wave directed along the cross-polar component according to L3 gives rise to a slightly higher reflection.

4.6 Consequence: RCS of Antennas as Measure of TX Matching

An important finding of this chapter is that, for opportune polarization of an incoming plane wave, the Radar Cross Section (RCS) of the loaded antenna, that includes a backing reflector, is identically equal to the matching in transmission. This concept has been rigorously demonstrated for E - or H -plane scan and generalized for general oblique inci-

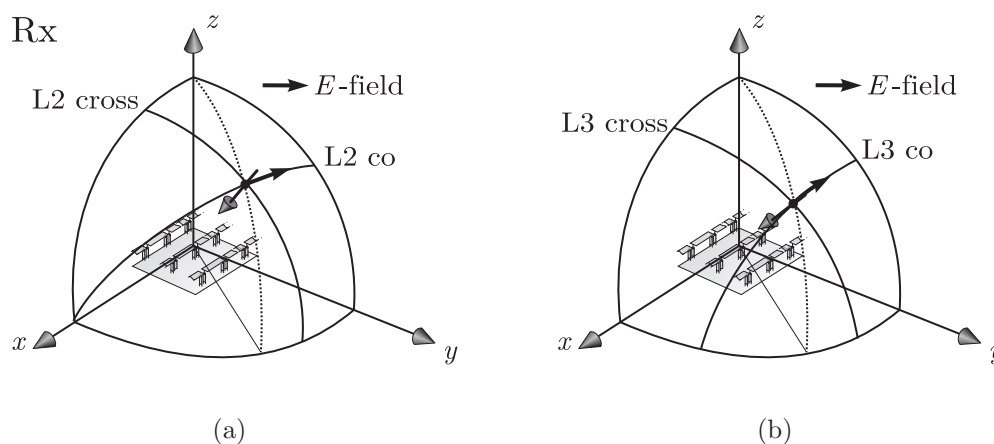


Figure 4.15: Obliquely incident plane wave perfectly polarized according to the (a) second and (b) third definition of Ludwig [9].

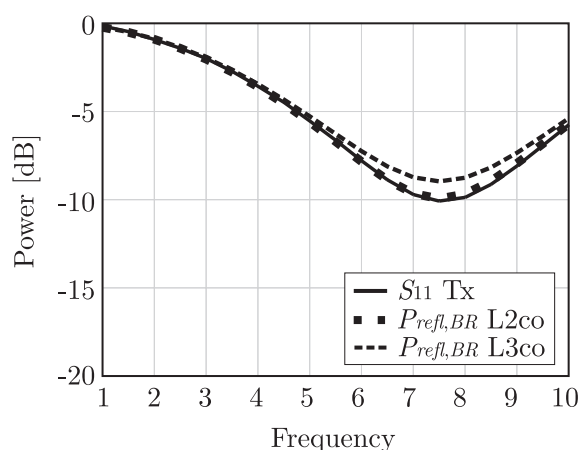


Figure 4.16: Active S_{11} of a backed connected array in transmit mode when scanning to $\theta = 45^\circ$ $\varphi = 45^\circ$. Comparison with reflected power in receive mode, for an incident plane wave from the same direction, polarized according to the second and third definition of Ludwig.

dence. As a consequence, to evaluate the Tx matching properties of the radiating part of a connected array, one can resort to RCS measurements, which can be interpreted in terms of self-scattering parameters. The advantage is that a simple and planar representative prototype can be manufactured without the inclusion of the lossy and expensive feeding network, but loading the planar array with matched resistors, physically implementing the analysis configuration of Fig. 4.2 rather than of Fig. 4.1. This will, on the one hand, save important costs because of the minimum number of elements that constitute a represen-

tative wideband connected array. On the other hand, this procedure allows isolating the characterization of the desirably radiating part of the antenna from the spurious radiation effects due to the feed lines.

Here, the equivalent network presented in Sec. 4.4.1 is used to interpret the results of a dual-band prototype demonstrator that has been manufactured to validate the design procedures presented in [62] (Fig. 4.17). The demonstrator represents a receiving connected array composed of 30×32 elements designed to be well matched in Tx on two separate frequency bands, 8.5-10.5 GHz for radar and 14.40-15.35 GHz for Tactical Common Data Link (TCDL). The antenna RCS has been measured and normalized to the RCS of a metal plate with the same physical dimension of the antenna. The performance of the array in terms of matching and efficiency has been evaluated for two angles: broadside and 45° in the E -plane. Figure 4.18 shows a comparison between the measurements and the calculated active reflection coefficient of a connected dipole in infinite array configuration. HFSS simulations are also reported for comparison. In the GF-based equivalent circuit, the stratification of the backing structure has been modelled using the same procedure used in [62]. The GF is built up from the equivalent transmission line in Fig. 4.19, which also shows an exploded view of the unit cell. A qualitatively good agreement between the experimental and theoretical results can be observed. A matching below the threshold value of -10 dB is achieved in the entire scan range in both the radar and TC DL bands. The discrepancy is mostly due to neglecting the parasitic capacitance typical of the used resistors (PCF0402) in the calculations. The inclusion of this capacitance [66] in both the simulation and the analytical model provides a better agreement with the measurements (see Fig. 4.20). This agreement between measured RCS and computational results validates the measurement strategy proposed in this section for the matching of antennas transmitting in the main planes.

4.7 Conclusions

Connected arrays constitute one of the most effective antenna solutions to implement the transition between radiated waves and guided waves, over broad frequency bandwidths. The equivalent circuits presented in this chapter provide an analytical and rigorous representation of the electromagnetic fields that enable this transition, in the case of a periodically excited, infinite array. The circuits are evaluated analytically and provide an expansion of the standard circuits for receiving antennas that allows their use also to evaluate the scattered power.

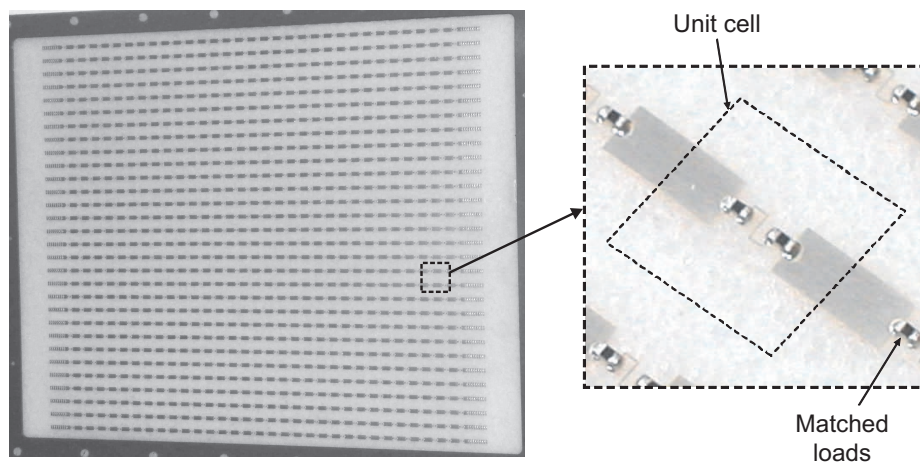


Figure 4.17: Picture of the dual-band 30×32 elements prototype array of connected dipoles.

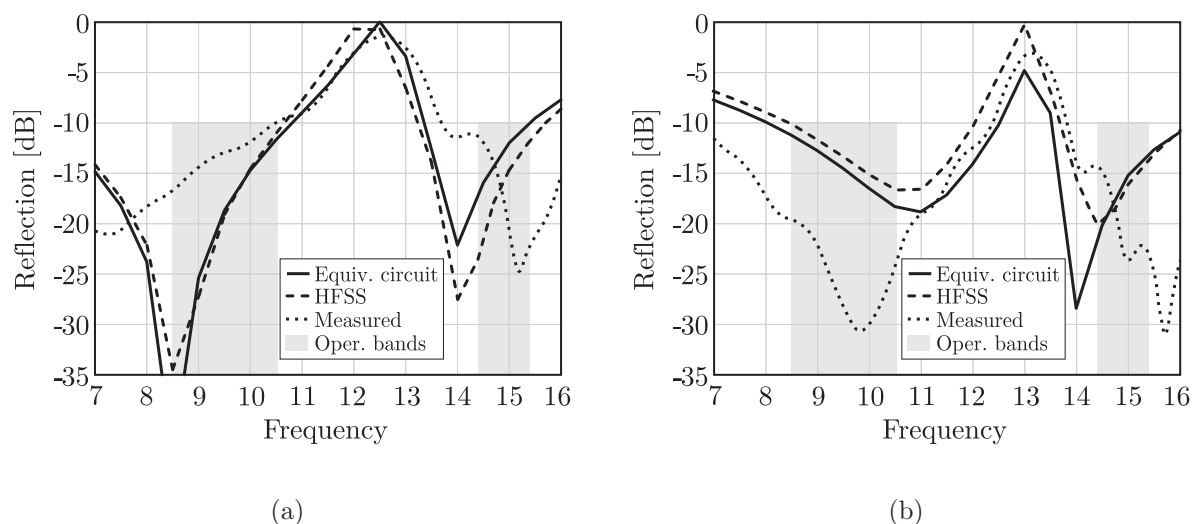


Figure 4.18: Reflection coefficients obtained via equivalent-circuit method and HFSS, compared with measured reflection coefficient in reception: (a) normal incidence and (b) oblique incidence (45° on the E -plane). Operative bands are highlighted in grey.

For the case where the array is well sampled and only the fundamental Floquet waves are propagating, the TE and TM field components in the vicinity of the array are described by means of two transmission lines. These lines also account for the presence of dielectric stratifications and/or frequency selective surfaces and/or backing reflector.

Both TE and TM waves contribute to the complete magnetic field in the periodic cell.

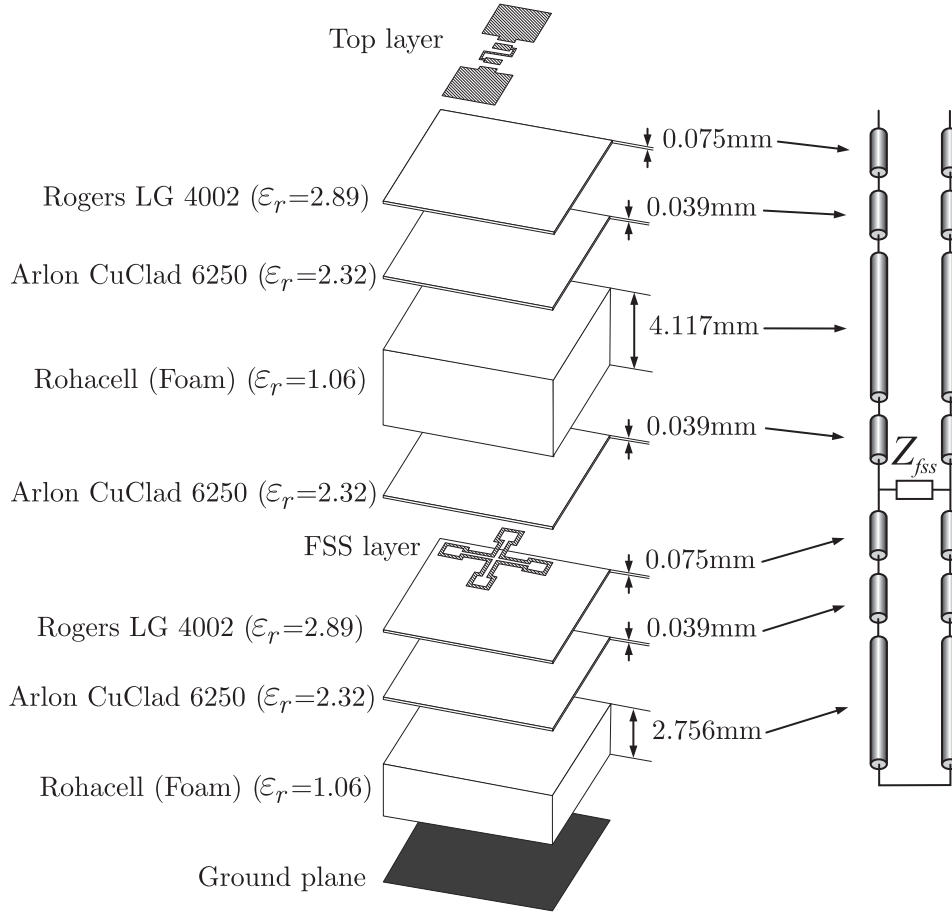


Figure 4.19: Stratification of the unit cell and equivalent transmission-line model of the backing structure.

Accordingly, ad hoc transformers weight the TE and TM equivalent transmission line, to obtain the total ($TE + TM$) average magnetic field in the entire cell at the plane where the antenna terminals are located. The projection of this magnetic field into the feed gap provides the electric currents at the dipole terminals. This projection is represented via another transformer. The near fields only contribute to the localized reactive energy and are represented via lumped loads.

This equivalent network provides the same quantitative information of full-wave numerical simulations, but much more physical insight, as each component is associated with a specific wave mechanism. Moreover, the results have been applied to the analysis of the scattering and absorption of a real connected dipole array backed by a frequency selective ground plane. Since the array is large in terms of wavelength, good agreement was achieved between measurements and results from the equivalent network. The RCS measurements

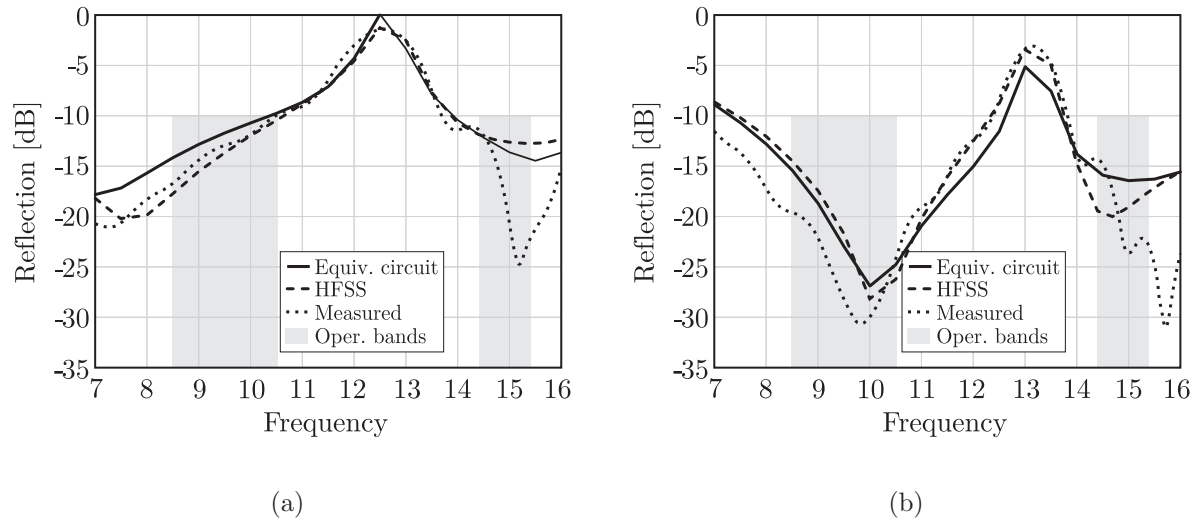


Figure 4.20: As in Fig. 4.18, but including parasitic capacitance of the resistors.

in the main planes can be used to characterize the active matching of the radiating part of the antenna in transmission.

The equivalent circuit was used in [67, 68] for the design of a connected array with inherent frequency selective properties for radar applications. The method was successfully validated by full-wave commercial electromagnetic solvers.

Chapter 5

Finite Connected Arrays

The modelling of connected arrays presented so far in this dissertation was based on infinite-array theory. However, when finiteness is included, edge effects perturb or even dominate the array behavior. These effects are more severe for arrays that are designed to operate over very broad frequency ranges. In fact, the high mutual coupling between the elements in wideband arrays facilitates the propagation of edge-born waves that can become dominant over large portions of the arrays. For example, strong edge effects characterize finite wideband arrays of tapered slot antennas [69–71]. The prediction of these behaviors requires finite-array simulations that are computationally unwieldy for currently available solvers. An enhanced method of moments technique was developed in [17] to analyze large finite arrays of Vivaldi antennas and confirmed the relevance of edge effects in such arrays. The wideband performance of connected arrays is due to the fact that the connections between neighboring elements allow currents to remain nearly constant with frequency [72]. The connections also support the propagation of guided waves from one element to the other. However, as discussed in [31, 73, 74], these guided waves can be very strongly excited at the edges of the array. As a consequence, the overall behavior of the finite array can be dramatically different with respect to the design based on infinite-array analysis. Even if not in the context of connected arrays, [75] and [76] also investigated in detail the effects of strong guided waves associated with the finiteness of wideband dipole arrays.

This chapter presents a Green’s function (GF)-based procedure to assess edge effects in finite connected arrays. The method is analytical and permits to accurately assess edge effects, already in the preliminary design phase of connected arrays. This appears to be a particularly advantageous design tool because it does not require as many computational resources as finite-array full-wave simulations. Specifically, this chapter will focus only on finiteness effects in the longitudinal direction, along which the dipoles are connected, to

present properties that are specific of connected arrays. In fact, the effects of finiteness associated with the transverse direction, orthogonal to the dipoles, are dominated by space-wave coupling. These effects have been extensively discussed in the dated literature [77] (and there cited references), more recently resorting to windowing type of approximations [78–81], and lately with analytically enhanced full-wave solutions in [71, 82–84]. These last works heavily relied on the ray field representations introduced in [85], and then refined in a number of more detailed works [86–89].

Here we investigate an infinite number of dipoles along the transverse direction, with each dipole fed at a finite number of points in the longitudinal direction, as shown in Fig. 5.1. The starting base for the analysis is the availability of transmission-line GF of infinitely extended connected arrays. The derivation of these GF was given in Chapter 2 for the connected slots and dipoles, and generalized for both transmitting and receiving arrays including loads in Chapter 4.

In the first part of this chapter, the current distribution is rigorously derived resorting to the transmission-line GF formalism. The global current distribution is obtained via a MoM-like numerical procedure, which requires only one unknown per elementary cell, independently from the cell geometrical parameters. This is possible thanks to the use of an integral equation with kernel characterized by the appropriate connected array GF. Results obtained using this methodology are compared with full-wave simulations using commercial software, showing excellent agreement at much lower computational costs. For practical designs, there is no limit to the longitudinal number of elementary cells that can be studied with this method. Both the cases of connected dipole arrays with and without backing reflectors are considered. By using this procedure, important design considerations regarding the role of the loads in the propagation of edge waves are provided. The method allows one to estimate the efficiency of connected arrays that are large or small in terms of the wavelength at very limited computational cost.

In the second part of the chapter, to gain a deeper physical insight into the wave mechanisms occurring in connected arrays, a different approach is proposed. This latter method is based on the representation of the electric current along each long dipole as the superposition of an infinite-array contribution plus edge-born waves. While infinite-array current components are rigorously derived resorting to the full GF formalism, edge-born waves are approximated as a staircase distribution. It is important to note that this approximation would be totally inadequate for determining the entire current distribution. However, it leads to small errors in absolute terms when applied only to the edge-born contributions. Thanks to this simplification, a single spectrally analytical approximation of the edge currents is obtained. The singularities of this spectrum can be investigated and the pertaining

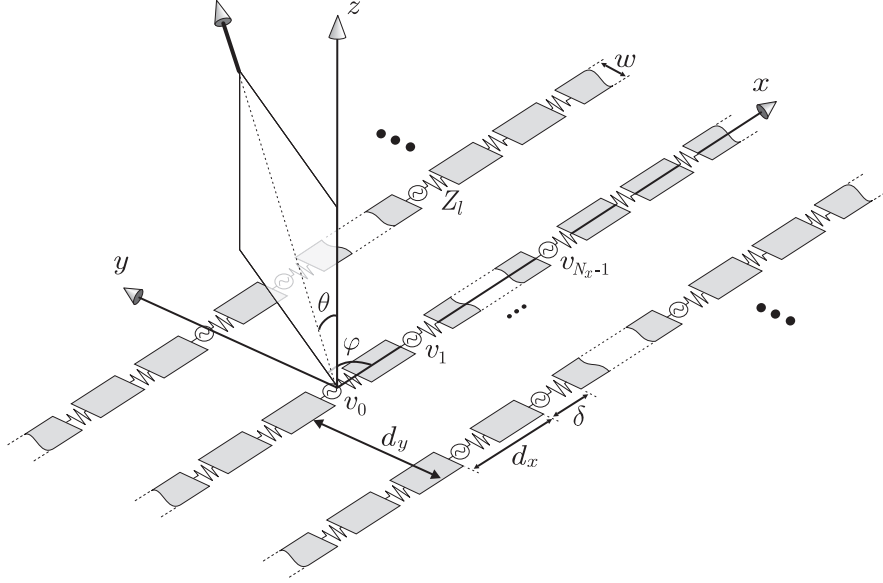


Figure 5.1: Two-dimensional connected array of dipoles with infinite \times finite number of feeds.

inverse Fourier integrals can be asymptotically evaluated to provide the analytical expressions for the spatial currents. These analytical steps are performed only in the cases of arrays in free space and scanning in the E -plane, to maintain the analytical formulation as simple as possible, while still highlighting the main mechanism. Important potentials remain for future developments of the theoretical formulation.

5.1 Set Up of the Spectral Equation: The Finite \times Infinite Array Case

The geometry of the problem under analysis is depicted in Fig. 5.1, for arrays of connected dipoles operating in transmission (Tx). The reception (Rx) case will be discussed later on in Sec. 5.2.1, since it does not present particular difficulties, but requires a somewhat different notation. The dipoles, of width w and separated by distance d_y along y , are electrically connected along the longitudinal direction (x). When the array is transmitting, each dipole is fed at N_x points ($0, N_x - 1$), spaced by period d_x . The excitations on the zeroth dipole ($y=0$) are realized by lumped voltage generators with internal source impedance Z_l and voltages v_{n_x} . For all other dipoles along the y direction, a progressing phase is imposed: $e^{-jk_{y0}n_y d_y}$, where $k_{y0} = k_0 \sin \theta \sin \varphi$, k_0 is the free-space wave number, and (θ, φ) indicate the pointing direction of the main beam. Note that, even if the dipoles are fed at a finite

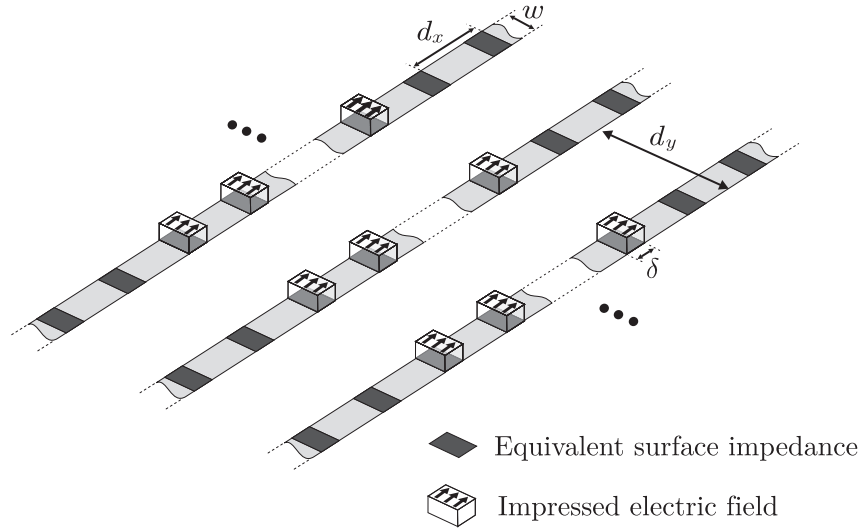


Figure 5.2: Equivalent planar problem of a connected array of dipoles with infinite \times finite number of feeds.

number of points (N_x), it is assumed that the loads are periodically distributed over the entire length of the infinitely extended dipoles. The impact of this hypothesis in the actual solution is minimal, just like the infinite length of the dipoles themselves, and it is only retained for the sake of a clearer and simpler formulation.

The equivalent planar problem is shown in Fig. 5.2 for an array in free space. The problem can also be set up with the dipole assumed to be backed by an infinite ground plane at distance h . In the present model we assume that both the ground plane and the dipoles are infinitely extended and thus the finiteness of the metallizations is not accounted for.

The derivation of the GF for doubly infinite, periodically excited, connected arrays with the inclusion of the loads was presented in Chapter 4. In the case of a finite number of feeds (N_x), a similar integral equation for the unknown current $i(x')$ along the zeroth dipole ($y = 0$) can be used. One should only take care that in the right hand side (RHS) of Eq. (4.5) the incident field is now defined over a finite number of feeds, with indices from 0 to $N_x - 1$. The incident field is assumed to be concentrated in the dipole gaps and uniformly distributed (δ -gap excitation). Thus, the relevant integral equation is given by:

$$\int_{-\infty}^{\infty} i(x') d_l(x, x') dx' = - \sum_{n'_x=0}^{N_x-1} \frac{v_{n'_x}}{\delta} \Pi_{\delta, n'_x}(x) + Z_l \sum_{n'_x=-\infty}^{\infty} \frac{i_{\delta}^{n'_x}}{\delta} \Pi_{\delta, n'_x}(x) \quad (5.1)$$

- d_l is the space domain Green's function once the dependence from the transverse dimension (y) is accounted for (see Eq. (4.6));

- the incident electric field at each feeding gap $e_{i,n'_x} = v_{n'_x}/\delta$ is expressed via $v_{n'_x} = v_0 e^{-jk_{x0}n'_x d_x}$, with $k_{x0} = k_0 \sin \theta \cos \varphi$ if the array is scanning toward (θ, φ) ;
- $i_\delta^{n_x}$ is the total current flowing in the n_x -th gap (see Eq. (5.5));
- $\Pi_{\delta,n_x}(x) = 1$ for $x \in (n_x d_x - \delta/2, n_x d_x + \delta/2)$ and 0 elsewhere.

By resorting to the same technique shown in Chapter 4, we can solve Eq. (5.1) in the Fourier domain, obtaining an expression for the spectral current distribution along the dipoles. The spectrum of the current can be written as follows:

$$I(k_x) = \frac{\text{sinc}(\frac{k_x \delta}{2})}{D_l(k_x)} \left(- \sum_{n'_x=0}^{N_x-1} v_{n'_x} e^{jk_x n'_x d_x} + Z_l \sum_{n'_x=-\infty}^{\infty} i_\delta^{n'_x} e^{jk_x n'_x d_x} \right) \quad (5.2)$$

For arrays in free space, the explicit expression of the Green's function $D_l(k_x)$ is given by:

$$D_l(k_x) = - \frac{\zeta_0(k_0^2 - k_x^2)}{2k_0 d_y} \sum_{m_y=-\infty}^{\infty} \frac{J_0(\frac{k_{ym} w}{2})}{\sqrt{k_0^2 - k_x^2 - k_{ym}^2}} \quad (5.3)$$

while in the case of a backing reflector at a distance h from the array, the following expression is found:

$$D_l(k_x) = - \frac{\zeta_0(k_0^2 - k_x^2)}{2k_0 d_y} \sum_{m_y=-\infty}^{\infty} \frac{J_0(\frac{k_{ym} w}{2})(1 - e^{-j2h\sqrt{k_0^2 - k_x^2 - k_{ym}^2}})}{\sqrt{k_0^2 - k_x^2 - k_{ym}^2}}. \quad (5.4)$$

The expression of the current spectrum in Eq. (5.2) is given only implicitly, since it depends on the unknown terms $i_\delta^{n'_x}$. In the remainder of this chapter, we propose two different methods to derive an explicit expression for the spatial current distribution over the dipoles. In Sec. 5.2, a rigorous numerical solution that involves a matrix inversion is presented. Instead, in Sec. 5.4, we introduce analytical approximations that allow to explicitly highlight the finiteness effects.

5.2 Numerical Solution

A simple numerical procedure to solve Eq. (5.2) is provided here. The currents $i_\delta^{n_x}$ can be expressed in terms of the spectrum at the left hand side (LHS). To this goal, let us recall the definition of the total currents in the gaps:

$$i_\delta^{n_x} = \frac{1}{\delta} \int_{n_x d_x - \delta/2}^{n_x d_x + \delta/2} i(x) dx. \quad (5.5)$$

Expressing the spatial current distribution $i(x)$ as inverse Fourier transform of (5.2), after a few simple algebraic manipulations, leads to:

$$i_\delta^{n_x} = \sum_{n'_x=-2}^{N_x+1} Y_{n_x n'_x} \left(v_{n'_x} - Z_l i_\delta^{n'_x} \right) \quad (5.6)$$

where the infinite summation (infinite loads) has been restricted to $N_x + 4$ elements, including two dummy elements at each edge of the array. These are typically sufficient, for non negligible values of Z_l , to truncate the infinite summation in the RHS of Eq. (5.2). The mutual admittance terms in Eq. (5.6) are defined as

$$Y_{n_x n'_x} = \frac{1}{2\pi} \int_{-\infty}^{\infty} \frac{-\text{sinc}^2\left(\frac{k_x \delta}{2}\right)}{D_l(k_x)} e^{-jk_x(n_x - n'_x)d_x} dk_x. \quad (5.7)$$

Equation (5.6) can be written in matrix form, which leads to a system of linear equations that can be solved by matrix inversion as

$$\mathbf{i}_\delta = [\mathbf{I} + Z_l \mathbf{Y}]^{-1} \mathbf{i}_{Z_l=0} \quad (5.8)$$

where $\mathbf{i}_\delta = \{i_\delta^{-2}, i_\delta^{-1}, \dots, i_\delta^{N_x+1}\}$ is the vector of the unknowns; $\mathbf{i}_{Z_l=0} = \mathbf{Y} \mathbf{v}$ represents the solution for the current in absence of the load and is known; $\mathbf{v} = \{0, 0, v_0, \dots, v_{N_x-1}, 0, 0\}$ is the vector of the impressed voltages; \mathbf{I} is the identity matrix. The inversion leads to the exact solution for the total currents on the gaps including the effects of the loads.

The elements of the admittance matrix in Eq. (5.7) can be evaluated numerically by performing the spectral integral with convenient deformations of the original integration path on the real k_x -axis. Figure 5.3 shows the complex topology and the branch cuts associated with the first (for $m_y = 0$) square root of the GF that appears in Eqs. (5.3) and (5.4). The branch points are in $\pm k_0$ in the case in which the array is scanned only in the longitudinal direction ($k_{y0} = 0$, or $\varphi = 0$). For highly-coupled elements (small factors $n_x - n'_x$), an integration path deformation as in Fig. 5.3(a) has been used to avoid the branch cuts. For large distances $(n_x - n'_x)d_x$, the integrands present faster oscillations on the

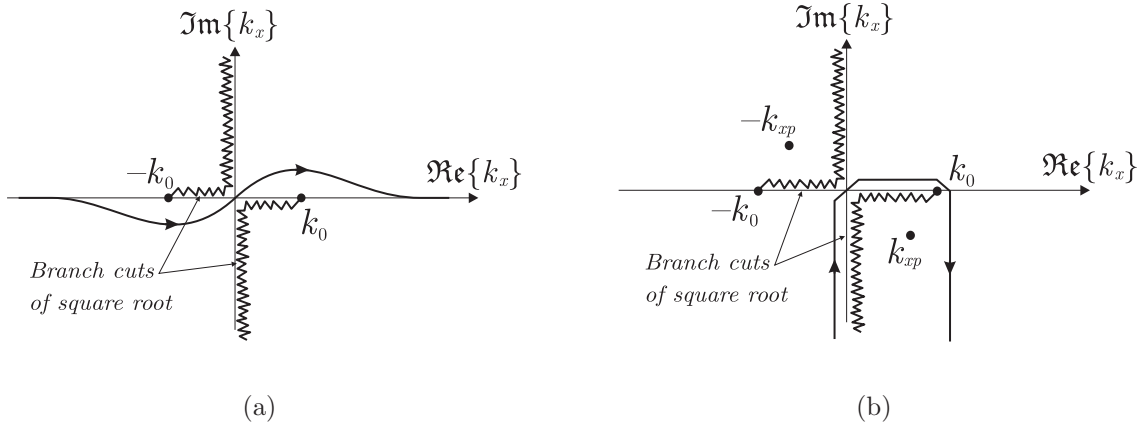


Figure 5.3: Deformation of the integration path in Eq. (5.7): (a) highly-coupled elements; (b) low-coupled elements.

real axis. Thus, a path deformation as in Fig. 5.3(b) usually guarantees faster convergence in the free-space cases and whenever poles of the stratification's GF are not captured in the deformation. In the case of the array operating in the presence of a backing reflector, the height of the array from the reflector is typically such that no poles are expected to be found on the real k_x -axis. Further poles could arise in the case the array is printed on a grounded dielectric slab. The presence of these poles would correspond to possible excitation of surface and leaky waves. However, these configurations can be easily avoided in the design, thus they will not be considered in the present context.

5.2.1 Receive Mode

In the receive mode, the source is assumed to be an incident plane wave from the direction (θ, φ) , since the response of the structure to any other source can be represented as the superposition of responses to a spectrum of plane waves.

For plane-wave incidence and arrays in free space, the incident electric field can be expressed in the spectral domain as

$$E_x^i(k_x, y = 0, z = 0) = e_{pw}^+ \delta(k_x - k_{x0}) \quad (5.9)$$

where e_{pw}^+ is the amplitude of the incoming plane wave. A more general expression of the incident field depends on the specific stratification considered. The case of connected arrays in the presence of backing reflector is of particular interest in this study and would imply a multiplying factor $(1 - e^{-jk_{z0}2h})$ in Eq. (5.9).

The total currents in the gaps can be expressed as

$$i_{\delta}^{n_x} = i_{pw, Z_l=0}^{n_x} - Z_l \sum_{n'_x=0}^{N_x-1} Y_{n_x n'_x} i_{\delta}^{n'_x} \quad (5.10)$$

where

$$i_{pw, Z_l=0}^{n_x} = e_{pw}^+ \frac{\text{sinc}\left(\frac{k_{x0}\delta}{2}\right)}{D_l(k_{x0})} e^{-jk_{x0}n_x d_x}. \quad (5.11)$$

The solution for the spatial current distribution in the receiving mode is obtained by substituting $\mathbf{i}_{Z_l=0}$ with $\mathbf{i}_{pw, Z_l=0}$ in Eq. (5.8), where the elements of the vector $\mathbf{i}_{pw, Z_l=0}$ are defined in the same way as in Eq. (5.11).

5.2.2 Results of the Numerical Solution

The active currents at the gaps calculated via Eq. (5.8) can be used to evaluate the active impedances of the finite array, given by $Z_{n_x}^a = v_{n_x}/i_{\delta}^{n_x} - Z_l$, as clear from Fig. 4.3(a).

Figure 5.4 shows a comparison between the numerical solution presented here and simulated result obtained via Ansoft HFSS [41]. Figure 5.4(a) refers to an array in free space that is excited at 15 feed points along x and is infinite along y . The array periods are $d_x = d_y = 0.45 \lambda_0$, where λ_0 is the wavelength at the calculation frequency f_0 . The other geometric parameters of the array are $w = 0.2 \lambda_0$ and $\delta = 0.2 \lambda_0$. Figure 5.4(b) refers to the same array where a backing reflector is included at a distance $h = 0.25 \lambda_0$ from the dipoles. Curves in Figs. 5.4(a) and (b) are shown for broadside radiation and scanning to 45° in the E -plane, while Fig. 5.4(c) refers to the same array in free space, scanning to 45° in the diagonal plane ($\varphi = 45^\circ$). A good agreement can be observed when full-wave HFSS simulations are compared to the numerical solution presented here. Note that, once the total currents on the gaps have been obtained, the total current on the array directly follows from Eq. (5.2), and subsequently all important parameters of the array, including the radiation patterns, can be obtained.

5.3 Efficiency of Finite Connected Arrays

In the previous section we have derived a reliable and fast solution for the current distributions at the feeds of a finite connected array. The main advantage of this formalism is that the efficiency of a scanning connected array can be evaluated much more accurately than

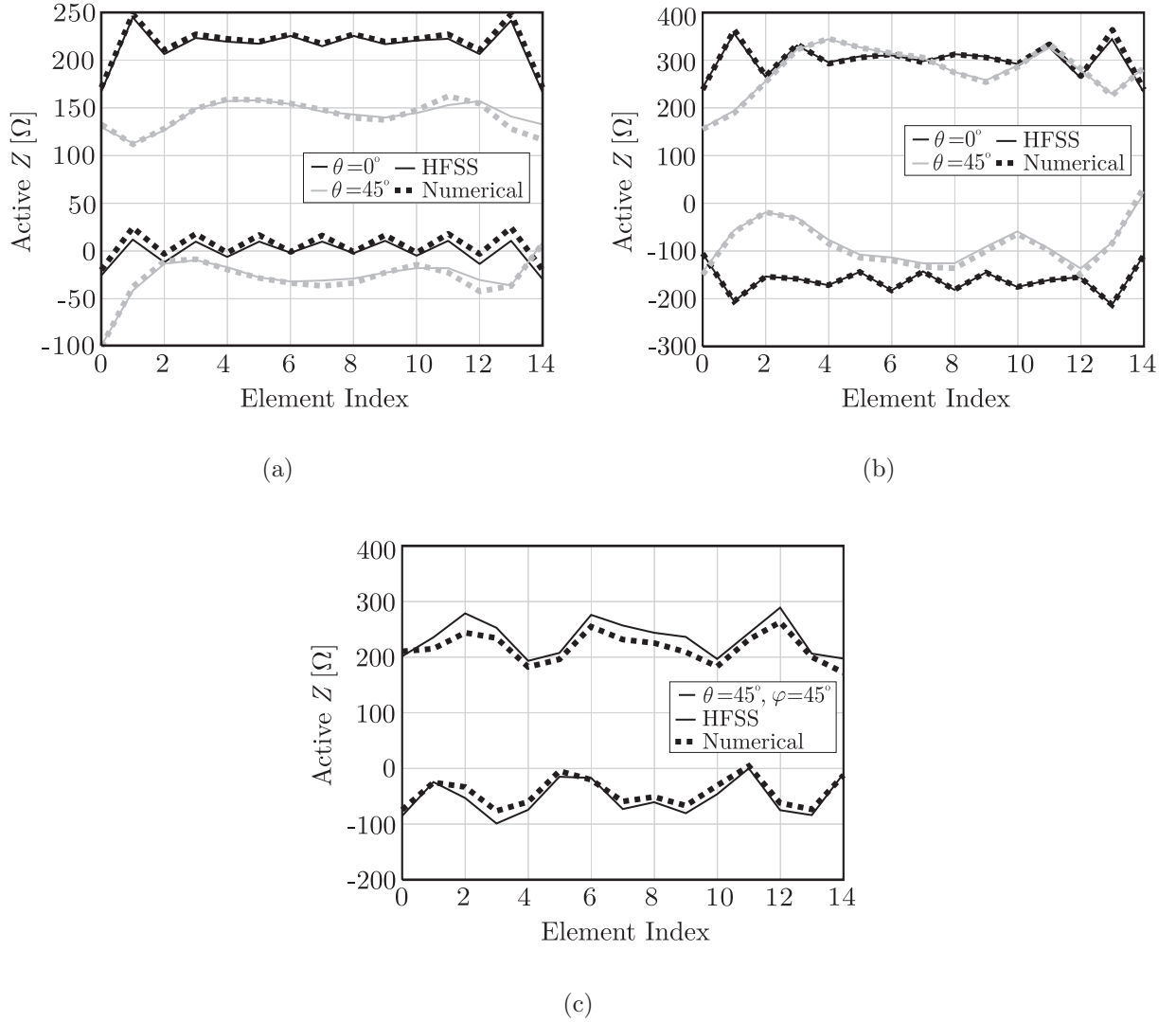


Figure 5.4: Active input impedances of a $15 \times$ infinite array of connected dipoles in (a) free space and (b) with backing reflector, for $\theta = 0^\circ$ and $\theta = 45^\circ$ in the E -plane, and (c) in free space for $\theta = 45^\circ$ in the diagonal plane ($\varphi = 45^\circ$): comparison between the numerical calculation and Ansoft HFSS.

would be possible with only infinite-array solutions. In the present context, the term array efficiency refers to the impedance mismatch at each of the N_x feed points of the array. The array is assumed to be fed by transmission lines with characteristic impedance Z_l that ensures the widest usable bandwidth at broadside. For each feed we can define an active reflection coefficient $\Gamma_{n_x} = (Z_{n_x}^a - Z_l)/(Z_{n_x}^a + Z_l)$, in which $Z_{n_x}^a$ is the active impedance at the n_x element. We can also associate with the same element a mismatch efficiency

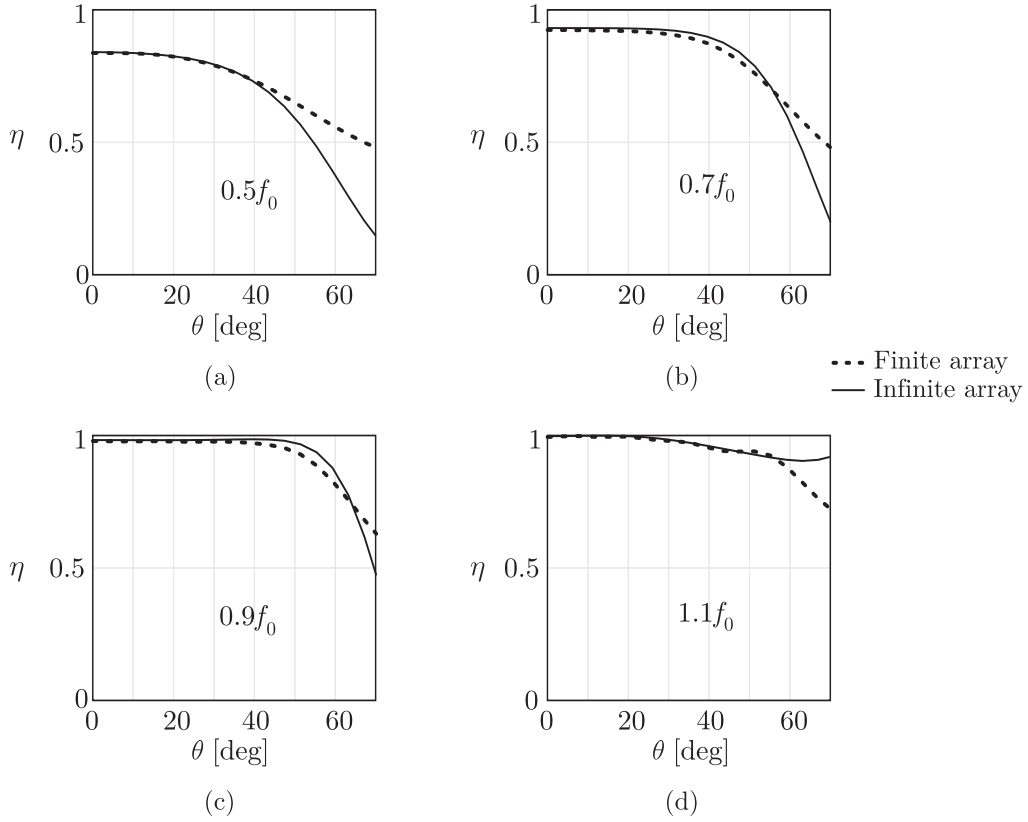


Figure 5.5: Efficiency of a connected arrays with backing reflector as a function of the scanning angle in the E -plane: comparison between infinite-array approximation and finite-array analysis ($Z_l = 400 \Omega$).

$\eta_{n_x} = 1 - |\Gamma_{n_x}|^2$. Clearly, the matching of each element will depend on the frequency and the scanning angle. As a consequence, the overall efficiency of the array $\eta(f, \theta)$ is defined as the average efficiency of the array as follows:

$$\eta(f, \theta) = \frac{1}{N_x} \sum_{n_x=0}^{N_x-1} \left(1 - \left| \frac{Z_{n_x}^a(f, \theta) - Z_c}{Z_{n_x}^a(f, \theta) + Z_c} \right|^2 \right). \quad (5.12)$$

Especially for small arrays scanning to wide angles, the current distributions over the finite arrays can be significantly different from the infinite-array ones. As a consequence, the active impedances are different from those that would be expected only on the base of infinite-array designs.

Figure 5.5 presents the overall array efficiency, defined as in Eq. (5.12), as a function of the scanning angle in the E -plane, for different frequencies. The array under analysis is composed of 8 elements and is operating in the presence of a backing reflector. The specific dimensions are taken from the array design discussed in Sec. 3.4 ($w = 0.05 \lambda_0$, $d_x = d_y =$

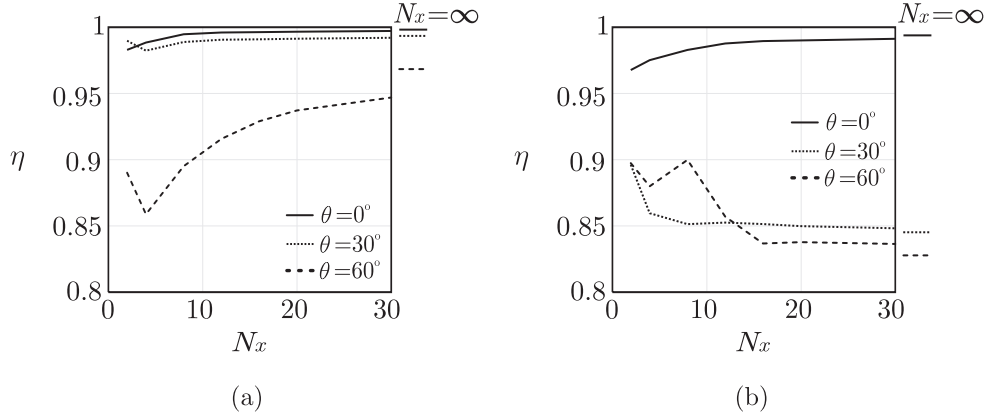


Figure 5.6: Efficiency of a connected arrays with backing reflector as a function of the number of elements, for different scanning angles in the E -plane. Also reported are the asymptotic values of the infinite-array cases. Geometrical parameters are such that array is well matched to (a) 400 Ω loads and (b) to 100 Ω loads.

0.45 λ_0 , $h = 0.31 \lambda_0$, $\delta = 0.125 \lambda_0$, with λ_0 being the wavelength at the frequency f_0) and refer to a load resistance of $Z_l = 400 \Omega$. It is apparent that, for larger scan angles, the finite-array simulations show important differences with respect to the infinite array ones. In practice, the differences between the exact and approximate modelling of the array are significant when the arrays are not perfectly matched. The availability of an accurate and rapid modelling tool for finite arrays is essential for real designs, especially if the threshold of acceptable functionality is defined for scanning toward $\theta = 45^\circ - 60^\circ$.

Figure 5.6 presents the resulting overall array efficiency, as a function of the number of elements of the array, for different scan angles. The figure presents results for two different arrays, both with backing reflector at $h = 0.31 \lambda_0$ and $h = 0.41 \lambda_0$, designed in such a way that the active impedances are well matched to feed lines with 400 Ω and 100 Ω characteristic impedance, respectively. A first predictable consideration is that, when the number of elements of the array tends to be large, the simulations assuming infinite or finite arrays imply similar efficiencies. A second, less obvious design aspect emerges from these calculations. For arrays designed to operate well when fed by low-impedance feeding lines, the edge effects are more important than for arrays designed to be fed by high-impedance lines. Thus, a designer should avoid antenna designs that apparently (with infinite-array simulations) require low input impedances, since in reality in these cases edge effects dominate a much larger portion of the array. Thus, the asymptotic behavior of the infinite array is only achieved with an unrealistically large number of elements. This can only be explained by digging deeper into the physics of finite connected arrays.

5.4 Spectral Integral Approximation

Although the numerical solution presented in Sec. 5.2 is efficient (one unknown per array element) and accurate, it does not provide physical insight into the nature of the edge waves. To obtain an alternative, more insightful representation it is useful to recall how the infinite-array auxiliary problem is set up. By simple extension of Eq. (5.1), the current $i_\infty(x')$ can be represented as the solution of the following integral equation:

$$\int_{-\infty}^{\infty} i_\infty(x') d_l(x, x') dx' = \sum_{n'_x=-\infty}^{\infty} \frac{Z_l i_{\delta, \infty}^{n'_x} - v_{n'_x}}{\delta} \Pi_{\delta, n'_x}(x). \quad (5.13)$$

Once the solution for the current $i_\infty(x')$ is assumed to be known (Sec. 4.3), the electric currents in a finite connected array can be expressed in a form that highlights edge effects as follows:

$$i(x') = i_\infty(x') + i_{edge}(x'). \quad (5.14)$$

The edge term represents the variation induced by finiteness effects. Using Eq. (5.14), the integral equation (5.1) for the finite array can be re-expressed as

$$\int_{-\infty}^{\infty} (i_\infty(x') + i_{edge}(x')) d_l(x, x') dx' = \sum_{n'_x=0}^{N_x+1} \frac{-v_{n'_x}}{\delta} \Pi_{\delta, n'_x}(x) + Z_l \sum_{n'_x=-\infty}^{\infty} \frac{i_{\delta, \infty}^{n'_x} + i_{\delta, edge}^{n'_x}}{\delta} \Pi_{\delta, n'_x}(x) \quad (5.15)$$

where the following notation was used

$$\sum_{n'_x=-\infty}^{\infty} = \sum_{n'_x=0}^{N_x+1} + \sum_{n'_x < 0, n'_x > N_x+1}. \quad (5.16)$$

Subtracting Eq. (5.13) from Eq. (5.15) leads to

$$\int_{-\infty}^{\infty} i_{edge}(x') d_l(x, x') dx' = - \sum_{n'_x < 0, n'_x > N_x+1} \frac{v_{n'_x}}{\delta} \Pi_{\delta, n'_x}(x) + Z_l \sum_{n'_x=-\infty}^{\infty} \frac{i_{\delta, edge}^{n'_x}}{\delta} \Pi_{\delta, n'_x}(x). \quad (5.17)$$

In this equation the only unknown is $i_{edge}(x')$ and in general it cannot be solved with a simple spectral domain approach. However, a particular geometrical case can be solved exactly in a spectral analytical form.

5.4.1 Simple Case: Low Frequency and Generator Distributed over the Entire Cell

A simple case that can be solved in closed form is obtained under the conditions

$$\begin{cases} d_x \ll \lambda_0 \\ d_x = \delta \end{cases}. \quad (5.18)$$

The first hypothesis implies that the edge-born currents can be considered constant over the cell of dimension d_x . This leads to the possible use of a stair-case approximation:

$$i_{edge}(x') \approx \sum_{n'_x=-\infty}^{\infty} i_{d_x,edge}^{n'_x} \Pi_{d_x,n'_x}(x'). \quad (5.19)$$

The second hypothesis, which implies that the load is distributed over the entire elementary cell, allows one to identify the same $i_{edge}(x)$ on the LHS and the RHS of Eq. (5.17). This leads to the following simplified integral equation

$$\int_{-\infty}^{\infty} i_{edge}(x') d_l(x, x') dx' = - \sum_{n'_x < 0, n'_x > N_x + 1} \frac{v_{n'_x}}{d_x} \Pi_{d_x, n'_x}(x) + \frac{Z_l}{d_x} i_{edge}(x). \quad (5.20)$$

This equation can be simply solved analytically once it is expressed in the spectral domain:

$$I_{edge}(k_x) = \frac{v_0 \operatorname{sinc}\left(\frac{k_x d_x}{2}\right)}{D_l(k_x) - \frac{Z_l}{d_x}} \sum_{n'_x < 0, n'_x > N_x + 1} e^{j(k_x - k_{x0})n'_x d_x}. \quad (5.21)$$

The spatial current distribution can be then evaluated as a single inverse Fourier integral, which avoids the necessity to perform the matrix inversion in Eq. (5.8). By integrating the spatial current distribution on the gaps, assuming $v_0 = 1$ Volt, we can express the currents at each feed point of the finite array as follows:

$$i_{\delta,edge}^{n_x} = \frac{1}{2\pi} \int_{-\infty}^{\infty} \frac{\operatorname{sinc}^2\left(\frac{k_x d_x}{2}\right)}{D_l(k_x) - \frac{Z_l}{d_x}} \sum_{n'_x < 0, n'_x > N_x + 1} e^{j(k_x - k_{x0})n'_x d_x} e^{-jk_x n_x d_x} dk_x. \quad (5.22)$$

This last spectral integral can be performed numerically along the path defined in Fig. 5.3(a). A validation of the procedure is shown in Figs. 5.7 and 5.8, which show the

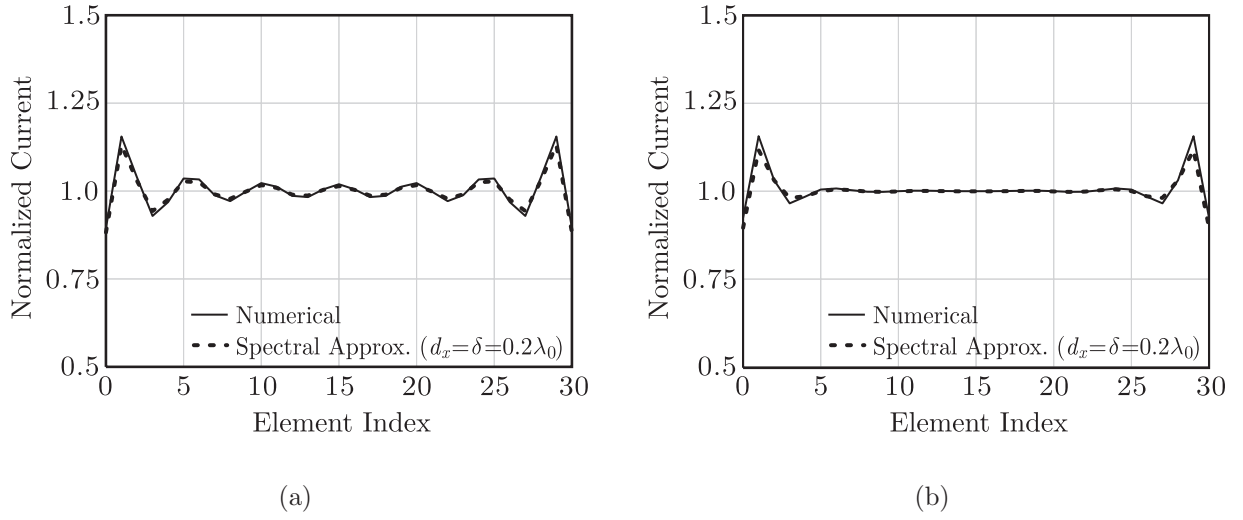


Figure 5.7: Comparison of the numerical solution in Sec. 5.2 and the spectral analytical integration, for arrays pointing at broadside: (a) in free space, (b) with backing reflector at distance $h = 0.1\lambda_0$.

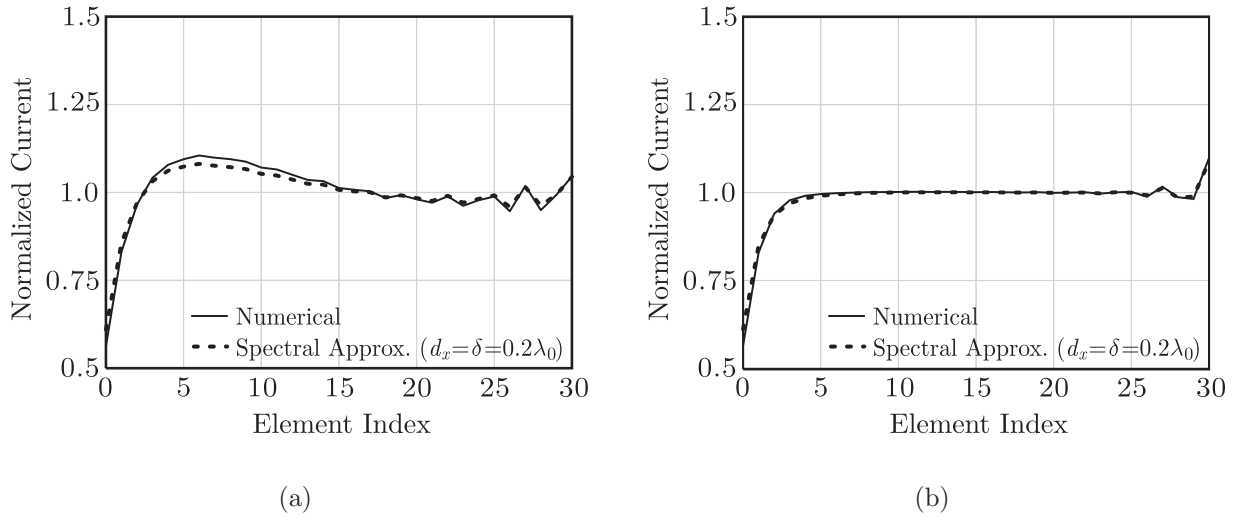


Figure 5.8: As in Fig. 5.7, but for arrays pointing toward $\theta = 60^\circ$ in the E -plane.

magnitude of the total currents in the gaps, normalized to the infinite-array solution. The results are for connected arrays in free space and in the presence of a backing reflector, when scanning toward broadside and toward $\theta = 60^\circ$, respectively. The arrays are fed at 31 points, spaced by $d_x = \delta = 0.2\lambda_0$. Source impedances of $Z_l = 188\ \Omega$ and $Z_l = 377\ \Omega$ are assumed for the array in free space and the one backed by a reflector (at

$h = 0.1 \lambda_0$), respectively. The remaining geometrical parameters of the arrays considered are $d_y = 0.2 \lambda_0$, $w = 0.08 \lambda_0$.

An excellent agreement is obtained between the results predicted by the integration procedure and the fully numerical inversion when Eqs. (5.18) are verified. It can be noted that, in the considered cases, the finiteness of the array can cause variations of the current distribution, with respect to the infinite-array solution, corresponding to a unit magnitude in the graphs, of up to 60% for large scan angles. These variations are still well represented by the integral solution since this solution does not include any important approximations in the simple cases. The same accuracy is maintained also for much smaller or larger arrays. Similar curves, describing edge effects in finite arrays have been first observed in [90], [91] and interpreted with a heuristic Gibbsian model.

5.4.2 Extrapolation of the Simple Case Solution

Equation (5.22) was obtained thanks to the simplifications in Eq. (5.18). Specifically, the second hypothesis is instrumental for the algebraic operations on the spectrum. If one assumes that it makes sense to have the load impedance Z_l distributed over the entire cell (d_x), while the feeding is only applied to a region (δ), with these two parameters being different, Eq. (5.22) can be extrapolated as follows:

$$i_{\delta,edge}^{n_x} = \frac{1}{2\pi} \int_{-\infty}^{\infty} \frac{\text{sinc}^2\left(\frac{k_x \delta}{2}\right)}{D_{load}(k_x)} \sum_{n'_x < 0, n'_x > N_x + 1} e^{j(k_x - k_{x0})n'_x d_x} e^{-jk_x n_x d_x} dk_x \quad (5.23)$$

where $D_{load}(k_x) = D_l(k_x) - Z_l/d_x$ and where δ , possibly different from d_x , now occurs in the argument of the sinc function.

Figure 5.9 shows a comparison of the numerical solution and the spectral integral solution for the currents in the gaps normalized to the infinite-array solution. The connected array is in free space with 15 feeds along x with 200Ω load impedance and it is scanning toward 45° in the E -plane. The four graphs refer to four different frequencies at which the array periodicity and the gap dimensions are $d_x = 0.1, 0.2, 0.4, 0.5 \lambda_0$ and $\delta = 0.04, 0.08, 0.16, 0.2 \lambda_0$, respectively.

The agreement in Fig. 5.9 is excellent at low frequencies and shows only minor deviations at higher frequencies, where the critical small period approximation that justifies the stair-case distribution begins to fail. Overall, it appears that while the low frequency approximation is instrumental to the spectral expression to work, the fact that the second hypothesis in Eq. (5.18) ($\delta = d_x$) does not hold is not important from the point of view of the accuracy

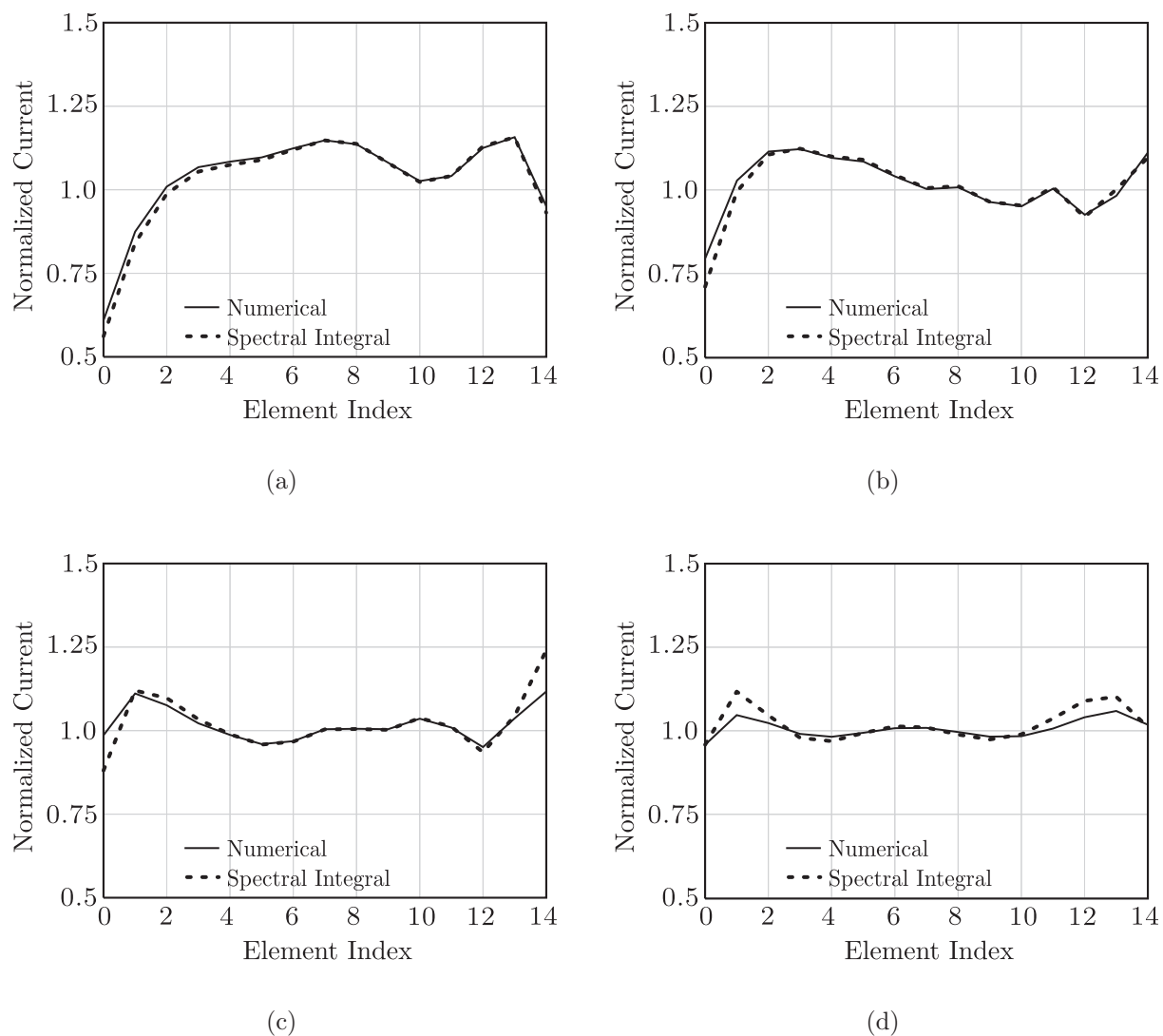


Figure 5.9: Comparison of the numerical solution and the spectral integral solution for a connected array in free space at four different frequencies: (a) $0.2 f_0$, (b) $0.4 f_0$, (c) $0.8 f_0$, (d) f_0 ; the load impedance is equal to 200Ω .

of the results. A possible explanation is that, to the first order, a good approximation of the reactive energy associated with the cell is already included in the infinite-array approximation and the gap dimension, and accordingly the parameter δ plays only a minor role in defining the edge-born currents.

5.5 Free Space Case: Uniform Asymptotic Evaluation of the Integral Approximation

Equation (5.23) represents a single integral expression for the edge-born currents in a connected array excited at a finite number of feed points. The asymptotic evaluation of this integral can provide the physical insight that is now missing. To maintain the formulation as simple as possible, only the case of connected arrays operating in free space will be considered. The first step to the evaluation is recognizing two separate terms, each associated with one edge of the array.

5.5.1 Contributions from the Two Edges

The summation over the auxiliary contributions from sources external to the array can be expressed in closed form. This leads to two contributions associated with the left and right edges of the array:

$$\begin{aligned} \sum_{n_x}^{ext} e^{j(k_x - k_{x0})n_x d_x} &= \sum_{n_x = -\infty}^{-1} e^{j(k_x - k_{x0})n_x d_x} + \sum_{n_x = N_x}^{\infty} e^{j(k_x - k_{x0})n_x d_x} = \\ &= \frac{e^{-j(k_x - k_{x0})d_x}}{1 - e^{-j(k_x - k_{x0})d_x}} + \frac{e^{j(k_x - k_{x0})N_x d_x}}{1 - e^{j(k_x - k_{x0})d_x}}. \end{aligned} \quad (5.24)$$

Note that the first summation converges for $\Im\{k_x\} < 0$, and the second one for $\Im\{k_x\} > 0$. The introduction of Eq. (5.24) in Eq. (5.23) leads to:

$$\begin{aligned} i_{\delta, edge}^{n_x} &= i_{\delta, edge1}^{n_x} + i_{\delta, edge2}^{n_x} = e^{jk_{x0}d_x} \frac{1}{2\pi} \int_{-\infty}^{\infty} \frac{\text{sinc}^2\left(\frac{k_x \delta}{2}\right)}{D_{load}(k_x)} \frac{e^{-jk_x(n_x+1)d_x}}{1 - e^{-j(k_x - k_{x0})d_x}} dk_x + \\ &e^{-jk_{x0}N_x d_x} \frac{1}{2\pi} \int_{-\infty}^{\infty} \frac{\text{sinc}^2\left(\frac{k_x \delta}{2}\right)}{D_{load}(k_x)} \frac{e^{-jk_x(n_x - N_x)d_x}}{1 - e^{j(k_x - k_{x0})d_x}} dk_x. \end{aligned} \quad (5.25)$$

This representation highlights the presence of a number of poles, which emerge from the zeros of $(1 - e^{j(k_x - k_{x0})d_x})$ associated with the Floquet Waves (FWs) in $k_{xm} = k_{x0} + \frac{2\pi m_x}{d_x}$. Indeed, using an identity similar to Eq. (A.71) and exploiting the polar representation of the cotangent [92], one can prove that

$$\frac{1}{1 - e^{j(k_x - k_{x0})d_x}} = \frac{1}{2} + \frac{j}{2} \cot\left(\left(k_x - k_{x0}\right)\frac{d_x}{2}\right) = \frac{1}{2} + \frac{j}{d_x} \sum_{m_x = -\infty}^{\infty} \frac{1}{k_x - k_{xm}}. \quad (5.26)$$

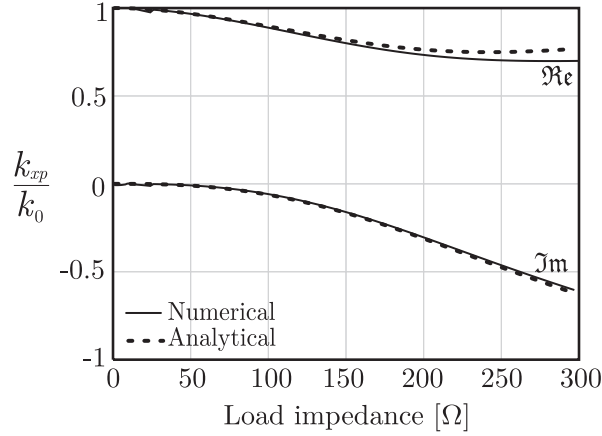


Figure 5.10: Real and imaginary part of the pole k_{xp} versus load resistance for an array in free space.

Besides FW poles, the integrand also possesses other types of singularities, specifically the branch points as in Fig. 5.3 and complex poles associated with the dispersion equation $D_{load}(k_x) = 0$. Their location in the complex plane depends on the actual value of the loads Z_l that characterize the feed lines. The approximate solution of this dispersion equation is reported in Appendix D (Sec. D.1). The real and imaginary part of the dominant pole are plotted in Fig. 5.10, for a case characterized by $d_x = d_y = 0.45 \lambda_0$ and $w = \delta = 0.2 \lambda_0$. The figure compares the analytical solution provided in Eq. (D.10) with a numerical solution based on Newton-Raphson method [42], which is a simple descent along the gradient following an accurate starting point. For a small load impedance, $k_{xp} \approx k_0$ and unattenuated waves are supported by the array. However, for large values of the impedance, the imaginary part of this propagation coefficient is highly negative. It should be noted that these poles correspond to purely attenuating waves due to losses (feed absorption). These are not leaky waves.

After the discussion on the singularities, also the approximate analytical evaluation of the two integrals in Eq. (5.25) is derived in Appendix D. A uniform asymptotic evaluation of the integral is performed in terms of Fresnel functions to properly describes the transition between guided waves and radiated waves. The inclusion of these transition functions enables the description of the currents also for scan-blindness angles.

The analytical expressions for the current contribution born from the left edge of the array is given by

$$i_{\delta,edge1}^{n_x} \approx \frac{e^{-jk_0X}}{X\sqrt{X}} \left(C_1 \frac{F_s(X(k_0 - k_{xp}))}{(k_0 - k_{xp})} + C_2 \frac{F_s(X(k_0 - k_{x0}))}{(k_0 - k_{x0})} \right) \quad (5.27)$$

with $X = (n_x + 1)d_x$. In Eq. (5.27) the slope Fresnel function is introduced: $F_s(x) = 2jx(1 - F(x))$, where $F(x)$ is the Kouyoumjian Fresnel function [93]. This function is defined in Eq. (D.65) in Appendix D.

Also in Eq. (5.27)

$$C_1 = C' \left(R(k_0) - \frac{j}{d_x(k_{xp} - k_{x0})} \right), \quad C_2 = \frac{jC'}{d_x(k_{xp} - k_{x0})} \quad (5.28)$$

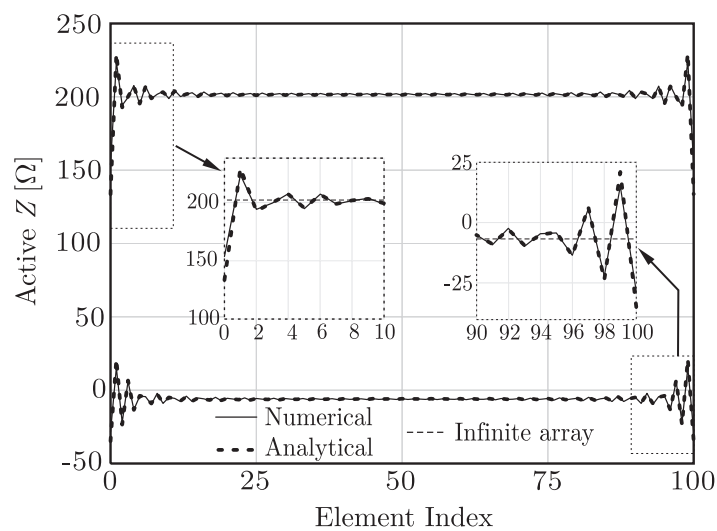
with $C' = C\sqrt{2k_0}(-e^{-j\pi/4}\pi)$ and $R(k_x)$ defined in Eq. (D.17). The current contribution born at the right edge of the array can be similarly expressed and is reported in the Appendix D.

5.5.2 Comments on the Analytical Solution

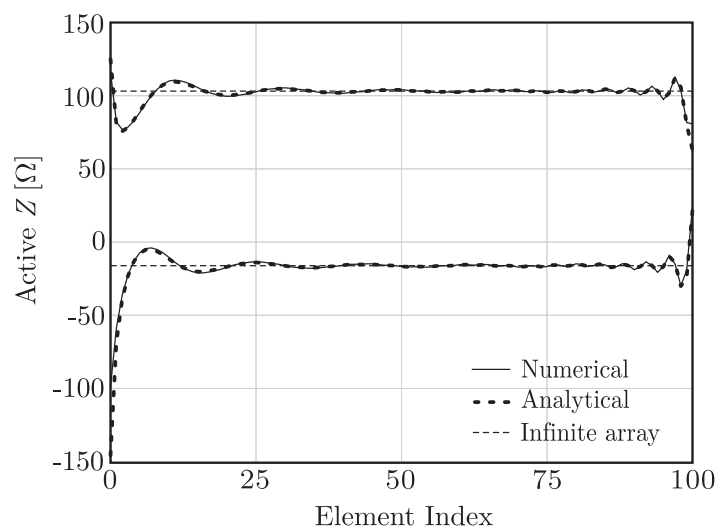
A comparison between the results obtained resorting to the analytical expressions in Eq. (5.27), or Eqs. (D.21) and (D.23), and the numerical method is shown in Fig. 5.11. The array is radiating broadside in Fig. 5.11(a) and toward $\theta = 60^\circ$ in the E -plane in Fig. 5.11(b). The considered example includes $N_x = 100$ feed points, and the geometrical parameters are $d_x = d_y = 0.4\lambda_0$, where λ_0 is the calculation frequency, and $w = \delta = 0.2\lambda_0$. It is apparent that the proposed analytical solution is extremely accurate also for arrays that are scanned to very wide angles.

The availability of an analytical expression allows one to give qualitative considerations on the nature of the electric current distribution. For high values of the loads Z_l , and observation points close to broadside, $k_{x0} \approx 0$ and the arguments of the F_s functions are large. This means that the current distribution from each edge is dominated by the spreading factor $x^{-3/2}$, which is associated with a rapid decay as a function of the distance from the end points. For lower values of Z_l , the load induced pole k_{xp} can be close to the branch point k_0 . Also, for observation toward wide scanning angles, k_{x0} is close to k_0 . When either of the two situations occurs, the transition functions argument tends to zero, and the Fresnel function can be approximated by $F(X) \approx \sqrt{\pi X}e^{j(\pi/4+X)}$ [93]. This implies that the dominant term to the current distribution is of the type $e^{-jk_{xp}x}$ or $e^{-jk_{x0}x}$, which does not present geometrical spreading and only a small exponential attenuation ($\Im\{k_{xp}\}$) or no attenuation at all ($k_{x0} \in \mathbb{R}$).

Specifically the $e^{-jk_{xp}x}$ dependence of the current distribution is shown here to emerge from an analytical GF for the first time. It expresses the idea that the load/source impedances attenuate the edge waves by consuming their energy. This mechanism is probably occurring in all arrays, not only in connected arrays, but to our knowledge was never given explicit evidence or demonstrated for any array.



(a)



(b)

Figure 5.11: Comparison between the analytical solution and the numerical method for an array of 100 elements in free space:(a) broadside and (b) $\theta = 60^\circ$.

5.6 Conclusions

This chapter has presented a novel analytical methodology to assess edge effects in connected arrays, which provides important guidelines for the design of broadband phased arrays.

Analysis

Starting from the knowledge of the connected array GF, we have first presented the derivation of a general purpose numerical procedure for the assessment of the finiteness effects in connected arrays. This procedure is of general applicability in terms of types of array and scan conditions. In fact, arrays with and without backing reflectors or dielectric stratifications and scanning in the E -, H - or diagonal planes can be analyzed. The numerical cost of the analysis is only the inversion of a matrix of dimension $N_x \times N_x$, where N_x is the number of feed points in the array along the longitudinal direction. The availability of such a numerical procedure provides unique design opportunities. It is particularly convenient when the performance of wideband wide-angle scanning arrays needs to be assessed in advance of measurements or full-wave, all inclusive, numerical simulations.

In a second step, the representation of the total current in terms of the infinite array plus edge-born waves has been introduced. Thanks to this representation, simplifications that would otherwise be unreasonable can be adopted. These lead to a single analytical expression for the spectrum of the edge-born waves in cases of general applicability.

Finally, for the specific case of a connected array of dipoles operating in free space and scanning only in the E -plane, an approximation of the pertinent inverse Fourier transforms leads to an analytical expression of the edge-born waves. The expression is given in terms of standard Fresnel functions which highlight similarities between the edge-induced currents in connected arrays and the edge-born currents in the canonical problems of diffraction from half planes [94, 95].

Design

From the design point of view the main findings of this investigation are that:

- Edge effects are fundamental to assess the behavior of connected arrays in wide-angle scan situations. Especially when the arrays are composed of a small number of elements (8-16), infinite-array simulations are just not good enough to predict the performance. The free-space case, treated here analytically, gives good physical understanding and guidelines.
- The intensity of the edge-born waves is only mitigated by the source/load impedances. The information of the load impedance is crucial to assess finite-array effects. This was previously anticipated by Hansen in [25] and Munk [75]. The origin of this phenomenon is believed to be explained here for the first time.

- The intensity of the edge waves is more important for low loading or source impedances. High impedances (400Ω) can mitigate truncation effects by attenuating the edge-born waves in connected arrays with a backing reflector.

Chapter 6

Practical Implementation of Feed Networks in Connected Arrays

The analytical models presented in the previous chapters can be readily exploited for the design of connected arrays. For example, in Chapter 3, the theoretical formulation was used for the dimensioning of the array elements, and a connected-dipole design was presented, with 40% relative bandwidth and wide-scan capability, up to 45° for all azimuth angles (Sec. 3.4). Moreover, a rigorous and analytical equivalent circuit representation of the array was derived in Chapter 4 and successfully used to predict the performance of a receiving dual-band connected-array prototype (Sec. 4.6). The closed-form expressions will be also used in Chapter 7 for the optimization of the radiating elements in a 7×7 prototype demonstrator for 3 to 5 GHz operation.

Besides the design of the radiating dipoles, the practical implementation of a feed network has to be realized, for matching the elements to a $50\ \Omega$ coaxial connection. For the design of the feeding structures, we perform all simulations with Ansoft HFSS [41]. As for all wideband phased arrays differentially fed, also in connected arrays balanced transmission lines should be used to feed the elements. However, these lines can support both differential and common-mode propagation. This phenomenon is unwanted and can be excited when asymmetry in the excitation is introduced, for example by scanning, or when the length of the feeding line is such that resonances occur. This specific problem will be the object of this chapter, that focuses on the implementation of the feed rather than the radiating aperture.

An analysis of the effects of common-mode resonances on the efficiency of a connected array was presented in [96]. Resonances of the same type were also observed and investigated for arrays of differentially-fed tapered slot antennas in [97]. Due to the electrical connection

between the array elements, and the corresponding high mutual coupling, standard baluns typically used for resonant dipoles are not effective in connected arrays. In fact, even with perfect baluns, common-mode resonances may occur. The reason is that, at oblique scanning, either the incident field or the field from the array itself will have a field component along the feed lines that may readily excite the common mode [26, pp. 278-279].

On the other hand, common-mode rejection circuits based on ferrite are available only at low frequencies (< 3 GHz) [98–100]. Moreover, other solutions based on active components or differential low noise amplifiers are not always employable [101, 102].

In particular, one of the applications that motivates this work is aircraft-to-satellite communication for in-flight entertainment (see Sec. 1.1.1). For this application, if one wishes to adopt a unique antenna for both the uplink and the downlink bands, a wide bandwidth (about 30% from 10.7 to 14.5 GHz) becomes necessary. Polarization purity is also required, with a specification for the X-pol level of at least -15 dB for every observation point. The simultaneous operation in transmit and receive in Ku-band does not allow the exploitation of either differential amplifiers or ferrite based transformers.

This chapter presents two novel low-cost Printed-Circuit-Board (PCB) based solutions to avoid common-mode resonances, without resorting to active components or Monolithic Microwave Integrated Circuit (MMIC) technology.

- The first solution presented aims at reducing the length of the resonating lines to shift the common-mode resonances to higher frequencies, so outside the operational band of the array. This effect is achieved by applying a denser sampling to the array. The same numbers of Transmit/Receive (T/R) modules is maintained by resorting to power dividers. A wide-band transition between Co-planar Strip (CPS) lines has been designed, based on microstrip-to-slot aperture coupling [103], to further reduce the length of continuous current paths. The same transition can be used as a balun, when coupling a CPS line to a microstrip (MS).

One disadvantage of this solution is that the bandwidth of the transformer depends on the input impedance of the radiating element. In particular, lower input impedances at the dipole terminals need to be achieved to ensure a wideband behavior of the transition.

- The second solution is based on a loop-shaped component that constitutes a choke for the common mode, while representing a small impedance change for the differential mode. Contrarily to the slot-coupling transformer, the loop bandwidth does not depend on the input impedance. The use of such a common-mode rejection loop

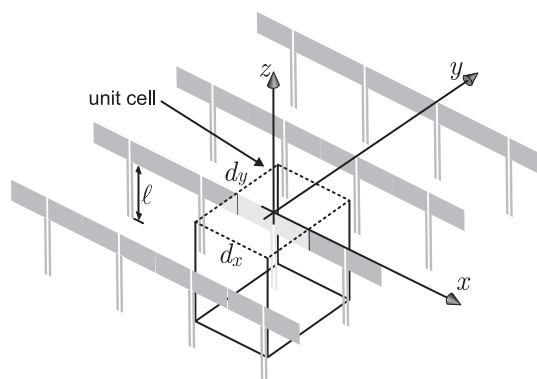


Figure 6.1: Two-dimensional array of dipoles fed by CPS lines. The periods along x and y are d_x and d_y , respectively. The length of the vertical feed lines is ℓ .

allows the design of linearly and doubly polarized arrays of connected dipoles with X-pol levels lower than -15 dB over about a 30% relative bandwidth.

Simulation results obtained with the aid of full-wave commercial electromagnetic CAD tools are presented for both feed structures.

6.1 Resonances Typical of Connected Arrays

Let us consider the simplified case of an infinite two-dimensional array of dipoles with periods d_x and d_y , as shown in Fig. 6.1. Backing reflectors reduce the intrinsic bandwidth of the dipoles, which is theoretically very large [30]. For the sake of generality, the array without backing reflector is studied to highlight only the frequency dependence introduced by the feed network. The array elements are fed by CPS lines, whose length is ℓ .

Three types of resonant effects may occur in these, otherwise broadband, connected arrays:

1. grating lobes;
2. phase matching between Floquet waves and guided waves;
3. common-mode resonances.

The first type of resonance is associated with the appearance in the visible region of an higher order Floquet wave and is typical of all arrays, connected and unconnected. The appearance of the grating lobes is defined by the condition

$$k_{zm} = \sqrt{k_0^2 - k_{xm}^2 - k_{ym}^2} = 0 \quad (6.1)$$

where $k_{xm} = k_0 \sin \theta \cos \varphi - \frac{2\pi m_x}{d_x}$, $k_{ym} = k_0 \sin \theta \sin \varphi - \frac{2\pi m_y}{d_y}$, k_0 is the free-space propagation constant, θ and φ are the angles toward which the array scans, and m_x and m_y are the Floquet-wave indices.

Inverting the condition $k_{zm} = 0$ for the frequency, when $m_x = -1$ and $m_y = 0$, we obtain

$$f = \frac{c}{d_x(\sqrt{1 - \sin^2 \theta \sin^2 \varphi} + \sin \theta \cos \varphi)} \quad (6.2)$$

with c indicating the speed of light in vacuum.

The second type of resonance only occurs in connected arrays. In an infinitely extended dipole structure, guided waves can propagate along the longitudinal direction. As described in Sec. 3.2.2, when the dipole is assumed to be in free space, these waves are represented in the spectral Green's Function (GF) as a pair of poles in $k_x = \pm k_0$. When the dipoles are fed at periodic locations along the longitudinal direction, the periodic GF is obtained by sampling the non-periodic GF in the pertaining Floquet wave numbers.

Thus, the resonance condition is $k_{xm} = k_{pole} = \pm k_0$. Accordingly, in terms of frequency, for $m_x = -1$ and $k_{pole} = -k_0$, we have

$$f = \frac{c}{d_x(\sin \theta \cos \varphi + 1)}. \quad (6.3)$$

The first two types of resonance do not depend on the feed network, thus they can be taken into account in an ideal model that does not include the feeding transmission lines.

6.1.1 Common-Mode Resonances

If differential lines are included in the model, their length is critical since they may induce other resonances due to common-mode propagation. The shorter the length of the feed lines, the higher the associated resonance frequency is. However, typically connected arrays involve the presence of a backing reflector. Accordingly, the transmission-line lengths are in the order of a quarter of the free-space wavelength, to reach the ground-plane level, where loads or source circuits are located. As an example, in the most standard design situation, the array period is about half a wavelength, and the vertical lines are a quarter wavelength. Hence, the feed lines and the dipole constitute a continuous electric path that is one wavelength long ($d_x + 2\ell = \lambda$), as illustrated in Fig. 6.3, giving rise to a strongly cross-polarizing standing wave.

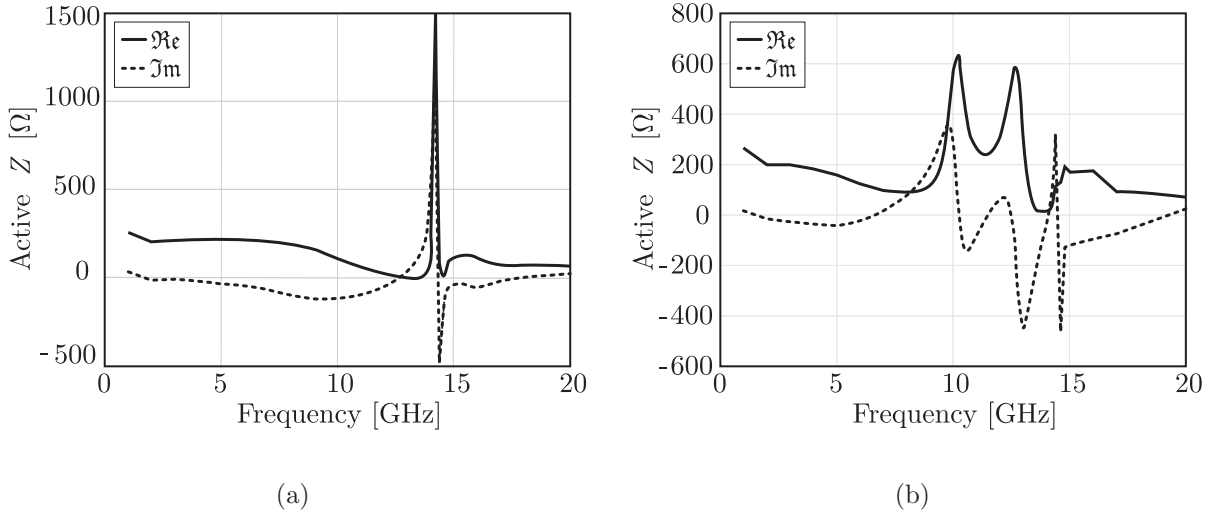


Figure 6.2: Active input impedance of an elementary cell in infinite-array environment, when the array is scanning towards $\theta = 45^\circ$ and $\varphi = 45^\circ$. The periods are $d_x = d_y = 15$ mm and the length on the vertical lines is (a) $\ell = 0.6$ mm and (b) $\ell = 7.5$ mm.

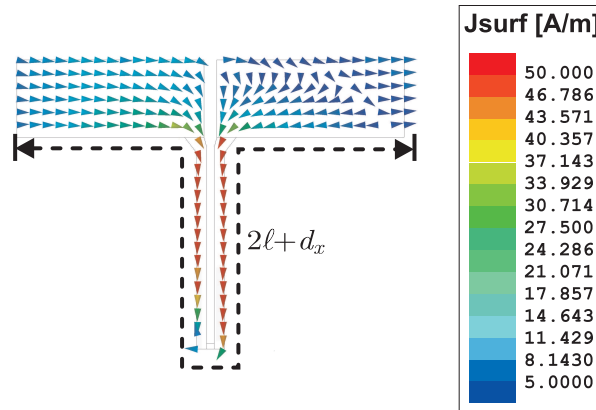


Figure 6.3: Vector surface current distribution on a unit cell of the infinite array at 10 GHz. The array is the same to which Fig. 6.2(b) refers.

The active input impedances for an array periodicity of $d_x = d_y = 15$ mm, and assuming $\ell = 0.6$ mm and $\ell = 7.5$ mm, are shown in Fig. 6.2(a) and 6.2(b), respectively. Simulations have been performed with Ansoft HFSS [41], exploiting the infinite-array-analysis approximation. The scan angle is considered to be $\theta = 45^\circ$ and $\varphi = 45^\circ$, since this is the most critical design case. Figure 6.2(a), which refers to the case of very short vertical lines, shows only two resonances associated with the grating lobe and the guided-wave

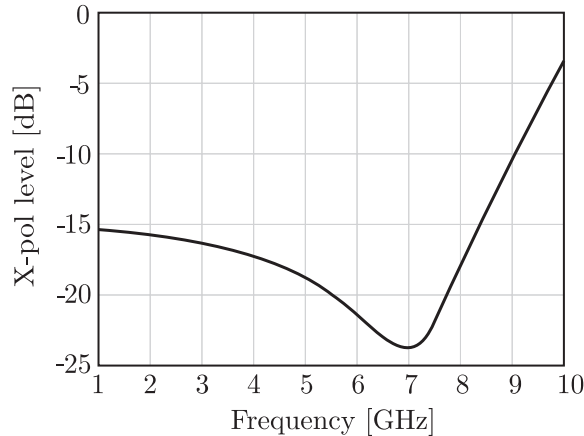


Figure 6.4: X-pol level as a function of the frequency when scanning towards $\theta = 45^\circ$ and $\varphi = 45^\circ$. The periods are $d_x = d_y = 15$ mm and the length of the vertical lines is $\ell = 7.5$ mm.

pole. The two resonances appear at about 14.5 and 13.5 GHz, respectively, as predicted by Eqs. (6.2) and (6.3). In addition to the grating lobe and the guided pole resonances, a peak of the input resistance appears at 10 GHz when long vertical lines are considered, as can be observed in Fig. 6.2(b). From the simulated vector current distribution in Fig. 6.3, it is evident that the resonance is attributable to common-mode propagation in the CPS lines.

According to the third definition of cross polarization by Ludwig [9], common-mode currents along z radiate highly cross-polarized fields when the diagonal plane is scanned ($\varphi = 45^\circ$). In Fig. 6.4, the ratio between co-polarized and cross-polarized fields rapidly increases in proximity of the resonance at 10 GHz. A possible approach to achieve lower levels of X-pol is to ensure that the length of the path $2\ell + d_x$ is significantly shorter than a wavelength. In that case, the common-mode resonances will appear at higher frequencies, outside the operational band of the array. Note that the resonance depicted in Fig. 6.3 is the one associated with common mode only and typically occurs at the lowest frequency. Other resonances may appear at higher frequencies, which involve combinations of common and differential modes that results in unbalanced currents.

6.2 Design of PCB Slot-Based Transformers

The path of the common-mode current can be shortened by introducing a series transformer that only allows the transmission of differential currents and constitutes an open circuit for the common mode. To realize such a component, one can resort to completely planar

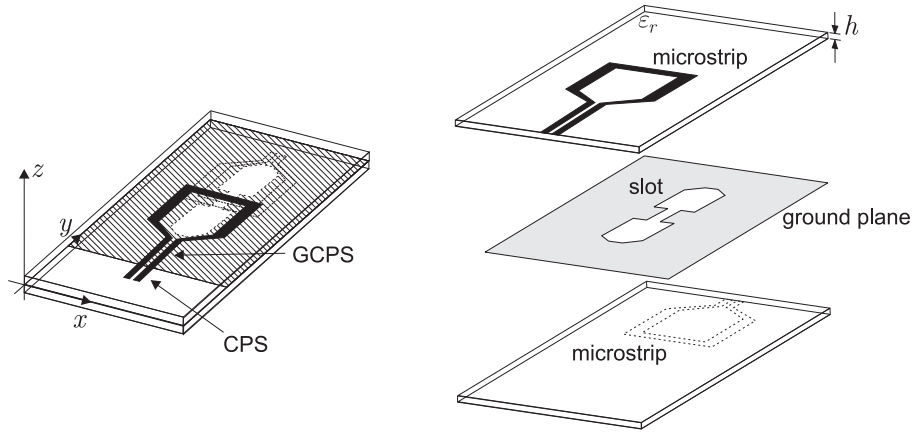


Figure 6.5: Layout of the CPS/GCPS transformer. The thickness of two dielectric substrates is h and the permittivity is ϵ_r .

slot coupling between microstrip lines as in [104].

6.2.1 CPS/GCPS Transformer

A schematic view of the component is shown in Fig. 6.5, where the ground plane on which the slot is etched is assumed to be of infinite extent along x . The component is divided into two parts separated by the ground plane. The part at $z = h$, hereafter the primary circuit, comprises a transition from CPS lines to Grounded CPS (GCPS) lines. A power divider then splits the circuit into two microstrip-like equal halves, which are eventually re-connected orthogonally to a coupling slot. The secondary circuit is the same as the primary, but mirrored with respect to the slot (at $z = -h$).

The initial input from the CPS lines can be associated with differential-mode or common-mode currents. Regardless of the type of input, the same equivalent circuit of the transition can be used, as shown in Fig. 6.6. However, it is clear from the right side of Fig. 6.6 that the common-mode input corresponds to a zero of electric current at the center of the slot. In turn, this translates in no electric current being excited in the secondary circuit of the transformer.

The common-mode rejection achieved by these type of components can be highlighted in Fig. 6.7, where the S_{12} for the common mode is reported as a function of the frequency. The common mode transmission is lower than -17 dB over a wide band. While such rejection is intrinsic in this type of transformer, the achievement of high transmission for the differential signal depends on the quality of the matching.

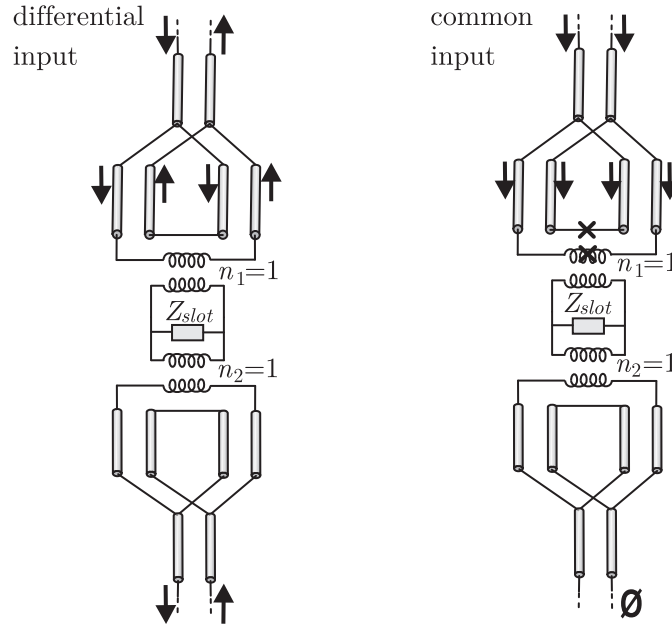


Figure 6.6: Equivalent transmission line model of the transition in Fig. 6.5, for differential and common inputs.

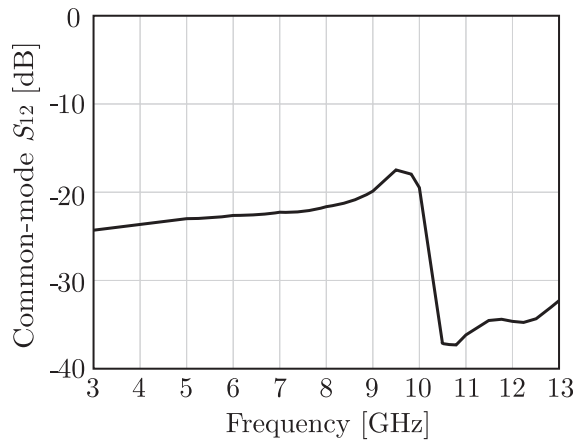


Figure 6.7: Common-mode rejection of the CPS/GCPS transition in Fig. 6.5. The transition is optimized for 100 Ω impedance of the differential mode.

Figure 6.8 shows the equivalent circuit transformation steps that can be applied to estimate the input impedance for the differential mode. The maximum power transfer for the differential mode is obtained when the element load impedance (Z_{cell}) is matched to the differential line impedance (Z_{0cell}), which is realized by the series of the two microstrip lines, each of impedance Z_{0MS} . Thus, the condition is $Z_{0cell} = 2Z_{0MS} = Z_{cell}$. Let us also

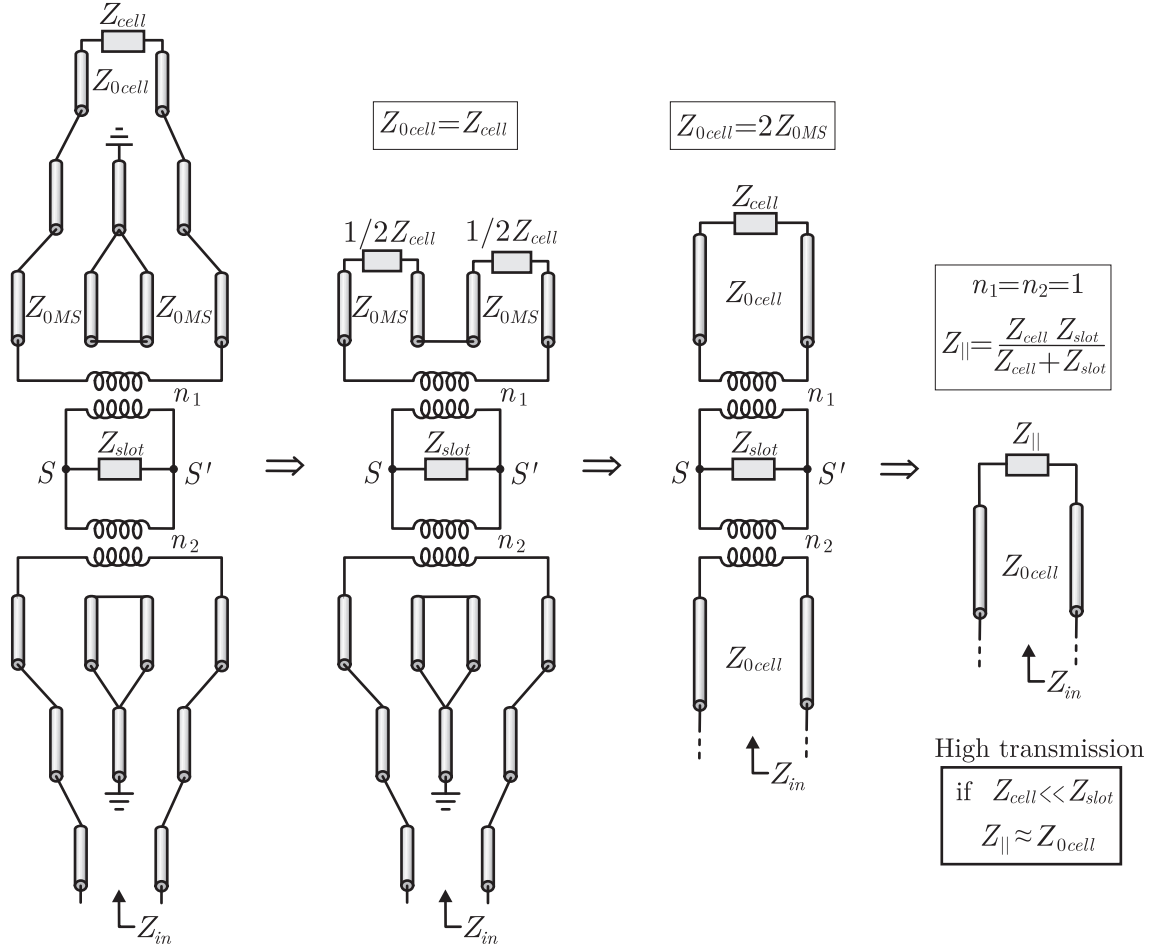


Figure 6.8: Equivalent circuit transformation steps for differential-mode current.

focus on the simplifying and realistic situation in which one wants to realize unitary turn ratios of the slot-to-microstrip transformers for both the primary and secondary circuits; that is, $n_1 = n_2 = 1$ in Fig. 6.8. In this case, the equivalent impedance at the slot level (S - S') looking upward is $Z_{||} = Z_{cell}Z_{slot}/(Z_{cell} + Z_{slot})$, where Z_{slot} is the impedance across the slot in the absence of the microstrip lines. Under the condition $Z_{cell} \ll Z_{slot}$, the presence of the slot is negligible and thus $Z_{||} \approx Z_{cell}$, so that the differential signal is completely transmitted to the secondary circuit. On the contrary, when the slot loading is comparable to the connected array loading, a significant part of the power supplied to the array is re-radiated by the slot before being transferred through the transition. This limits the useful bandwidth of the transformer. Since the condition for high transmission levels is $Z_{cell} \ll Z_{slot}$, a resonant slot with high impedance, together with a smaller value of Z_{cell} ,

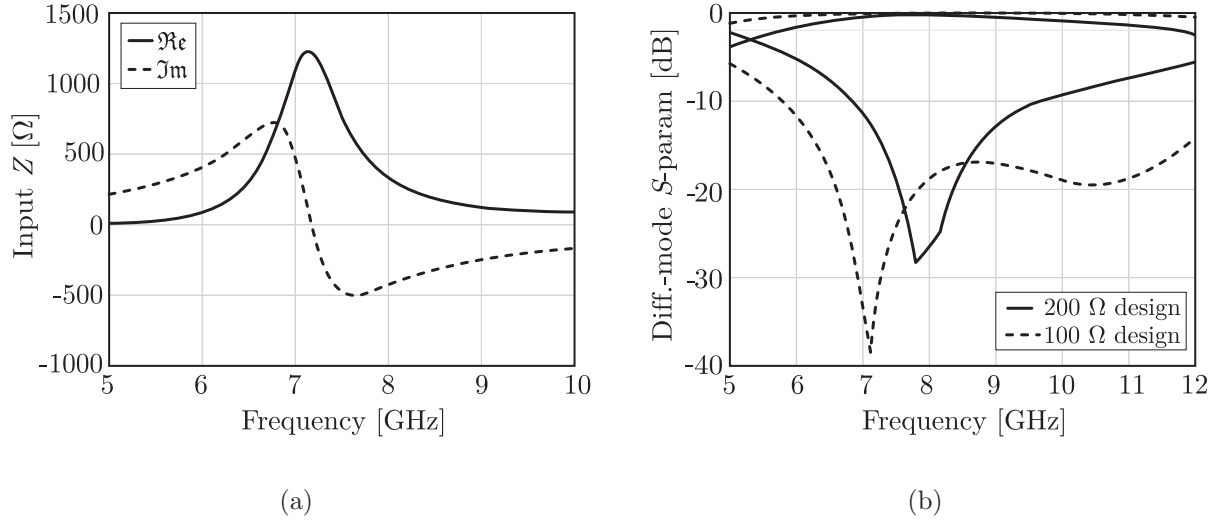


Figure 6.9: (a) Input impedance of the slot etched on an infinite ground plane, in the absence of the microstrip circuits. (b) Reflection and transmission coefficient of two transition optimized for $Z_{0cell} = 200 \Omega$ and $Z_{0cell} = 100 \Omega$.

implies larger useful bandwidths for the transformer. To highlight this effect, we considered two transitions using the same slot, whose impedance is shown in Fig. 6.9(a). The first transition is optimized for $Z_{0cell} = 200 \Omega$, while the second is optimized for $Z_{0cell} = 100 \Omega$. Figure 6.9(b) shows the S-parameters associated with these two transitions. It is clear that the relative bandwidth associated with the lower impedance cell is much larger.

6.2.2 CPS/MS Balun

The design of CPS/GCPS transformers described in the previous section can be easily adapted to CPS/MS balun designs. The primary circuit and the slot remain the same, while in the secondary circuit one of the two microstrip lines becomes a quarter-wavelength open stub and the other constitutes the unbalanced MS input. The geometry of the balun is shown in Fig. 6.10.

6.3 Performance of the Feed Network: Array Design

The transformer described in Sec. 6.2 can be the key component of a periodic cell of a two-dimensional connected array. To minimize the number of T/R modules in a realistic

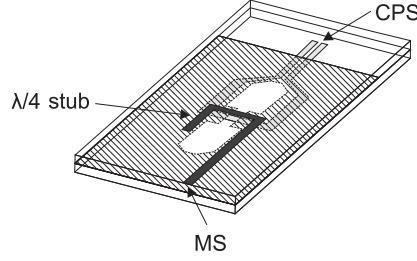


Figure 6.10: Layout of the CPS/MS balun transformer.

large array, the periods in x and y are maintained at $0.5 \lambda_0$ at the highest useful frequency (10 GHz). As examples, let us consider the following two configurations:

1. In each periodic cell of the array there is only one feed point with the corresponding transformer (see Fig. 6.11(a)). In this case, the periods are $d_x = d_y = \lambda_0/2$ and the impedance of the unit cell is $Z_{cell} = 200 \Omega \approx \zeta_0/2$, where ζ_0 is the free-space characteristic impedance. Accordingly, a transformer optimized for $Z_{0cell} = 200 \Omega$ is considered.
2. Each periodic cell is fed at two points, with a separation distance of $\lambda_0/4$ (see Fig. 6.11(b)). The impedance at each feed point is then $Z_{cell} = 100 \Omega$ and the transformer is also designed for $Z_{0cell} = 100 \Omega$. The factor 2 in the value of the input impedance is clear from Eq. (2.36), since the impedance is proportional to the ratio d_x/d_y . A Wilkinson power divider is included to maintain the same number of T/R modules.

The two cases differ for the operational bandwidth of the transformers, as was shown in Fig. 6.9(b). Therefore, the active reflection coefficients for the case 2 when scanning toward $\theta = 45^\circ$ and $\varphi = 45^\circ$ exhibits a wider -10 dB relative bandwidth, as expected (Fig. 6.12(a)). However, for the 200Ω design, even within the frequency band in which a good matching is achieved, high losses are observed in terms of X-pol levels. Figure 6.12(b) shows the X-pol levels for the two considered cases. The difference between the two curves can be associated with the different length p of the dipole and the primary circuit of the transformer (see Fig. 6.11). In Case 1, the length p becomes longer than one equivalent wavelength at the highest frequency, allowing common-mode resonances to appear inside the bandwidth of the array. Case 2 instead permits having a shorter length p , shifting the resonance at frequencies higher than 10 GHz. As a consequence, a sensibly lower X-pol level is obtained with the second approach.

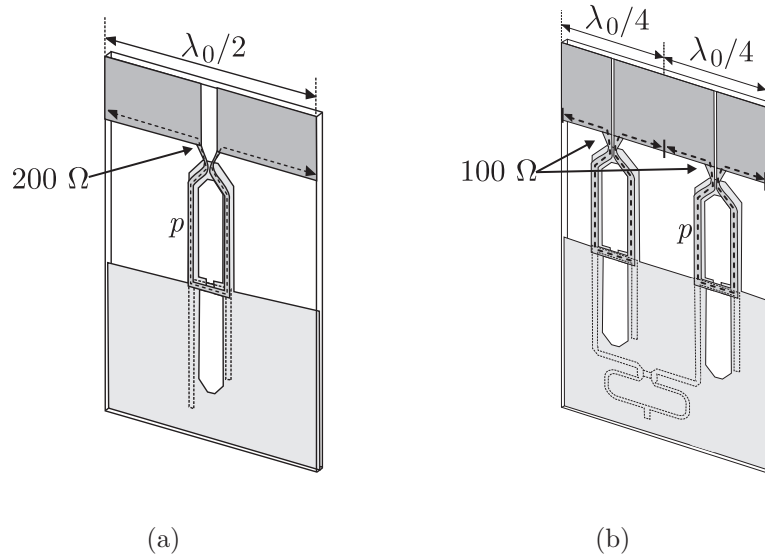


Figure 6.11: Geometry of a periodic cell a connected dipole array with (a) single feed per cell and with (b) double feed per cell.

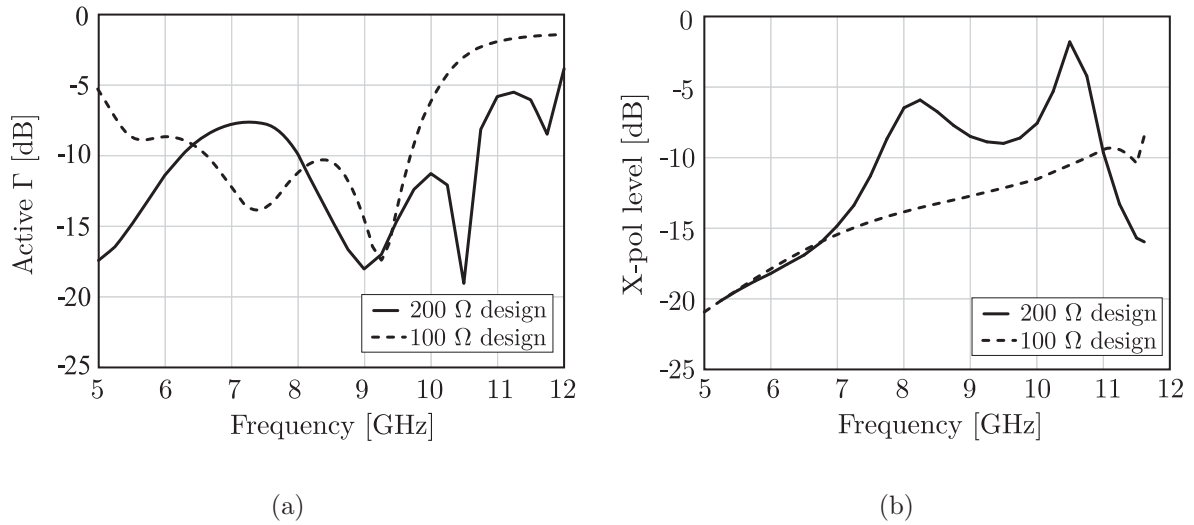


Figure 6.12: (a) Active reflection coefficient and (b) X-pol level for the two geometries in Fig. 6.11, when scanning towards $\theta = 45^\circ$ and $\varphi = 45^\circ$.

6.3.1 Finite Ground Planes

Note that the transformer in Sec. 6.2 has been introduced assuming infinite ground planes surrounding the slots. In practice, when used to feed connected arrays, the ground plane

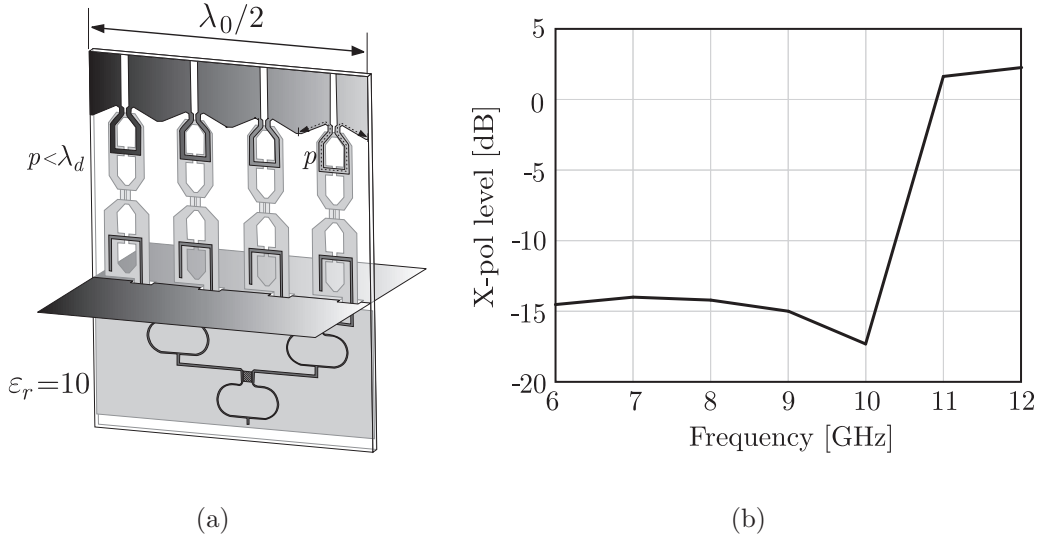


Figure 6.13: (a) Geometry of a periodic cell a backed connected array with 4 feeds per cell and (b) X-pol level when scanning towards $\theta = 45^\circ$ and $\varphi = 45^\circ$.

will be finite. The effect of this finiteness is not negligible, but was accounted for in the simulations presented in this section.

6.3.2 Backed Array

It has been shown that the proposed solution to the common mode yields an improved polarization purity for an array in free space. The transformer is not effective in an array with half wavelength spacing between the elements, because continuous current paths in the order of a wavelength are still undergoing common-mode propagation. Moreover, its bandwidth performance demands for lower values of the load impedance. The solution was to split the periodic cell into two subcells along the longitudinal direction (x), each comprising a transformer but both connected to the same T/R module. The load impedance is then reduced by a factor 2, from 200 to 100 Ω .

When a backing reflector is included for increased front-to-back ratio, the input impedance of the array element has a value of about 400 Ω . To reduce this value to 100 Ω , an even denser sampling ($\times 4$) is required. The same transformer could be used by reducing its size with high permittivity dielectrics. A possible array unit cell would be then the one depicted in Fig. 6.13(a). The series of two transformers has been used for each feed point. The X-pol level obtained with this design is lower than -14 dB for frequencies below 10 GHz. The

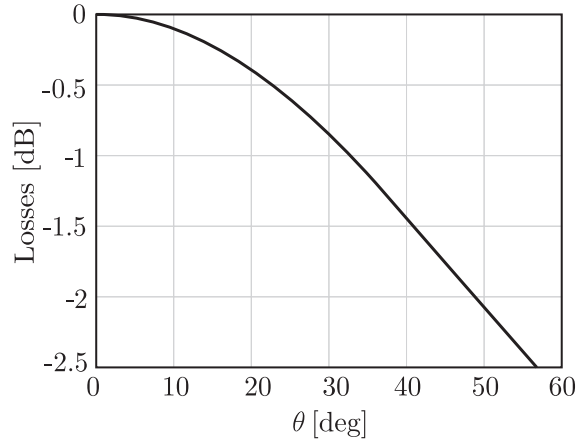


Figure 6.14: Losses due to destructive interference of the four contributions in the power combiners of the structure in Fig. 6.13(a), when scanning in the E -plane.

common-mode resonance still appears at higher frequencies, outside the operational band of the array, when the length p becomes about one effective wavelength in the dielectric (λ_d).

6.3.3 Limitations of Over-Sampling the Unit Cell

One disadvantage of this solution is that the contributions from the 4 feed structures within the unit cell sum up in-phase only when the array is pointing at broadside or scanning in the H -plane. E -plane scanning introduces incoherence between the 4 contributions, which translates into power dissipation inside the resistors of the Wilkinson power dividers. These losses increase with wider scan angles, as shown in Fig. 6.14.

6.4 Common-Mode Rejection Loop Design

To overcome the disadvantages related to over-sampling the unit cell, a second solution to reject common-mode propagation on the vertical feed lines is now presented. Let us consider a loop-shaped component as in Fig. 6.15.

When a common-mode input is applied, at low frequencies the currents flowing in the loop are equal in phase. Therefore, the loop only behaves as a small series inductance for the common mode. As the frequency increases, currents with different phases instead flow in different portions of the loop. This is illustrated in Fig. 6.16, which shows the magnetic field in a cross section of the loop structure, calculated via Ansoft HFSS [41], at 7 and 15

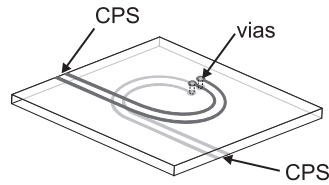
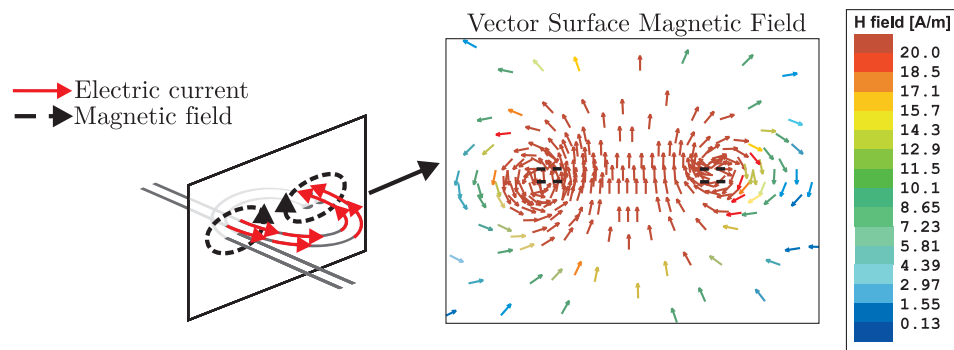
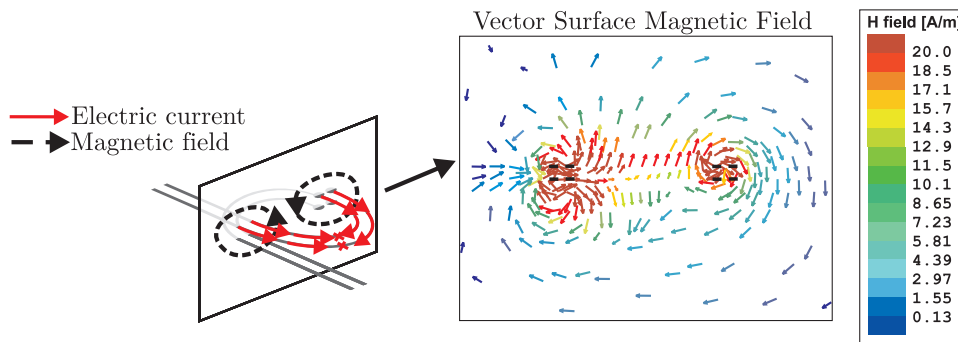


Figure 6.15: Geometry of the loop-shaped transformer for common-mode rejection.



(a)



(b)

Figure 6.16: Schematic of the vector current distribution and vector magnetic field on a transverse section of the loop calculated via Ansoft HFSS at (a) 7 GHz and (b) 15 GHz.

GHz, respectively. The loop radius is 1.06 mm and the loop is printed on a 0.254 mm thin dielectric substrate with relative permittivity 2.2. The first configuration in Fig. 6.16(a) corresponds to the case in which most electric currents in the loop are in phase, generating coherently adding magnetic fields. This, in turn, produces a magnetic field circuitation

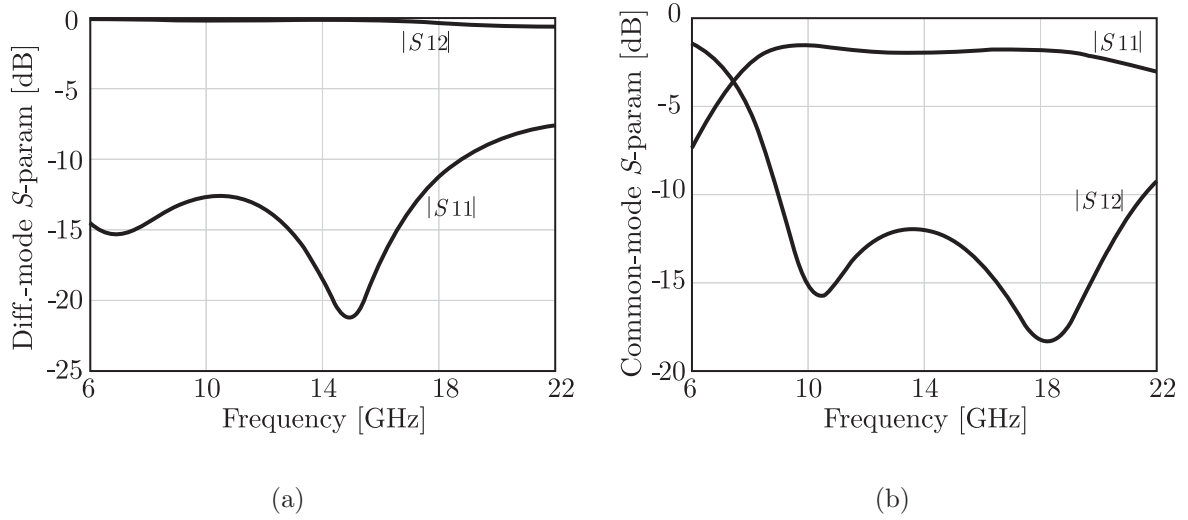


Figure 6.17: S-parameters of the loop in Fig. 6.18 pertaining to (a) differential and (b) common modes.

(closed-path integral) with high contributions in the center of the selected cross section. The second configuration in Fig. 6.16(b) corresponds to the case in which the electric currents in the loop are essentially divided into two parts with opposite phases, generating cancelling magnetic fields. As a consequence, the magnetic field circuitation has close-to-zero contributions in the center of the selected cross section. Thus, at frequencies higher than a certain threshold, the average distributed inductance of the loop becomes lower, as the magnetic fields no longer add up coherently. Within a frequency range of more than an octave, the characteristic inductance will tend to very low values, which creates a strong impedance discontinuity. This effect is quantified in Fig. 6.17, by the S-parameters pertaining to differential (a) and common mode (b). A 10 dB common-mode rejection is observed from about 9 to 22 GHz, while no significant mismatch is experienced by the differential mode up to 18 GHz.

6.4.1 Performance of the Loop-Shaped Feed Structure

A loop-shaped feed network has been designed to be included in a backed array of connected dipoles operating from 10.7 to 14.5 GHz, for in-flight entertainment application. The structure is shown in Fig. 6.18. Since the active input impedance of a connected dipole element typically exhibits high values (about $400\ \Omega$), the loop can be used to implement an impedance transformation for the differential mode. To this aim, a two-section transformer

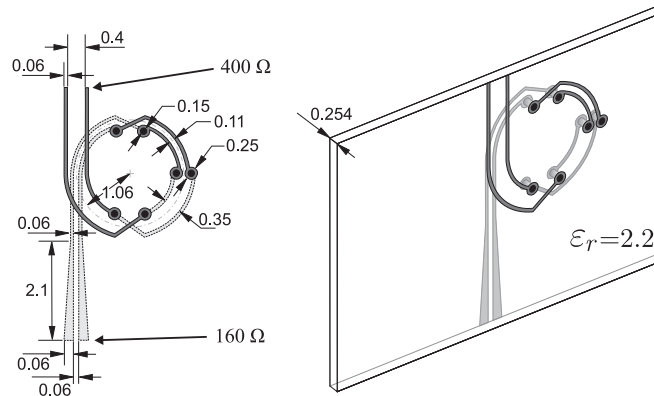


Figure 6.18: Dimensions (in mm) of the loop-shaped transformer.

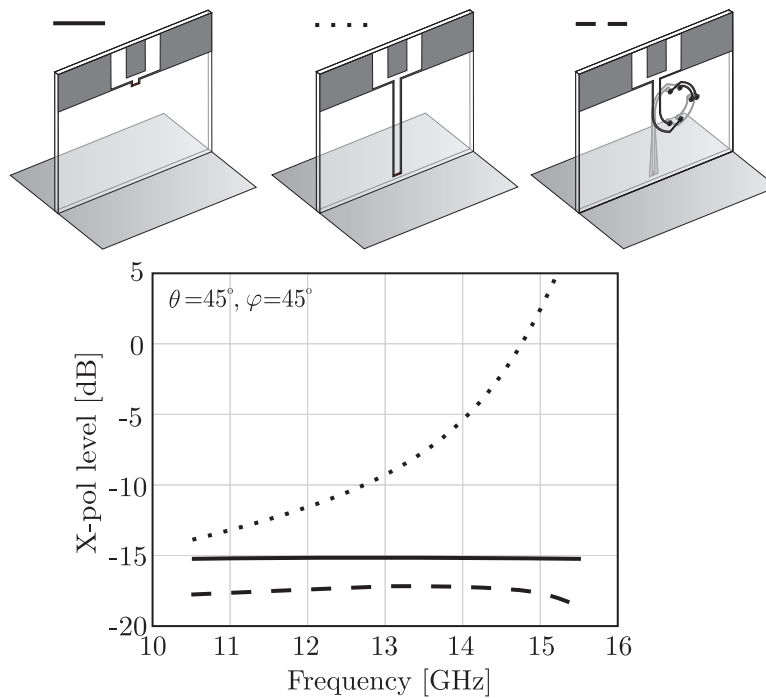


Figure 6.19: Performance of the loop when included in the connected dipole array unit cell.

from 400 to 200 Ω and a tapered line from 200 to 160 Ω have been implemented. The total length of the loop corresponds to half a wavelength at 14.9 GHz for a substrate with $h = 0.254$ mm and relative permittivity 2.2. Two inverters have been added to compensate for the slightly different radius of the inner and outer conductors within the loop, thus reducing the spurious radiation of the loop when a differential input is applied.

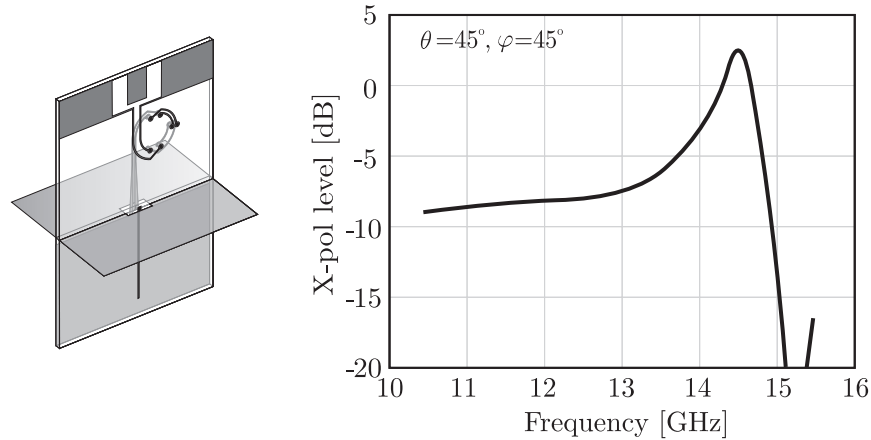


Figure 6.20: Performance of the loop when included in the connected dipole array unit cell.

Figure 6.19 shows the X-pol levels pertaining to an array of connected dipoles with and without vertical feed lines, compared with an array that includes the loop-shaped feed structure. It is evident that, when the common-mode rejection loop is used, the degradation of polarization purity introduced by the vertical lines is strongly mitigated over the bandwidth of interest. In fact, the X-pol level becomes lower than -17 dB over more than 40 % relative bandwidth.

6.4.2 Single-Polarization Array Design

The results in Fig. 6.19 pertain to a differential excitation located at the ground plane level. A more realistic coaxial feed requires the inclusion of a transition from CPS to microstrip (MS). A simple CPS-to-MS transition would introduce a further unbalance of the current along the differential lines, giving rise to a resonance as shown in Fig. 6.20. To avoid this problem, a sleeve balun has been designed. The resulting performance of the overall structure is presented in Fig. 6.21, which shows the geometry of the array unit cell, the active reflection coefficients for broadside and for $\theta = 45^\circ$ in the main planes (normalized to an port impedance of 160Ω), and the X-pol ratio for $\theta = 45^\circ$ and $\varphi = 45^\circ$. A reflection coefficient lower than -10 dB is achieved over more than 30% relative bandwidth, and the X-pol level is at least 14 dB lower than the co-polar component. The array period is 8.2 mm (about 0.4λ with λ being the wavelength at the highest frequency) and the profile of the array is 11.7 mm (about 0.57λ).

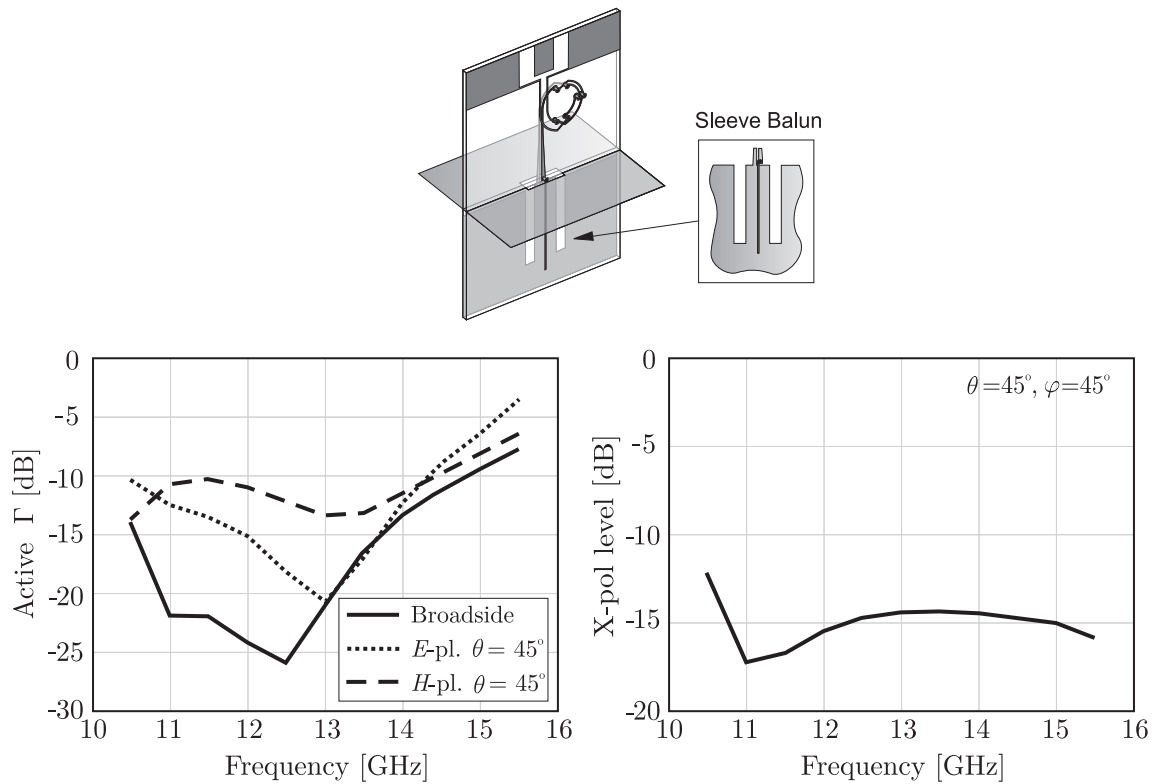


Figure 6.21: Performance of the loop when included in the unit cell of a linearly polarized connected dipole array.

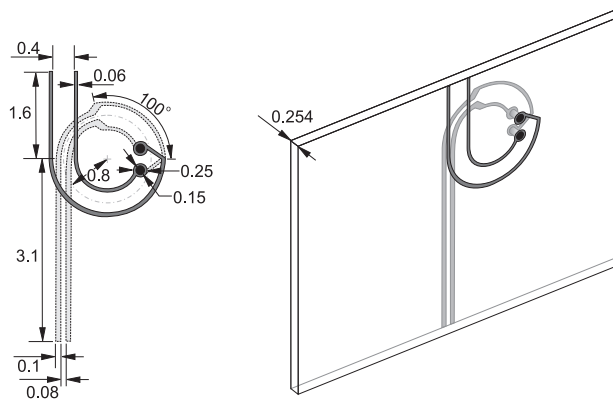


Figure 6.22: Dimensions (in mm) of the loop-shaped transformer for the dual-pol array.

6.4.3 Dual-Polarization Array Design

For the dual-pol array design, a slightly different loop-shaped feed has been designed, as shown in Fig. 6.22. The radius of this loop is reduced with respect to the linear polarization

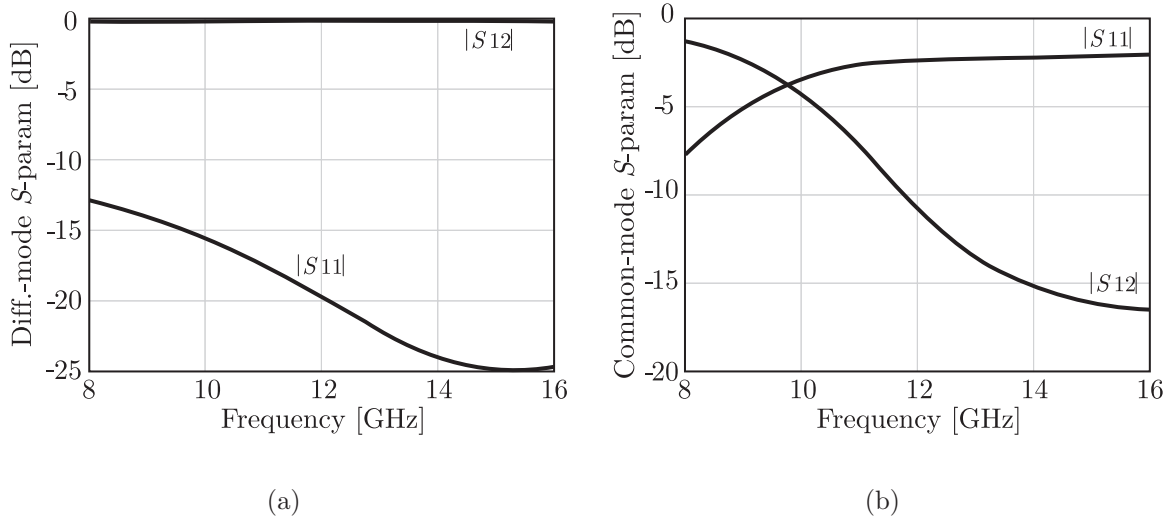


Figure 6.23: S-parameters of the loop in Fig. 6.22 pertaining to (a) differential and (b) common modes.

case, from 1.06 mm to 0.8 mm. The loop is composed of two quarter wave sections of CPS lines to implement an impedance transformation for the differential mode from 400 to 160 Ω . To have two sections approximately equal to a quarter wavelength at the highest frequency of interest, the point of transition has been rotated by 100° with respect to the corresponding point for the previous configuration. The S-parameters of the loop are reported in Fig. 6.23, while the array performance is shown in Fig. 6.24. Considering the points of -10 dB matching, a relative bandwidth of 35% is achieved, while the X-pol level is below -18.5 dB over the operational bandwidth. Note that a stringent, but frequent requirement for polarization sensitive arrays is that the cross-polarized field is at least 15 dB lower than the co-polarized one.

6.5 Conclusions

In this chapter, two novel solutions for the practical implementation of the feed networks in connected arrays have been presented. Both feed structures are based on PCB technology, to limit the costs and the complexity, without resorting to active component or to MMIC technology.

First, an aperture-coupling-based transformer has been described, acting as a common-mode rejection circuit. To guarantee the effectiveness of this component, the periodic cell has been split into two or more subcells along the longitudinal direction (x). Infinite-

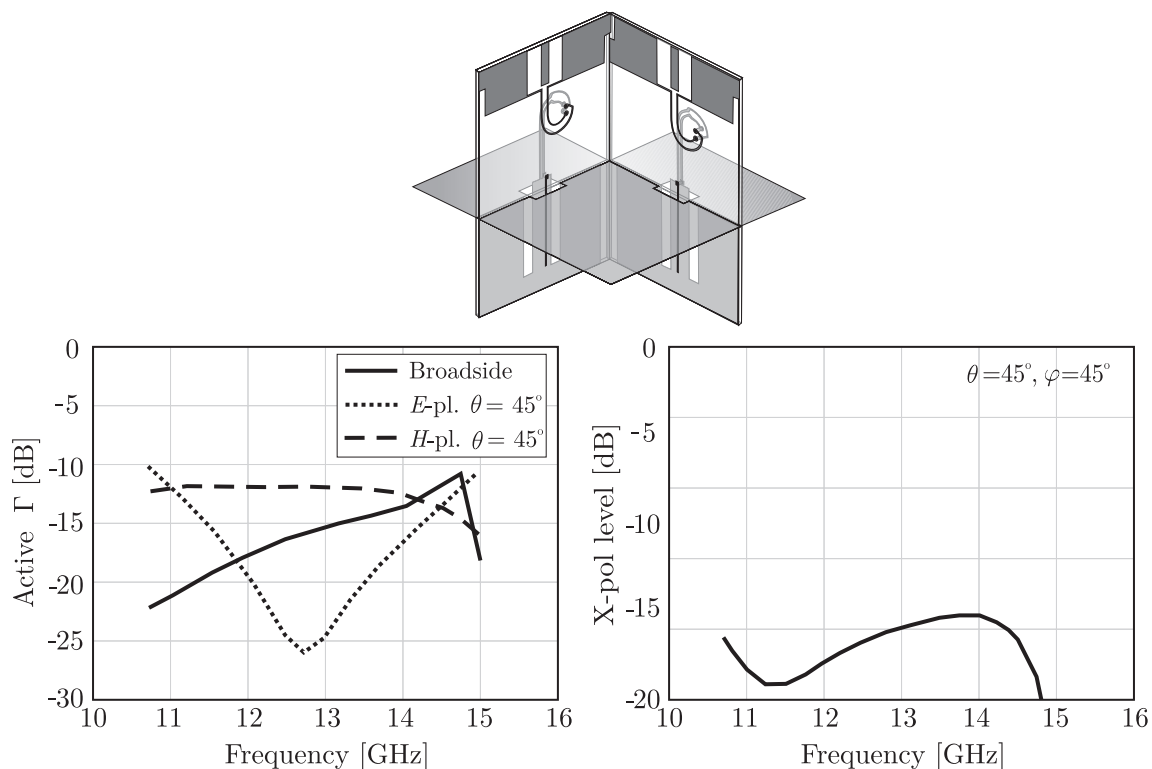


Figure 6.24: Performance of the loop when included in the unit cell of a dual-pol connected dipole array.

array simulations have shown the capability of the transformer to lower the X-pol levels. However, the efficiency of this solution decreases when scanning in the E -plane, since the contributions from the subcells do not sum up with same phase.

Another practical way to design the feed network of a connected array has been proposed as valid solution to common-mode resonances. It is based on a loop-shaped transformer that constitutes a strong impedance mismatch for the common mode. The performance has been characterized via full-wave simulations performed with Ansoft HFSS. Simulated results show a 10 dB common-mode rejection over a more than one octave bandwidth (9 to 20 GHz). The inclusion of the loop component into the feed lines of a connected array of dipoles has also been investigated. The design of a linearly polarized and a doubly polarized array has been presented. This array has been shown to operate over 35% relative bandwidth when scanning up to 45° , and X-pol levels below -18.5 dB within the entire scan volume.

Chapter 7

Experimental Validation

7.1 A 3 to 5 GHz Singly-Polarized Connected Array

Based on the analytical formulation developed in the first part of this thesis, a wideband, wide-scan phased array of connected dipoles has been designed and fabricated for 3 to 5 GHz operation. The dipole element is combined with the loop-shaped transformer described in Sec. 6.4 for the realization of the feed network. Measured results from a 7×7 prototype demonstrator are presented for experimental validation.

7.1.1 Design Strategy

The first step of the design is to optimize the dimensions of the unit cell of a connected-dipole array in the presence of a backing reflector (Fig. 7.1). The dipoles are horizontally placed in the $(x-y)$ plane. The array periods are d_x and d_y along the longitudinal and transverse direction of the dipole, respectively. The following parameters can be adjusted to optimize the performance in the band from 3 to 5 GHz: the dipole width (w), the size of the feed gap (δ), the distance from the ground plane (h) and the array periods (d_x, d_y). A first choice of the parameters is obtained with the aid of a genetic algorithm that minimizes the following fitness function:

$$\max_f(\Gamma_B, \Gamma_{E\theta_{max}}, \Gamma_{H\theta_{max}}) \quad (7.1)$$

where Γ_B , $\Gamma_{E\theta_{max}}$ and $\Gamma_{H\theta_{max}}$ are the active reflection coefficient for broadside, scanning to θ_{max} in the E -plane and scanning to θ_{max} in the H -plane, respectively. For each frequency f , these functions are analytically dependent on the parameters that characterize the array, therefore the procedure is essentially immediate.

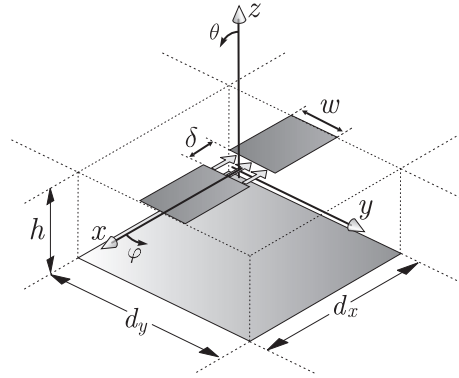


Figure 7.1: Unit cell of a connected array of planar dipoles with delta-gap excitation.

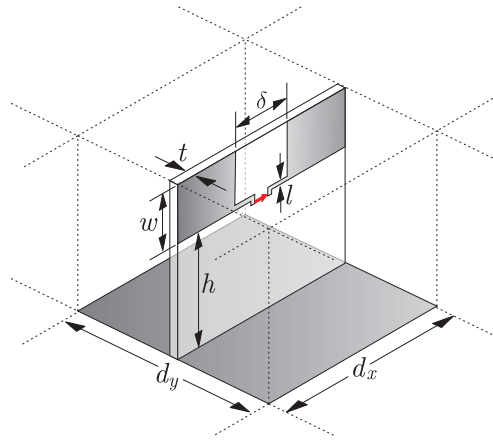


Figure 7.2: Unit cell of a connected array of vertically arranged dipoles excited with balanced co-planar strip lines.

This preliminary design assumes that the dipoles are horizontally placed, parallel to the backing reflector and fed by idealized delta-gap sources. An equivalent but more realistic structure is obtained by considering the dipoles printed on thin vertical PCBs, with relative permittivity ϵ_r and thickness t , and fed by balanced co-planar strip lines, as displayed in Fig. 7.2. The size of the feed gap (δ) and the width of the inductive lines that connect the dipole arms to the feed (l) can be fine-tuned with the aid of Ansoft HFSS [41] to obtain the same active input impedance of the ideal planar element. The following set of parameters has been found to yield good matching in the frequency range from 3 to 5 GHz within a 45° scan volume: $w = 7.56$ mm, $\delta = 7.875$ mm, $h = 15.12$ mm, and $l = 0.15$ mm. The array periods are $d_x = d_y = 25.2$ mm, which corresponds to 0.42λ at 5 GHz. A dielectric substrate of Rogers 4003 has been selected, with relative permittivity $\epsilon_r = 3.55$

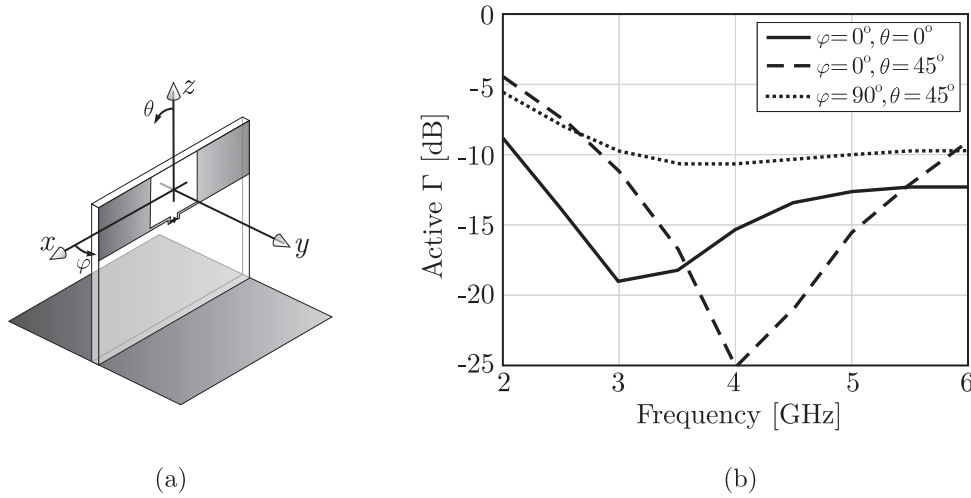


Figure 7.3: Connected array of dipoles without vertical feeding lines: (a) array unit cell; (b) active reflection coefficient, assuming a $350\ \Omega$ feeding line, for broadside and $\theta = 45^\circ$ in the E - and the H -planes.

and thickness $t = 1.118$ mm. At this stage, the elements are assumed to be fed at the dipole level, without the inclusion of vertical transmission lines.

Referring to the coordinate system in Fig. 7.3(a), the active reflection coefficient of the periodic array unit cell is shown in Fig. 7.3(b), assuming a $350\ \Omega$ feeding line. Curves are shown for scanning at broadside and to $\theta = 45^\circ$ in the main planes (E - and H -planes). It can be noted that, when observing only at broadside (continuous line), the considered connected dipole element can achieve bands in the order of 4:1 in the presence of a backing reflector. However, the input resistance is lowered by a factor of $\cos \theta$ when scanning in the E -plane and increased by a factor of $\sec \theta$ when scanning in the H -plane. Consequently, even in this case of ideally fed dipoles, the usable bandwidth within a 45° scan volume is reduced to about an octave (3 to 6 GHz).

Even if not reported for sake of brevity, the X-pol level of this element for observation at $\theta = 45^\circ$ in the diagonal plane (D -plane, $\varphi = 45^\circ$) is of about -15 dB. As mentioned in Sec. 1.2, such a value of X-pol is typical of perfectly linear radiating currents oriented along the x - or y -axis, according to the third definition of cross polarization by Ludwig [9].

To highlight the effect of common-mode propagation on the feed lines, Fig. 7.4 shows the performance of a similar array geometry, in which the same dipole elements are fed by vertical co-planar strip (CPS) lines, to reach the ground plane level, where the feed is located (Fig. 7.4(a)). The lines perform an impedance transformation from $350\ \Omega$ to $100\ \Omega$. The active reflection coefficient and the X-pol level are shown in Figs. 7.4(b) and 7.4(c), respectively, for observation at $\theta = 45^\circ$ in the D -plane. It is apparent that the inclusion

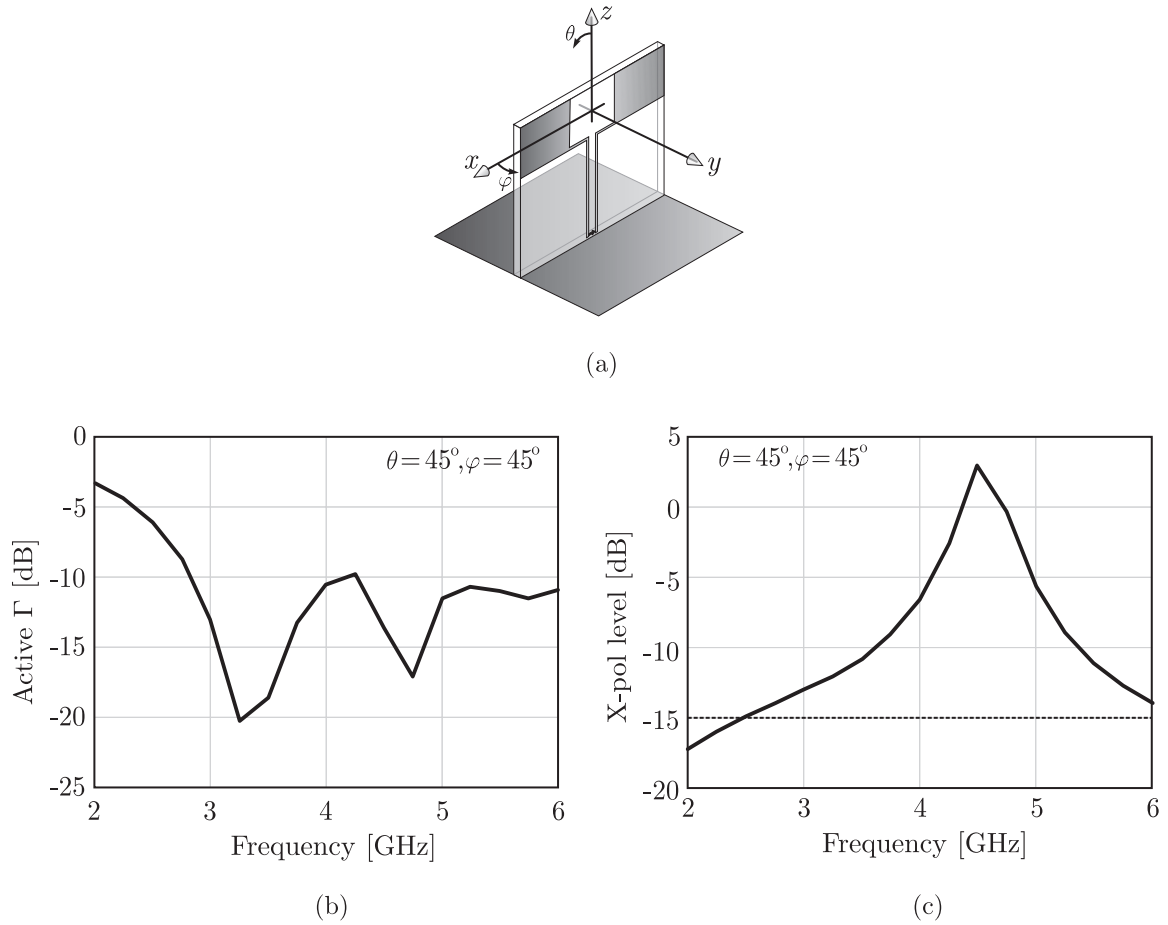


Figure 7.4: Connected array of dipoles with vertical feeding lines: (a) array unit cell; (b) active reflection coefficient, assuming a 100Ω feeding line, for $\theta = 45^\circ$ in the D -plane; (c) X-pol level for the same observation angle.

of long vertical feed lines has only a marginal impact on the matching. However, a catastrophic resonance appears in the X-pol level. This degradation is due to the propagation of common-mode currents on the CPS lines. The values of X-pol are much higher than the values typically observed for printed linearly polarized dipoles (≈ -15 dB).

Thus, it is important to note that the effect of common-mode resonances on the array efficiency should not be analyzed in terms of matching properties only for those applications in which the polarization purity is crucial. The usable bandwidth defined by the X-pol levels can be radically different from the bandwidth defined by the matching characteristics.

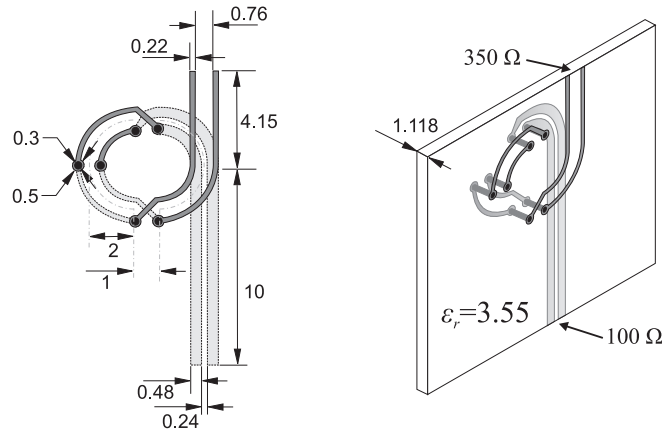


Figure 7.5: Dimensions (in mm) of the loop-shaped transformer.

7.2 Prototype Array: Simulations

To reject common-mode propagation on the vertical feeding lines, we consider a loop-shaped component as in Fig. 7.5. The loop radius is 2 mm and the loop is printed part on the bottom layer and part on the top layer of a 1.216 mm thick Rogers 4003 dielectric substrate with relative permittivity of 3.55.

As explained in Sec. 6.4, when a common-mode input is applied, at low frequencies the currents flowing in the loop are equal in phase and therefore the loop only behaves as a small series inductance for the common mode. As the frequency increases, different portions of the loops are flown by currents with different phases generating cancelling magnetic fields, which in turn produce a magnetic field circuitation with close to zero contributions in the center of a loop's cross section. Consequently, at frequencies higher than a certain threshold, the average distributed inductance of the loop becomes lower, creating a strong impedance discontinuity. This effect is quantified in Fig. 7.6, by the S-parameters pertaining to differential and common modes. A 10 dB common-mode rejection is observed for frequencies higher than 4.5 GHz, while no significant mismatch is experienced by the differential mode from 2 to 6 GHz.

Since the active input impedance of a connected dipole element typically exhibits high values ($350\ \Omega$), the loop can be used to implement an impedance transformation for the differential mode. To this aim, a two-section transformer from $350\ \Omega$ to $100\ \Omega$ has been implemented. The total length of the loop corresponds to a quarter wavelength in the dielectric at 3.5 GHz. Two inverters have been added to compensate for the slightly different radius of the inner and outer conductors within the loop, thereby reducing the

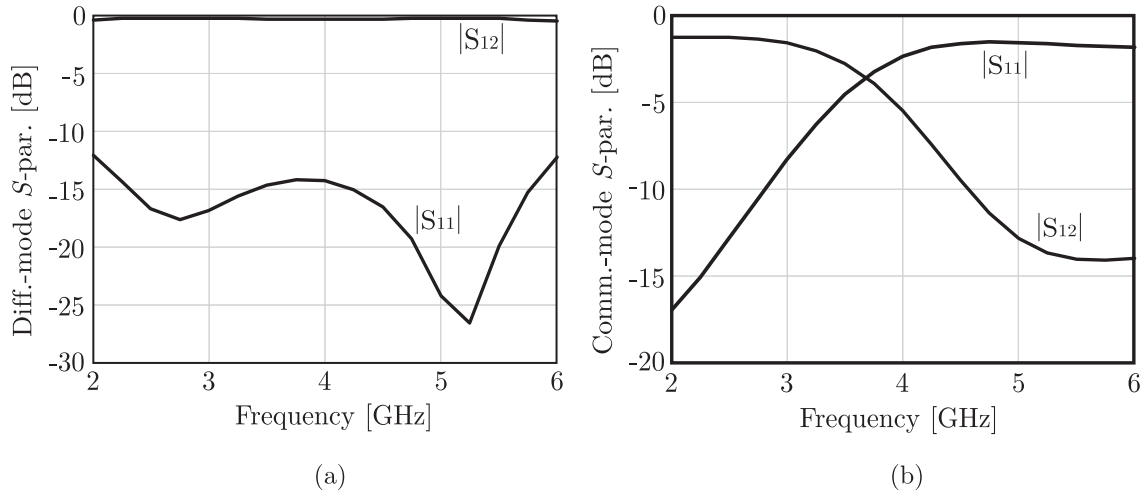


Figure 7.6: S-parameters of the loop transformer pertaining to (a) differential mode and (b) common mode.

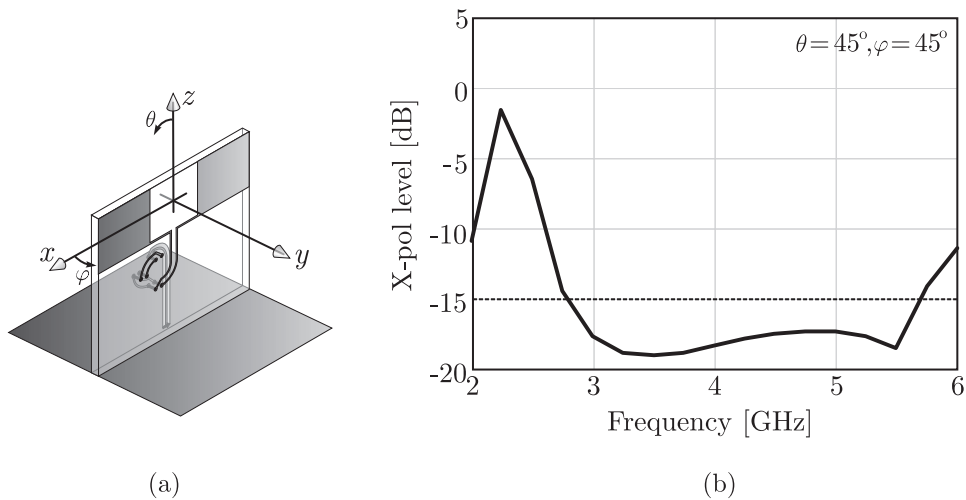


Figure 7.7: (a) Array element with the inclusion of the loop-shaped transformer in the feeding lines and (b) X-pol performance.

spurious radiation of the loop when a differential input is applied.

Figure 7.7 shows the X-pol levels of an array of connected dipoles including the loop-shaped feeding structure of Fig. 7.5. By comparing Fig. 7.7(b) with Fig. 7.4(c) it is evident that, when the common-mode rejection loop is used, the degradation of polarization performance introduced by the vertical lines is strongly mitigated over the bandwidth of interest. In fact, the X-pol ratio becomes lower than -17 dB over the band of operation.

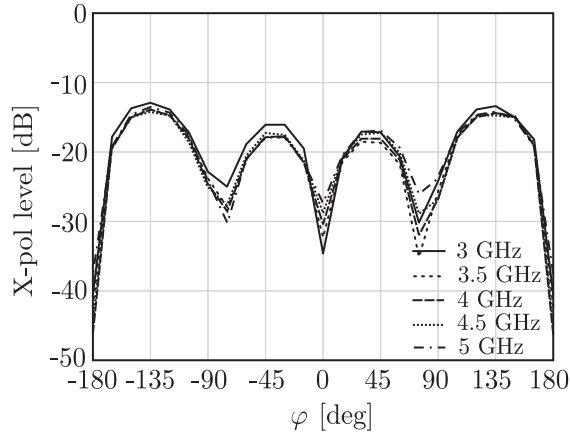


Figure 7.8: X-pol level of the element in Fig. 6.19(a) for $\theta = 45^\circ$, as a function of the azimuthal angle φ and for different frequencies.

Although the cross polarization maintains low levels for this particular observation angle, the element in Fig. 7.7(a) is not symmetric with respect to the (z - y) plane, due to the presence of the loop. For this reason the X-pol can be different in the two diagonal planes ($\varphi = 45^\circ$ and $\varphi = 135^\circ$). To highlight this effect, Fig. 7.8 shows the X-pol level for maximum elevation angle $\theta = 45^\circ$ as a function of the azimuth φ . The maximum value of X-pol is in the proximity of the diagonal planes $\varphi = \pm 135^\circ$ and it is approximately -13 dB in the worst case (at 3 GHz) and about -15 dB for all other frequencies in the operational band.

The previous results pertain to a differential excitation located at the ground plane level. A more realistic coaxial feed requires the inclusion of a transition from CPS to microstrip line. To this purpose, a sleeve balun has been designed, and a tapered line to reach $50\ \Omega$ impedance has been included. The geometry of the array unit cell and dimensions of the balun are shown in Fig. 7.9(a). The resulting performance of the overall structure are presented in Figs. 7.9(b) and (c), which show the active VSWR for broadside and for $\theta = 45^\circ$ in the main planes (normalized to $50\ \Omega$ impedance line), and the X-pol ratio for observation at $\theta = 45^\circ$ in several azimuthal planes. A VSWR lower than 2.4 is achieved over 50% relative bandwidth. The polarization bandwidth is limited by the band of the balun. The cross-pol level achieved by this configuration is at least 13 dB lower than the co-polar component over a 30% bandwidth.

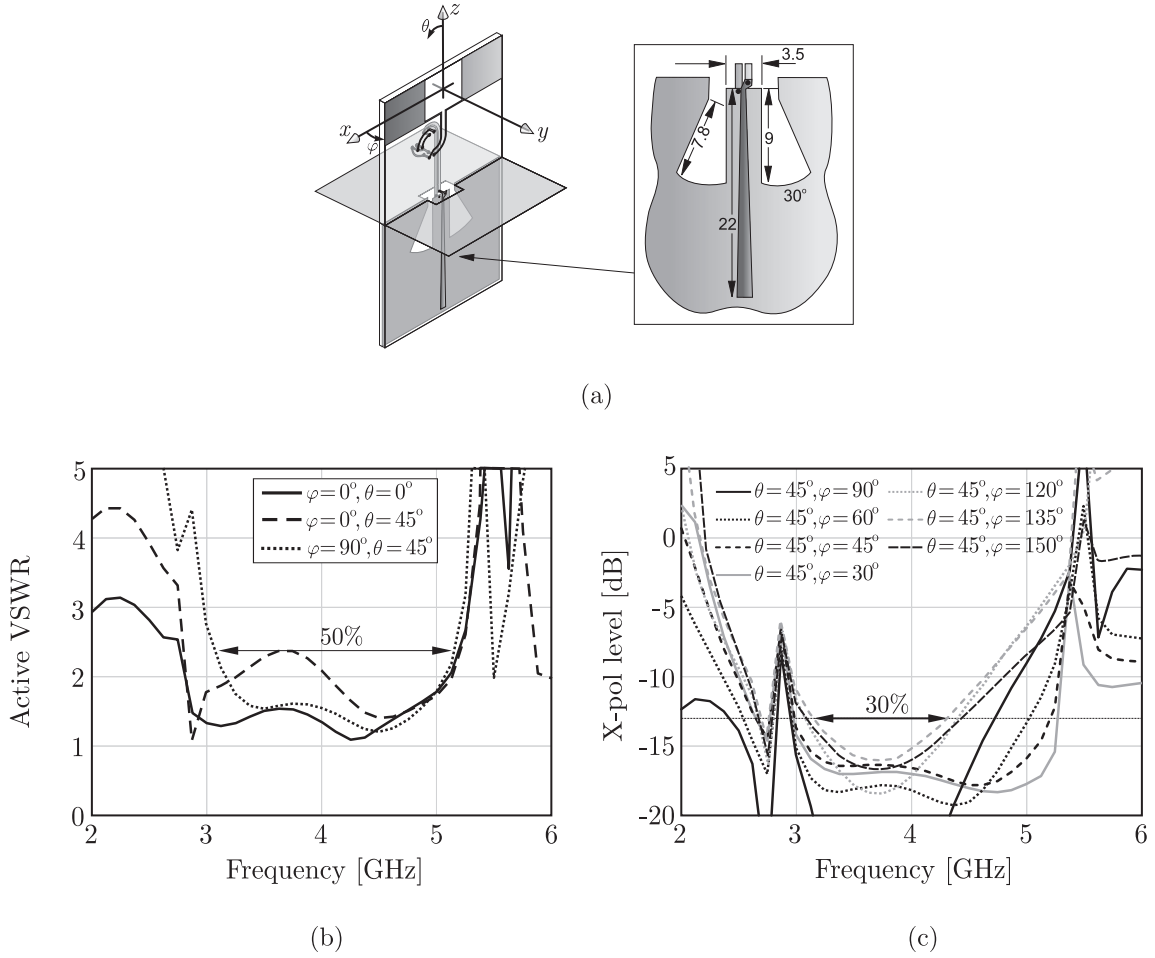


Figure 7.9: Performance of the loop when included in the unit cell of a linearly polarized connected dipole array: (a) array unit cell with dimensions of the balun; (b) active VSWR for for broadside and for $\theta = 45^\circ$ in the main planes ($50\ \Omega$ impedance); (c) X-pol level for observation at $\theta = 45^\circ$ and several azimuth angles.

7.3 Prototype Array: Measurements

Based on the design described in the previous section, a 7×7 prototype array has been manufactured. The array is singly polarized and consists of 7 vertically arranged PCBs like the one shown in Fig. 7.10. The external arms of the two dipoles at the edges include 8 series resistors with increasing values of resistance (from 10 to $400\ \Omega$). This ensures that the surface current gradually decreases to zero close to the edges, to limit truncation effects. Edge effects in arrays of connected dipoles can be remarkably strong, due to the electrical connection between the element that supports guided waves along the array. However,

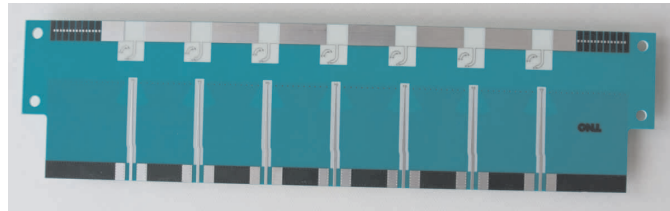


Figure 7.10: Printed boards of the prototype array.

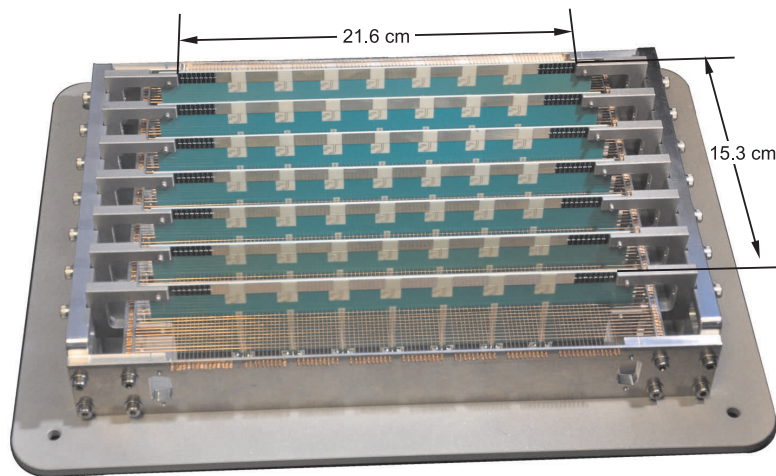


Figure 7.11: 7×7 prototype array with dimensions.

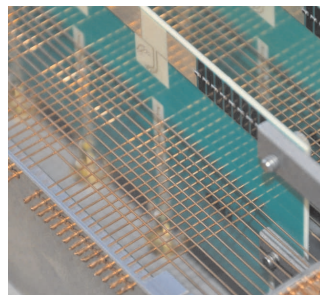


Figure 7.12: Discrete ground plane made by a wire grid.

these effects were investigated in detail in Chapter 5 and can be controlled by means of ad-hoc designs based on high-impedance elements.

The entire array is shown in Fig. 7.11, assembled with a mechanical support structure.

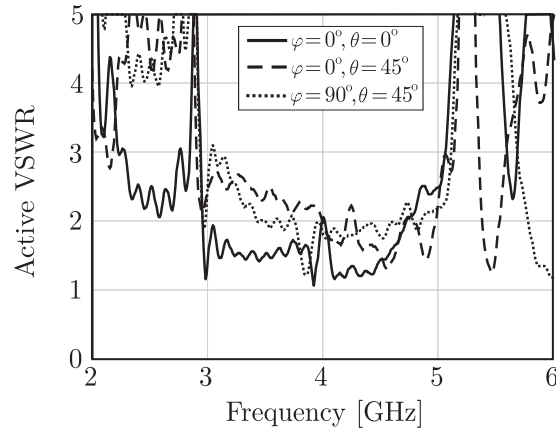


Figure 7.13: Measured active VSWR of the central element of the array: curves are shown for broadside radiation and scanning to 45° in the E - and H -plane.

7.3.1 Practical Implementation of the Backing Reflector

A particularly complicate manufacturing aspect is associated with the practical implementation of the backing reflector. In fact, a continuous metallic plane has to be placed horizontally and intersect the entire set of PCBs. The problem was solved by replacing the continuous plane with a discrete grid composed by wires. Simulation results showed only minor changes to the behavior of the array, as long as the distance between wires does not exceed $\lambda/10$ at the highest frequency of operation. Since there is no necessity for the set of wires along x and the one along y to be in electrical contact, this solution simplify the assembling of the antenna by avoiding the need for soldering. A close-up of the grid is shown in Fig. 7.12.

7.3.2 Measured Results

The measured active VSWR is shown in Fig. 7.13 for the central element of the arrays. The active parameters are evaluated via a post-processing summation of the passive measured S-parameters with opportune weights for the elements to account for scanning. Curves are shown for broadside radiation and for scanning to 45° in the E - and H -plane. Although some oscillations around the expected values can be observed, the measured results are in good agreement with the predictions presented in Fig. 7.9(b). Good matching performance is achieved for broadside radiation, for which a VSWR better than 2.5 is observed over the entire bandwidth of operation (3 to 5 GHz). The matching worsens for scanning, for which edge effects are more important. However, values of VSWR lower than 2.5 are observed

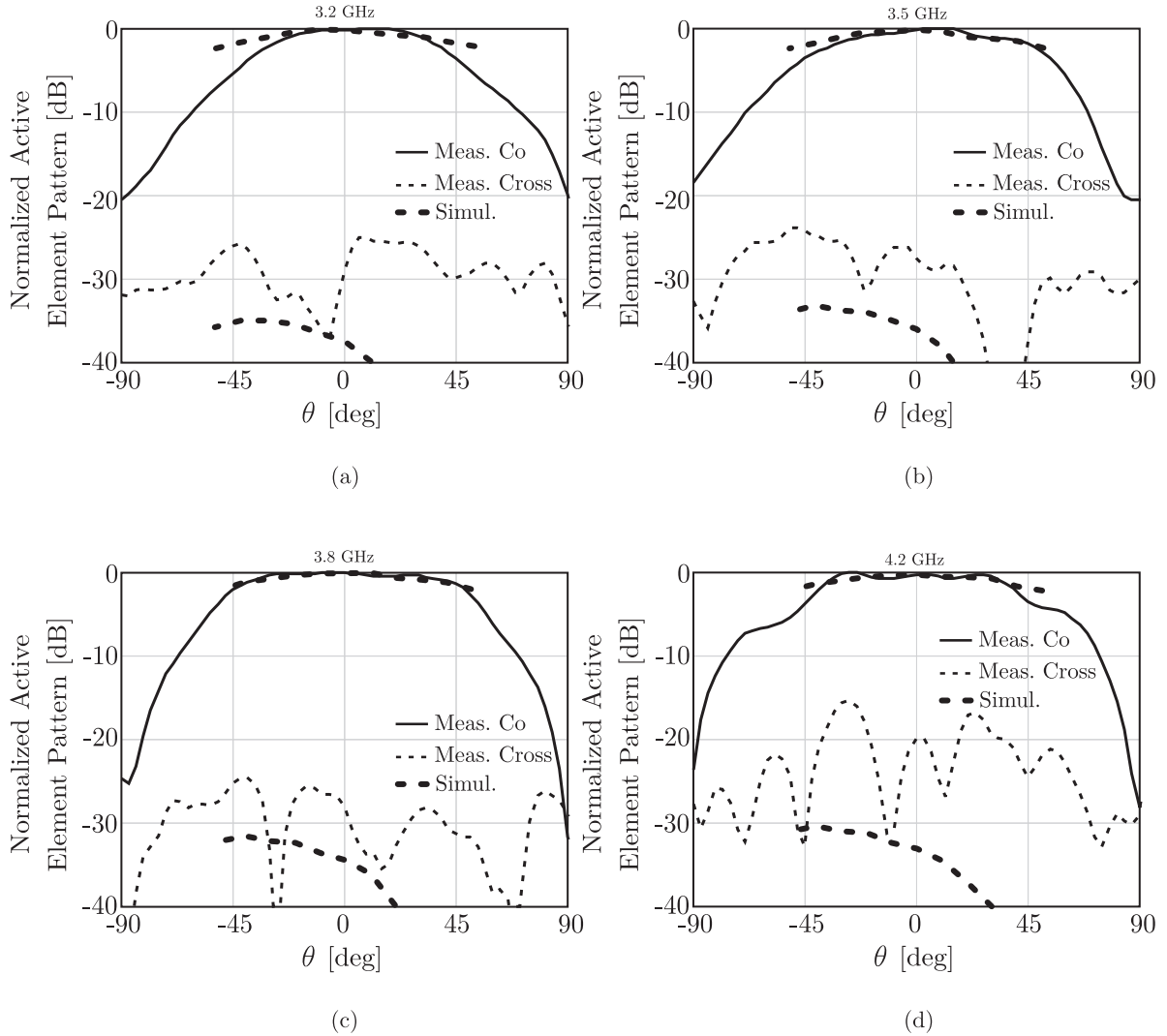


Figure 7.14: Measured normalized active element patterns in the E -plane for four frequencies: (a) 3.2 GHz, (b) 3.5 GHz, (c) 3.8 GHz, (d) 4.2 GHz. Active element patterns obtained with infinite-array simulations are also plotted.

on most of the operational band.

The measured normalized active element patterns in the E -, H - and D -planes are shown in Figs. 7.14, 7.15 and 7.16. Both co-polar and cross-polar components are presented for four frequencies within the design band. The active element patterns obtained with infinite-array simulations are also plotted for observations within a scan volume of $\pm 50^\circ$. The infinite-array simulations predict lower X-pol levels in the main planes with respect to measured results. Differences are mainly due to finiteness effects and non-ideality of the

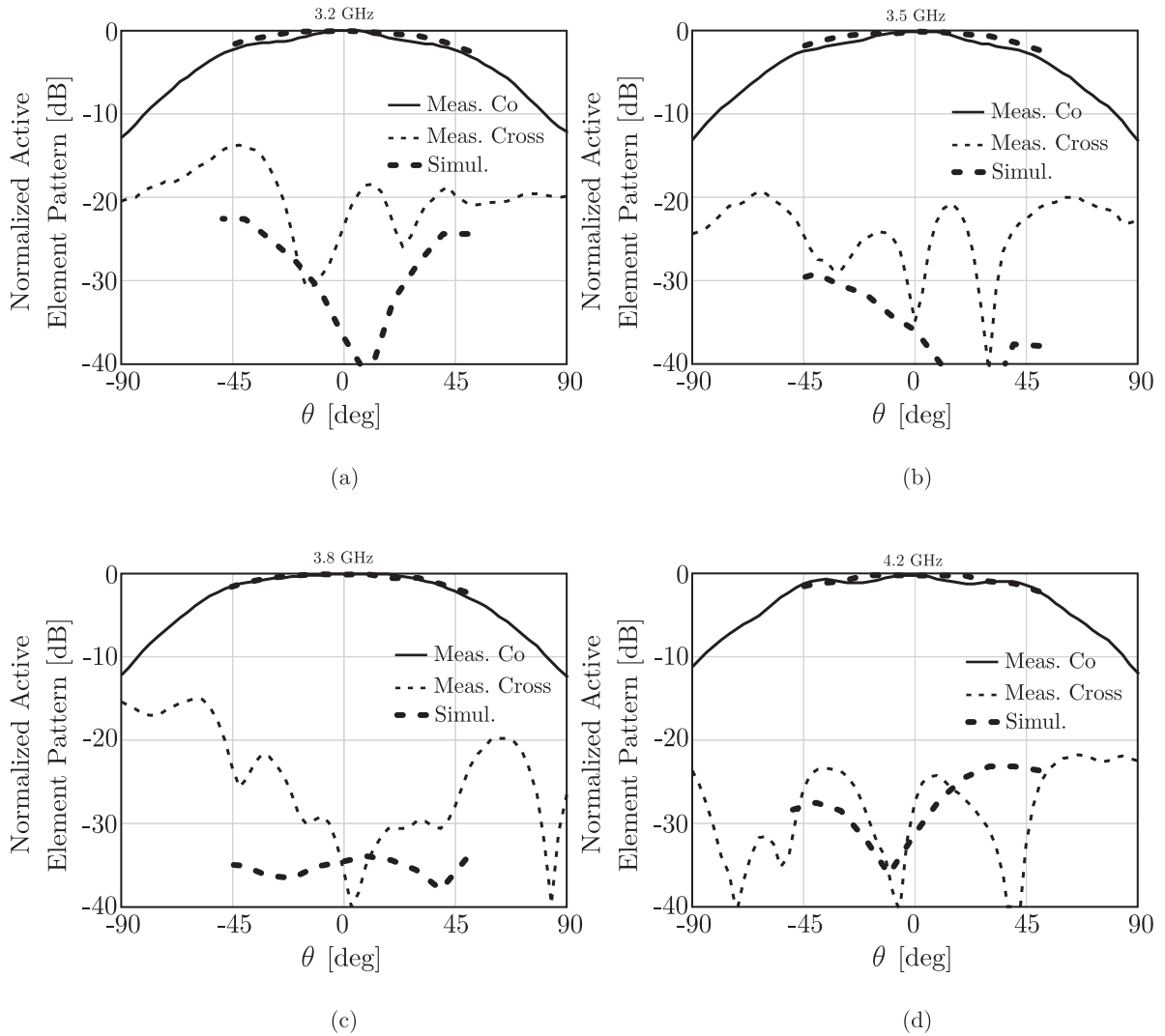


Figure 7.15: Measured normalized active element patterns in the H -plane for four frequencies: (a) 3.2 GHz, (b) 3.5 GHz, (c) 3.8 GHz, (d) 4.2 GHz. Active element patterns obtained with infinite-array simulations are also plotted.

measurements.

The aim of the design was the realization of an array with good polarization purity. Figure 7.17 presents the X-pol levels as a function of theta and for all the frequencies in the band from 3 to 5 GHz. The scan volume $\pm 45^\circ$ and the frequency range of about 30% (from 3.15 to 4.25 GHz) are highlighted by a white frame. Within these values, the normalized X-pol patterns are below -12 dB. A comparison between simulated and measured X-pol level for observation at $\theta = 45^\circ$ in the diagonal plane is presented in Fig. 7.18. The measured

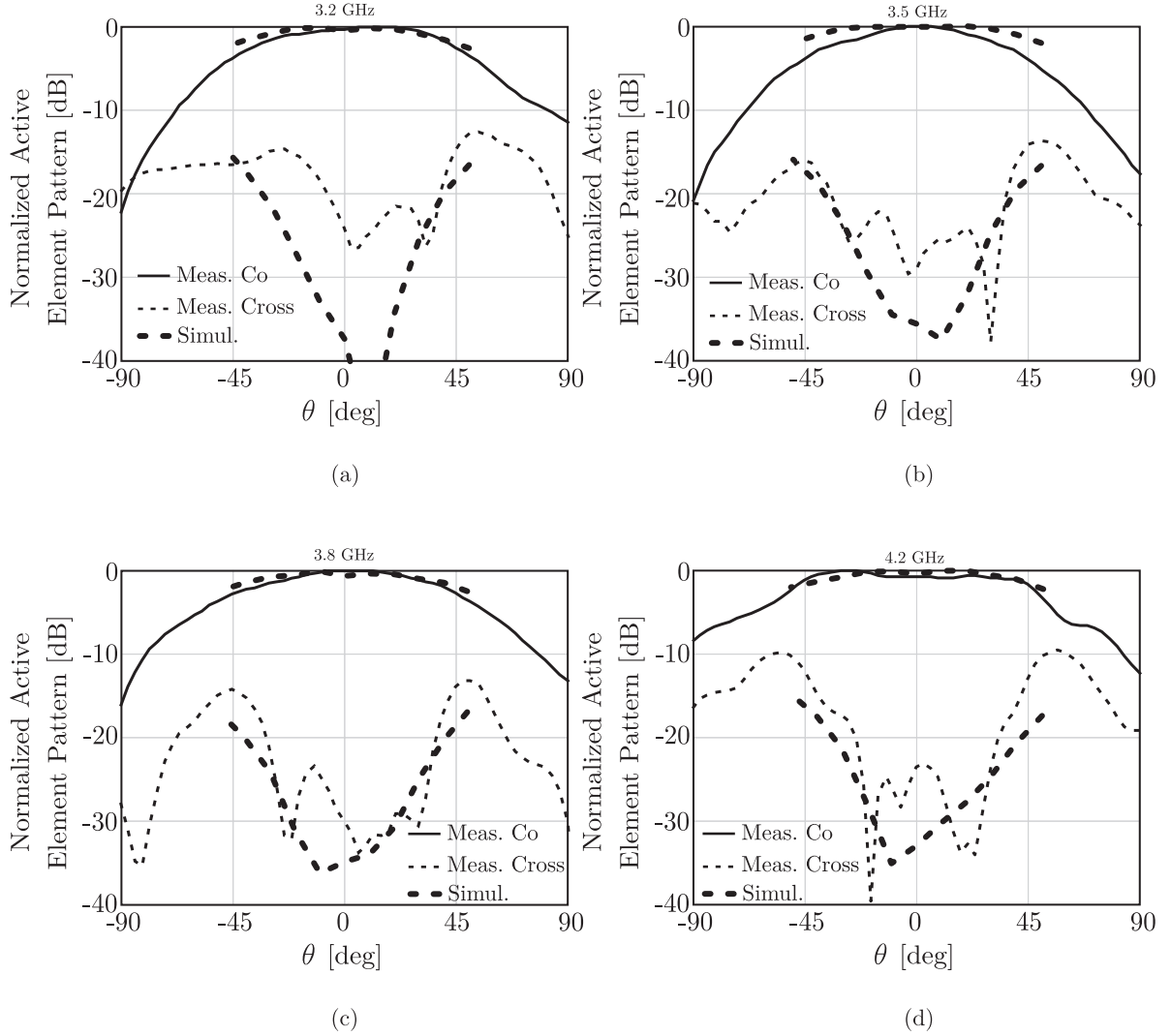
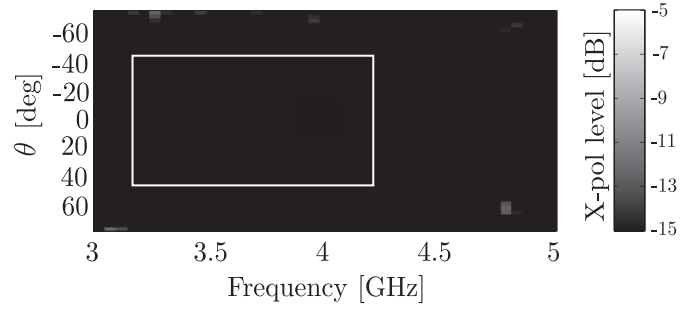


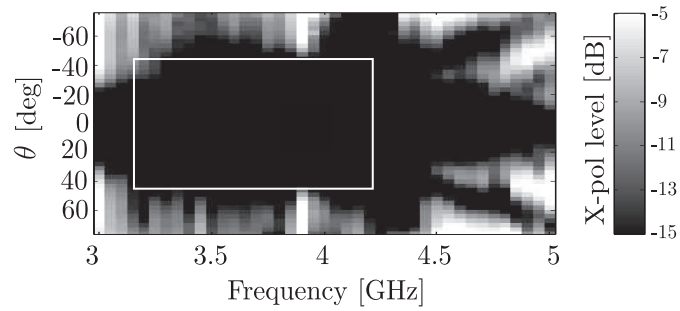
Figure 7.16: Measured normalized active element patterns in the D -plane for four frequencies: (a) 3.2 GHz, (b) 3.5 GHz, (c) 3.8 GHz, (d) 4.2 GHz. Active element patterns obtained with infinite-array simulations are also plotted.

values oscillate around the expected ones and are lower than -12 dB over about a 30% bandwidth.

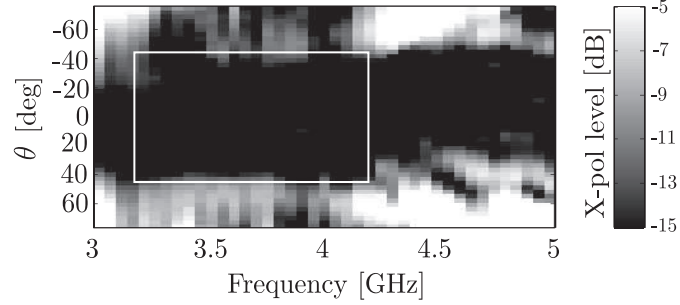
The configuration used for the measurements is schematically presented in Figs. 7.19 and 7.20. The $\hat{\theta}$ and $\hat{\varphi}$ unit vectors coincide with the co-polar and cross-polar components for observation in the main planes. Different is the case of the diagonal planes, for which we first measured the θ and φ components of the field, as shown in Fig. 7.20(b). A convenient rotation of the reference system is considered so that the dipoles are oriented along the



(a)



(b)



(c)

Figure 7.17: X-pol level as a function of the elevation angle θ and the frequency for (a) E -plane, (b) H -plane and (c) D -plane.

y' -axis. The measurement data are then used to evaluate the co-polar and cross-polar components according to the third definition of Ludwig (L3), which is given by

$$\hat{\mathbf{i}}_{co} = \sin \varphi' \hat{\boldsymbol{\theta}}' + \cos \varphi' \hat{\boldsymbol{\varphi}}' \quad (7.2)$$

$$\hat{\mathbf{i}}_{cross} = \cos \varphi' \hat{\boldsymbol{\theta}}' - \sin \varphi' \hat{\boldsymbol{\varphi}}'. \quad (7.3)$$

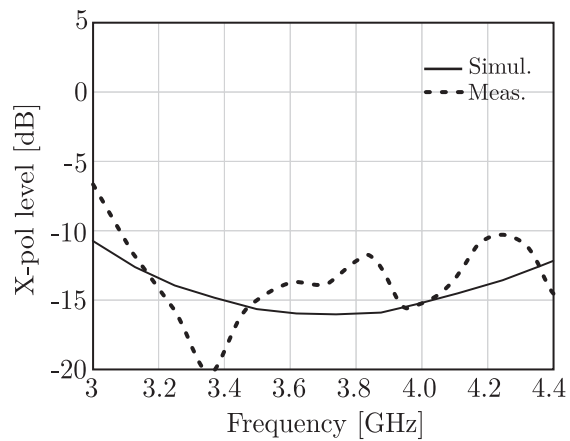


Figure 7.18: Comparison between simulated and measured X-pol level for scanning to 45° in the diagonal plane.

An equivalent procedure can be adopted to evaluate the L3-components in a direct way by rotating also the transmitting horn of 45° , as displayed in Fig. 7.21.

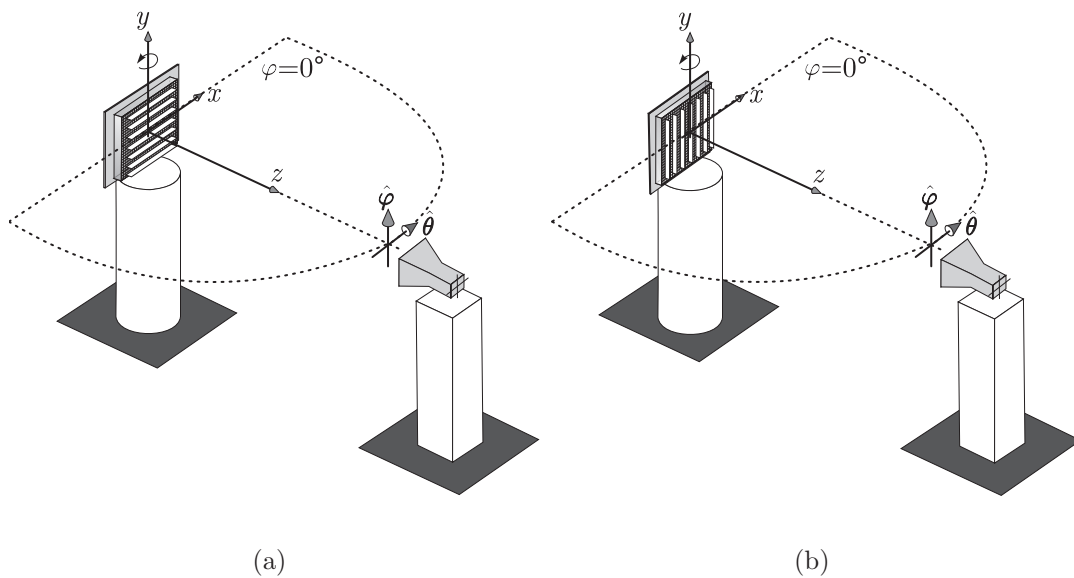


Figure 7.19: Configuration and coordinate reference system considered for the measurement of the radiation patterns in (a) the E -plane and (b) the H -plane.

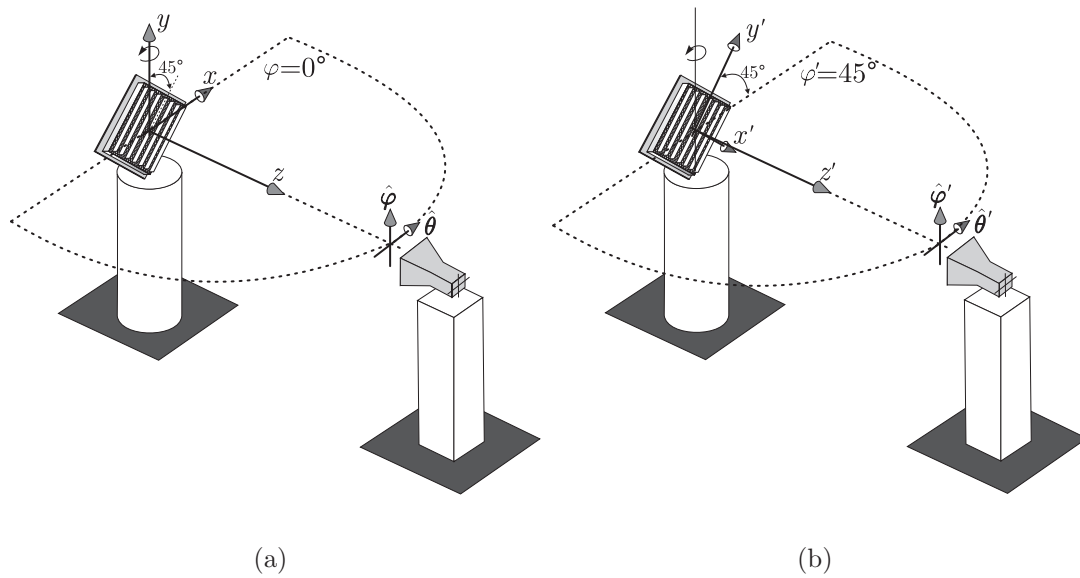


Figure 7.20: Configuration and coordinate reference system considered for the measurement of θ and φ components of the radiation patterns in the D -plane: (a) initial and (b) rotated coordinate reference system.

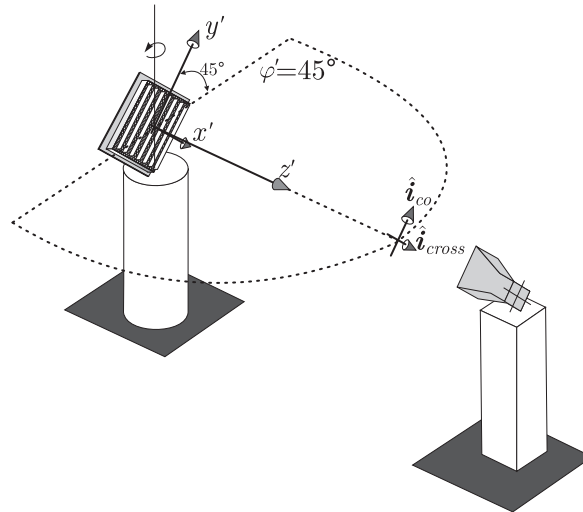


Figure 7.21: Configuration and coordinate reference system considered for the measurement of co-polar and cross-polar components of the radiation patterns in the D -plane (according to the third definition of Ludwig [9]).

7.4 Conclusions

A wideband, wide-scan angle array of connected dipoles has been designed and fabricated. Measured results from a 7×7 prototype demonstrator have been presented for experimen-

tal validation. To avoid common-mode resonances that typically affect this type of arrays, loop-shaped transformers are included in the feed network. The common-mode rejection implemented by these transformers allows to maintain the cross-polarization levels to low values over about 30% relative bandwidth, for elevation angle up to 45° in all azimuth planes. The measured results are in good agreement with expectation based on infinite array analysis.

The proposed feed structure is believed to be an efficient practical way to implement the matching network of a connected array, as valid solution to common-mode resonances. The loop-shaped feeding structure is based on PCB technology, to limit the costs and the complexity, without resorting to active component or to Monolithic Microwave Integrated Circuit (MMIC) technology.

The realization of the ground plane was shown to be a critical aspect of the manufacturing. The problem was solved by replacing the continuous plane with a discrete grid composed of wires. The goodness of the results validates this method for ground plane implementation. The array can keep low polarization levels (<-12 dB) of a volume of 45° and a band of 30%. These results are believed to be among the best reported for wideband wide-scanning applications without penalty in polarization efficiency and with spacing kept at about 0.45λ at the higher frequency of operation.

Chapter 8

Conclusions and Recommendations

This dissertation described the research work carried out over a period of four years (from September 2007 to August 2011) at TNO Defence, Security and Safety, in The Hague, Netherlands.

The project dealt with theoretical and practical aspects of connected array antennas, covering both analysis and design. The topic treated is nowadays of particular interest in the field of wideband arrays, because this antenna solution is able to simultaneously achieve broad bandwidth and low cross polarization.

Connected arrays are believed to have an enormous potential for several applications and future developments, for both their advantageous physical properties and their effective analytical mathematical representation.

In this chapter, we summarize the conclusions and the most significant results of the research.

8.1 Analytical Description of Connected Arrays

The thesis extended the theoretical formulation, based on Green's functions (GF), previously developed in [32, 36, 37]. These works reported the derivation of the GF of transmitting connected array of unloaded slots. In the present research, the formulation was generalized to the case of array of connected dipoles, both in transmit and receive mode, and including the presence of loads.

From the described procedure, analytical expressions were derived for the main antenna parameters, such as the input impedance, the current distribution over the array and the radiation patterns. The main benefit is that the description of the properties of the arrays is fully analytical, and thus involves essentially no computational cost. This constitutes a

crucial advantage with respect to most other types of antenna arrays, for which numerical solutions are required for the modelling, with increased computational load. Another important advantage with respect to numerical solutions is that the analytical expressions can be expanded in several terms, each with a well-defined physical meaning. This results in a gain in physical insight on the wave phenomena.

8.2 Connected Dipoles Versus Connected Slots

From the rigorous GF formulation, a comparison was made between the connected arrays of dipoles and slots. The arrays were assumed to be backed by a ground plane and their performance was investigated for wide-scan coverage.

Similar bandwidth performance can be achieved for broadside radiation in the two cases. However, for the array of slots, leaky poles can be excited in the structure when scanning. Such poles are not present in the dual structure composed of dipoles, for which the dispersion equation highlights only the presence of TEM microstrip-like poles. As a consequence, differences in performance appear when scanning is accounted for.

The study also revealed that the reactive energy localized in the feeding gaps of the connected dipoles can be tuned to achieve broad band matching, independently on the scan angle. A similar effect is not present in the slot case, where the reactive energy associated with size of the feed gap is modelled as a series inductance. As such, it does not affect the real part of the impedance and cannot be used to improve bandwidth performance when scanning.

Finally, we presented a connected array of dipoles with 40% bandwidth, when scanning in elevation to 45° . The band is defined as the frequency range within which the array shows an active S_{11} lower than -10 dB when pointing at broadside and at 45° in the E - and H -planes.

8.3 Equivalent Circuit Representation

A convenient circuit representation was derived in Chapter 4. The circuit describes rigorously and analytically the transition between free-space radiation and guiding transmission line. The equivalent network is valid for periodically excited, infinite connected arrays. Contrarily to standard Thévenin circuit for receiving antennas, this representation can be used to evaluate the power scattered by the antenna.

The circuit provides the same quantitative information of full-wave numerical simulations,

but is ‘computationally free’ and gives much more physical insight. This is because each component is associated with a specific wave mechanism.

- A set of four transmission lines accounts for the transverse electric (TE) and magnetic (TM) field components radiated by the array in the upper and lower half spaces. These transmission lines can also include the presence of dielectric stratifications and/or frequency selective surfaces and/or backing reflector.
- Two transformers weight the TE and TM equivalent transmission line, to obtain the total ($TE + TM$) average magnetic field in the entire cell at the array plane. The projection of this magnetic field onto the feed gap provides the electric currents at the dipole terminals. This projection is represented via another transformer.
- The reactive field in the vicinity of the array is described by means of two lumped reactive loads, associated with the capacitance of the gap and the self-inductance of the dipole.

Moreover, the results have been applied to the analysis of the scattering and absorption of a connected dipole array prototype. The array is backed by the combination of a continuous metallic plane and a frequency selective backing reflector, for dual-band operation. Comparisons between measured and equivalent-network based simulations showed outstanding agreement. The Radar Cross section (RCS) measurements in the main planes were used to characterize the active matching of the radiating part of the antenna in transmission. This measurement technique has the advantage to be simple and cost-effective, since the antenna can be characterized without the inclusion of the complicate and expensive feed network. The method is useful when one wants to separate the characterization of the antenna from the spurious radiation from the feed lines.

8.4 Finite Connected Arrays

Finiteness effects in connected arrays were characterized. These effects can be particularly severe in connected arrays, due to electrical connection and the high mutual coupling between the elements.

First, we presented an efficient numerical procedure that requires only one unknown per elementary cell, independently from the cell geometrical parameters. This is possible thanks to the use of an appropriate connected array GF in the integral equation. This procedure is of general applicability and can be used for arrays with and without backing reflectors

and for arbitrary scan angles. The numerical cost of the analysis is only the inversion of a matrix of dimension $N_x \times N_x$, where N_x is the number of feed points in the array along the longitudinal direction. Such a numerical procedure is particularly convenient when the performance of the array for wide-angle scanning needs to be assessed in advance of measurements or full-wave, all inclusive, numerical simulations, or in an optimization phase.

Moreover, an analytical approximation of the spatial current distribution on the finite array was derived, for the specific case of a connected array of dipoles operating in free space, and scanning only in the E -plane. The key step is to represent the total current as sum of the infinite-array contribution and edge-born waves. Some simplifications can be adopted for the edge term that would otherwise be unreasonable. The final analytical expression is given in terms of Fresnel functions. Important potentials remain for the extension of the analytical formulation to more general cases. In particular, the generalization for arrays with backing reflector and for general oblique scanning, although more complicate to be treated analytically, are believed to be of particular interest for future developments.

One important finding of the study for practical array designs is that the edge waves propagation strongly depends on the load impedance. More specifically, the intensity of the edge waves is more important for low source/load impedances. High impedances in the order of 400Ω imply reduced edge-born effects in connected arrays with a backing reflector.

8.5 Practical Design of a Connected Array

The theoretical formulation was entirely based on idealized delta-gap sources as excitation of the dipole element. Issues related to the implementation of the more realistic feed network were also discussed. Two effective solutions were proposed and validated with full-wave simulations. Both feed structures are based on Printed Circuit Board (PCB) technology, to limit the costs and the complexity, without resorting to active component or to Monolithic Microwave Integrated Circuit (MMIC) technology.

First, an aperture-coupling-based transformer was designed, which acts as a common-mode rejection circuit. To guarantee the effectiveness of this component, the periodic cell was split into two or more subcells along the longitudinal direction. Infinite-array simulations showed the capability of the transformer to lower the X-pol levels. However, the efficiency of this solution decreases when the E -plane is scanned, since the contributions from the subcells do not sum up with coherent phases.

Another practical way to design the feed network of a connected array involved the inclusion

of a common-mode rejection loop. Simulated results showed common-mode rejection better than 10 dB over a bandwidth exceeding one octave. The inclusion of the loop component into the feed lines of a connected array of dipoles has also been investigated. The design of a linearly polarized and a doubly polarized array was presented. This latter was shown to operate over 35% relative bandwidth when scanning up to 45° , with X-pol levels below -18.5 dB within the entire scan volume.

Measured results from a 7×7 prototype demonstrator were presented for experimental validation of the loop-shaped transformer. The array exhibits good matching ($VSWR < 2.5$) over a band 3 to 5 GHz. The array exhibits low polarization levels (< -12 dB) in a volume of 45° and a band of 30%. The measured results are in good agreement with expectation based on infinite array analysis. These results are believed to be remarkable for a wideband wide-scanning array without penalty in polarization efficiency and with spacing kept at about 0.45λ at the higher frequency of operation.

8.6 Outlook

Connected arrays are characterized by wideband operation. In particular, a dipole array in the presence of a backing reflector can be matched over a 50% bandwidth within a $\pm 45^\circ$ scan volume. However, the performance in practical designs is limited by the feed structure rather than by the radiating elements themselves. The combination of the dipole element and the balun proposed in this research was shown to achieve good matching and polarization purity over a bandwidth of about 30%. To improve the performance of the overall array, feeding structures with wider operational bandwidths need to be developed. This is the object of an ongoing joint project between TNO and University of Ancona, Italy.

The prototype connected array described in Chapter 7 is composed by vertically arranged printed circuit boards (PCBs) that have to be assembled together by means of an additional mechanical support. The backing reflector was realized by a discrete wire grid to avoid soldering. A more practical fabrication would result from a fully planar implementation of the array. In that case, the feeding lines have to be realized by vertical pins or vias instead of coplanar strip lines. The current limit for the planar realization is the maximum processable aspect ratio of the pins by the PCB manufacturers. In fact, pins with very high length-to-diameter ratios are needed to reach the level of the backing reflector. However, novel technologies are being developed by several companies that allow the realization of higher length-to-diameter ratios for pins or vias. This would allow a completely planar

realization with a single multi-layered PCB.

From an analytical point of view, an interesting extension of the theoretical models is the generalization of the analysis of connected arrays for different types of excitation. In the present research, we only considered idealized differential sources for the transmission case and plane-wave incidence for reception. The properties of the array can be characterized for more general excitations; e.g. a generalized delta-gap source that accounts for both differential and common mode, or incident Gaussian or Airy beams if the array is placed in the focal plane of a quasi-optical system.

8.7 Impact of the Research

The work described in this thesis has led to a number of journal and conference publications (listed on p. 187 of this dissertation). Furthermore, the research developed within this work has had an important role at TNO, Defense, Security and Safety in the framework of the following projects.

- Advanced Antenna Concepts for Aircraft in Flight Entertainment (ACTiFE) [105, 106]: this activity is supported by the European Space Agency, contracts no. C19865 and 4000101757.
- Merging Electronics and Micro&nano-PHOTONICS in Integrated Systems (MEMPHIS) [107]: this project is supported by the Dutch ministry of Economic Affairs and the Dutch ministry of Education, Culture and Science through the Smart Mix program.
- TNO Radar Program: this program aims at developing novel radar concepts and technologies for scalable front ends; it is supported by the Dutch ministry of Defence [4, 108].
- Integrated Technology Mast Systems (ITMS): this work is supported by TNO and by the Dutch ministry of Defense [109].

In the framework of these projects, one international patent has been granted and four prototype antennas have been manufactured. Moreover, the work described in Chapter 3 was awarded with the *Best Innovative Paper Prize* at the 30th ESA Workshop on Antennas for Earth Observation, Science, Telecommunication and Navigation Space Missions, in Noordwijk, Netherlands.

Appendix A

Spectral Green's Functions of Plane-Stratified Media

The aim of this appendix is to derive the spectral representation of the dyadic Green's function (GF) in planar stratified media, following the formalism described in [39,110]. The formulation is general and may be applied to any arbitrary region uniform along the planes transverse to the direction of stratification. The uniformity along the transversal directions suggests to resort to a spectral representation of the electromagnetic field by means of plane waves. The representation allows to link the electromagnetic field in the stratified media to arbitrarily oriented electric or magnetic currents. Moreover, two examples will be given that are of interest for the analysis of connected arrays: an elementary electric source in free space and in the presence of a backing reflector.

A.1 Electromagnetic Field in Terms of z -Directed Vector Potentials

The electromagnetic field can be expressed as function of auxiliary vector potentials \mathbf{A} (magnetic) and \mathbf{F} (electric) as follows:

$$\begin{aligned}\mathbf{E} &= -jk\zeta \left(\mathbf{A} + \frac{1}{k^2} \nabla \nabla \cdot \mathbf{A} \right) - \nabla \times \mathbf{F} \\ \mathbf{H} &= -j \frac{k}{\zeta} \left(\mathbf{F} + \frac{1}{k^2} \nabla \nabla \cdot \mathbf{F} \right) + \nabla \times \mathbf{A}\end{aligned}\tag{A.1}$$

where $\zeta = \sqrt{\mu/\varepsilon}$ is the impedance of the medium and $k^2 = \omega^2\mu\varepsilon$, with ω being the angular

frequency. Although omitted for lightness of notation, the fields and the vector potentials in (A.1) are functions of the position in space $\mathbf{r} = x\hat{\mathbf{x}} + y\hat{\mathbf{y}} + z\hat{\mathbf{z}}$. \mathbf{A} and \mathbf{F} satisfy the equations

$$\begin{aligned}\nabla^2 \mathbf{A} + k^2 \mathbf{A} &= -\mathbf{J} \\ \nabla^2 \mathbf{F} + k^2 \mathbf{F} &= -\mathbf{M}.\end{aligned}\tag{A.2}$$

Since the selection of the vector potentials is arbitrary, for structures that exhibit a cylindrical symmetry (invariant along $\boldsymbol{\rho} = x\hat{\mathbf{x}} + y\hat{\mathbf{y}}$), also when stratified in z , one convenient choice to scalarize the problem is taking \mathbf{A} and \mathbf{F} along z , i.e. $\mathbf{A} = A_z\hat{\mathbf{z}}$, $\mathbf{F} = F_z\hat{\mathbf{z}}$. If we assume that the sources have no component along z , the potentials satisfy the homogenous scalar wave equations

$$\begin{aligned}\nabla^2 A_z + k^2 A_z &= 0 \\ \nabla^2 F_z + k^2 F_z &= 0.\end{aligned}\tag{A.3}$$

With the above choice of the wave potentials, the fields in (A.1) are given by

$$\begin{aligned}\mathbf{E} &= -jk\zeta \left(A_z\hat{\mathbf{z}} + \frac{1}{k^2} \nabla \partial_z A_z \right) - \nabla \times F_z\hat{\mathbf{z}} \\ \mathbf{H} &= -j\frac{k}{\zeta} \left(F_z\hat{\mathbf{z}} + \frac{1}{k^2} \nabla \partial_z F_z \right) + \nabla \times A_z\hat{\mathbf{z}}.\end{aligned}\tag{A.4}$$

Representing ∇ as $\nabla_t + \partial_z\hat{\mathbf{z}}$, the fields can be also written as

$$\begin{aligned}\mathbf{E} &= -jk\zeta \left[\left(1 + \frac{1}{k^2} \partial_z^2 \right) A_z\hat{\mathbf{z}} + \frac{1}{k^2} \nabla_t \partial_z A_z \right] - \nabla_t \times F_z\hat{\mathbf{z}} \\ \mathbf{H} &= -j\frac{k}{\zeta} \left[\left(1 + \frac{1}{k^2} \partial_z^2 \right) F_z\hat{\mathbf{z}} + \frac{1}{k^2} \nabla_t \partial_z F_z \right] + \nabla_t \times A_z\hat{\mathbf{z}}.\end{aligned}\tag{A.5}$$

The above expressions allow us to decompose the fields into transverse electric (TE) and transverse magnetic (TM) components with respect to z :

$$\begin{aligned}\mathbf{E} &= \mathbf{E}_{TM} + \mathbf{E}_{TE} \\ \mathbf{H} &= \mathbf{H}_{TM} + \mathbf{H}_{TE}.\end{aligned}\tag{A.6}$$

The TM fields are the ones due to A_z , while the TE fields are the ones associated with F_z :

$$\begin{aligned}
\mathbf{E}_{TM} &= -jk\zeta \left[\left(1 + \frac{1}{k^2} \partial_z^2 \right) A_z \hat{\mathbf{z}} + \frac{1}{k^2} \nabla_t \partial_z A_z \right] \\
\mathbf{E}_{TE} &= -\nabla_t \times F_z \hat{\mathbf{z}} \\
\mathbf{H}_{TM} &= \nabla_t \times A_z \hat{\mathbf{z}} \\
\mathbf{H}_{TE} &= -j \frac{k}{\zeta} \left[\left(1 + \frac{1}{k^2} \partial_z^2 \right) F_z \hat{\mathbf{z}} + \frac{1}{k^2} \nabla_t \partial_z F_z \right].
\end{aligned} \tag{A.7}$$

The boundary conditions to be satisfied by these equations depend on the particular problem. For stratified regions, the solution is obtained by imposing the continuity of the tangential fields at the interfaces.

A.2 TE-TM Transmission Lines in Unbounded (x, y) -Domains

Let us represent the wave potentials in terms of their Fourier transforms with respect to the variables x and y :

$$\frac{A_z}{F_z}(x, y, z) = \frac{1}{4\pi^2} \int_{-\infty}^{\infty} \int_{-\infty}^{\infty} \frac{I_{TM}}{V_{TE}}(k_x, k_y, z) e^{-j(k_x x + k_y y)} dk_x dk_y \tag{A.8}$$

or, more synthetically,

$$\frac{A_z}{F_z}(\boldsymbol{\rho}, z) = \frac{1}{4\pi^2} \int_{-\infty}^{\infty} \int_{-\infty}^{\infty} \frac{I_{TM}}{V_{TE}}(\mathbf{k}_\rho, z) e^{-j\mathbf{k}_\rho \cdot \boldsymbol{\rho}} d\mathbf{k}_\rho \tag{A.9}$$

where $\mathbf{k}_\rho = k_x \hat{\mathbf{x}} + k_y \hat{\mathbf{y}}$ and $\boldsymbol{\rho} = x \hat{\mathbf{x}} + y \hat{\mathbf{y}}$.

Since the potentials A_z and F_z satisfy the homogenous wave equations (A.3), it follows that I_{TM} and V_{TE} satisfy the z -transmission-line equations

$$\begin{aligned}
(\nabla_t^2 + \partial_z^2) A_z + k^2 A_z &= 0 \xrightarrow{\text{Fourier T.}} \partial_z^2 I_{TM} + k_z^2 I_{TM} = 0 \\
(\nabla_t^2 + \partial_z^2) F_z + k^2 F_z &= 0 \xrightarrow{\text{Fourier T.}} \partial_z^2 V_{TE} + k_z^2 V_{TE} = 0.
\end{aligned} \tag{A.10}$$

In the last equation, we exploited the property $\nabla_t \xrightarrow{\text{Fourier T.}} -j\mathbf{k}_\rho$, which implies that $\nabla_t^2 \xrightarrow{\text{Fourier T.}} -k_\rho^2$, and we defined $k_z = \sqrt{k^2 - k_\rho^2}$ ($\Im\{k_z\} < 0$).

Introducing the Fourier spectra of the fields

$$\begin{bmatrix} \mathbf{E} \\ \mathbf{H} \end{bmatrix}(\boldsymbol{\rho}, z) = \frac{1}{4\pi^2} \int_{-\infty}^{\infty} \int_{-\infty}^{\infty} \begin{bmatrix} \tilde{\mathbf{E}} \\ \tilde{\mathbf{H}} \end{bmatrix}(\mathbf{k}_\rho, z) e^{-j\mathbf{k}_\rho \cdot \boldsymbol{\rho}} d\mathbf{k}_\rho \quad (\text{A.11})$$

we can rewrite Eqs. (A.5) and (A.7) in the spectral domain as follows:

$$\begin{aligned} \tilde{\mathbf{E}} &= -jk\zeta \left[\left(1 + \frac{1}{k^2} \partial_z^2 \right) I_{TM} \hat{\mathbf{z}} - j \frac{\mathbf{k}_\rho}{k^2} \partial_z I_{TM} \right] + j\mathbf{k}_\rho \times V_{TE} \hat{\mathbf{z}} \\ \tilde{\mathbf{H}} &= -j \frac{k}{\zeta} \left[\left(1 + \frac{1}{k^2} \partial_z^2 \right) V_{TE} \hat{\mathbf{z}} - j \frac{\mathbf{k}_\rho}{k^2} \partial_z V_{TE} \right] - j\mathbf{k}_\rho \times I_{TM} \hat{\mathbf{z}} \end{aligned} \quad (\text{A.12})$$

with

$$\begin{aligned} \tilde{\mathbf{E}}_{TM} &= -jk\zeta \left[\left(1 + \frac{1}{k^2} \partial_z^2 \right) I_{TM} \hat{\mathbf{z}} - j \frac{\mathbf{k}_\rho}{k^2} \partial_z I_{TM} \right] \\ \tilde{\mathbf{E}}_{TE} &= j\mathbf{k}_\rho \times V_{TE} \hat{\mathbf{z}} \\ \tilde{\mathbf{H}}_{TM} &= -j\mathbf{k}_\rho \times I_{TM} \hat{\mathbf{z}} \\ \tilde{\mathbf{H}}_{TE} &= -j \frac{k}{\zeta} \left[\left(1 + \frac{1}{k^2} \partial_z^2 \right) V_{TE} \hat{\mathbf{z}} - j \frac{\mathbf{k}_\rho}{k^2} \partial_z V_{TE} \right]. \end{aligned} \quad (\text{A.13})$$

The quantities I_{TM} and V_{TE} are solutions of the transmission-line equations (A.10). Thus, we can write

$$\begin{aligned} \tilde{\mathbf{E}}_{TM} &= j\zeta \frac{k_z}{k} I_{TM} \mathbf{k}_\rho - j\zeta \frac{k_\rho^2}{k} I_{TM} \hat{\mathbf{z}} \\ \tilde{\mathbf{E}}_{TE} &= j\mathbf{k}_\rho \times V_{TE} \hat{\mathbf{z}} \\ \tilde{\mathbf{H}}_{TM} &= -j\mathbf{k}_\rho \times I_{TM} \hat{\mathbf{z}} \\ \tilde{\mathbf{H}}_{TE} &= j \frac{1}{\zeta} \frac{k_z}{k} V_{TE} \mathbf{k}_\rho - j \frac{1}{\zeta} \frac{k_\rho^2}{k} V_{TE} \hat{\mathbf{z}} \end{aligned} \quad (\text{A.14})$$

where we used the equalities $\partial_z I_{TM} = -jk_z I_{TM}$ and $\partial_z V_{TE} = -jk_z V_{TE}$. These arise from the hypothesis that only one travelling progressive wave exists for both $z > 0$ and $z < 0$. We can define now the following quantities:

$$\begin{aligned} V_{TM} &= \zeta \frac{k_z}{k} I_{TM} \\ I_{TE} &= \frac{1}{\zeta} \frac{k_z}{k} V_{TE} \end{aligned} \quad (\text{A.15})$$

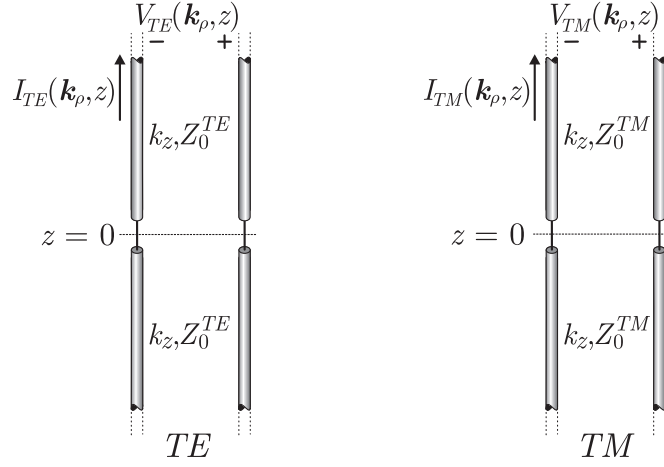


Figure A.1: Equivalent z -transmission lines pertaining to TE and TM modes for a source placed in the (x, y) -plane in free space.

so that (V_{TE}, I_{TE}) and (V_{TM}, I_{TM}) are the voltage and current solutions in two equivalent transmission lines along z (z -tx line) associated with TM and TE modes, respectively. These transmission lines are depicted in Fig. A.1 and their characteristic impedances are given by:

$$\begin{aligned} Z_0^{TM} &= \zeta \frac{k_z}{k} \\ Z_0^{TE} &= \zeta \frac{k}{k_z}. \end{aligned} \quad (\text{A.16})$$

The expressions of the spectral fields in Eqs. (A.14) become

$$\begin{aligned} \tilde{\mathbf{E}}_{TM} &= jV_{TM}\mathbf{k}_\rho - j\zeta \frac{k_\rho^2}{k} I_{TM}\hat{\mathbf{z}} \\ \tilde{\mathbf{E}}_{TE} &= j\mathbf{k}_\rho \times V_{TE}\hat{\mathbf{z}} \\ \tilde{\mathbf{H}}_{TM} &= -j\mathbf{k}_\rho \times I_{TM}\hat{\mathbf{z}} \\ \tilde{\mathbf{H}}_{TE} &= jI_{TE}\mathbf{k}_\rho - j\frac{1}{\zeta} \frac{k_\rho^2}{k} V_{TE}\hat{\mathbf{z}}. \end{aligned} \quad (\text{A.17})$$

Let us now introduce the unit vectors $\hat{\boldsymbol{\alpha}}$ and $\hat{\mathbf{k}}_\rho$, that are the spectral counterpart of the spatial unit vectors $\hat{\boldsymbol{\varphi}}$ and $\hat{\boldsymbol{\rho}}$, respectively, according to the cylindrical coordinate system in Fig. A.2:

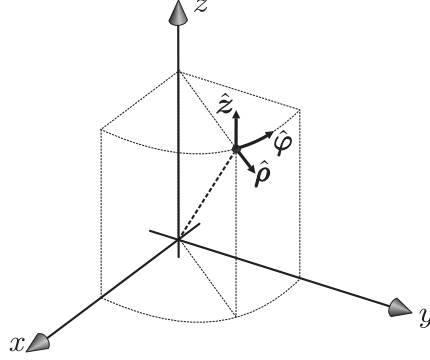


Figure A.2: Cylindrical right-hand coordinate system.

$$\begin{aligned}\hat{\mathbf{k}}_\rho &= \frac{\mathbf{k}_\rho}{k_\rho} = \frac{k_x \hat{\mathbf{x}} + k_y \hat{\mathbf{y}}}{\sqrt{k_x^2 + k_y^2}} \\ \hat{\boldsymbol{\alpha}} &= \hat{\mathbf{z}} \times \hat{\mathbf{k}}_\rho = \frac{k_x \hat{\mathbf{y}} - k_y \hat{\mathbf{x}}}{\sqrt{k_x^2 + k_y^2}}.\end{aligned}\tag{A.18}$$

With the above notation, Eqs. (A.17) can be written as

$$\begin{aligned}\tilde{\mathbf{E}}_{TM} &= j k_\rho V_{TM} \hat{\mathbf{k}}_\rho - j \zeta \frac{k_\rho^2}{k} I_{TM} \hat{\mathbf{z}} \\ \tilde{\mathbf{E}}_{TE} &= -j k_\rho V_{TE} \hat{\boldsymbol{\alpha}} \\ \tilde{\mathbf{H}}_{TM} &= j k_\rho I_{TM} \hat{\boldsymbol{\alpha}} \\ \tilde{\mathbf{H}}_{TE} &= j k_\rho I_{TE} \hat{\mathbf{k}}_\rho - j \frac{1}{\zeta} \frac{k_\rho^2}{k} V_{TE} \hat{\mathbf{z}}.\end{aligned}\tag{A.19}$$

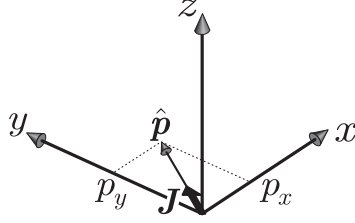
A.3 Spectral Green's Function for Electric Source

A.3.1 (x, y) -Oriented Electric Source

Let us assume that the source is an electric current localized at $z = 0$:

$$\mathbf{J}(x, y, 0) = \delta(x, y) \hat{\mathbf{p}}\tag{A.20}$$

where $\hat{\mathbf{p}} = p_x \hat{\mathbf{x}} + p_y \hat{\mathbf{y}}$ is a space independent unit vector that defines the orientation of the elementary dipole in the (x, y) -plane, as shown in Fig. A.3. The continuity of the tangential fields at the plane where the source is located leads to

Figure A.3: (x, y) -oriented electric source placed in the origin.

$$\hat{z} \times (\mathbf{H}(x, y, 0^+) - \mathbf{H}(x, y, 0^-)) = \delta(x, y) \hat{\mathbf{p}} \quad (\text{A.21})$$

$$\hat{z} \times (\mathbf{E}(x, y, 0^+) - \mathbf{E}(x, y, 0^-)) = 0. \quad (\text{A.22})$$

The tangential electric field is continuous everywhere, while the tangential magnetic field has a space impulsive discontinuity in the origin.

By using the Fourier representation of the δ -function:

$$\delta(x, y) = \frac{1}{4\pi^2} \int_{-\infty}^{\infty} \int_{-\infty}^{\infty} e^{-j(k_x x + k_y y)} dk_x dk_y \quad (\text{A.23})$$

we can write the continuity conditions for the tangential magnetic field in the spectral domain, projected onto the unit vectors $\hat{\boldsymbol{\alpha}}$ and $\hat{\mathbf{k}}_\rho$:

$$\begin{aligned} \hat{z} \times (\tilde{\mathbf{H}}_{TM}(\mathbf{k}_\rho, 0^+) - \tilde{\mathbf{H}}_{TM}(\mathbf{k}_\rho, 0^-)) \cdot \hat{\mathbf{k}}_\rho &= \hat{\mathbf{p}} \cdot \hat{\mathbf{k}}_\rho \\ \hat{z} \times (\tilde{\mathbf{H}}_{TE}(\mathbf{k}_\rho, 0^+) - \tilde{\mathbf{H}}_{TE}(\mathbf{k}_\rho, 0^-)) \cdot \hat{\boldsymbol{\alpha}} &= \hat{\mathbf{p}} \cdot \hat{\boldsymbol{\alpha}} \end{aligned} \quad (\text{A.24})$$

Using Eqs. (A.19), one can write

$$\begin{aligned} -jk_\rho (I_{TM}^J(\mathbf{k}_\rho, 0^+) - I_{TM}^J(\mathbf{k}_\rho, 0^-)) &= \hat{\mathbf{p}} \cdot \hat{\mathbf{k}}_\rho \\ jk_\rho (I_{TE}^J(\mathbf{k}_\rho, 0^+) - I_{TE}^J(\mathbf{k}_\rho, 0^-)) &= \hat{\mathbf{p}} \cdot \hat{\boldsymbol{\alpha}} \end{aligned} \quad (\text{A.25})$$

where the subscript J indicates that the source is an electric current. Equations (A.25) state that the spectral currents I_{TE}^J and I_{TM}^J exhibit a discontinuity in the origin equal to

$$\begin{aligned} I_{TM,g}^J &= \frac{\hat{\mathbf{p}} \cdot \hat{\mathbf{k}}_\rho}{-jk_\rho} \\ I_{TE,g}^J &= \frac{\hat{\mathbf{p}} \cdot \hat{\boldsymbol{\alpha}}}{jk_\rho}. \end{aligned} \quad (\text{A.26})$$

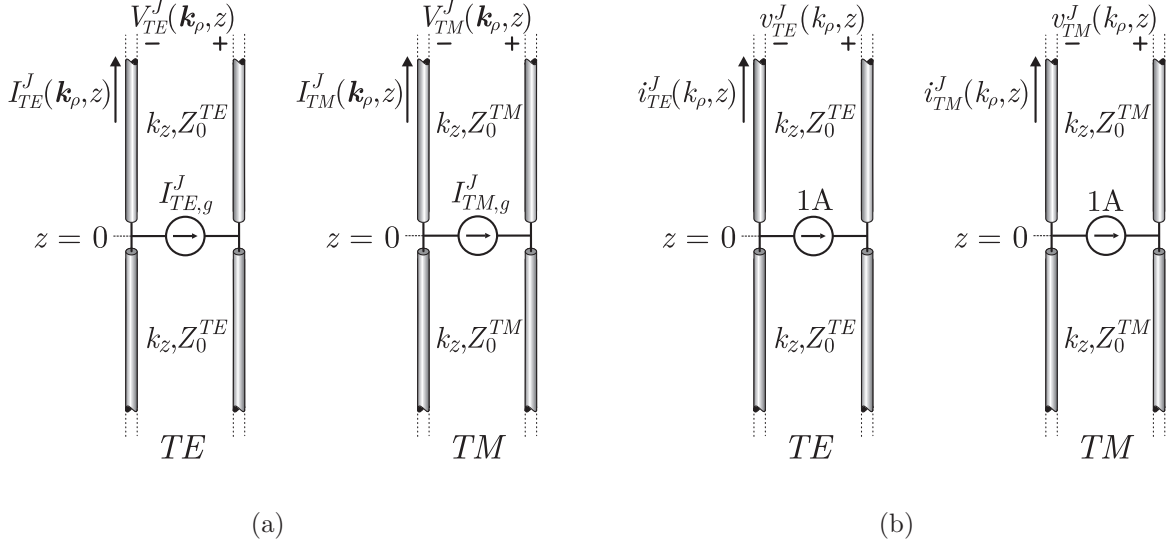


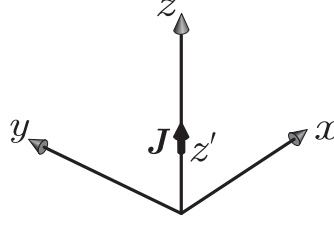
Figure A.4: Equivalent z -transmission lines pertaining to TE and TM modes for a dipole placed in the (x, y) -plane in free space: (a) not normalized and (b) normalized equivalent generators.

These generators are placed in parallel to the transmission lines as in Fig. A.4(a), due to the continuity of the voltages V_{TE}^J and V_{TM}^J in the origin (derived from the spectral version of Eq. (A.22)). The voltage and the current on the transmission line can be normalized by the amplitude of the generators to obtain equivalent transmission lines fed by unit generators (Fig. A.4(b)):

$$\begin{aligned}
 v_{TE}^J &= \frac{V_{TE}^J}{I_{TE,g}^J} = jk_\rho \frac{V_{TE}^J}{\hat{\mathbf{p}} \cdot \hat{\boldsymbol{\alpha}}} & i_{TE}^J &= \frac{I_{TE}^J}{I_{TE,g}^J} = jk_\rho \frac{I_{TE}^J}{\hat{\mathbf{p}} \cdot \hat{\boldsymbol{\alpha}}} \\
 v_{TM}^J &= \frac{V_{TM}^J}{I_{TM,g}^J} = -jk_\rho \frac{V_{TM}^J}{\hat{\mathbf{p}} \cdot \hat{\mathbf{k}}_\rho} & i_{TM}^J &= \frac{I_{TM}^J}{I_{TM,g}^J} = -jk_\rho \frac{I_{TM}^J}{\hat{\mathbf{p}} \cdot \hat{\mathbf{k}}_\rho}.
 \end{aligned} \tag{A.27}$$

By substituting (A.27) in (A.19), we obtain

$$\begin{aligned}
 \tilde{\mathbf{E}} &= \tilde{\mathbf{E}}_{TE} + \tilde{\mathbf{E}}_{TM} = \underbrace{\left(-\hat{\mathbf{k}}_\rho \hat{\mathbf{k}}_\rho v_{TM}^J - \hat{\boldsymbol{\alpha}} \hat{\boldsymbol{\alpha}} v_{TE}^J + \zeta \frac{k_\rho}{k} i_{TM}^J \hat{\mathbf{z}} \hat{\mathbf{k}}_\rho \right)}_{\underline{\underline{G^{EJ}(k_x, k_y, z)}}} \cdot \hat{\mathbf{p}} \\
 \tilde{\mathbf{H}} &= \tilde{\mathbf{H}}_{TE} + \tilde{\mathbf{H}}_{TM} = \underbrace{\left(-\hat{\boldsymbol{\alpha}} \hat{\mathbf{k}}_\rho i_{TM}^J + \hat{\mathbf{k}}_\rho \hat{\boldsymbol{\alpha}} i_{TE}^J - \frac{k_\rho}{\zeta k} v_{TE}^J \hat{\mathbf{z}} \hat{\boldsymbol{\alpha}} \right)}_{\underline{\underline{G^{HJ}(k_x, k_y, z)}}} \cdot \hat{\mathbf{p}}
 \end{aligned} \tag{A.28}$$

Figure A.5: z -oriented electric source placed at $z = z'$.

where we introduced the spectral domain dyadic Green's functions (GFs). By performing the dyadic products, the GFs can be written in explicit matrix form as follows:

$$\begin{aligned} \underline{\underline{G}}^{EJ}(k_x, k_y, z) &= \begin{bmatrix} G_{xx}^{EJ} & G_{xy}^{EJ} & G_{xz}^{EJ} \\ G_{yx}^{EJ} & G_{yy}^{EJ} & G_{yz}^{EJ} \\ G_{zx}^{EJ} & G_{zy}^{EJ} & G_{zz}^{EJ} \end{bmatrix} = \begin{bmatrix} -\frac{v_{TM}^J k_x^2 + v_{TE}^J k_y^2}{k_\rho^2} & \frac{(v_{TE}^J - v_{TM}^J) k_x k_y}{k_\rho^2} & 0 \\ \frac{(v_{TE}^J - v_{TM}^J) k_x k_y}{k_\rho^2} & -\frac{v_{TE}^J k_x^2 + v_{TM}^J k_y^2}{k_\rho^2} & 0 \\ \frac{\zeta k_x}{k} i_{TM}^J & \frac{\zeta k_y}{k} i_{TM}^J & 0 \end{bmatrix} \\ \underline{\underline{G}}^{HJ}(k_x, k_y, z) &= \begin{bmatrix} G_{xx}^{HJ} & G_{xy}^{HJ} & G_{xz}^{HJ} \\ G_{yx}^{HJ} & G_{yy}^{HJ} & G_{yz}^{HJ} \\ G_{zx}^{HJ} & G_{zy}^{HJ} & G_{zz}^{HJ} \end{bmatrix} = \begin{bmatrix} \frac{(i_{TM}^J - i_{TE}^J) k_x k_y}{k_\rho^2} & \frac{i_{TE}^J k_x^2 + i_{TM}^J k_y^2}{k_\rho^2} & 0 \\ -\frac{i_{TM}^J k_x^2 + i_{TE}^J k_y^2}{k_\rho^2} & \frac{(i_{TE}^J - i_{TM}^J) k_x k_y}{k_\rho^2} & 0 \\ \frac{k_y}{\zeta k} v_{TE}^J & -\frac{k_x}{\zeta k} v_{TE}^J & 0 \end{bmatrix}. \end{aligned} \quad (\text{A.29})$$

The expressions (A.29) are valid only for sources without any vertical component. The extension to sources oriented along z is given in next section.

A.3.2 z -Oriented Electric Source

When a vertical electric source is placed at $z = z'$ as shown in Fig. A.5, the potentials A_z and F_z satisfy the following equations:

$$\begin{aligned} \nabla^2 A_z + k^2 A_z &= -\delta(x, y, z - z') \\ \nabla^2 F_z + k^2 F_z &= 0 \end{aligned} \quad (\text{A.30})$$

or, in the spectral domain,

$$\begin{aligned} \partial_z^2 I_{TM}^{Jz} + k_z^2 I_{TM}^{Jz} &= -\delta(z - z') \\ \partial_z^2 V_{TE}^{Jz} + k_z^2 V_{TE}^{Jz} &= 0. \end{aligned} \quad (\text{A.31})$$

Using these expressions and defining $V_{TM}^{Jz} = j \frac{\zeta}{k} \partial_z I_{TM}^{Jz}$, $I_{TE}^{Jz} = j / \frac{1}{\zeta k} \partial_z V_{TE}^{Jz}$, the spectral fields in Eqs. (A.12) can be written as:

$$\begin{aligned}\tilde{\mathbf{E}} &= -j\frac{\zeta}{k}(k_\rho^2 I_{TM}^{Jz} - \delta(z - z'))\hat{\mathbf{z}} + jk_\rho V_{TM}^{Jz}\hat{\mathbf{k}}_\rho - jk_\rho V_{TE}^{Jz}\hat{\boldsymbol{\alpha}} \\ \tilde{\mathbf{H}} &= -j\frac{k_\rho^2}{k\zeta}V_{TE}^{Jz}\hat{\mathbf{z}} + jk_\rho I_{TE}^{Jz}\hat{\mathbf{k}}_\rho + jk_\rho I_{TM}^{Jz}\hat{\boldsymbol{\alpha}}.\end{aligned}\quad (\text{A.32})$$

Since vertical electric sources radiate only *TM* components, the spectral fields reduce to

$$\begin{aligned}\tilde{\mathbf{E}}_{TM} &= -j\frac{\zeta}{k}(k_\rho^2 I_{TM}^{Jz} - \delta(z - z'))\hat{\mathbf{z}} + jk_\rho V_{TM}^{Jz}\hat{\mathbf{k}}_\rho \\ \tilde{\mathbf{H}}_{TM} &= jk_\rho I_{TM}^{Jz}\hat{\boldsymbol{\alpha}}.\end{aligned}\quad (\text{A.33})$$

To impose the boundary conditions of the tangential electromagnetic field at the interface $z = z'$, we can replace the longitudinal electric source \mathbf{J} with an equivalent transverse magnetic source:

$$\mathbf{M}_e = \frac{1}{j\omega\varepsilon}\hat{\mathbf{z}} \times \nabla_t(\mathbf{J} \cdot \hat{\mathbf{z}}).\quad (\text{A.34})$$

Continuity conditions can be then imposed on the tangential components of the total electric and magnetic field as follows:

$$\hat{\mathbf{z}} \times (\mathbf{H}(x, y, z = z'^+) - \mathbf{H}(x, y, z = z'^-)) = 0 \quad (\text{A.35})$$

$$\hat{\mathbf{z}} \times (\mathbf{E}(x, y, z = z'^+) - \mathbf{E}(x, y, z = z'^-)) = -\mathbf{M}_e. \quad (\text{A.36})$$

In the spectral domain, using $(\omega\varepsilon)^{-1} = \zeta/k$ and $\nabla_t \xrightarrow{\text{Fourier T.}} -j\mathbf{k}_\rho$, one obtains the following expression for the equivalent magnetic source:

$$\tilde{\mathbf{M}}_e = \frac{-\zeta}{jk}j\hat{\mathbf{z}} \times \mathbf{k}_\rho \delta(z - z') = \frac{-\zeta k_\rho}{k}\delta(z - z')\hat{\boldsymbol{\alpha}}.\quad (\text{A.37})$$

The continuity is then expressed as follows:

$$jk_\rho \hat{\mathbf{z}} \times \hat{\boldsymbol{\alpha}} (I_{TM}^{Jz}(\mathbf{k}_\rho, z = z'^+) - I_{TM}^{Jz}(\mathbf{k}_\rho, z = z'^-)) = 0 \quad (\text{A.38})$$

$$\begin{aligned}jk_\rho \hat{\mathbf{z}} \times \hat{\mathbf{k}}_\rho (V_{TM}^{Jz}(\mathbf{k}_\rho, z = z'^+) - V_{TM}^{Jz}(\mathbf{k}_\rho, z = z'^-)) &= \frac{\zeta k_\rho}{k}\hat{\boldsymbol{\alpha}} \Rightarrow \\ (V_{TM}^{Jz}(\mathbf{k}_\rho, z = z'^+) - V_{TM}^{Jz}(\mathbf{k}_\rho, z = z'^-))\hat{\boldsymbol{\alpha}} &= -j\frac{\zeta}{k}\hat{\boldsymbol{\alpha}}.\end{aligned}\quad (\text{A.39})$$

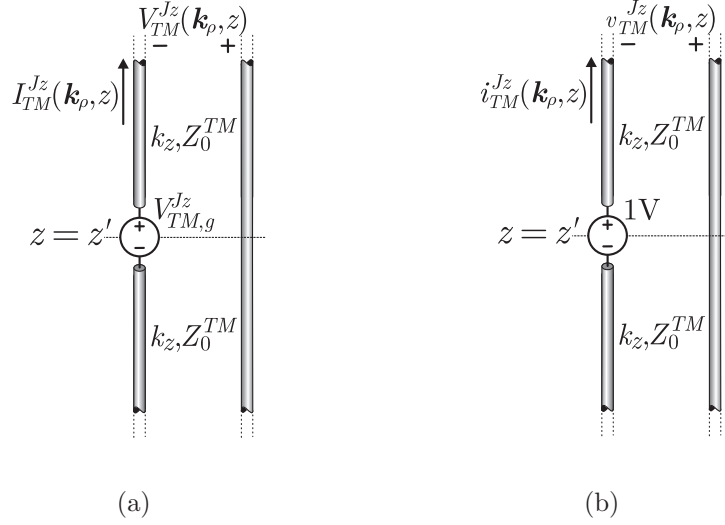


Figure A.6: Equivalent z -transmission lines for a dipole oriented along z in free space: (a) not normalized and (b) normalized equivalent generators.

Equation (A.39) states that there is a discontinuity of the voltage at $z = z'$. A voltage generator $V_{TM,g}^{Jz} = -j\frac{\zeta}{k}$ represents this discontinuity in the equivalent transmission line in Fig. A.6(a). The generator is in series with respect to the transmission line, since the current must be continuous, as clear from Eq. (A.38). Currents and voltages in the equivalent transmission line can be normalized as in Fig. A.6(b) to obtain a unit voltage generator: $i_{TM}^{Jz} = I_{TM}^{Jz}/V_{TM,g}^{Jz}$, $v_{TM}^{Jz} = V_{TM}^{Jz}/V_{TM,g}^{Jz}$.

With this normalization, Eqs. (A.33) become

$$\begin{aligned}
 \tilde{\mathbf{E}}_{TM} &= \underbrace{\left(-\frac{\zeta}{k} \left(k_\rho^2 \frac{\zeta}{k} i_{TM}^{Jz} - j\delta(z-z') \right) \hat{\mathbf{z}}\hat{\mathbf{z}} + \frac{\zeta k_\rho}{k} v_{TM}^{Jz} \hat{\mathbf{k}}_\rho \hat{\mathbf{z}} \right)}_{\underline{\underline{\mathbf{G}^{EJ}(k_x, k_y, z)}}} \cdot \hat{\mathbf{z}} \\
 \tilde{\mathbf{H}}_{TM} &= \underbrace{\left(\frac{\zeta k_\rho}{k} i_{TM}^{Jz} \hat{\boldsymbol{\alpha}} \hat{\mathbf{z}} \right)}_{\underline{\underline{\mathbf{G}^{HJ}(k_x, k_y, z)}}} \cdot \hat{\mathbf{z}}.
 \end{aligned} \tag{A.40}$$

In conclusion, the remaining element of the dyadic spectral Green's function, due to the electric sources along z can be written as

$$\underline{\underline{G}}^{EJ}(k_x, k_y, z) = \begin{bmatrix} 0 & 0 & \frac{\zeta k_x}{k} v_{TM}^{Jz} \\ 0 & 0 & \frac{\zeta k_y}{k} v_{TM}^{Jz} \\ 0 & 0 & -\frac{\zeta}{k} \left(\frac{\zeta k_\rho^2}{k} i_{TM}^{Jz} - j\delta(z-z') \right) \end{bmatrix} \quad (\text{A.41})$$

$$\underline{\underline{G}}^{HJ}(k_x, k_y, z) = \begin{bmatrix} 0 & 0 & -\frac{\zeta k_y}{k} i_{TM}^{Jz} \\ 0 & 0 & \frac{\zeta k_x}{k} i_{TM}^{Jz} \\ 0 & 0 & 0 \end{bmatrix}.$$

A.3.3 Dyadic Spectral GF of an Arbitrarily Oriented Electric Source

Equations (A.29) and (A.41) can be combined to have expressions that are valid in the general case of an arbitrary electric source that can be oriented along $\hat{\mathbf{x}}$, $\hat{\mathbf{y}}$ or $\hat{\mathbf{z}}$. The general dyadic GFs are then given by

$$\underline{\underline{G}}^{EJ}(k_x, k_y, z) = \begin{bmatrix} -\frac{v_{TM}^J k_x^2 + v_{TE}^J k_y^2}{k_\rho^2} & \frac{(v_{TE}^J - v_{TM}^J) k_x k_y}{k_\rho^2} & \frac{\zeta k_x}{k} v_{TM}^{Jz} \\ \frac{(v_{TE}^J - v_{TM}^J) k_x k_y}{k_\rho^2} & -\frac{v_{TE}^J k_x^2 + v_{TM}^J k_y^2}{k_\rho^2} & \frac{\zeta k_y}{k} v_{TM}^{Jz} \\ \frac{\zeta k_x}{k} i_{TM}^J & \frac{\zeta k_y}{k} i_{TM}^J & -\frac{\zeta}{k} \left(\frac{\zeta k_\rho^2}{k} i_{TM}^{Jz} - j\delta(z-z') \right) \end{bmatrix} \quad (\text{A.42})$$

$$\underline{\underline{G}}^{HJ}(k_x, k_y, z) = \begin{bmatrix} \frac{(i_{TM}^J - i_{TE}^J) k_x k_y}{k_\rho^2} & \frac{i_{TE}^J k_x^2 + i_{TM}^J k_y^2}{k_\rho^2} & -\frac{\zeta k_y}{k} i_{TM}^{Jz} \\ -\frac{i_{TM}^J k_x^2 + i_{TE}^J k_y^2}{k_\rho^2} & \frac{(i_{TE}^J - i_{TM}^J) k_x k_y}{k_\rho^2} & \frac{\zeta k_x}{k} i_{TM}^{Jz} \\ \frac{k_y}{\zeta k} v_{TE}^J & -\frac{k_x}{\zeta k} v_{TE}^J & 0 \end{bmatrix}. \quad (\text{A.43})$$

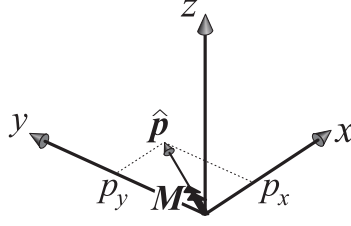
A.4 Spectral Green's Function for Magnetic Source

The expressions for the spectral GFs associated with a generic magnetic source can be derived following a procedure similar to the one that led to Eqs. (A.42) and (A.43).

A.4.1 (x, y) -Oriented Magnetic Source

Let us assume that the source is an impulsive magnetic current placed at $z = 0$ and oriented along the unit vector $\hat{\mathbf{p}} = p_x \hat{\mathbf{x}} + p_y \hat{\mathbf{y}}$ in the (x, y) -plane, as in Fig. A.7:

$$\mathbf{M}(x, y, 0) = \delta(x, y) \hat{\mathbf{p}}. \quad (\text{A.44})$$

Figure A.7: (x, y) -oriented magnetic source placed in the origin.

The tangential magnetic field is continuous at the plane where the source is located, while the tangential electric field presents a discontinuity in the origin:

$$\hat{z} \times (\mathbf{H}(x, y, 0^+) - \mathbf{H}(x, y, 0^-)) = 0 \quad (\text{A.45})$$

$$\hat{z} \times (\mathbf{E}(x, y, 0^+) - \mathbf{E}(x, y, 0^-)) = -\delta(x, y)\hat{\mathbf{p}}. \quad (\text{A.46})$$

The continuity of the electric field in Eq. (A.46) can be also expressed in the spectral domain and projected onto the unit vectors $\hat{\boldsymbol{\alpha}}$ and $\hat{\mathbf{k}}_\rho$:

$$\begin{aligned} \hat{z} \times \left(\tilde{\mathbf{E}}_{TE}(\mathbf{k}_\rho, 0^+) - \tilde{\mathbf{E}}_{TE}(\mathbf{k}_\rho, 0^-) \right) \cdot \hat{\mathbf{k}}_\rho &= -\hat{\mathbf{p}} \cdot \hat{\mathbf{k}}_\rho \\ \hat{z} \times \left(\tilde{\mathbf{E}}_{TM}(\mathbf{k}_\rho, 0^+) - \tilde{\mathbf{E}}_{TM}(\mathbf{k}_\rho, 0^-) \right) \cdot \hat{\boldsymbol{\alpha}} &= -\hat{\mathbf{p}} \cdot \hat{\boldsymbol{\alpha}}. \end{aligned} \quad (\text{A.47})$$

By substituting the spectral fields with their explicit expression in (A.19), we can write

$$\begin{aligned} jk_\rho (V_{TE}^M(\mathbf{k}_\rho, 0^+) - V_{TE}^M(\mathbf{k}_\rho, 0^-)) &= -\hat{\mathbf{p}} \cdot \hat{\mathbf{k}}_\rho \\ jk_\rho (V_{TM}^M(\mathbf{k}_\rho, 0^+) - V_{TM}^M(\mathbf{k}_\rho, 0^-)) &= -\hat{\mathbf{p}} \cdot \hat{\boldsymbol{\alpha}}. \end{aligned} \quad (\text{A.48})$$

where the subscript M indicates that the source is a magnetic current. Thus, the spectral voltages V_{TE}^M and V_{TM}^M exhibit in the origin a discontinuity represented by the following generators:

$$\begin{aligned} V_{TE,g}^M &= -\frac{\hat{\mathbf{p}} \cdot \hat{\mathbf{k}}_\rho}{jk_\rho} \\ V_{TM,g}^M &= -\frac{\hat{\mathbf{p}} \cdot \hat{\boldsymbol{\alpha}}}{jk_\rho}. \end{aligned} \quad (\text{A.49})$$

The generators are placed in series to the transmission lines as in Fig. A.8(a) to satisfy the continuity of the currents I_{TE}^M and I_{TM}^M in the origin (derived from the spectral version of

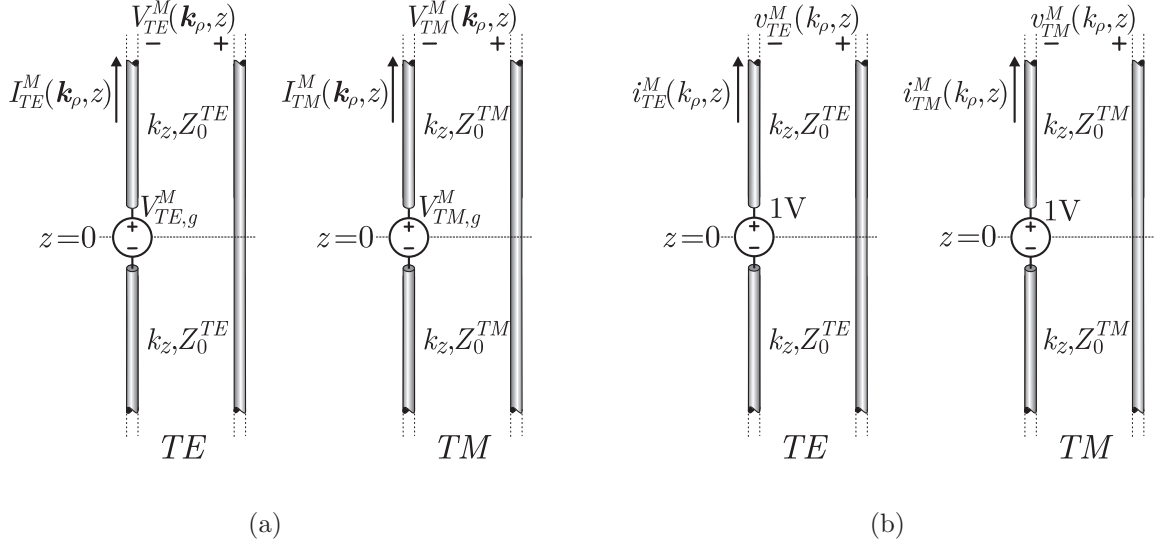


Figure A.8: Equivalent z -transmission lines pertaining to TE and TM modes for a magnetic dipole placed in the (x, y) -plane in free space: (a) not normalized and (b) normalized equivalent generators.

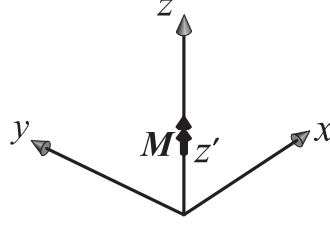
Eq. (A.45)). Normalizing the voltages and the currents by the amplitude of the generators, one obtains equivalent transmission lines fed by unit generators (Fig. A.8(b)):

$$\begin{aligned}
 v_{TM}^M &= \frac{V_{TM}^M}{V_{TM,g}^M} = -jk_\rho \frac{V_{TM}^M}{\hat{\mathbf{p}} \cdot \hat{\boldsymbol{\alpha}}} & i_{TM}^M &= \frac{I_{TM}^M}{V_{TM,g}^M} = -jk_\rho \frac{I_{TM}^M}{\hat{\mathbf{p}} \cdot \hat{\boldsymbol{\alpha}}} \\
 v_{TE}^M &= \frac{V_{TE}^M}{V_{TE,g}^M} = -jk_\rho \frac{V_{TE}^M}{\hat{\mathbf{p}} \cdot \hat{\mathbf{k}}_\rho} & i_{TE}^M &= \frac{I_{TE}^M}{V_{TE,g}^M} = -jk_\rho \frac{I_{TE}^M}{\hat{\mathbf{p}} \cdot \hat{\mathbf{k}}_\rho}.
 \end{aligned} \tag{A.50}$$

By substituting (A.50) in (A.19), we obtain:

$$\begin{aligned}
 \tilde{\mathbf{E}} &= \tilde{\mathbf{E}}_{TE} + \tilde{\mathbf{E}}_{TM} = \underbrace{\left(-\hat{\mathbf{k}}_\rho \hat{\boldsymbol{\alpha}} v_{TM}^M + \hat{\boldsymbol{\alpha}} \hat{\mathbf{k}}_\rho v_{TE}^M + \zeta \frac{k_\rho}{k} i_{TM}^M \hat{\mathbf{z}} \hat{\boldsymbol{\alpha}} \right)}_{\underline{\underline{\mathbf{G}}^{EM}(k_x, k_y, z)}} \cdot \hat{\mathbf{p}} \\
 \tilde{\mathbf{H}} &= \tilde{\mathbf{H}}_{TE} + \tilde{\mathbf{H}}_{TM} = \underbrace{\left(-\hat{\boldsymbol{\alpha}} \hat{\boldsymbol{\alpha}} i_{TM}^M - \hat{\mathbf{k}}_\rho \hat{\mathbf{k}}_\rho i_{TE}^M + \frac{k_\rho}{\zeta k} v_{TE}^M \hat{\mathbf{z}} \hat{\mathbf{k}}_\rho \right)}_{\underline{\underline{\mathbf{G}}^{HM}(k_x, k_y, z)}} \cdot \hat{\mathbf{p}}
 \end{aligned} \tag{A.51}$$

By performing the dyadic products, the explicit matrix from of the GF can be written as

Figure A.9: z -oriented magnetic source placed at $z = z'$.

$$\begin{aligned}
 \underline{\underline{G}}^{EM}(k_x, k_y, z) &= \begin{bmatrix} G_{xx}^{EM} & G_{xy}^{EM} & G_{xz}^{EM} \\ G_{yx}^{EM} & G_{yy}^{EM} & G_{yz}^{EM} \\ G_{zx}^{EM} & G_{zy}^{EM} & G_{zz}^{EM} \end{bmatrix} = \begin{bmatrix} \frac{(v_{TM}^M - v_{TE}^M)k_x k_y}{k_\rho^2} & -\frac{v_{TM}^M k_x^2 + v_{TE}^M k_y^2}{k_\rho^2} & 0 \\ \frac{v_{TE}^M k_x^2 + v_{TM}^M k_y^2}{k_\rho^2} & \frac{(v_{TE}^M - v_{TM}^M)k_x k_y}{k_\rho^2} & 0 \\ -\frac{\zeta k_y}{k} i_{TM}^M & \frac{\zeta k_x}{k} i_{TM}^M & 0 \end{bmatrix} \\
 \underline{\underline{G}}^{HM}(k_x, k_y, z) &= \begin{bmatrix} G_{xx}^{HM} & G_{xy}^{HM} & G_{xz}^{HM} \\ G_{yx}^{HM} & G_{yy}^{HM} & G_{yz}^{HM} \\ G_{zx}^{HM} & G_{zy}^{HM} & G_{zz}^{HM} \end{bmatrix} = \begin{bmatrix} -\frac{i_{TE}^M k_x^2 + i_{TM}^M k_y^2}{k_\rho^2} & \frac{(i_{TM}^M - i_{TE}^M)k_x k_y}{k_\rho^2} & 0 \\ \frac{(i_{TM}^M - i_{TE}^M)k_x k_y}{k_\rho^2} & -\frac{i_{TM}^M k_x^2 + i_{TE}^M k_y^2}{k_\rho^2} & 0 \\ \frac{k_x}{\zeta k} v_{TE}^M & \frac{k_y}{\zeta k} v_{TE}^M & 0 \end{bmatrix}. \tag{A.52}
 \end{aligned}$$

A.4.2 z -Oriented Magnetic Source

When a vertical magnetic source is located at $z = z'$, as in Fig. A.9, the potentials are solutions of

$$\begin{aligned}
 \nabla^2 A_z + k^2 A_z &= 0 \\
 \nabla^2 F_z + k^2 F_z &= -\delta(x, y, z - z'). \tag{A.53}
 \end{aligned}$$

In the spectral domain Eq. (A.53) can be written as

$$\begin{aligned}
 \partial_z^2 I_{TM}^{Mz} + k_z^2 I_{TM}^{Mz} &= 0 \\
 \partial_z^2 V_{TE}^{Mz} + k_z^2 V_{TE}^{Mz} &= -\delta(z - z'). \tag{A.54}
 \end{aligned}$$

Using Eq. (A.54), and noting that vertical magnetic sources radiate only TE components, the spectral electric and magnetic fields in Eq. (A.12) can be expressed as follows:

$$\begin{aligned}
 \tilde{\mathbf{E}} &= -jk_\rho V_{TE}^{Mz} \hat{\boldsymbol{\alpha}} \\
 \tilde{\mathbf{H}} &= -\frac{1}{k\zeta} (jk_\rho^2 V_{TE}^{Mz} - j\delta(z - z')) \hat{\mathbf{z}} - \frac{k_\rho}{k\zeta} \partial_z V_{TE}^{Mz} \hat{\mathbf{k}}_\rho. \tag{A.55}
 \end{aligned}$$

Defining $I_{TE}^{Mz} = j \frac{1}{k\zeta} \partial_z V_{TE}^{Mz}$, we can write

$$\begin{aligned}\tilde{\mathbf{E}} &= -jk_\rho V_{TE}^{Mz} \hat{\boldsymbol{\alpha}} \\ \tilde{\mathbf{H}} &= -\frac{1}{k\zeta} (jk_\rho^2 V_{TE}^{Mz} - j\delta(z-z')) \hat{\mathbf{z}} + jk_\rho I_{TE}^{Mz} \hat{\mathbf{k}}_\rho.\end{aligned}\quad (\text{A.56})$$

To impose boundary conditions on the tangential electromagnetic field at the interface $z = z'$, we can replace the longitudinal source with an equivalent transverse electric source

$$\mathbf{J}_e = -\frac{1}{j\omega\mu} \hat{\mathbf{z}} \times \nabla_t (\mathbf{M} \cdot \hat{\mathbf{z}}) \quad (\text{A.57})$$

or, in the spectral domain,

$$\tilde{\mathbf{J}}_e = \frac{k_\rho \delta(z-z')}{k\zeta} \hat{\boldsymbol{\alpha}}. \quad (\text{A.58})$$

The continuity of the fields can be imposed in the spectral domain as follows:

$$-jk_\rho \hat{\mathbf{z}} \times \hat{\boldsymbol{\alpha}} (V_{TE}^{Mz}(k_x, k_y, z = z'^+) - V_{TE}^{Mz}(k_x, k_y, z = z'^-)) = 0 \quad (\text{A.59})$$

$$\begin{aligned}jk_\rho \hat{\mathbf{z}} \times \hat{\mathbf{k}}_\rho (I_{TE}^{Mz}(k_x, k_y, z = z'^+) - I_{TE}^{Mz}(k_x, k_y, z = z'^-)) &= \frac{k_\rho}{k\zeta} \hat{\boldsymbol{\alpha}} \Rightarrow \\ (I_{TE}^{Mz}(k_x, k_y, z = z'^+) - I_{TE}^{Mz}(k_x, k_y, z = z'^-)) \hat{\boldsymbol{\alpha}} &= -j \frac{1}{k\zeta} \hat{\boldsymbol{\alpha}}.\end{aligned}\quad (\text{A.60})$$

The discontinuity is represented by a current generator $I_{TE,g}^{Mz} = \frac{-j}{k\zeta}$, which is in parallel with respect to the transmission line in Fig. A.10(a), to satisfy the continuity of the voltage in Eq. (A.59). Currents and voltages can be normalized as in Fig. A.10(b) to obtain a unit current generator: $i_{TE}^{Mz} = I_{TE}^{Mz} / I_{TE,g}^{Mz}$, $v_{TE}^{Mz} = V_{TE}^{Mz} / I_{TE,g}^{Mz}$.

With this normalization, Eqs. (A.56) become

$$\begin{aligned}\tilde{\mathbf{E}}_{TE} &= \underbrace{\left(-\frac{k_\rho}{k\zeta} v_{TE}^{Mz} \hat{\boldsymbol{\alpha}} \hat{\mathbf{z}} \right)}_{\underline{\underline{\mathbf{G}^{EM}(k_x, k_y, z)}}} \cdot \hat{\mathbf{z}} \\ \tilde{\mathbf{H}}_{TE} &= \underbrace{\left(-\frac{1}{k\zeta} \left(\frac{k_\rho^2}{k\zeta} v_{TE}^{Mz} - j\delta(z-z') \right) \hat{\mathbf{z}} \hat{\mathbf{z}} + \frac{k_\rho}{k\zeta} i_{TE}^{Mz} \hat{\mathbf{k}}_\rho \hat{\mathbf{z}} \right)}_{\underline{\underline{\mathbf{G}^{HM}(k_x, k_y, z)}}} \cdot \hat{\mathbf{z}}.\end{aligned}\quad (\text{A.61})$$

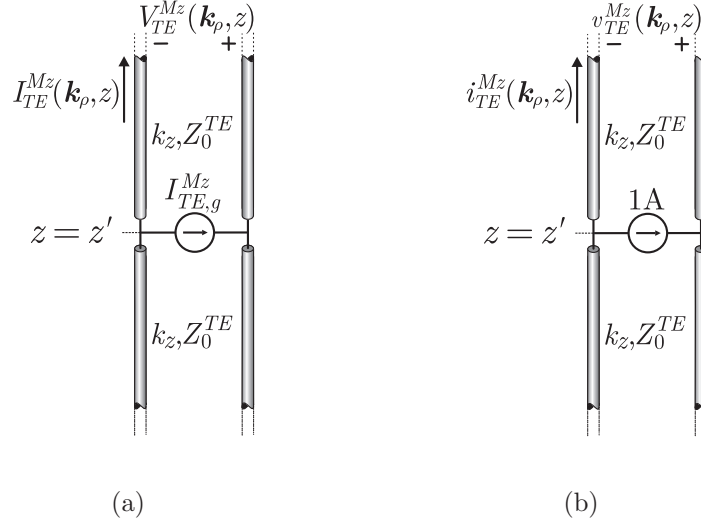


Figure A.10: Equivalent z -transmission lines pertaining to TE and TM modes for a magnetic source oriented along z in free space: (a) not normalized and (b) normalized equivalent generators.

In conclusion, the spectral dyadic Green's function for a magnetic sources along z can be written as

$$\begin{aligned} \underline{\underline{G}}^{EM}(k_x, k_y, z) &= \begin{bmatrix} 0 & 0 & \frac{k_y}{k\zeta} v_{TE}^{Mz} \\ 0 & 0 & -\frac{k_x}{k\zeta} v_{TE}^{Mz} \\ 0 & 0 & 0 \end{bmatrix} \\ \underline{\underline{G}}^{HM}(k_x, k_y, z) &= \begin{bmatrix} 0 & 0 & \frac{k_x}{k\zeta} i_{TE}^{Mz} \\ 0 & 0 & \frac{k_y}{k\zeta} i_{TE}^{Mz} \\ 0 & 0 & -\frac{1}{k\zeta} \left(\frac{k^2}{k\zeta} v_{TE}^{Mz} - j\delta(z-z') \right) \end{bmatrix}. \end{aligned} \quad (\text{A.62})$$

A.4.3 Dyadic Spectral GF of an Arbitrarily Oriented Magnetic Source

Equations (A.52) and (A.62) can be combined to have expressions that are valid in the general case of an arbitrary magnetic source. The general dyadic GFs are then given by

$$\underline{\underline{G}}^{EM}(k_x, k_y, z) = \begin{bmatrix} \frac{(v_{TM}^M - v_{TE}^M)k_x k_y}{k_\rho^2} & -\frac{v_{TM}^M k_x^2 + v_{TE}^M k_y^2}{k_\rho^2} & \frac{k_y}{k\zeta} v_{TE}^{Mz} \\ \frac{v_{TE}^M k_x^2 + v_{TM}^M k_y^2}{k_\rho^2} & \frac{(v_{TE}^M - v_{TM}^M)k_x k_y}{k_\rho^2} & -\frac{k_x}{k\zeta} v_{TE}^{Mz} \\ -\frac{\zeta k_y}{k} i_{TM}^M & \frac{\zeta k_x}{k} i_{TM}^M & 0 \end{bmatrix} \quad (\text{A.63})$$

$$\underline{\underline{G}}^{HM}(k_x, k_y, z) = \begin{bmatrix} -\frac{i_{TE}^M k_x^2 + i_{TM}^M k_y^2}{k_\rho^2} & \frac{(i_{TM}^M - i_{TE}^M) k_x k_y}{k_\rho^2} & \frac{k_x}{k\zeta} i_{TE}^{Mz} \\ \frac{(i_{TM}^M - i_{TE}^M) k_x k_y}{k_\rho^2} & -\frac{i_{TM}^M k_x^2 + i_{TE}^M k_y^2}{k_\rho^2} & \frac{k_y}{k\zeta} i_{TE}^{Mz} \\ \frac{k_x}{\zeta k} v_{TE}^M & \frac{k_y}{\zeta k} v_{TE}^M & -\frac{1}{k\zeta} \left(\frac{k_\rho^2}{k\zeta} v_{TE}^{Mz} - j\delta(z - z') \right) \end{bmatrix}. \quad (\text{A.64})$$

A.5 Evaluation of G_{xx}^{EJ} for a Dipole in Free Space and with Backing Reflector

For the theoretical formulation of connected array of dipoles, it is useful to evaluate the xx component of the dyadic electric Green's function due to an electric source in two particular cases of interest: delta source in free space and in the presence of a backing reflector.

A.5.1 Free Space

The generic expression of the term G_{xx} from the dyadic GF in Eq. (A.42) was given by

$$G_{xx}(k_x, k_y, z, z') = -\frac{k_x^2 v_{TM}^J(\mathbf{k}_\rho, z) + k_y^2 v_{TE}^J(\mathbf{k}_\rho, z)}{k_\rho^2}. \quad (\text{A.65})$$

In the case of free space, the voltage and current in the transmission line in Fig. A.11(a) are given by

$$\begin{aligned} v_{TM}^J(\mathbf{k}_\rho, z) &= \frac{Z_0^{TM}(\mathbf{k}_\rho)}{2} e^{-jk_z|z|} \\ v_{TE}^J(\mathbf{k}_\rho, z) &= \frac{Z_0^{TE}(\mathbf{k}_\rho)}{2} e^{-jk_z|z|}. \end{aligned} \quad (\text{A.66})$$

By substituting (A.16) and (A.66) in (A.65) we obtain, after few algebraic steps,

$$G_{xx}^{fs}(k_x, k_y, z, z' = 0) = -\frac{\zeta_0}{2k_0} \frac{k_0^2 - k_x^2}{\sqrt{k_0^2 - k_x^2 - k_y^2}} e^{-jk_z|z|}. \quad (\text{A.67})$$

A.5.2 Backing Reflector

If the source is located at a distance h from a metallic ground plane, the voltage and current on the equivalent transmission line change accordingly as in Fig. A.11(b):

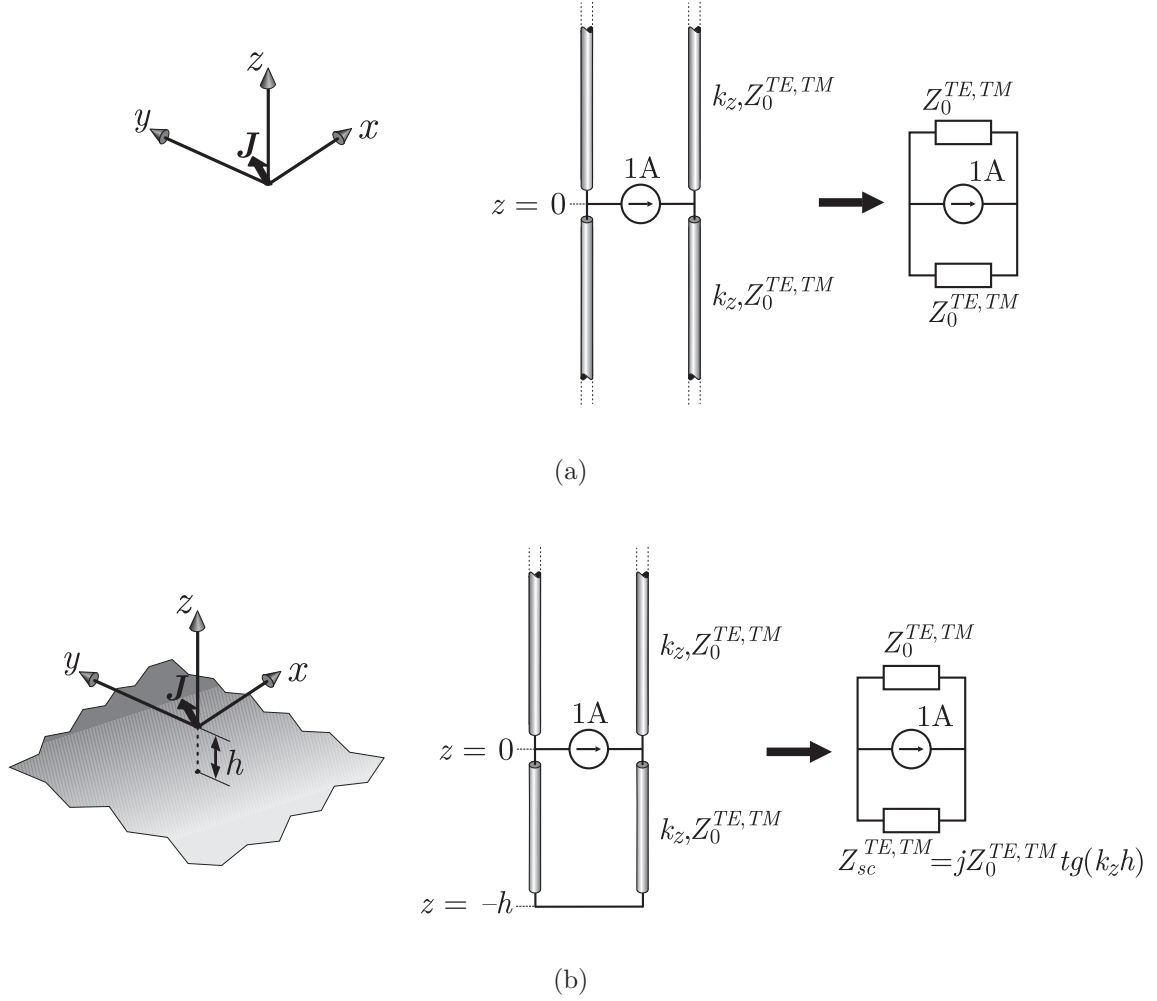


Figure A.11: Equivalent z -transmission lines for a dipole orthogonal to z (a) in free space and (b) with a backing reflector.

$$v_{TM}^J(\mathbf{k}_\rho, z) = \frac{Z_0^{TM}(\mathbf{k}_\rho) Z_{sc}^{TM}(\mathbf{k}_\rho)}{Z_0^{TM}(\mathbf{k}_\rho) + Z_{sc}^{TM}(\mathbf{k}_\rho)} e^{-jk_z z} = \frac{j Z_0^{TM}(\mathbf{k}_\rho) \tan(k_z h)}{1 + j \tan(k_z h)} e^{-jk_z z}, \text{ for } z > 0 \quad (\text{A.68})$$

and analogously

$$v_{TE}^J(\mathbf{k}_\rho, z) = \frac{j Z_0^{TE}(\mathbf{k}_\rho) \tan(k_z h)}{1 + j \tan(k_z h)} e^{-jk_z z}, \text{ for } z > 0. \quad (\text{A.69})$$

The substitution of (A.16) and (A.69) in the general expression of the scalar GF, after some algebra, leads to

$$G_{xx}^{br}(k_x, k_y, z, z' = 0) = -\frac{\zeta_0}{k_0} \frac{k_0^2 - k_x^2}{\sqrt{k_0^2 - k_x^2 - k_y^2}} \frac{e^{-jk_z z}}{1 - j \cot(k_z h)}. \quad (\text{A.70})$$

Noting that

$$\begin{aligned} 1 - j \cot(k_z h) &= 1 - j \frac{\cos(k_z h)}{\sin(k_z h)} = 1 - j \frac{\frac{e^{jk_z h} + e^{-jk_z h}}{2}}{\frac{e^{jk_z h} - e^{-jk_z h}}{2j}} = \\ &= 1 + \frac{e^{jk_z h} + e^{-jk_z h}}{e^{jk_z h} - e^{-jk_z h}} = \frac{2e^{jk_z h}}{e^{jk_z h} - e^{-jk_z h}} = \frac{2}{1 - e^{-j2k_z h}} \end{aligned} \quad (\text{A.71})$$

we can express the (A.70) also as

$$G_{xx}^{br}(k_x, k_y, z, z' = 0) = -\frac{\zeta_0}{2k_0} \frac{k_0^2 - k_x^2}{\sqrt{k_0^2 - k_x^2 - k_y^2}} (1 - e^{-j2k_z h}) e^{-jk_z z}. \quad (\text{A.72})$$

Appendix B

Radiation Patterns from Connected Arrays

This appendix presents the derivation of the far-field radiation pattern from a connected array of dipoles backed by a ground plane. Two approaches will be used: a windowing approach, which is based on the analysis of a single periodic cell in infinite array environment; a finite array formulation, which is more accurate because it also holds for small arrays. The far fields can be easily expressed from the spectral current distribution, which is known in closed form for the considered geometry, as shown in Chapter 2.

B.1 Plane-Wave Spectrum Approximation of the Far Field

If one is only interested in the far-field radiation patterns, a simple windowing approach in both x and y directions can be used to evaluate the patterns analytically. It is known that the electric and magnetic fields can be obtained from the vector potentials by means of straightforward derivatives. Hence, the starting point is the derivation of the magnetic vector potential \mathbf{A} , which is oriented along the dipoles depicted in Fig. 2.6 ($\mathbf{A} = A_x \hat{\mathbf{x}}$). The field radiated by a connected array of dipoles backed by a ground plane is equivalent to the one radiated by the dipole array and its image. Thus, from its definition, the potential in any point \mathbf{r} can be expressed as

$$A_x(\mathbf{r}) = \frac{\mu}{4\pi} \int_{\text{Array+Image}} \frac{e^{-jk_0|\mathbf{r}-\mathbf{r}'|}}{|\mathbf{r}-\mathbf{r}'|} j_x(\mathbf{r}') d\mathbf{r}' \quad (\text{B.1})$$

where \mathbf{r}' is any point on the dipoles or their images with respect to the ground plane, and k_0 represents the propagation constant of the free space. From the image theorem, it is known that the integration in Eq. (B.1) is the sum of the integration associated with two planar current distributions located in $z = 0$ and $z = -2h_d$ and with opposite signs:

$$A_x(\mathbf{r}) = A_x^{dip}(\mathbf{r}) + A_x^{im}(\mathbf{r}) = \frac{\mu}{4\pi} \int_{Array} \frac{e^{-jk_0|\mathbf{r}-\mathbf{r}'|}}{|\mathbf{r}-\mathbf{r}'|} j_x^{dip}(\mathbf{r}') d\mathbf{r}' + \frac{\mu}{4\pi} \int_{Image} \frac{e^{-jk_0|\mathbf{r}-\mathbf{r}'|}}{|\mathbf{r}-\mathbf{r}'|} j_x^{im}(\mathbf{r}') d\mathbf{r}' \quad (\text{B.2})$$

with $j_x^{im}(x', y', z' = -2h_d) = -j_x^{dip}(x', y', z' = 0)$. Each of the two integrals can be transformed in the spectral domain and evaluated asymptotically. Using the identity

$$\frac{e^{-jk_0|\mathbf{r}-\mathbf{r}'|}}{4\pi|\mathbf{r}-\mathbf{r}'|} = \frac{1}{8\pi^2 j} \int_{-\infty}^{\infty} \int_{-\infty}^{\infty} \frac{e^{-jk_x x - jk_y y - jk_z |z-z'|}}{k_z} dk_x dk_y \quad (\text{B.3})$$

where $k_z = \sqrt{k_0^2 - k_x^2 - k_y^2}$, we can write, for $z > 0$,

$$A_x(\mathbf{r}) = \frac{\mu}{8\pi^2 j} \int_{-\infty}^{\infty} \int_{-\infty}^{\infty} \frac{e^{-jk_x x - jk_y y - jk_z z}}{k_z} J_x(k_x, k_y) dk_x dk_y - \frac{\mu}{8\pi^2 j} \int_{-\infty}^{\infty} \int_{-\infty}^{\infty} \frac{e^{-jk_x x - jk_y y - jk_z (z+2h_d)}}{k_z} J_x(k_x, k_y) dk_x dk_y. \quad (\text{B.4})$$

The function J_x is the Fourier Transform of the electrical current on any of the two current sheets (plane of the dipoles and image plane). To perform asymptotically the integral in Eq. (B.4), it is sufficient to observe that the electric current spectra are slowly varying functions of k_x and k_y in the surrounding of the saddle point ($k_{xs} = k_0 \sin \theta \cos \varphi$, $k_{ys} = k_0 \sin \theta \sin \varphi$, $k_{zs} = k_0 \cos \theta$), where θ and φ are defined with respect to x , y and $|z - z'|$. Accordingly, one can approximate the integral in Eq. (B.4) as:

$$A_x(\mathbf{r}) \approx J_x(k_0 \sin \theta \cos \varphi, k_0 \sin \theta \sin \varphi) \frac{\mu e^{-jk_0 r}}{4\pi r} (1 - e^{-jk_0 2h_d \cos \theta}). \quad (\text{B.5})$$

B.2 Radiation Pattern from a Finite Connected Array

Considering a finite array of dipoles phased along y , under the hypothesis of spatial functional separability, the electric current can be expressed as

$$j(x', y') = \sum_{n_y=-N_y/2}^{N_y/2} i_{n_y}(x') j_t(y' - n_y d_y) \quad (\text{B.6})$$

where the transverse y -dependence is chosen to satisfy the edge singularity condition as in Eq. (2.3).

If the different dipole elements are excited with uniform amplitude and progressive phase shift, and the array is large enough, one can in first approximation assume the all the dipoles present the same amplitude current distribution; that is, the electric current on different dipoles are related by $i_{n_y}(x) = i_{n_y=0}(x) e^{-jk_{y0} n_y d_y}$, where $k_{y0} = k_0 \sin\theta \sin\varphi$ is the transverse excitation law when the array is scanning toward (θ, φ) :

$$j(x', y') \approx \sum_{n_y=-N_y/2}^{N_y/2} i(x') e^{-jk_{y0} n_y d_y} j_t(y' - n_y d_y). \quad (\text{B.7})$$

$i(x')$ represents the current distribution on the zeroth dipole and can be expressed as

$$i(x) = \frac{1}{2\pi} \int_{-\infty}^{\infty} \frac{V_e(k_x)}{D_\infty(k_x)} e^{-jk_x x} dk_x \quad (\text{B.8})$$

where $D_\infty(k_x)$ was defined in Eq. (2.31) and Eq. (A.72). In the following we will assume that the length of the dipoles is infinite while the number of feeding points in each dipoles are finite. The numerator $V_e(k_x)$ represents the Fourier Transform of the excitation, which, when one assumes a finite train of δ -gap generators, becomes

$$V_e(k_x) = V_0 \text{sinc} \left(\frac{k_x \delta_d}{2} \right) \sum_{n_x=-N_x/2}^{N_x/2} e^{j(k_x - k_{x0}) n_x d_x} \quad (\text{B.9})$$

B.2.1 Longitudinal Windowing Approximation

The spatial electric current $i(x)$ and consequently its spectrum $I(k_x)$ can be evaluated according to two different levels of approximation. The strongest approximation is the one which is routinely considered by commercial simplified software tools as Ansoft HFSS [41]: the infinite array approximation, followed by the windowing. It consists of assuming, as for the transverse current, that the amplitude of the excitation of each feed is uniform and only a phase shift is impressed.

A windowing approximation corresponds to evaluate the currents on a single periodic cell in infinite array environment and then calculate the pattern radiated by a finite number of these cells, by multiplication for an array factor. The current distribution on an infinite array of connected dipoles was given in Eq. (2.34) and is equal to

$$i(x) = \frac{1}{d_x} \sum_{m_x=-\infty}^{\infty} \frac{-V_0 \text{sinc}\left(\frac{k_{xm}\delta_d}{2}\right)}{D_\infty(k_{xm})} e^{-jk_{xm}x}. \quad (\text{B.10})$$

The Fourier transform for a finite (N_x) of cells is then given by

$$\begin{aligned} I_w(k_x) &= \int_{-\frac{N_x}{2}d_x - \frac{d_x}{2}}^{\frac{N_x}{2}d_x + \frac{d_x}{2}} i(x) e^{jk_x x} dx = \\ &= -\frac{V_0}{d_x} \sum_{n_x=-N_x/2}^{N_x/2} \int_{n_x d_x - \frac{d_x}{2}}^{n_x d_x + \frac{d_x}{2}} \sum_{m_x=-\infty}^{\infty} \frac{\text{sinc}\left(\frac{k_{xm}\delta_d}{2}\right)}{D_\infty(k_{xm})} e^{-jk_{xm}x} e^{jk_x x} dx = \\ &= -\frac{V_0}{d_x} \sum_{n_x=-N_x/2}^{N_x/2} \int_{-\frac{d_x}{2}}^{\frac{d_x}{2}} \sum_{m_x=-\infty}^{\infty} \frac{\text{sinc}\left(\frac{k_{xm}\delta_d}{2}\right)}{D_\infty(k_{xm})} e^{-jk_{xm}(x+n_x d_x)} e^{jk_x(x+n_x d_x)} dx = \quad (\text{B.11}) \\ &= -\frac{V_0}{d_x} \sum_{n_x=-N_x/2}^{N_x/2} \sum_{m_x=-\infty}^{\infty} \frac{\text{sinc}\left(\frac{k_{xm}\delta_d}{2}\right)}{D_\infty(k_{xm})} e^{j(k_x - k_{xm})n_x d_x} \int_{-\frac{d_x}{2}}^{\frac{d_x}{2}} e^{j(k_x - k_{xm})x} dx = \\ &= -\frac{V_0}{d_x} \sum_{n_x=-N_x/2}^{N_x/2} \sum_{m_x=-\infty}^{\infty} \frac{\text{sinc}\left(\frac{k_{xm}\delta_d}{2}\right)}{D_\infty(k_{xm})} e^{j(k_x - k_{xm})n_x d_x} d_x \text{sinc}\left(\frac{(k_x - k_{xm})d_x}{2}\right). \end{aligned}$$

We can observe that

$$e^{j(k_x - k_{xm})n_x d_x} = e^{j(k_x - (k_{x0} - \frac{2\pi m_x}{d_x}))n_x d_x} = e^{j(k_x - k_{x0})n_x d_x} e^{-j2\pi m_x n_x} = e^{j(k_x - k_{x0})n_x d_x} \quad (\text{B.12})$$

since m_x and n_x are integers. Therefore, when a windowing approximation is considered, the current spectrum is given by

$$I_w(k_x) = -V_0 \sum_{n_x = -N_x/2}^{N_x/2} e^{j(k_x - k_0)n_x d_x} \sum_{m_x = -\infty}^{\infty} \frac{\text{sinc}\left(\frac{k_{xm}\delta_d}{2}\right) \text{sinc}\left(\frac{(k_x - k_{xm})d_x}{2}\right)}{D_\infty(k_{xm})}. \quad (\text{B.13})$$

In Eq. (B.5), $J_x(k_y, k_y)$ can be expressed as the product of two separate variables: i.e. $J_x(k_y, k_y) = J_x^y(k_y)I(k_x)$. The Fourier transform of the transverse current distribution is expressed in terms of Bessel function as $J_x^y(k_y) = J_0(k_y w_d/2)$. Exploiting the windowing approximation $I(k_x) = I_w(k_x)$, the total current spectrum can be expressed as

$$J_x(k_x, k_y) \approx -V_0 AF(k_y - k_{y0}, N_y, d_y) J_0\left(\frac{k_y w_d}{2}\right) AF(k_x - k_{x0}, N_x, d_x) \sum_{m_x = -\infty}^{\infty} \frac{\text{sinc}\left(\frac{k_{xm}\delta_d}{2}\right) \text{sinc}\left(\frac{(k_x - k_{xm})d_x}{2}\right)}{D_\infty(k_{xm})} \quad (\text{B.14})$$

where we introduced the array factor function $AF(k - k_d, N, d) = \sum_{n=-N/2}^{N/2} e^{j(k - k_d)nd}$.

B.2.2 Longitudinal Green's Function

Since the elements that compose a connected array support guided waves along the array, the windowing approximation also along the longitudinal direction can lead to inaccurate prediction of the radiation patterns. A more accurate representation can be derived directly from the current spectrum on a finite array. The complication in the analysis is only apparent since we have actually provided the analytical closed-form expression for the spectrum of the longitudinal current in the case of a finite number of δ -gap sources in (B.9). The two-dimensional current spectrum in this case is given by

$$J_x(k_x, k_y) \approx -V_0 AF(k_y - k_{y0}, N_y, d_y) AF(k_x - k_{x0}, N_x, d_x) J_0\left(\frac{k_y w_d}{2}\right) \frac{\text{sinc}\left(\frac{k_x \delta_d}{2}\right)}{D_\infty(k_{xm})} \quad (\text{B.15})$$

B.2.3 Far-Fields Expressions from the Vector Potential

In the far field region, the electric field can be approximated as purely transverse, with no radial component [52]. If $\mathbf{A}_t = A_\theta \hat{\boldsymbol{\theta}} + A_\varphi \hat{\boldsymbol{\varphi}}$, the electric far field is equal to

$$\begin{aligned} E_r &\simeq 0 \\ E_\theta &\simeq -j\omega A_\theta \Rightarrow \mathbf{E} \simeq -j\omega \mathbf{A}_t. \\ E_\varphi &\simeq -j\omega A_\varphi \end{aligned} \quad (\text{B.16})$$

If \mathbf{A} is only directed along x , we have

$$\begin{pmatrix} A_r \\ A_\theta \\ A_\varphi \end{pmatrix} = \begin{pmatrix} \sin\theta \cos\varphi A_x \\ \cos\theta \cos\varphi A_x \\ -\sin\varphi A_x \end{pmatrix} \quad (\text{B.17})$$

The final expression of the far field is given by

$$\begin{aligned} E_\theta &\simeq -j\omega \cos\theta \cos\varphi A_x \\ E_\varphi &\simeq j\omega \sin\varphi A_x \end{aligned} \quad (\text{B.18})$$

with A_x given in Eq. (B.5) with the current spectra expressed as in Eq. (B.14) or (B.15) for longitudinal windowing or finite array GF, respectively.

Appendix C

Admittance Matrix Evaluation: IEMEN Approach

An equivalent circuit representation of connected arrays was presented in Chapter 4. The circuit was rigorously derived for transmitting arrays, from the expansion of the input impedance in different terms. The aim of this appendix is to prove that this circuit can be used also to describe the array in reception, as in Fig. 4.8.

To show the validity of the circuit in reception, we use the approach described in [63,64] for the analysis of multi-layer frequency selective surfaces. This technique allows to represent each transition between layers in terms of a generalized impedance or admittance matrix, obtained directly from the solution of an integral equation with reduced kernel. Similarly, the connected array represented in Fig. 4.1 can be described as a transition at $z = 0$ characterized by an admittance matrix, as depicted in Fig. C.1.

This appendix reports the main algebraic steps that lead to the analytical expression for the elements of the admittance matrix representing the antenna. It is then proved that the admittance parameters are equivalent to the ones given by the circuit in Fig. 4.8.

C.1 Integral Equation

Referring to the original and equivalent problems in Figs. 4.1 and 4.2, boundary conditions are imposed as

$$\mathbf{e}_{tot} = Z_{surf} \mathbf{j}. \quad (\text{C.1})$$

We proceed as in [64], by expressing the total electric field as the superposition of two

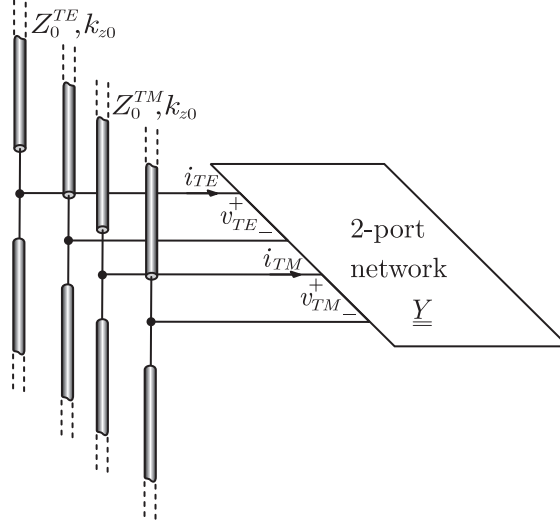


Figure C.1: Multimode equivalent network of a well sampled connected array in free space.

terms associated with radiated and localized contributions, respectively. We refer to these two contributions as accessible and non-accessible modes ($\mathbf{e}_{tot} = \mathbf{e}_{tot}^a + \mathbf{e}_{tot}^{na}$). Therefore, Eq. (C.1) becomes

$$\mathbf{e}_{tot}^{na} = -\mathbf{e}_{tot}^a + Z_{surf} \mathbf{j}. \quad (\text{C.2})$$

The total localized electric field can be expressed in integral form by introducing the non-accessible portion of the Green's function (GF). Considering only the x -component of electric field and current, Eq. (C.2) becomes

$$\int_{\Sigma_c \cup \Sigma_g} j_x(\boldsymbol{\rho}') g_{xx}^{na}(\boldsymbol{\rho}, \boldsymbol{\rho}') d\boldsymbol{\rho}' = -e_{tot,x}^a(\boldsymbol{\rho}) + Z_{surf} j_x(\boldsymbol{\rho}). \quad (\text{C.3})$$

where $\boldsymbol{\rho} = x\hat{\mathbf{x}} + y\hat{\mathbf{y}}$. The surfaces Σ_c and Σ_g were defined in Fig. 4.2. The infinite-array periodic GF for electric source and electric observation point located at the same height ($z = z' = 0$) is given by

$$g_{xx}(\boldsymbol{\rho}, \boldsymbol{\rho}', z = 0) = \frac{1}{d_x d_y} \sum_{m=-\infty}^{\infty} G_{xx}(\mathbf{k}_{\rho m}) e^{-j\mathbf{k}_{\rho m} \cdot (\boldsymbol{\rho} - \boldsymbol{\rho}')} \quad (\text{C.4})$$

where $\mathbf{k}_{\rho m} = k_{xm}\hat{\mathbf{x}} + k_{ym}\hat{\mathbf{y}}$ and G_{xx} is the xx component of the dyadic electric Green's function in the spectral domain. The accessible and non-accessible portions of the GF are defined as

$$g_{xx}(\boldsymbol{\rho}, \boldsymbol{\rho}') = g_{xx}^a(\boldsymbol{\rho}, \boldsymbol{\rho}') + g_{xx}^{na}(\boldsymbol{\rho}, \boldsymbol{\rho}') = \frac{1}{d_x d_y} G_{xx}(\mathbf{k}_{\rho 0}) e^{-j\mathbf{k}_{\rho 0} \cdot (\boldsymbol{\rho} - \boldsymbol{\rho}')} + \frac{1}{d_x d_y} \sum_{m \neq 0}^{\infty} G_{xx}(\mathbf{k}_{\rho m}) e^{-j\mathbf{k}_{\rho m} \cdot (\boldsymbol{\rho} - \boldsymbol{\rho}')}. \quad (\text{C.5})$$

In last equation, for a periodic well sampled array of connected dipoles, the accessible modes are the TE and TM components of the radiated or incident plane wave (fundamental Floquet mode). The non-accessible contribution is instead associated with all the other higher-order modes representing the reactive energy localized in the proximity of the dipoles.

We can then write the accessible field as the sum of two components:

$$e_{tot,x}^a(\boldsymbol{\rho}) = \sum_{Ti \in \{TE, TM\}} v_{Ti} e_{x, Ti}(\boldsymbol{\rho}). \quad (\text{C.6})$$

Also the current can be expanded as sum of two components weighted for the same coefficients v_{Ti} (as in Eq. (3) of [64]):

$$j_x(\boldsymbol{\rho}) = \sum_{Ti \in \{TE, TM\}} v_{Ti} j_{x, Ti}(\boldsymbol{\rho}). \quad (\text{C.7})$$

By substituting the last two modal expansions into (C.3), we obtain

$$\sum_{Ti \in \{TE, TM\}} v_{Ti} \int_{\Sigma_c \cup \Sigma_g} j_{x, Ti}(\boldsymbol{\rho}') g_{xx}^{na}(\boldsymbol{\rho}, \boldsymbol{\rho}') d\boldsymbol{\rho}' = - \sum_{Ti \in \{TE, TM\}} v_{Ti} (e_{x, Ti}(\boldsymbol{\rho}) - Z_{surf} j_{x, Ti}(\boldsymbol{\rho})). \quad (\text{C.8})$$

Since last equation is valid for all possible values of v_{Ti} , we can equate the single Ti term at both sides, leading to two integral equations:

$$\int_{\Sigma_c \cup \Sigma_g} j_{x, Ti}(\boldsymbol{\rho}') g_{xx}^{na}(\boldsymbol{\rho}, \boldsymbol{\rho}') d\boldsymbol{\rho}' = -e_{x, Ti}(\boldsymbol{\rho}) + Z_{surf} j_{x, Ti}(\boldsymbol{\rho}) \quad (\text{C.9})$$

for Ti referring to TE or TM . As done in [64], from the solutions $j_{x,Ti}$ of Eq. (C.9), resorting to the explicit expressions, the impedance matrix representing the antenna can be calculated as

$$y_{TiTj} = \int_{cell} j_{x,Tj}(\boldsymbol{\rho}) e_{x,Ti}^*(\boldsymbol{\rho}) d\boldsymbol{\rho} \quad (\text{C.10})$$

which relates i_{Ti} and v_{Ti} via $i_{Ti} = \sum_{Tj \in \{TE, TM\}} v_{Tj} y_{TiTj}$.

C.2 Closed-Form Evaluation of the Admittance Matrix

The expression of the vector electric field mode functions are given by [64]:

$$\begin{aligned} \mathbf{e}_{TE}(\boldsymbol{\rho}) &= \frac{1}{k_{\rho 0}} \frac{1}{\sqrt{d_x d_y}} (k_{x0} \hat{\mathbf{x}} + k_{y0} \hat{\mathbf{y}}) e^{-j\mathbf{k}_{\rho 0} \cdot \boldsymbol{\rho}} \\ \mathbf{e}_{TM}(\boldsymbol{\rho}) &= \frac{1}{k_{\rho 0}} \frac{1}{\sqrt{d_x d_y}} (k_{y0} \hat{\mathbf{x}} - k_{x0} \hat{\mathbf{y}}) e^{-j\mathbf{k}_{\rho 0} \cdot \boldsymbol{\rho}}. \end{aligned} \quad (\text{C.11})$$

The projection of the field onto the unit vector $\hat{\mathbf{x}}$ leads to:

$$\mathbf{e}_{Ti}(\boldsymbol{\rho}) \cdot \hat{\mathbf{x}} = e_{x,Ti}(\boldsymbol{\rho}) = \frac{n_{Ti}}{\sqrt{d_x d_y}} e^{-j\mathbf{k}_{\rho 0} \cdot \boldsymbol{\rho}} \quad (\text{C.12})$$

where $n_{TE} = k_{y0}/k_{\rho 0} = \sin \varphi$ and $n_{TM} = k_{x0}/k_{\rho 0} = \cos \varphi$.

Equation (C.10) can be then written as

$$y_{TiTj} = \int_{cell} j_{x,Tj}(\boldsymbol{\rho}) \frac{n_{Ti}}{\sqrt{d_x d_y}} e^{j\mathbf{k}_{\rho 0} \cdot \boldsymbol{\rho}} d\boldsymbol{\rho}. \quad (\text{C.13})$$

Noting that the Fourier Transform of the spatial current is given by

$$\int_{cell} j_{x,Tj}(\boldsymbol{\rho}) e^{j\mathbf{k}_{\rho 0} \cdot \boldsymbol{\rho}} d\boldsymbol{\rho} = J_{Tj}(\mathbf{k}_{\rho}) = J_0 \left(\frac{k_{y0} w}{2} \right) I_{Tj}(k_{x0}) \quad (\text{C.14})$$

the elements of the admittance matrix can be expressed as

$$y_{TiTj} = \frac{J_0 \left(\frac{k_{y0} w}{2} \right) n_{Ti}}{\sqrt{d_x d_y}} I_{Tj}(k_{x0}). \quad (\text{C.15})$$

C.2.1 Analytical Solution for the Current Spectrum

The solution of the integral equation (C.9) can be obtained in the spectral domain following the same steps described in Secs. 4.2 and 4.3, leading to an expression similar to Eq. (4.11):

$$I_{Ti}(k_{xm}) = \frac{-E_{x,Ti}(k_{xm}) + Z_l i_{0,Ti}^{tot} \operatorname{sinc}\left(\frac{k_{xm}\delta}{2}\right)}{D_l^{na}(k_{xm})} \quad (\text{C.16})$$

with

$$D_l^{na}(k_x) = \frac{1}{d_y} \sum_{m_y \neq 0} G_{xx}(k_x, k_{ym}) J_0\left(\frac{k_{y0}w}{2}\right). \quad (\text{C.17})$$

The total current flowing in the dipole gap can be evaluated as follows:

$$\begin{aligned} i_{0,Ti}^{tot} &= \frac{1}{\delta} \int_{-\delta/2}^{\delta/2} i_{Ti} dx' = \\ &= \frac{1}{\delta} \int_{-\delta/2}^{\delta/2} \frac{1}{d_x} \sum_{m_x=-\infty}^{\infty} \left(\frac{-E_{x,Ti}(k_{xm}) + Z_l i_{0,Ti}^{tot} \operatorname{sinc}\left(\frac{k_{xm}\delta}{2}\right)}{D_l^{na}(k_{xm})} \right) e^{-jk_{xm}x'} dx'. \end{aligned} \quad (\text{C.18})$$

The expression of the incident field in the spectral domain, under plane-wave illumination, is given by

$$E_{x,Ti}(k_{xm}) = e_{x,Ti} d_x \delta_{m_x} \quad (\text{C.19})$$

where $e_{x,Ti}$ is the amplitude of the incident electric field and δ_{m_x} is 1 for $m_x = 0$ and 0 otherwise. From Eq. (C.19) and using the identity $\frac{1}{\delta} \int_{-\delta/2}^{\delta/2} e^{-jk_{xm}x'} dx' = \operatorname{sinc}(k_{xm}\delta/2)$, the average current in the gap can be algebraically manipulated as follows:

$$\begin{aligned} i_{0,Ti}^{tot} &= \frac{1}{d_x} \sum_{m_x=-\infty}^{\infty} \left(\frac{-e_{x,Ti} d_x \operatorname{sinc}\left(\frac{k_{xm}\delta}{2}\right) \delta(m_x) + Z_l i_{0,Ti}^{tot} \operatorname{sinc}^2\left(\frac{k_{xm}\delta}{2}\right)}{D_l^{na}(k_{xm})} \right) \\ &= \frac{-e_{x,Ti} \operatorname{sinc}\left(\frac{k_{x0}\delta}{2}\right)}{D_l^{na}(k_{x0})} + \frac{1}{d_x} \sum_{m_x=-\infty}^{\infty} Z_l i_{0,Ti}^{tot} \frac{\operatorname{sinc}^2\left(\frac{k_{xm}\delta}{2}\right)}{D_l^{na}(k_{xm})} \\ &= \frac{-e_{x,Ti} \operatorname{sinc}\left(\frac{k_{x0}\delta}{2}\right)}{D_l^{na}(k_{x0})} - Z_l Y_{na} i_{0,Ti}^{tot}. \end{aligned} \quad (\text{C.20})$$

where we defined $Y_{na} = \frac{1}{Z_{na}} = -\frac{1}{d_x} \sum_{m_x=-\infty}^{\infty} \frac{\text{sinc}^2(k_{xm}\delta/2)}{D_l^{na}(k_{xm})}$. Note that $Y_{na} = 1/Z_{na} = Y_{m_x=0}^{m_y \neq 0} + Y_{m_x \neq 0}^{m_y}$, according to the definitions given in Eqs. (4.20) and (4.21).

The explicit expression of $i_{0,Ti}^{tot}$ is given by

$$i_{0,Ti}^{tot} = \frac{Z_{na}}{Z_{na} + Z_l} \frac{-e_{x,Ti} \text{sinc}(\frac{k_{x0}\delta}{2})}{D_l^{na}(k_{x0})}. \quad (\text{C.21})$$

The substitution of Eq. (C.21) in (C.16) leads to

$$I_{Ti}(k_{xm}) = \frac{-e_{x,Ti} d_x}{D_l^{na}(k_{x0})} \left(\delta(m_x) + \frac{Z_l Z_{na}}{Z_l + Z_{na}} \frac{1}{d_x} \frac{\text{sinc}(k_{x0}\delta/2) \text{sinc}(k_{xm}\delta/2)}{D_l^{na}(k_{x0})} \right). \quad (\text{C.22})$$

C.2.2 Analytical Solution for the Admittance Matrix

To evaluate the elements of the admittance matrix with Eq. (C.15), we are only interested in the value of the current spectrum in k_{x0} :

$$I_{Ti}(k_{x0}) = \frac{-e_{x,Ti} d_x}{D_l^{na}(k_{x0})} \left(1 - \frac{Z_l Z_{na}}{Z_l + Z_{na}} Y_{m_x=0}^{m_y \neq 0} \right) \quad (\text{C.23})$$

where $Y_{m_x=0}^{m_y \neq 0} = -\frac{1}{d_x} \frac{\text{sinc}^2(k_{x0}\delta/2)}{D_l^{na}(k_{x0})}$ was already introduced in Eq. (4.21).

It is convenient to multiply and divide for $-\frac{1}{d_x} \text{sinc}^2(k_{x0}\delta/2)$:

$$\begin{aligned} I_{Ti}(k_{x0}) &= -e_{x,Ti} d_x \left(1 - \frac{Z_l Z_{na}}{Z_l + Z_{na}} Y_{m_x=0}^{m_y \neq 0} \right) \frac{-\frac{1}{d_x} \text{sinc}^2(k_{x0}\delta/2)}{D_l^{na}(k_{x0})} \frac{1}{-\frac{1}{d_x} \text{sinc}^2(k_{x0}\delta/2)} = \\ &= \frac{e_{x,Ti} d_x}{\frac{1}{d_x} \text{sinc}^2(k_{x0}\delta/2)} \left(1 - \frac{Z_l Z_{na}}{Z_l + Z_{na}} Y_{m_x=0}^{m_y \neq 0} \right) Y_{m_x=0}^{m_y \neq 0}. \end{aligned} \quad (\text{C.24})$$

Let us perform a few algebraic manipulations to express the current spectrum in a more compact form:

$$\frac{Z_l Z_{na}}{Z_l + Z_{na}} = \frac{1}{Y_l + Y_{na}} = \frac{1}{Y_l + Y_{m_x=0}^{m_y \neq 0} + Y_{m_x \neq 0}^{m_y}}. \quad (\text{C.25})$$

Thus, we can define an admittance term \hat{Y}_l as follow:

$$\begin{aligned}\hat{Y}_l &= \left(1 - \frac{Z_l Z_{na} Y_{m_x=0}^{m_y \neq 0}}{Z_l + Z_{na}}\right) Y_{m_x=0}^{m_y \neq 0} = \left(1 - \frac{Y_{m_x=0}^{m_y \neq 0}}{Y_l + Y_{m_x=0}^{m_y \neq 0} + Y_{m_x \neq 0}^{m_y}}\right) Y_{m_x=0}^{m_y \neq 0} = \\ &= \frac{(Y_l + Y_{m_x \neq 0}^{m_y}) Y_{m_x=0}^{m_y \neq 0}}{(Y_l + Y_{m_x \neq 0}^{m_y}) + Y_{m_x=0}^{m_y \neq 0}}.\end{aligned}\quad (\text{C.26})$$

Using (C.26), the current spectrum can be expressed as

$$I_{Ti}(k_{x0}) = \frac{e_{x,Ti} d_x}{\frac{1}{d_x} \text{sinc}^2(k_{x0} \delta / 2)} \hat{Y}_l. \quad (\text{C.27})$$

By substituting Eq. (C.27) in (C.15), we can write

$$y_{TiTj} = n_{Ti} n_{Tj} \tilde{Y}_l. \quad (\text{C.28})$$

The equivalent admittance \tilde{Y}_l is a simple function of Z_l and higher modal ($m_x \neq 0, m_y \neq 0$) components of Z_a :

$$\tilde{Y}_l = n^2 \frac{(Y_l + Y_{m_x \neq 0}^{m_y}) Y_{m_x=0}^{m_y \neq 0}}{(Y_l + Y_{m_x \neq 0}^{m_y}) + Y_{m_x=0}^{m_y \neq 0}} \quad (\text{C.29})$$

with n defined as in Eq. (4.25).

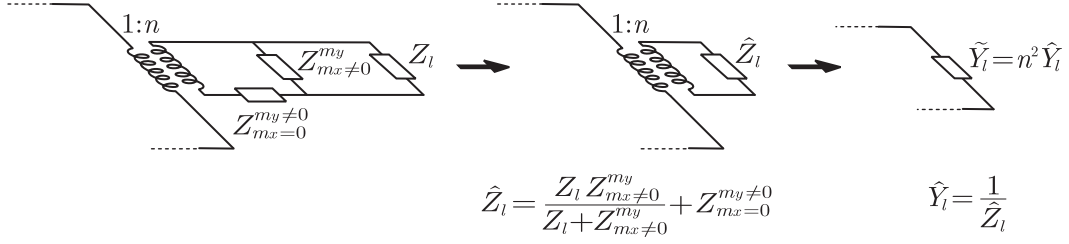
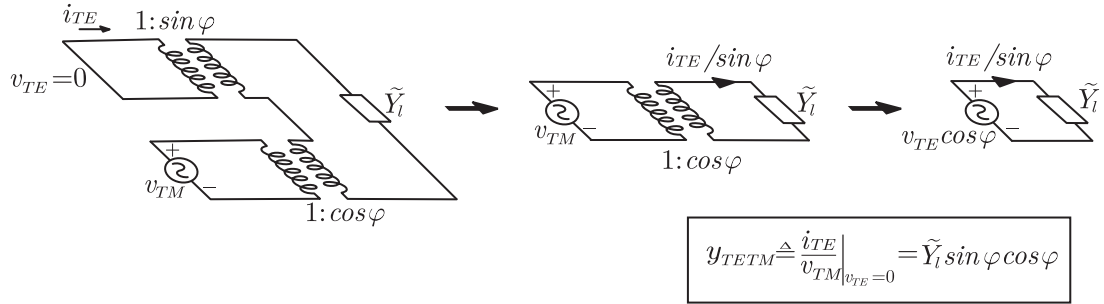
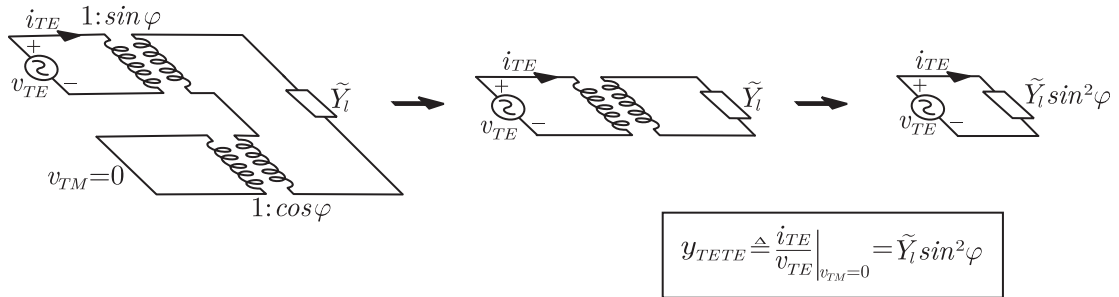
C.2.3 Circuit Steps to Validate the Equivalent Circuit in Reception

The 2×2 admittance parameters given by Eq. (C.28) are consistent with the equivalent circuit proposed in Fig. 4.8, hence validating it.

This can be easily verified recognizing in the analytical expressions of \tilde{Y}_l the terms that were highlighted in Sec. 4.4. \hat{Y}_l and \tilde{Y}_l can be then represented as in Fig. C.2.

Applying the transformation steps to the equivalent circuit of the connected array in reception as in Fig. C.3 allows obtaining, from the operative definition, $y_{TE, TM}$. Analogously, Fig. C.4 describes the steps to evaluate $y_{TE, TE}$. The expressions are found to be

$$\begin{aligned}y_{TETM} &= \tilde{Y}_l \sin \varphi \cos \varphi \\ y_{TETE} &= \tilde{Y}_l \sin^2 \varphi.\end{aligned}\quad (\text{C.30})$$

Figure C.2: Circuit representation of \tilde{Y}_l as function of Z_l and higher modal components of Z_a .Figure C.3: Circuit transformation step for the calculation of the $y_{TE, TM}$ element.Figure C.4: Circuit transformation step for the calculation of the $y_{TE, TE}$ element.

Therefore, the element of the admittance matrix evaluated from the equivalent circuit are the same as the analytical ones in Eq. (C.28). Analogous steps for $y_{TM, TM}$ are not reported for the sake of brevity.

Appendix D

Asymptotic Evaluation of Edge-Current Integrals

The total currents at each gap of a finite connected array of dipoles were expressed in Sec. 5.5 in terms of two spectral integrals:

$$\begin{aligned}
 i_{\delta,edge}^{n_x} = i_{\delta,edge1}^{n_x} + i_{\delta,edge2}^{n_x} = e^{jk_{x0}d_x} \frac{1}{2\pi} \int_{-\infty}^{\infty} \frac{\text{sinc}^2\left(\frac{k_x\delta}{2}\right)}{D_{load}(k_x)} \frac{e^{-jk_x(n_x+1)d_x}}{1 - e^{-j(k_x-k_{x0})d_x}} dk_x + \\
 e^{-jk_{x0}N_x d_x} \frac{1}{2\pi} \int_{-\infty}^{\infty} \frac{\text{sinc}^2\left(\frac{k_x\delta}{2}\right)}{D_{load}(k_x)} \frac{e^{-jk_x(n_x-N_x)d_x}}{1 - e^{j(k_x-k_{x0})d_x}} dk_x.
 \end{aligned} \tag{D.1}$$

where $D_{load}(k_x) = D_l(k_x) - Z_l/d_x$. The integrand shows a number of polar singularities, which emerge from the zeros of term $(1 - e^{j(k_x-k_{x0})d_x})$ associated with the Floquet Waves (FWs) in $k_{xm} = k_{x0} + \frac{2\pi m}{d_x}$. Branch singularities are due to the presence of square roots in the GF $D_l(k_x)$. Other complex poles are associated with the dispersion equation $D_{load}(k_x) = 0$. The integrals defining $i_{\delta,edge1}^{n_x}$ and $i_{\delta,edge2}^{n_x}$ in Eq. (D.1) are converging over different integration paths. The convergence of the integral $i_{\delta,edge1}^{n_x}$ requires a counter-clock circling of the poles (see Fig. D.1). On the contrary, the integration path of $i_{\delta,edge2}^{n_x}$ should be deformed in the half plane $\Im\{k_x\} > 0$. These different complex plane topologies suggest two specular uniform asymptotic evaluations for the two integrals. In the following the focus will be on $i_{\delta,edge1}^{n_x}$, since the evaluation of $i_{\delta,edge2}^{n_x}$ can be performed in essentially the same way, once the change of variable $k'_x = -k_x$ is introduced.

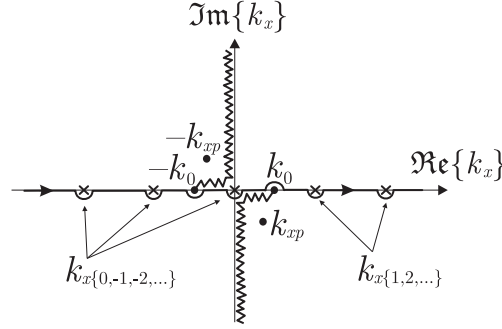


Figure D.1: Original integration path for the evaluation of $i_{\delta, edge1}^{n_x}$ in Eq. (D.1).

D.1 Analysis of the Singularities

Before proceeding with the asymptotic evaluation, it is useful to isolate the zeroth order ($m_y = 0$) from the higher order FWs ($m_y \neq 0$) in the transverse GF terms pertaining to the free space case (Eq. (5.3)). This is obtained by representing $D_l(k_x)$ as follows:

$$D_l(k_x) = -\frac{\zeta_0}{2k_0 d_y} \left(\sqrt{k_0^2 - k_x^2} + (k_0^2 - k_x^2) \sum_{m_y \neq 0} \frac{J_0\left(\frac{k_{ym} w}{2}\right)}{\sqrt{k_0^2 - k_x^2 - k_{ym}^2}} \right). \quad (\text{D.2})$$

Using this representation it is simple to express the loaded transverse GF $D_{load}(k_x)$ in terms of $k_z = \sqrt{k_0^2 - k_x^2}$ as follows:

$$D_{load}(k_x) = -\frac{\zeta_0}{2k_0 d_y} \left(k_z + k_z j \Psi(k_x) + \frac{2k_0 d_y Z_l}{\zeta_0 d_x} \right) \quad (\text{D.3})$$

where

$$j \Psi(k_x) = \sum_{m_y \neq 0} \frac{J_0\left(\frac{k_{ym} w}{2}\right)}{\sqrt{k_0^2 - k_x^2 - k_{ym}^2}}. \quad (\text{D.4})$$

Since for well sampled arrays the function $\Psi(k_x)$ is slowly varying with k_x , it is legitimate to approximate $\Psi(k_x) \approx \Psi(0) \equiv \Psi$. This approximation helps to recognize Eq. (D.3) as a second degree polynomial function of k_z , which can be expressed highlighting its roots:

$$D_{load}(k_x) = -\frac{j \Psi \zeta_0}{2k_0 d_y} (k_z - k_{zp1})(k_z - k_{zp2}) \quad (\text{D.5})$$

where

$$k_{zp2} = j \frac{1}{2\Psi} \left(1 \pm \sqrt{1 - j \frac{\Psi 8k_0 d_y Z_l}{\zeta_0 d_x}} \right). \quad (\text{D.6})$$

Using Eq. (D.5), the contribution due to the first edge in Eq. (D.1) can be then expressed as follows:

$$i_{\delta, edge1}^{n_x} = \frac{jk_0 d_y e^{jk_x d_x}}{\Psi \zeta_0 \pi} \int_{-\infty}^{\infty} \frac{\text{sinc}^2\left(\frac{k_x \delta}{2}\right)}{(k_z - k_{zp1})(k_z - k_{zp2})} \frac{e^{-jk_x(n_x+1)d_x}}{1 - e^{-j(k_x - k_{x0})d_x}} dk_x. \quad (\text{D.7})$$

In Eq. (D.7) the denominator D_{load} is expressed with explicit roots in k_z . These roots define the branch cuts of the complex plane, in particular the top/bottom Riemann sheet, i.e. $\Im\{k_z\} \leq 0$. The roots are also associated with poles in k_x plane, as in will be discussed in the following.

D.1.1 Load Dependent Pole

It is simple to verify that k_{zp1} is associated with values of k_x far from the the branch points for any values of Z_l . It is then useful to locate in the k_x plane the poles associated with k_{zp2} , as a function of the load impedance Z_l . For $Z_l = 0$, from Eq. (D.6), it results $k_{zp2} = 0$ and consequently $k_{xp} = k_0$. For small values of Z_l a second order approximation of the square root function in Eq. (D.6) for small argument leads to:

$$\sqrt{1 - j \frac{\Psi 8k_0 d_y Z_l}{\zeta_0 d_x}} \approx 1 - j \frac{\Psi 4k_0 d_y Z_l}{\zeta_0 d_x} - \frac{1}{8} \left(\frac{j \Psi 4k_0 d_y Z_l}{\zeta_0 d_x} \right)^2 \quad (\text{D.8})$$

which implies

$$k_{zp2} = -\frac{2k_0 d_y Z_l}{\zeta_0 d_x} - j 4\Psi \left(\frac{k_0 d_y Z_l}{\zeta_0 d_x} \right)^2 = -k_0(n_r + j n_i) \quad (\text{D.9})$$

where n_r and n_i are very small real positive functions of the geometrical parameters at play. Consequently, the approximate expression of k_{xp} is now as follows:

$$k_{xp} = \sqrt{k_0^2 - k_{zp2}^2} = \sqrt{k_0^2(1 - (n_r + j n_i)^2)} \approx k_0 \left(1 - \frac{(n_r + j n_i)^2}{2} \right) = k_0 \left(1 - \frac{n_r^2 - n_i^2}{2} \right) - j k_0 n_r n_i \quad (\text{D.10})$$

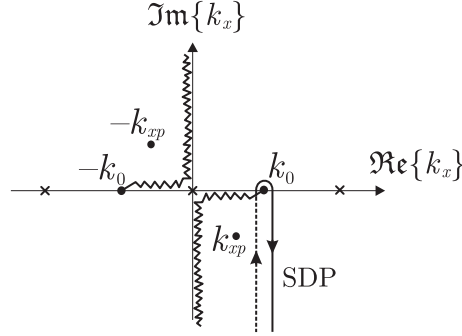


Figure D.2: Deformation of the integration path for the evaluation of $i_{\delta,edge1}^{n_x}$ in Eq. (D.1): Steepest Descent Path.

which explicitly shows that, for small values of the load impedance Z_l , the dominant poles are located close to the branch point k_0 and show small imaginary parts that tend to become more negative as Z_l increases. The pole k_{xp} has a negative imaginary part. The corresponding root in k_z was chosen with negative imaginary part, implying that the pole k_{xp} represented in (D.10) is not associated with a leaky-wave, but with a damped wave. Since the damped wave is located in the top Riemann sheet of the complex k_x -plane, k_{xp} is not captured when deforming the integration path along the Steepest Descent Path (SDP) to perform an uniform asymptotic evaluation of the integral as in Fig. D.2.

D.2 Asymptotic Evaluation in Terms of Fresnel Functions

Multiplying and dividing the integrand of Eq. (D.7) for the factor $(k_z + k_{zp2})$ we obtain, after a few algebraic steps, the following expression:

$$i_{\delta,edge1}^{n_x} = -\frac{jk_0 d_y e^{jk_{x0} d_x}}{\Psi \zeta_0 \pi} \int_{-\infty}^{\infty} (k_z + k_{zp2}) \frac{\text{sinc}^2\left(\frac{k_x \delta}{2}\right)}{(k_z - k_{zp1})(k_x^2 - k_{xp}^2)} \frac{e^{-jk_x(n_x+1)d_x}}{1 - e^{-j(k_x - k_{x0})d_x}} dk_x. \quad (\text{D.11})$$

This integral can be deformed into the SDP around the saddle point $k_x = k_0$ as in Fig. D.2. Note that in the deformation none of the poles associated with the FWs are captured since the original integration path shown in Fig. D.1 surrounds all poles counter-clockwise. The poles defined by k_{zp1} and k_{zp2} in Eq. (D.6) are also not captured in the deformation. From Eq. (D.11) we can then define two contributions as follows:

$$i_{\delta,edge1}^{n_x} \approx i_{\delta,edge1}^{n_x,a} + i_{\delta,edge1}^{n_x,b} \quad (D.12)$$

where

$$i_{\delta,edge1}^{n_x,a} = C\sqrt{2k_0} \int_{SDP} \frac{\sqrt{k_0 - k_x}}{k_x - k_{xp}} \frac{e^{-jk_x(n_x+1)d_x}}{1 - e^{-j(k_x - k_{x0})d_x}} dk_x \quad (D.13)$$

$$i_{\delta,edge1}^{n_x,b} = Ck_{zp2} \int_{SDP} \frac{1}{k_x - k_{xp}} \frac{e^{-jk_x(n_x+1)d_x}}{1 - e^{-j(k_x - k_{x0})d_x}} dk_x. \quad (D.14)$$

The term

$$C = \frac{-jk_0 d_y e^{jk_{x0}d_x} \text{sinc}^2(k_0\delta/2)}{\Psi\zeta_0\pi(k_{zp1})(k_0 + k_{xp})} \quad (D.15)$$

includes both the constants and the slower varying portions of the integrand from Eq. (D.11), approximated in $k_x = k_0$. The integrand in Eq. (D.14) presents no square root type of branches. Accordingly, in the upward and downward path that define the SDP the integrand is the same, so that the two half paths contributions cancel out.

The integral in Eq. (D.13), instead, requires an uniform asymptotic evaluation since the poles in k_{xp} and in k_{x0} can be close to the branch point k_0 for particular geometrical, loading or scanning configurations. Before performing the evaluation, it is convenient to express the integrand in a form where the mentioned poles in k_{xp} and in k_{x0} are shown explicitly [111]. This can be achieved by adding and subtracting the quantity $(j/d_x)/(k_0 - k_{x0})$ as follows:

$$\frac{1}{1 - e^{-j(k_x - k_{x0})d_x}} = R(k_x) - \frac{j}{d_x} \frac{1}{k_x - k_{x0}} \quad (D.16)$$

where we defined the function

$$R(k_x) = \frac{1}{1 - e^{-j(k_x - k_{x0})d_x}} + \frac{j}{d_x} \frac{1}{k_x - k_{x0}}. \quad (D.17)$$

The function $R(k_x)$ is a smooth regular function in the vicinity of the SDP and consequently can be approximated with its value at the saddle point $R(k_x) \approx R(k_0)$. The integral in Eq. (D.13) can be split into two contributions as follows:

$$i_{\delta,edge1}^{n_x} \approx C\sqrt{2k_0}R(k_{x0}) \int_{-\infty}^{\infty} \frac{\sqrt{k_0 - k_x}}{k_x - k_{xp}} e^{-jk_x n_x d_x} dk_x - \frac{jC\sqrt{2k_0}}{d_x} \int_{-\infty}^{\infty} \frac{\sqrt{k_0 - k_x}}{(k_x - k_{x0})(k_x - k_{xp})} e^{-jk_x n_x d_x} dk_x. \quad (D.18)$$

While the first of the two integrals in Eq. (D.18) is already in a canonical form, the second one can be brought to the same form by recognizing that

$$\frac{1}{(k_x - k_{x0})(k_x - k_{xp})} = \frac{1}{k_{x0} - k_{xp}} \left(\frac{1}{k_x - k_{x0}} - \frac{1}{k_x - k_{xp}} \right). \quad (D.19)$$

After these manipulations, the three terms composing (D.18) can be all expressed analytically resorting to the following mathematical identity (proof in Sec. D.3):

$$\int_{-\infty}^{\infty} \frac{\sqrt{k_0 - k_x}}{k_x - k_p} e^{-jk_x x} dk_x = -e^{-j\pi/4} \sqrt{\frac{\pi}{x}} e^{-jk_0 x} \frac{F_s(x(k_0 - k_p))}{x(k_0 - k_p)} \quad (D.20)$$

where the slope Fresnel function is introduced: $F_s(x) = 2jx(1 - F(x))$. Here $F(x)$ is the Kouyoumjian Fresnel function [93], which is defined in Eq. (D.65). Using (D.20), after a few simple algebraic manipulations, the final expression of the current contribution born from the left edge of the array is given by

$$i_{\delta,edge1}^{n_x} \approx \frac{e^{-jk_0 X}}{X\sqrt{X}} \left(C_1 \frac{F_s(X(k_0 - k_{xp}))}{(k_0 - k_{xp})} + C_2 \frac{F_s(X(k_0 - k_{x0}))}{(k_0 - k_{x0})} \right) \quad (D.21)$$

with $X = (n_x + 1)d_x$. In Eq. (D.21)

$$C_1 = C' \left(R(k_0) - \frac{j}{d_x(k_{xp} - k_{x0})} \right), \quad C_2 = \frac{jC'}{d_x(k_{xp} - k_{x0})} \quad (D.22)$$

and $C' = C\sqrt{2k_0}(-e^{-j\pi/4}\pi)$. By proceeding in the same way, the expression for the current born at the right edge of the array can be expressed as

$$i_{\delta,edge2}^{n_x} \approx \frac{e^{-jk_0 X}}{X\sqrt{X}} \left(C_1 \frac{F_s(X(k_0 - k_{xp}))}{(k_0 - k_{xp})} + C_2 \frac{F_s(X(k_0 + k_{x0}))}{(k_0 - k_{x0})} \right) \quad (D.23)$$

where $X = (N_x - n_x)d_x$, $R(k_0)$, C_1 and C_2 are defined with the substitution $k_{x0} \rightarrow -k_{x0}$ and in the definition of C in Eq. (D.15) the exponential $e^{jk_{x0}d_x}$ is replaced by $e^{-jk_{x0}N_x d_x}$.

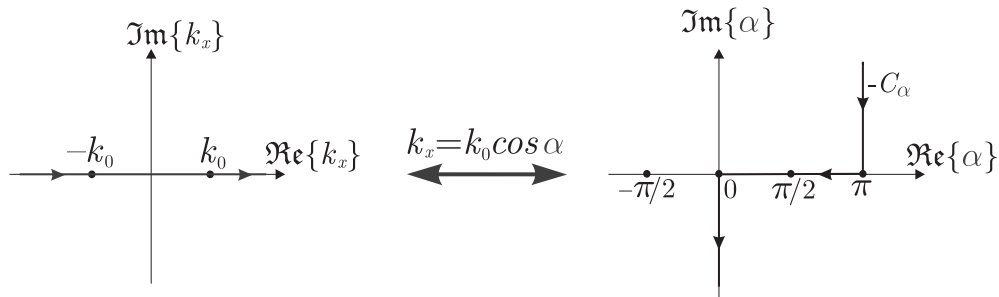


Figure D.3: Mapping of the original integration path in the variable k_x into the integration path $-C_\alpha$ in the variable α .

D.3 On the Evaluation of the Integral $\int_{-\infty}^{\infty} \frac{\sqrt{k_0 - k_x}}{k_x - k_{xp}} e^{-jk_x x} dk_x$

The aim of this section is to evaluate in closed form the following spectral integral:

$$I = \int_{-\infty}^{\infty} \frac{\sqrt{k_0 - k_x}}{k_x - k_{xp}} e^{-jk_x x} dk_x. \quad (D.24)$$

Let us perform the following variable substitution:

$$\begin{aligned} k_x &= k_0 \cos \alpha, & k_{xp} &= k_0 \cos \alpha_p \\ \frac{dk_x}{d\alpha} &= \frac{d(k_0 \cos \alpha)}{d\alpha} = \frac{k_0 d(\cos \alpha)}{d\alpha} = -k_0 \sin \alpha. \end{aligned} \quad (D.25)$$

The original path of integration is mapped into $-C_\alpha$, which indicates the path $(\pi + j\infty, \pi + j0) \cup (\pi + j0, 0 + j0) \cup (0 + j0, 0 - j\infty)$, as shown in Fig. D.3.

The integral I can be then written as

$$I = \sqrt{k_0} \int_{C_\alpha} \frac{\sqrt{1 - \cos \alpha}}{\cos \alpha - \cos \alpha_p} e^{-jk_0 x \cos \alpha} \sin \alpha d\alpha. \quad (D.26)$$

Note that the inversion of the integration path from $-C_\alpha$ to C_α introduces a multiplication for (-1) , which cancels out with (-1) deriving from the Jacobean of the transformation. When performing this variable transformation, it is important to guarantee the convergence, so that the exponential does not explode for $\Im\{\alpha\} = \alpha_i = \pm\infty$.

By performing the following algebraic steps

$$\begin{aligned}
\cos(\alpha - \theta) &= \cos(\alpha_r + j\alpha_i - \theta) = \cos(\alpha_r - \theta) \cos(j\alpha_i) - \sin(\alpha_r - \theta) \sin(j\alpha_i) = \\
&= \cos(\alpha_r - \theta) \frac{e^{-\alpha_i} + e^{\alpha_i}}{2} - \sin(\alpha_r - \theta) \frac{e^{-\alpha_i} + e^{\alpha_i}}{2j} = \\
&= \cos(\alpha_r - \theta) \cosh(\alpha_i) - j \sin(\alpha_r - \theta) \sinh(\alpha_i)
\end{aligned} \tag{D.27}$$

we can write

$$e^{-jkr \cos(\alpha - \theta)} = e^{-jkr \cos(\alpha_r - \theta) \cosh(\alpha_i)} e^{-kr \sin(\alpha_r - \theta) \sinh(\alpha_i)}. \tag{D.28}$$

The convergence is then guaranteed if

$$\begin{aligned}
\alpha_i > 0 &\Rightarrow \sinh(\alpha_i) > 0 \text{ converges if } \sin(\alpha_r - \theta) > 0 \Rightarrow \theta < \alpha_r < \theta + \pi \\
\alpha_i < 0 &\Rightarrow \sinh(\alpha_i) < 0 \text{ converges if } \sin(\alpha_r - \theta) < 0 \Rightarrow \theta - \pi < \alpha_r < \theta
\end{aligned} \tag{D.29}$$

Using the following trigonometric properties:

$$\begin{aligned}
\sqrt{1 - \cos \alpha} &= \sqrt{1 - \left(1 - 2 \sin^2 \frac{\alpha}{2}\right)} = \sqrt{2} \sin \frac{\alpha}{2} \\
\cos \alpha - \cos \alpha_p &= \left(1 - 2 \sin^2 \frac{\alpha}{2}\right) - \left(1 - 2 \sin^2 \frac{\alpha_p}{2}\right) = 2 \left(\sin^2 \frac{\alpha_p}{2} - \sin^2 \frac{\alpha}{2}\right) \\
\sin \alpha &= 2 \sin \frac{\alpha}{2} \cos \frac{\alpha}{2}
\end{aligned} \tag{D.30}$$

Eq. (D.26) becomes

$$I = \sqrt{2k_0} \int_{C_\alpha} \frac{\sin^2 \frac{\alpha}{2} \cos \frac{\alpha}{2}}{\sin^2 \frac{\alpha_p}{2} - \sin^2 \frac{\alpha}{2}} e^{-jk_0 x \cos \alpha} d\alpha. \tag{D.31}$$

A few algebraic manipulations can be applied to the fraction in the integrand:

$$\frac{\sin^2 \frac{\alpha}{2}}{\sin^2 \frac{\alpha_p}{2} - \sin^2 \frac{\alpha}{2}} = \frac{\sin^2 \frac{\alpha}{2} - \sin^2 \frac{\alpha_p}{2} + \sin^2 \frac{\alpha_p}{2}}{\sin^2 \frac{\alpha_p}{2} - \sin^2 \frac{\alpha}{2}} = -1 + \frac{\sin^2 \frac{\alpha_p}{2}}{\sin^2 \frac{\alpha_p}{2} - \sin^2 \frac{\alpha}{2}}. \tag{D.32}$$

The integral I can be then expressed as the sum of two contributions $I = I_1 + I_2$, where the two terms are given by

$$\begin{aligned}
 I_1 &= -\sqrt{2k_0} \int_{C_\alpha} \cos \frac{\alpha}{2} e^{-jk_0 x \cos \alpha} d\alpha \\
 I_2 &= \sqrt{2k_0} \int_{C_\alpha} \frac{\sin^2 \frac{\alpha_p}{2}}{\sin^2 \frac{\alpha_p}{2} - \sin^2 \frac{\alpha}{2}} \cos \frac{\alpha}{2} e^{-jk_0 x \cos \alpha} d\alpha
 \end{aligned} \tag{D.33}$$

Both these integrals can be deformed into the $SDP(0)$ and the standard procedure is adopted to integrate from $-\infty$ to ∞ as in Sec. D.3.1. With the variable transformation $\tau^2 = -j2 \sin^2(\frac{\alpha-\theta}{2})$,

$$\int_{SDP(\theta)} e^{-jkr \cos(\alpha-\theta)} d\alpha = e^{j\pi/4} \sqrt{2} e^{-jkr} \int_{-\infty}^{\infty} \frac{e^{-kr\tau^2}}{\sqrt{1-j\frac{\tau^2}{2}}} d\tau \tag{D.34}$$

The procedure leads for the first integral to

$$I_1 = \int_{SDP(0)} G_1(\alpha) e^{-jk_0 x \cos \alpha} d\alpha = e^{j\pi/4} \sqrt{2} e^{-jk_0 x} \int_{-\infty}^{\infty} G_1(\tau) \frac{e^{-k_0 x \tau^2}}{\sqrt{1-j\frac{\tau^2}{2}}} d\tau \tag{D.35}$$

where $G_1(\alpha) = -\sqrt{2k_0} \cos \frac{\alpha}{2}$ and thus

$$G_1(\tau) = -\sqrt{2k_0} \cos \frac{\alpha}{2} = -\sqrt{2k_0} \sqrt{1 - \sin^2(\alpha/2)} = -\sqrt{2k_0} \sqrt{1 - j\frac{\tau^2}{2}}. \tag{D.36}$$

The first integral in Eq. (D.33) can be expressed as

$$\begin{aligned}
 I_1 &= e^{j\pi/4} \sqrt{2} e^{-jk_0 x} \int_{-\infty}^{\infty} \left(-\sqrt{2k_0} \sqrt{1 - j\frac{\tau^2}{2}} \right) \frac{e^{-k_0 x \tau^2}}{\sqrt{1 - j\frac{\tau^2}{2}}} d\tau = \\
 &= -e^{j\pi/4} 2\sqrt{k_0} e^{-jk_0 x} \int_{-\infty}^{\infty} e^{-k_0 x \tau^2} d\tau = \\
 &= -2e^{j\pi/4} \sqrt{\frac{\pi}{x}} e^{-jk_0 x}
 \end{aligned} \tag{D.37}$$

where we used the identity [110]:

$$\int_{-\infty}^{\infty} e^{-\Omega \tau^2} d\tau = \sqrt{\frac{\pi}{\Omega}}. \tag{D.38}$$

Let us now concentrate on the integral I_2 of Eq. (D.33). We can write

$$I_2 = e^{j\pi/4} \sqrt{2} e^{-jk_0 x} \int_{-\infty}^{\infty} G_2(\tau) \frac{e^{-k_0 x \tau^2}}{\sqrt{1 - j \frac{\tau^2}{2}}} d\tau \quad (\text{D.39})$$

with

$$G_2(\tau) = \sqrt{2k_0} \sin^2 \frac{\alpha_p}{2} \frac{\cos \frac{\alpha}{2}}{\sin^2 \frac{\alpha_p}{2} - \sin^2 \frac{\alpha}{2}} = \sqrt{2k_0} \tau_p^2 \frac{\sqrt{1 - j \frac{\tau^2}{2}}}{\tau_p^2 - \tau^2}. \quad (\text{D.40})$$

The integral can be rewritten as follows:

$$I_2 = -2e^{j\pi/4} \sqrt{k_0} e^{-jk_0 x} \tau_p^2 \int_{-\infty}^{\infty} \frac{e^{-k_0 x \tau^2}}{\tau^2 - \tau_p^2} d\tau \quad (\text{D.41})$$

The integral appearing in Eq. (D.41) can be expressed in terms of the Kouyoumjian Fresnel function $F(y)$ (Sec. D.3.2) using

$$\int_{-\infty}^{\infty} \frac{e^{-s^2 x}}{s^2 - s_0^2} ds = -\sqrt{\frac{\pi}{x}} \frac{F(jx s_0^2)}{s_0^2} \Rightarrow \int_{-\infty}^{\infty} \frac{e^{-k_0 x \tau^2}}{\tau^2 - \tau_p^2} d\tau = -\sqrt{\frac{\pi}{k_0 x}} \frac{F(jk_0 x \tau_p^2)}{\tau_p^2} \quad (\text{D.42})$$

The term $F(jk_0 x \tau_p^2)$ can be easily algebraically manipulated as follows:

$$\begin{aligned} F(jk_0 x \tau_p^2) &= F(-jk_0 x 2j \sin^2(\alpha_p/2)) = && (\cos \alpha = 1 - 2 \sin^2(\alpha/2)) \\ &= F\left(2k_0 x \frac{1 - \cos(\alpha_p)}{2}\right) = && (k_{xp} = k_0 \cos \alpha_p) \\ &= F(x(k_0 - k_{xp})) \end{aligned} \quad (\text{D.43})$$

Therefore, the final expression of the second integral I_2 is given by

$$I_2 = 2e^{j\pi/4} e^{-jk_0 x} \sqrt{\frac{\pi}{x}} F(x(k_0 - k_{xp})) \quad (\text{D.44})$$

Combining Eqs. (D.44) and (D.37) we obtain

$$I = I_1 + I_2 = -2e^{j\pi/4} \sqrt{\frac{\pi}{x}} e^{-jk_0 x} (1 - F(x(k_0 - k_{xp}))). \quad (\text{D.45})$$

Multiplying and dividing for $2jx(k_0 - k_{xp})$, and defining the slope Fresnel function as $F_s(z) = 2jz(1 - F(z))$, we have

$$I = -e^{-j\pi/4} \sqrt{\frac{\pi}{x}} e^{-jk_0 x} \frac{F_s(x(k_0 - k_{xp}))}{x(k_0 - k_{xp})}. \quad (\text{D.46})$$

D.3.1 Steepest Descent Path

We now report a standard procedure to evaluate the following integral

$$I = \int_{C_\alpha} e^{-jkr \cos(\alpha - \theta)} d\alpha. \quad (\text{D.47})$$

We may deform this integration path into any path that verifies the convergence requirements. It is rather clear that a path into which the exponential is always decaying and not oscillating as a function of α is the most convenient for numerical integration in the first place and also, as we will see in the following, for analytical purposes. Equation (D.28) shows explicitly that the condition $\cos(\alpha_r - \theta) \cosh(\alpha_i) = 1$ is the path that guarantees this. The locus of points in the α plane that verifies this condition is called Steepest Descent Path (SDP). $\alpha_r = \theta$ indicates the saddle point, i.e. the point in which the integrand's value is e^{-jkr} . In all the other points along the SDP the exponential decays as rapidly as possible, thus it is convenient to perform the integration into this path.

Let us now perform the integral (D.47) by means of the most appropriate change of variable. Since $-jkr \cos(\alpha - \theta)$ on the SDP is equal to $-jkr - kr \sin(\alpha_r - \theta) \sinh(\alpha_i)$ and the real part of this expression is always decaying on the SDP, a substitution of the kind

$$-jkr \cos(\alpha - \theta) = -jkr - kr\tau^2 \quad (\text{D.48})$$

is well suited. τ going from $-\infty$ to $+\infty$ on the real axis guarantees the same behavior of the integrand but this time on a simpler domain:

$$I = \int_{-\infty}^{\infty} e^{-jkr} e^{-kr\tau^2} \frac{d\alpha}{d\tau} d\tau \quad (\text{D.49})$$

Let us now calculate $\frac{d\alpha}{d\tau}$. The condition

$$-jkr \cos(\alpha - \theta) = -jkr \left(1 - 2 \sin^2\left(\frac{\alpha - \theta}{2}\right) \right) = -jkr - kr\tau^2 \quad (\text{D.50})$$

implies that

$$-j2 \sin^2\left(\frac{\alpha - \theta}{2}\right) = \tau^2. \quad (\text{D.51})$$

Taking the square root of both sides, we have

$$\pm e^{-j\pi/4} \sqrt{2} \sin\left(\frac{\alpha - \theta}{2}\right) = \tau. \quad (\text{D.52})$$

It is clear that the \pm symbol is anomalous and will be shortly defined. The differential of the transformation can be calculated as

$$\frac{d\alpha}{d\tau} = \frac{1}{\frac{d\tau}{d\alpha}} = \frac{1}{\pm e^{-j\pi/4} \frac{\sqrt{2}}{2} \cos\left(\frac{\alpha - \theta}{2}\right)} = \frac{\pm e^{j\pi/4} \sqrt{2}}{\cos\left(\frac{\alpha - \theta}{2}\right)}. \quad (\text{D.53})$$

This last expression can be more conveniently written as a function of τ , which leads to

$$\frac{\pm e^{j\pi/4} \sqrt{2}}{\cos\left(\frac{\alpha - \theta}{2}\right)} = \frac{\pm e^{j\pi/4} \sqrt{2}}{\sqrt{1 - \sin^2\left(\frac{\alpha - \theta}{2}\right)}} = \frac{\pm e^{j\pi/4} \sqrt{2}}{\sqrt{1 - j\frac{\tau^2}{2}}}. \quad (\text{D.54})$$

Thus, the integral (D.49) becomes

$$I = \pm e^{j\pi/4} \sqrt{2} e^{-jkr} \int_{-\infty}^{\infty} \frac{e^{-kr\tau^2}}{\sqrt{1 - j\frac{\tau^2}{2}}} d\tau. \quad (\text{D.55})$$

This integral is undefined by the \pm symbol. The uncertainty derives from the presence of the multivalued function $\sqrt{\cdot}$ that led to Eq. (D.52). The ambiguity is solved by looking at the differential $\frac{d\alpha}{d\tau}$. On the integration path in τ ranging from $-\infty$ to ∞ , $d\tau$ is positive. Thus $\frac{d\alpha}{d\tau}$ is a complex function having the same argument of $d\alpha$. Let us take any point on the integration path in α for instance $\alpha = \theta$. Since $\left.\frac{d\alpha}{d\tau}\right|_{\alpha=\theta} = \pm e^{j\pi/4} \sqrt{2}$,

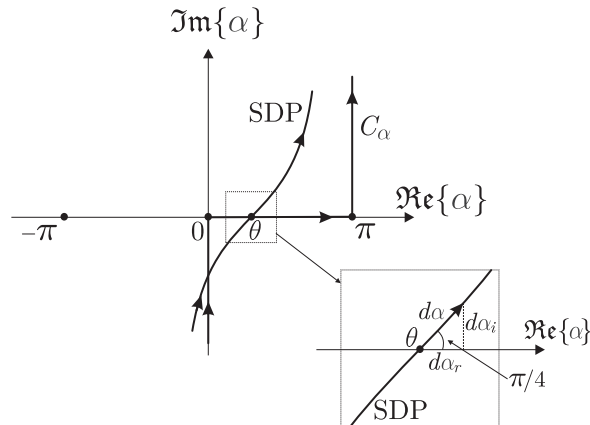


Figure D.4: Argument of $d\alpha$ on the SDP around the saddle point.

$$\begin{aligned}
 \text{"+" implies: } \arg\left(\frac{d\alpha}{d\tau}(\alpha = \theta)\right) &= \pi/4 \\
 \text{"-" implies: } \arg\left(\frac{d\alpha}{d\tau}(\alpha = \theta)\right) &= 5\pi/4
 \end{aligned}
 \tag{D.56}$$

The $d\alpha|_{\alpha=\theta}$ represents an infinitesimal change on the SDP in the proximity of the saddle point. In this point, the SDP forms an angle of $\pi/4$ with the real α -axis ($d\alpha_r = d\alpha_i$), as shown in Fig. D.4. This implies that the right choice for the sign Eq. (D.55) is given by $\frac{d\alpha}{d\tau}(\alpha = \theta) = +e^{j\pi/4}\sqrt{2}$.

Eventually the integral on the SDP can be well performed in the τ domain as

$$I = \int_{SDP(\theta)} e^{-jkr \cos(\alpha-\theta)} d\alpha = e^{j\pi/4}\sqrt{2}e^{-jkr} \int_{-\infty}^{\infty} \frac{e^{-kr\tau^2}}{\sqrt{1 - j\frac{\tau^2}{2}}} d\tau.
 \tag{D.57}$$

D.3.2 Fresnel Integral

We now present the solution of the following canonical integral in terms of Fresnel functions:

$$I_0 = \int_{-\infty}^{\infty} \frac{e^{-s^2 x}}{s^2 - s_0^2} ds
 \tag{D.58}$$

where $s_0^2 = jb^2$. This starting integral converges for x real, $x > 0$ or for x complex but with $\Re\{x\} > 0$, so that $e^{-s^2 x}$ tends to 0 for s large ($e^{-s^2(x_r + jx_i)} = e^{-s^2 x_r} e^{-js^2 x_i}$). Let us also

assume that $s_0^2 = jb^2$, where b is real, and that x is real and positive ($x > 0$). However, the extension to complex b or x is possible. The integral can be written as

$$I_0 = \int_{-\infty}^{\infty} \frac{e^{-(s^2-jb^2+jb^2)x}}{s^2-jb^2} ds = e^{-jb^2x} \int_{-\infty}^{\infty} \frac{e^{-(s^2-jb^2)x}}{s^2-jb^2} ds = e^{-jb^2x} \int_{-\infty}^{\infty} \left(\int_x^{\infty} e^{-(s^2-jb^2)\xi} d\xi \right) ds \quad (\text{D.59})$$

The integral in the parentheses converges only for $e^{jb^2\infty} = 0$; that is, for $\Im\{b^2\} > 0$. This is equivalent to accept some losses in the medium (in k) to have the convergence of the entire representation. If one then interchanges the order of the integration, obtains

$$I_0 = e^{-jb^2x} \int_x^{\infty} e^{jb^2\xi} \left(\int_{-\infty}^{\infty} e^{-s^2\xi} ds \right) d\xi. \quad (\text{D.60})$$

The integral in ds has a known closed form [110]:

$$\int_{-\infty}^{\infty} e^{-s^2\xi} ds = \sqrt{\frac{\pi}{\xi}}. \quad (\text{D.61})$$

Therefore, we can write

$$I_0 = \sqrt{\pi} e^{-jb^2x} \int_x^{\infty} \frac{e^{jb^2\xi}}{\sqrt{\xi}} d\xi. \quad (\text{D.62})$$

This form can be further simplified by performing another change of variable in the integration:

$$\xi = -\frac{\theta^2}{b^2} \Rightarrow \xi b^2 = -\theta^2, \quad \pm j\sqrt{\xi}b = \theta, \quad \frac{d\xi}{d\theta} = -\frac{2\theta}{b^2}. \quad (\text{D.63})$$

The sign \pm will have to be better defined. The integral becomes

$$I_0 = \sqrt{\pi} e^{-jb^2x} \int_{\pm j\sqrt{xb}}^{\infty} \mp j b \frac{e^{-j\theta^2}}{\theta} \frac{2\theta}{b^2} d\theta = \frac{\mp 2j\sqrt{\pi} e^{-jb^2x}}{b} \int_{\pm j\sqrt{xb}}^{\infty} e^{-j\theta^2} d\theta. \quad (\text{D.64})$$

We can now express this formula in terms of the Kouyoumjian Fresnel function, which is defined as follows [93]:

$$F(y) = 2j\sqrt{y}e^{jy} \int_{\sqrt{y}}^{\infty} e^{-jt^2} dt; \quad -\frac{3\pi}{2} < \arg(y) \leq \frac{\pi}{2}. \quad (\text{D.65})$$

By substituting $\sqrt{-xb^2} = \sqrt{y}$, where the choice of the positive branch is arbitrary for the moment, we obtain

$$-\frac{F(-xb^2)}{2\sqrt{xb}e^{-jxb^2}} = \int_{j\sqrt{xb}}^{\infty} e^{-jt^2} dt; \quad -\frac{3\pi}{2} < \arg(-xb^2) \leq \frac{\pi}{2} \quad (\text{D.66})$$

This expression can be substituted in Eq. (D.64), which yields

$$I_0 = \frac{\mp 2j\sqrt{\pi}e^{-jb^2x}}{b} \frac{F(-xb^2)}{\mp 2\sqrt{xb}e^{-jxb^2}} = j\sqrt{\frac{\pi}{x}} \frac{F(-xb^2)}{b^2}. \quad (\text{D.67})$$

Regarding the choice on the branch, it is clear that in this case the selection of the sign is irrelevant, provided that the choice in the change of variable (D.63) is coherent with the choice in the definition of the Fresnel function.

Bibliography

- [1] K. Kegel and R. Bolt, "ACTiFE, Advanced Antenna Concepts for Aircraft in-Flight Entertainment, Identification antenna requirements," European Space Agency, Noordwijk, Netherland, Tech. Rep. 3 WP 0300, ESA Contract no. C19865, May 2007.
- [2] The SKA website. [Online]. Available: <http://www.skatelescope.org/>
- [3] M. Ferlet, N. Geis, J. Goicoechea, D. K. Griffin, A. M. Heras, K. Isaak, T. Nakagawa, T. Onaka, N. Rando, B. Swinyard, N. Takahashi, and S. Vives, "SPICA assessment study report: Revealing the origins of planets and galaxies, Assessment study report," European Space Agency, Noordwijk, Netherland, Tech. Rep. ESA/SRE(2009)6, Dec. 2009.
- [4] M. P. G. Otten, "Radar program final report," TNO Defence, Security and Safety, The Hague, Netherlands, Tech. Rep. Program no. V703, Mar. 2011.
- [5] C. L. Carilli and S. Rawlings, Eds., *Science with the Square Kilometer Array*. New Astronomy Reviews, vol.48, Amsterdam: Elsevier, Dec. 2004.
- [6] M. V. Ivashina, M. N. M. Kehn, P. S. Kildal and R. Maaskant, "Decoupling efficiency of a wideband Vivaldi focal plane array feeding a reflector antenna," *IEEE Trans. Antennas Propag.*, vol. 57, no. 2, pp. 373-382, Feb. 2009.
- [7] D. H. Schaubert, A. van Ardenne, and C. Craeye, "The Square Kilometer Array (SKA) antenna," in *Proc. IEEE Int. Symp. on Phased Array Systems and Technology*, Boston, MA, USA, Oct. 2003, pp. 351-358.
- [8] S. G. Hay, F. R. Cooray, J. D. O'Sullivan, N-T. Huang, and R. Mittra, "Numerical and experimental studies of a dual-polarized planar connected-array antenna for the Australian Square Kilometer Array Pathfinder," in *Proc. IEEE Antennas Propag. Symp.*, Charleston, SC, USA, Jun. 2009, pp. 1-4.

-
- [9] A. C. Ludwig, "The definition of cross polarization," *IEEE Trans. Antennas Propag.*, vol. AP-21, no. 1, pp. 116-119, Jan. 1973.
- [10] D. Cavallo, "An investigation of the performance of Ultra-Wide-Band (UWB) tapered slot antennas and arrays," M.S. thesis, Dept. Engineering, University of Sannio, Benevento, Italy, 2007.
- [11] T.-H. Chio and D. H. Schaubert, "Parameter study and design of wide-band widescan dual-polarized tapered slot antenna arrays," *IEEE Trans. Antennas Propag.*, vol. 48, no. 6, pp. 879-886, Jun. 2000.
- [12] J. J. Lee, S. Livingston, and R. Koenig, "A low-profile wide-band (5:1) dual-pol array," *IEEE Antennas Wireless Propag. Lett.*, vol. 2, pp. 46-49, 2003.
- [13] D. H. Schaubert, J. Shin, and G. Wunsch, "Characteristics of single-polarized phased array of tapered slot antennas," in *Proc. IEEE Int. Symp. on Phased Array Systems and Technology*, Boston, MA, USA, Oct. 1996, pp. 102-106.
- [14] Y. S. Kim and K. S. Yngvesson, "Characterization of tapered slot antennas feeds and feed array," *IEEE Trans. Antennas Propag.*, vol. 38, no. 10, pp. 1559-1564, Oct. 1990.
- [15] D. H. Schaubert, "Radiation characteristic of linearly tapered slot antennas," in *Proc. IEEE Antennas Propag. Int. Symp.*, San Jose, CA, USA, Jun. 1989, vol. 3, pp. 1324-1327.
- [16] D. T. McGrath, N. Schuneman, T. H. Shively, and J. Irion II, "Polarization properties of scanning arrays," in *Proc. IEEE Int. Symp. on Phased Array Systems and Technology*, Boston, MA, USA, Oct. 2003, pp. 295-299.
- [17] R. Maaskant, "Analysis of Large Antenna Systems," Ph.D. dissertation, Eindhoven University of Technology, Eindhoven, Netherlands, 2010.
- [18] R. B. Waterhouse, "Design and performance of large phased arrays of aperture stacked patches," *IEEE Trans. Antennas Propag.*, vol. 49, no. 2, pp. 292-297, Feb. 2001.
- [19] R. B. Waterhouse, "Design and scan performance of large, probe-fed stacked microstrip patch arrays," *IEEE Trans. Antennas Propag.*, vol. 50, no. 6, pp. 893-895, Jun. 2002.

- [20] W. S. T. Rowe, R. B. Waterhouse, and C. T. Huat, "Performance of a scannable linear array of hi-lo stacked patches," *IEE Proc. Microw. Antennas Propag.*, vol. 150, no. 1, pp. 1-4, Feb. 2003.
- [21] M. A. Gonzalez de Aza, J. Zapata, and J. A. Encinar, "Broad-band cavity-backed and capacitively probe-fed microstrip patch arrays," *IEEE Trans. Antennas Propag.*, vol. 48, no. 5, pp. 784-789, May 2000.
- [22] M. C. van Beurden, A. B. Smolders, M. E. J. Jeuken, G. H. C. van Werkhoven, and E. W. Kolk, "Analysis of wide-band infinite phased arrays of printed folded dipoles embedded in metallic boxes," *IEEE Trans. Antennas Propag.*, vol. 50, no. 9, pp. 1266-1273, Sep. 2002.
- [23] C. Baum, "Some characteristics of planar distributed sources for radiating transient pulses," Sensor and Simulation Notes, Note 100, AF Weapons Lab., pp. 1-31, Mar. 1970.
- [24] N. Inagaki, Y. Isogai, and Y. Mushiake, "Ichimatsu Moyou antenna - Self-complementary antenna with periodic feeding points," *Trans. IECE Jpn.*, vol. 62-B, no. 4, pp. 388-395, Apr. 1979.
- [25] R. C. Hansen, "Linear connected arrays," *IEEE Antennas Wireless Propag. Lett.*, vol. 3, pp. 154-156, 2004.
- [26] B. A. Munk, *Finite Antenna Arrays and FSS*. Hoboken: John Wiley & Sons, Inc., 2003.
- [27] H. A. Wheeler, "The radiation resistance of an antenna in an infinite array or waveguide," *Proc. IRE*, vol. 36, no. 4, pp. 478-487, Apr. 1948.
- [28] H. A. Wheeler, "Simple relations derived from a phased array antenna made of an infinite current sheet," *IEEE Trans. Antennas Propag.*, vol. AP-13, no. 4, pp. 506-514, Jul. 1965.
- [29] J.J. Lee, S. Livingstone, and R. Koenig, "Wide band slot array antennas," in *Proc. IEEE Antennas Propag. Symp.*, Columbus, OH, USA, Jun. 2003, vol. 2, pp. 452-455.
- [30] A. Neto and J. J. Lee, "Infinite bandwidth long slot array antenna," *IEEE Antennas Wireless Propag. Lett.*, vol 4, pp. 75-78, 2005.

- [31] A. Neto and J.J. Lee, "Ultrawide-band properties of long slot arrays" *IEEE Trans. Antennas Propag.*, vol. 54, no. 2, pp. 534-543, Feb. 2006.
- [32] A. Neto and S. Maci, "Green's function of an infinite slot printed between two homogeneous dielectrics. Part I: magnetic currents," *IEEE Trans. Antennas Propag.*, vol. 51, no. 7, pp. 1572-1581, Jul. 2003.
- [33] J. J. Lee, S. Livingston, and D. Nagata, "A low profile 10:1 (200-2000 MHz) wide band long slot array," in *Proc. IEEE Antennas Propag. Int. Symp.*, San Diego, CA, USA, Jul. 5-11, 2008.
- [34] X. Dardenne and C. Craeye, "Simulation of the effects of a ground plane on the radiation characteristics of self-complementary arrays," in *Proc. IEEE Antennas Propag. Int. Symp.*, Columbus, OH, USA, Jun. 2003, vol. 1, pp. 383-386.
- [35] J.J. Lee, S. Livingston, R. Koenig, D. Nagata, and L. L. Lai, "Compact light weight UHF arrays using long slot apertures," *IEEE Trans. Antennas Propag.*, vol. 54, no. 7, pp. 2009-2015, Jul. 2006.
- [36] S. Maci and A. Neto, "Green's function of an infinite slot printed between two homogeneous dielectrics. Part II: uniform asymptotic solution," *IEEE Trans. Antennas Propag.*, vol. 52, no. 3, pp. 666-676, Mar. 2004.
- [37] A. Neto and S. Maci, "Input impedance of slots printed between two dielectric media and fed by a small Δ -gap," *IEEE Antennas Wireless Propag. Lett.*, vol. 3, pp. 113-116, 2004.
- [38] A. P. Prudnikov, Yu. A. Brychkov, and O. I. Marichev, *Integrals and Series, Volume 2: Special Functions*. Amsterdam: Gordon and Breach Science Publisher, 1986.
- [39] L. B. Felsen and N. Marcuvitz, *Radiation and Scattering of Waves*. New York: IEEE Press, 1994.
- [40] R. E. Collin, *Field Theory of Guided Waves*. New York: McGraw-Hill, 1960.
- [41] Ansoft HFSS, ver. 11, Ansoft Corporation, Pittsburgh, PA, [Online]. Available: <http://www.ansoft.com/>
- [42] A. Ralston, *A First Course in Numerical Analysis*. New York: McGraw-Hill, 1965.

- [43] P. Focardi, A. Neto, and R. McGrath, "Coplanar-waveguide-based terahertz hot-electron bolometer mixers: Improved embedding circuit description," *IEEE Trans. Microw. Theory Tech.*, vol. 50, no. 10, pp. 2374-2383, Oct. 2002.
- [44] D. Cavallo, A. Neto, G. Gerini, and G. Toso, "On the potentials of connected slots and dipoles in the presence of a backing reflector," in *Proc. 30th ESA Workshop on Antennas for Earth Observation, Science, Telecommunication and Navigation Space Missions*, Noordwijk, Netherlands, May 2008, pp. 407-410.
- [45] A. Neto, D. Cavallo, G. Gerini, R. Grooters, and G. Toso, "Array antenna," European Patent WO/2009/128716, Oct. 22, 2009.
- [46] N. Amitay, V. Galindo, and C.P. Wu, *Theory and Analysis of Phased Array Antennas*. New York: John Wiley and Sons, Inc., 1972.
- [47] A. A. Oliner and R. G. Malech, "Mutual coupling in infinite scanning arrays," in *Microwave Scanning Antennas*, vol. II, R. C. Hansen, Ed. New York: Academic Press, 1966, ch. 3.
- [48] A. Ishimaru, R. J. Coe, G. E. Miller, and W. P. Geren, "Finite periodic structure approach to large scanning array problems," *IEEE Trans. Antennas Propag.*, vol. AP-33, no. 11, pp. 1213-1220, Nov. 1985.
- [49] Ansoft Designer, ver. 3.5, Ansoft Corporation, Pittsburgh, PA, [Online]. Available: <http://www.ansoft.com/>
- [50] C. G. Montgomery, R. H. Dicke, and E. M. Purcell, *Principles of Microwave Circuits*. Radiation Lab. Ser., vol. 18. New York: McGraw-Hill, 1948, pp. 317-333.
- [51] J. D. Kraus, *Antennas*. New York: McGraw-Hill, 1950, p. 46.
- [52] C. A. Balanis, *Antenna Theory, Analysis and Design, Third Edition*. Hoboken: John Wiley & Sons, Inc., 2005.
- [53] S. Silver, Ed., *Microwave Antenna Theory and Design, First Edition*. New York: McGraw-Hill, 1949, pp. 45-48.
- [54] S. Ramo and J. R. Whinnery, *Fields and Waves in Modern Radio, Second Edition*. New York: John Wiley & Sons, Inc., 1953, p. 564.

- [55] R. B. Green, "Scattering from Conjugate-Matched Antennas," *IEEE Trans. Antennas Propag.*, vol. AP-14, no. 1, pp. 17-21, Jan. 1966.
- [56] J. Van Bladel, "On the Equivalent Circuit of a Receiving Antenna," *IEEE Antennas Propag. Mag.*, vol. 44, no. 1, pp. 164-165, Feb. 2002.
- [57] A. W. Love, "Comment on the equivalent circuit of a receiving antenna," *IEEE Antennas Propag. Mag.*, vol. 44, no. 5, pp. 124-125, Oct. 2002.
- [58] R. E. Collin, "Limitations on the Thévenin and Norton equivalent circuits for a receiving antenna," *IEEE Antennas Propag. Mag.*, vol. 45, no. 2, pp. 119-124, Apr. 2003.
- [59] A. W. Love, "Comment on "Limitations of the Thévenin and Norton equivalent circuits for a receiving antenna",," *IEEE Antennas Propag. Mag.*, vol. 45, no.4, pp. 98-99, Aug. 2003.
- [60] J. B. Andersen and R. G. Vaughan, "Transmitting, receiving, and scattering properties of antennas," *IEEE Antennas Propag. Mag.*, vol. 45, no.4, pp. 93-98, Aug. 2003.
- [61] D.-H. Kwon, D. M. Pozar, "Optimal characteristics of an arbitrary receive antenna," *IEEE Trans. Antennas Propag.*, vol. 57, no. 12, pp. 3720-3727, Dec. 2009.
- [62] M. Pasian, S. Monni, A. Neto, M. Ettorre, and G. Gerini, "Frequency selective surfaces for extended bandwidth backing reflector functions," *IEEE Trans. Antennas Propag.*, vol. 58, no. 1, pp. 43-50, Jan. 2010.
- [63] S. Monni, "Frequency selective surfaces integrated with phased array antennas: Analysis and design using Multimode Equivalent Networks," Ph.D. dissertation, Eindhoven University of Technology, Eindhoven, Netherlands, 2005.
- [64] S. Monni, G. Gerini, A. Neto, and A. G. Tijhuis, "Multimode equivalent networks for the design and analysis of frequency selective surfaces," *IEEE Trans. Antennas Propag.*, vol. 55, no. 10, pp. 2824-2835, Oct. 2007.
- [65] N. Appannagarri, I. Bardi, R. Edlinger, J. Manges, M. Vogel, Z. Cendes, and J. Hadden, "Modeling phased array antennas in Ansoft HFSS," in *Proc. IEEE Int. Conf. on Phased Array Systems and Technology*, Dana Point, CA , USA, May 2000, pp. 323-326.

- [66] R. S. Johnson, C. Wakeman, and W. Cuviallo, "Frequency response of thin film chip resistor," in *Proc. of the 25th CARTS USA 2005*, Palm Springs, CA, USA, Mar. 2005, pp. 136-141.
- [67] D. Cavallo, S. Savoia, G. Gerini, A. Neto, and V. Galdi, "Design of a low profile printed array of loaded dipoles with inherent frequency selectivity properties," in *Proc. 5th European Conference on Antennas and Propag., (EuCAP 2011)*, Rome, Italy, Apr. 2011.
- [68] S. Savoia, "Design of an array of connected dipoles with inherent frequency selectivity properties for radar applications," M.S. thesis, Dept. Engineering, University of Sannio, Benevento, Italy, 2010.
- [69] H. Holter, T.-H. Chio and D. H. Schaubert, "Experimental results of 144-element dual-polarized endfire tapered-slot phased arrays," *IEEE Trans. Antennas and Propag.*, vol. 48, no. 11, pp. 1707-1718, Nov. 2000.
- [70] C. Craeye, "On the radiation characteristics of finite dual-polarized arrays of tapered-slot antennas," in *Proc. IEEE Antennas Propag. Int. Symp.*, Monterey, CA, USA, Jun. 2004, vol. 3, pp. 2691-2694.
- [71] C. Craeye and X. Dardenne, "Element pattern analysis of wide-band arrays with the help of a finite-by-infinite array approach," *IEEE Trans. Antennas and Propag.*, vol. 54, no. 2, pp. 519-526, Feb. 2006.
- [72] R. C. Hansen, "Connected Arrays," in *Phased Array Antennas, Second Edition*, Hoboken: John Wiley & Sons, Inc., 2009, pp. 465-477.
- [73] D. Bekers, "Finite Antenna Arrays - An Eigencurrent Approach," Ph.D. dissertation, Eindhoven University of Technology, Eindhoven, Netherlands, 2004.
- [74] J. L. Volakis, *Antenna Engineering Handbook, Fourth Edition*. New York: McGraw-Hill, 2007.
- [75] D. S. Janning and B. A. Munk, "Effects of surface waves on the currents of truncated periodic arrays," *IEEE Trans. Antennas and Propag.*, vol. 50, no. 9, pp. 1254-1265, Sep. 2002.
- [76] O. A. Civi and P. H. Pathak, "Array guided surface waves on a finite planar array of dipoles with or without a grounded substrate," *IEEE Trans. Antennas and Propag.*, vol. 54, no. 8, pp. 2244-2252, Aug. 2006.

- [77] N. Amitay, V. Galindo, and C.P. Wu, *Theory and Analysis of Phased Array Antennas*. New York: John Wiley & Sons, Inc., New York, 1972.
- [78] A. K. Skrivervik and J. R. Mosig, "Finite phased array of microstrip patch antennas: the infinite array approach," *IEEE Trans. Antennas and Propag.*, vol. 40, no. 5, pp. 579-582, May 1992.
- [79] A. K. Skrivervik and J. R. Mosig, "Analysis of finite phase arrays of microstrip patches," *IEEE Trans. Antennas and Propag.*, vol. 41, no. 8, pp. 1105-1114, Aug. 1993.
- [80] A. J. Roscoe and R. A. Perrott, "Large finite array analysis using infinite array data," *IEEE Trans. Antennas and Propag.*, vol. 42, no. 7, pp. 983-992, Jul. 1994.
- [81] K. A. Shubert and B. A. Munk, "Matching properties of arbitrarily large dielectric covered phased arrays," *IEEE Trans. Antennas and Propag.*, vol. 31, no. 1, pp. 54-59, Jan. 1983.
- [82] F. Capolino and M. Albani, "Truncation effects in a semi-infinite periodic array of thin strips: a discrete Wiener-Hopf formulation," *Radio Sci.*, vol. 44, no. RS2S91, Apr. 2009, doi:10.1029/2007RS003821.
- [83] A. Neto, S. Maci, G. Vecchi, and M. Sabbadini, "A truncated Floquet wave diffraction method for the full wave analysis of large phased arrays - part I: basic principles and 2-D cases" *IEEE Trans. Antennas and Propag.*, vol. 48, no. 3, pp. 594-600, Mar. 2000.
- [84] H.-T. Chou, H.-K. Ho, P. H. Pathak, P. Nepa, and O. A. Civi, "Efficient hybrid discrete Fourier transform-moment method for fast analysis of large rectangular arrays," *IEE Proc. Microw. Antennas Propag.*, vol. 149, no. 1, pp. 1-6, Aug. 2002.
- [85] L. Carin and L. B. Felsen, "Time harmonic and transient scattering by finite periodic flat strip arrays: hybrid (ray)-(Floquet mode)-(MoM) algorithm," *IEEE Trans. Antennas and Propag.*, vol. 41, no. 4, pp. 412-421, Apr. 1993.
- [86] F. Capolino, M. Albani, S. Maci, and R. Tiberio, "High-frequency analysis of an array of line sources on a truncated ground plane" *IEEE Trans. Antennas and Propag.*, vol. 46, no. 4, pp. 570-578, Apr. 1998.
- [87] O. A. Civi, P. H. Pathak, and H.-T. Chou, "On the Poisson sum formula for the analysis of wave radiation and scattering from large finite arrays," *IEEE Trans. Antennas and Propag.*, vol. 47, no. 5, pp. 958-959, May 1999.

- [88] F. Capolino, M. Albani, S. Maci, and L. B. Felsen, "Frequency domain Greens function for a planar periodic semi-infinite phased array. Part I: Truncated Floquet wave formulation," *IEEE Trans. Antennas and Propag.*, vol. 48, no. 1, pp. 67-74, Jan. 2000.
- [89] F. Capolino, M. Albani, S. Maci, and L. B. Felsen, "Frequency domain Greens function for a planar periodic semi-infinite phased array. Part II: Diffracted wave phenomenology," *IEEE Trans. Antennas and Propag.*, vol. 48, no. 1, pp. 75-85, Jan. 2000.
- [90] R. C. Hansen and D. Gammon, "A Gibbsian model for finite scanned arrays," *IEEE Trans. Antennas and Propag.*, vol. 44, no. 2, pp. 243-248, Feb 1996.
- [91] R. C. Hansen, "Finite array scan impedance Gibbsian models," *Radio Sci.*, vol. 31, no. 6, pp. 1631-1637, Mar. 1996, doi:10.1029/96RS01366.
- [92] M. Abramowitz and I. A. Stegun, Ed., *Handbook of Mathematical Functions, With Formulas, Graphs, and Mathematical Tables*. New York: Dover Publications, Inc., 1965.
- [93] R. G. Kouyoumjian and P. H. Pathak, "A uniform geometrical theory of diffraction for an edge in a perfectly conducting surface," *Proc. IEEE*, vol. 62, no. 11, pp. 1448-1461, Nov. 1974.
- [94] M. Norn and E. Wolf, *Principles of Optics, Seventh Edition*. Cambridge: Cambridge University Press, 1999.
- [95] P. C. Clemmow, *The Plane Wave Spectrum Representation of Electromagnetic Fields*. New York: IEEE Press, 1996.
- [96] S. G. Hay and J. D. O'Sullivan, "Analysis of common-mode effects in a dual-polarized planar connected-array antenna," *Radio Sci.*, vol. 43, no. RS6S04, Dec. 2008, doi:10.1029/2007RS003798.
- [97] E. de Lera Acedo, E. Garcia, V. Gonzalez-Posadas, J. L. Vazquez-Roy, R. Maaskant, and D. Segovia, "Study and design of a differentially-fed tapered slot antenna array," *IEEE Trans. Antennas Propag.*, vol. 58, no. 1, pp. 68-78, Jan. 2010.
- [98] Laird Technologies. (2011) Common mode chokes. [Online]. Available: <http://www.lairdtech.com/Products/EMI-Solutions/Ferrite-Products/Ferrite-Common-Mode-Chokes/>

- [99] NIC Components Corporation. (2011) Surface mount common mode chokes. [Online]. Available: <http://www.niccomp.com/products/>
- [100] Murata Manufacturing Company, Ltd. (2011) Selection guide of chip common mode choke coils. [Online]. Available: <http://www.murata.com/products/emc/>
- [101] J. D. O'Sullivan, F. Cooray, C. Granet, R. Gough, S. Hay, D. Hayman, M. Kesteven, J. Kot, A. Grancea, and R. Shaw, "Phased array feed development for the Australian SKA pathfinder," presented at Int. Union Radio Sci. XXIX Gen. Assembly, Chicago, IL, USA, Aug. 2008.
- [102] J. G. B. de Vaate, L. Bakker, E. E. M. Woestenburg, R. H. Witvers, G. W. Kant, and W. van Cappellen, "Low cost low noise phased-array feeding systems for SKA pathfinders," in *Proc. 13th Int. Symp. on Antenna Tech. & Applied Electromagnetics (ANTEM)*. Toronto, Canada, Feb. 15-18, 2009, pp. 1-4.
- [103] J. B. Knorr, "Slot-line transitions," *IEEE Trans. Microw. Theory Tech.*, vol. MTT-22, no. 5, pp. 548-554, May 1974.
- [104] N. Herscovici and D. M. Pozar, "Full-wave analysis of aperture-coupled microstrip lines," *IEEE Trans. Microw. Theory Tech.*, vol. 39, no. 7, pp. 1108-1114, Jul. 1991.
- [105] A. Neto, D. Cavallo, R. Grooters, and G. Gerini, "Advanced antenna concepts for aircraft in-flight entertainment: Preliminary definition of a connected array antenna demonstrator," European Space Agency, Noordwijk, Netherland, Tech. Rep. 6 WP 0600, ESA Contract no. C19865, Jun. 2009.
- [106] R. Grooters, G. Gerini, A. Neto, R. Bolt, and D. Cavallo, "ACTiFE phase 2, System/demonstrator definition of single panel connected array antenna," European Space Agency, Noordwijk, Netherland, Tech. Rep. 21 WP 2100, ESA Contract no. 4000101757, Feb. 2011.
- [107] P. de Hek, K. Van Caekenberghe, R. van Dijk, "A 3-14 GHz pseudo-differential distributed low noise amplifier," in *Proc. European Microwave Integrated Circuits Conference (EuMIC)*, Paris, France, Sep. 2010, pp. 337-340.
- [108] M. P. G. Otten and A. G. Huizing, "Requirements for scalable multifunction RF systems," TNO Defence, Security and Safety, The Hague, Netherlands, Tech. Rep. TNO-DV2009 A553, Jul. 2010.

-
- [109] R. Bolt, D. Bekers, R. van Dijk, and G. Gerini, “Communications in future combatant,” TNO Defence, Security and Safety, The Hague, Netherlands, Tech. Rep. 31379, Jun. 2010.
- [110] S. Maci, Z. Sipus, A. Freni, A. Mazzinghi, and S. Skokic, *Advanced Mathematics for Antenna Analysis*. Class notes for European School of Antennas Course, Dubrovnik, Croatia, May 10-18, 2010.
- [111] B. L. Van der Waerden, “On the method of saddle points,” *Appl. Sci. Res.* vol. B2, pp. 33-45, 1951.

List of Publications

Journal Papers

- J1.** A. Neto, D. Cavallo, G. Gerini, and G. Toso, "Scanning performances of wide band connected arrays in the presence of a backing reflector," *IEEE Trans. Antennas Propag.*, vol. 57, no. 10, pp. 3092-3102, Oct. 2009.
- J2.** D. Cavallo, A. Neto, and G. Gerini, "PCB slot based transformers to avoid common-mode resonances in connected arrays of dipoles," *IEEE Trans. Antennas Propag.*, vol. 58, no. 8, pp. 2767-2771, Aug. 2010.
- J3.** D. Cavallo, A. Neto, and G. Gerini, "Green's function based equivalent circuits for connected arrays in transmission and in reception," *IEEE Trans. Antennas Propag.*, vol. 59, no. 5, pp. 1535-1545, May 2011.
- J4.** A. Neto, D. Cavallo, and G. Gerini, "Edge-born waves in connected arrays: a finite \times infinite analytical representation," *IEEE Trans. Antennas Propag.*, accepted for publication.
- J5.** D. Cavallo, A. Neto, and G. Gerini, "A 3 to 5 GHz prototype connected array of dipoles for wide-scanning, low X-pol applications," *IEEE Trans. Antennas Propag.*, in preparation.
- J6.** D. Cavallo, A. Neto, G. Gerini, "Analytical description and design of printed dipole arrays for wideband wide-scan applications," *IEEE Trans. Antennas Propag.*, under review.

Conference Papers

- C1.** D. Cavallo, A. Neto, and G. Gerini, "Connected array antennas for ultrawide band radar applications," *IEEE Conference on Microwave, Communication, Antennas and*

Electronic Systems (COMCAS 2008), Tel Aviv, Israel, May 13-14, 2008.

- C2. D. Cavallo, A. Neto, G. Gerini, and G. Toso, "On the potentials of connected slots and dipoles in the presence of a backing reflector," *30th ESA Workshop on Antennas for Earth Observation, Science, Telecommunication and Navigation Space Missions*, Noordwijk, Netherlands, May 27-30, 2008. (**Awarded with the Best Innovative Paper Prize**)
- C3. D. Cavallo, A. Neto, and G. Gerini, "Toward the design of a wide-scan, wide-band, low-cross-pol printed array," *URSI Forum 2008*, Brussels, Belgium, May 30, 2008.
- C4. D. Cavallo, A. Neto, G. Gerini, and G. Toso, "On the potentials of connected array technology for wide band, wide scanning, dual polarized applications," *IEEE Antennas and Propagation Society International Symposium*, San Diego, CA, July 5-12, 2008.
- C5. A. Neto, D. Cavallo, G. Gerini, G. Toso, and F. E. van Vliet, "A comparison between the Green's functions of connected slots and dipoles in the presence of a backing reflector," *38th European Microwave Conference (EuMC)*, Amsterdam, Netherlands, October 27-31, 2008, pp. 508-510.
- C6. A. Neto, D. Cavallo, and G. Gerini, "UWB, wide angle scanning, planar arrays based on connected dipoles concept," *Sensors & Electronics Technology Panel Specialist Meeting (SET-120) on Ultra Wideband Radar Systems*, Toulouse, France, October 27-28, 2008.
- C7. D. Cavallo, A. Neto, G. Gerini, and G. Toso, "Scanning performances of wide band connected arrays of slots and dipoles," *3rd European Conference on Antennas and Propagation (EUCAP 2009)*, Berlin, Germany, March 23-27, 2009, pp. 1222-1224.
- C8. D. Cavallo, A. Neto, G. Gerini, and G. Toso, "A wide-band dual-polarized array of connected dipoles," *5th ESA Workshop on Millimetre Wave Technology and Applications and 31st ESA Antenna Workshop*, Noordwijk, Netherlands, May 18-20, 2009, pp. 209-216.
- C9. A. Neto, D. Cavallo, and G. Gerini, "Common mode, differential mode and baluns: the secrets," *5th ESA Workshop on Millimetre Wave Technology and Applications and 31st ESA Antenna Workshop*, Noordwijk, Netherlands, May 18-20, 2009, pp. 718-723.

- C10. D. Cavallo, A. Neto, G. Gerini, and G. Toso, "A wide-band dual-pol array of printed dipoles," *IEEE Antennas and Propagation Society International Symposium*, Charleston, SC, June 1-5, 2009, p. IF114.1.
- C11. D. Cavallo, A. Neto, and G. Gerini, "Analysis of common-mode resonances in arrays of connected dipoles and possible solutions," *6th European Radar Conference (EuRAD)*, Rome, Italy, September 30 - October 2, 2009, pp. 441-444.
- C12. D. Cavallo, A. Neto, and G. Gerini, "Common mode resonances in UWB connected arrays of dipoles: measurements from the demonstrator and exit strategy," *11th Edition of the International Conference on Electromagnetics in Advanced Applications (ICEAA)*, Turin, Italy, September 14-18, 2009, pp. 435-438. (**invited paper**)
- C13. G. Gerini, D. Cavallo, A. Neto, and F. van den Bogaart, "Connected arrays of dipoles for telecom and radar applications: the solution for the common mode problem," *Wide Band Sparse Element Array Antennas (WiSE) End Symposium*, Wassenaar, Netherlands, Mach 4, 2010. (**invited paper**)
- C14. D. Cavallo, A. Neto, G. Gerini, and A. Micco, "A novel printed-circuit-board feeding structure for common-mode rejection in wide-scanning connected arrays of dipoles," *4th European Conference on Antennas and Propagation (EUCAP 2010)*, Barcelona, Spain, April 12-16, 2010.
- C15. D. Cavallo, A. Neto, G. Gerini, and D. Morello, "A dual-band planar array of connected dipoles: experimental validation based on bistatic RCS measurements," *4th European Conference on Antennas and Propagation (EUCAP 2010)*, Barcelona, Spain, April 12-16, 2010. (**convined paper**)
- C16. A. Neto, D. Cavallo, and G. Gerini, "Performance of wide band connected arrays in scanning: the equivalent circuit and its validation through a dual-band prototype demonstrator," *IEEE Antennas and Propagation Society International Symposium*, Toronto, Ontario, Canada, July 11-17, 2010.
- C17. D. Cavallo, A. Neto, and G. Gerini, "A 10.5-14.5 GHz wide-scanning connected array of dipoles with common-mode rejection loops to ensure polarization purity," *IEEE Antennas and Propagation Society International Symposium*, Toronto, Ontario, Canada, July 11-17, 2010.
- C18. D. Cavallo, A. Neto, G. Gerini, and F. Smits, "Connected arrays of dipoles for broad band, wide angle scanning, dual polarized applications: A novel solution to the

- common mode problem,” *IEEE International Symposium on Phased Array Systems & Technology*, Boston, MA, October 12-15, 2010.
- C19.** D. Cavallo, A. Neto, and G. Gerini, “Rigorous equivalent circuits for connected arrays and their exploitation in antenna matching characterization,” *32th ESA Antenna Workshop on Antennas for Space Applications*, ESTEC, Noordwijk, Netherlands, October 5-8, 2010.
- C20.** A. Neto, D. Cavallo, and G. Gerini, “Finiteness of connected arrays: how to control guided edge waves with proper loading impedances,” *32th ESA Antenna Workshop on Antennas for Space Applications*, ESTEC, Noordwijk, Netherlands, October 5-8, 2010.
- C21.** D. Cavallo, S. Savoia, G. Gerini, A. Neto, and V. Galdi, “Design of a low profile printed array of loaded dipoles with inherent frequency selectivity properties,” *5th European Conference on Antennas and Propagation (EUCAP 2011)*, Rome, Italy, April 11-15, 2011.
- C22.** A. Neto, D. Cavallo, and G. Gerini, “Finiteness effects in wideband connected arrays: Analytical models to highlight the effect of the loading impedances,” *5th European Conference on Antennas and Propagation (EUCAP 2011)*, Rome, Italy, April 11-15, 2011. (**convened paper**)
- C23.** A. Neto, D. Cavallo, and G. Gerini, “Truncation effects in connected arrays: Analytical models to describe the edge-induced wave phenomena,” *IEEE Antennas and Propagation Society International Symposium*, Spokane, Washington, USA, July 3-8, 2011.
- C24.** D. Cavallo, A. Neto, and G. Gerini, “Theoretical analysis and design of connected arrays of dipoles with inter-element capacitance,” *USNC/URSI National Radio Science Meeting*, Spokane, Washington, USA, July 3-8, 2011.

Thesis Co-Supervised

- T1.** A. Micco, “Feeding network for connected arrays to avoid common-mode resonances,” M.Sc. thesis, University of Sannio, Benevento, Italy, 2009.
- T2.** D. Morello, “Characterization of antenna arrays in receive mode: Application to finite connected arrays,” M.Sc. thesis, University of Sannio, Benevento, Italy, 2009.

- T3.** S. Savoia, “Design of an array of connected dipoles with inherent frequency selectivity properties for radar applications,” M.Sc. thesis, University of Sannio, Benevento, Italy, 2010.

Patents

- P1.** European Patent: Array Antenna, 2009 (Publication No.: EP2110883-A1; WO2009128716-A1; EP2274796-A1, Inventors: A. Neto, D. Cavallo, G. Gerini, R. Grooters, G. Toso)

Awards

- A1.** “Best Innovative Paper Prize” at the 30th ESA Workshop on Antennas for Earth Observation, Science, Telecommunication and Navigation Space Missions, 27-30 May, Noordwijk, Netherlands, with the paper “On the potentials of connected slots and dipoles in the presence of a backing reflector”. Coauthors: Andrea Neto, Giampiero Gerini and Giovanni Toso.

Summary

Connected Array Antennas: Analysis and Design

Many of today's satellite communication and radar systems necessitate phased array antennas that are capable of wideband/multi-band operation and good polarization purity over a wide scan volume. However, the antenna solutions typically used for wideband wide-scan applications trade-off matching performance against polarization purity. For this reason, in recent years, a new approach has arisen for the design of broadband arrays, aiming at reducing cross polarization. This antenna solution consists of arrays of long dipoles or slots periodically fed, and are referred to as connected arrays of slot or dipoles. Connected array antennas represent one of the most promising concepts in the field of very wideband arrays, for being able to achieve both broad band and low cross polarization. The wideband performance is due to the fact that the connections between neighboring elements allow currents to remain nearly constant with frequency. Another attractive feature of connected arrays is their capability to achieve good polarization purity, in virtue of the planarity of the radiators.

Besides the advantageous physical properties, connected arrays are based on simple geometries that lead to the derivation of analytical solutions for the antenna parameters. Closed-form expressions based on a spectral Green's function representation are derived for the input impedance, the current distribution over the array and the radiation patterns. Important advantages result from this representation with respect to numerical solutions: above all, the reduction of computational costs and the gain in physical insight on the wave phenomena.

A convenient circuit representation of the array unit cell is derived. The circuit describes rigorously and analytically the transition between free-space radiation and guiding transmission line. Contrarily to standard Thévenin circuit for receiving antennas, this representation can be used to evaluate the power scattered by the antenna. The results have been applied to the analysis of the scattering and absorption of a real connected-dipole prototype array backed by a frequency selective ground plane. Good agreement was achieved between

measurements and results from the equivalent network. A novel measurement technique based on passive RCS measurements in the main planes was used to characterize the active matching of the radiating part of the antenna in transmission.

Finiteness effects can be particularly severe in connected arrays, due to electrical connection and the high mutual coupling between the elements. As a consequence, the overall behavior of a finite wideband array can be sensibly different with respect to infinite array analysis. Thus, it is crucial to include edge effects already in the preliminary assessment of the array performance. An efficient numerical procedure is derived for the characterization of the edge effects. The method requires only one unknown per elementary cell, independently from the cell geometrical parameters. This is possible thanks to the use of an appropriate connected array Green's function in the integral equation. This procedure is of general applicability and can be used for arrays with and without backing reflectors and for arbitrary scan angle.

An alternative analytical representation is also derived to provide physical insight on the nature of the edge-waves. The analytical approximation of the spatial current distribution on the finite array is derived, for the specific case of a connected array of dipoles operating in free space, and scanning only in the E -plane. The key step is to represent the total current as sum of the infinite array contribution plus edge-born waves. The final analytical expression is given in terms of Fresnel functions and allows qualitative considerations on the nature of the electric current distribution, in terms of spreading and attenuation.

The analytical expressions represent a powerful tool that can be used both for modelling and design. A connected array of dipoles with 40% bandwidth, when scanning in elevation to 45° , has been designed. Practical designs require the implementation of ad hoc feed structures that avoid common-mode currents to propagate on the feed lines. This problem has been addressed and feed structures that perform common-mode rejection have been designed. Measurements from a prototype demonstrator were presented for validation and showed good performance.

About the Author



Daniele Cavallo was born on May 1, 1983 in Benevento, Italy. He received his B.Sc. degree in Telecommunication Engineering (summa cum laude) from University of Sannio, Benevento, Italy in January 2005. For his B.Sc. thesis, he carried out a three-months internship with The Waves Group at the Department of Engineering, University of Sannio, from October to December 2004. In July 2007 he received his M.Sc. degree (summa cum laude and special honors)

from the same university. His M.Sc. project was carried out from January to June 2007 at the Netherlands Organization for Applied Scientific Research (TNO) Defense, Security and Safety, The Hague, Netherlands. The project dealt with an investigation of the performance of ultra-wideband tapered slot antennas and arrays, under the supervision of prof.dr.ir. A. Neto and prof.dr.ir. G. Gerini from TNO, and prof.dr.ir. V. Galdi from University of Sannio.

Since January 2007, he has been with the Antenna Group at TNO Defence, Security and Safety, as researcher in the antenna field. Here he worked on the analysis and design of connected arrays within the ACTiFE, MEMPHIS, ITM projects, and for the TNO internal Radar program. This work resulted in four manufactured prototype demonstrators and one international patent in 2008.

In September 2007 he started working towards the Ph.D. degree in the Electromagnetics group, Eindhoven University of Technology, Eindhoven, Netherlands. The research has resulted in 6 journal publications, 20 conference papers, and 4 invited papers at international conferences. This research has been carried out in collaboration with the supervisors prof.dr.ir. G. Gerini (TNO and Eindhoven University of technology) and prof.dr.ir. A. Neto (with TNO until January 2010, now with Delft University of technology).

He has supervised and co-supervised the following M.Sc. students and post-graduate trainees at TNO: M. Verdi (University of Florence), A. Micco (University of Sannio), D. Morello (University of Sannio), C. Casali (Ingegneria dei Sistemi (IDS), Pisa), S. Savoia (University of Sannio).

From March 2008, he has been a visiting research fellow at Delft University of Technology, Delft, Netherlands.

He is serving as a reviewer for IEEE Transaction on Antennas and Propagation (TAP) and IEEE Antennas and Wireless Propagation Letters (AWPL). He has co-chaired the session on Phased Array Feeding and Impedance Matching at the 2010 IEEE International Symposium on Antennas and Propagation (APSURSI '10), Toronto, Canada, July 11-17, 2010.

He was first author of the paper awarded with the best innovative paper prize at the 30th ESA Antenna Workshop in 2008.

Acknowledgements

This dissertation is the result of the research carried out at TNO Defence, Security and Safety, in The Hague over a period of four years, from September 2007 to August 2011.

The completion of this work would not have come about without the substantial support of many individuals. I consider myself very lucky having had the chance to work with them and I am indebted to each one of them. First and foremost, I would like to give a heartfelt, special thanks to my supervisors prof.dr. Giampiero Gerini and prof.dr. Andrea Neto. They have been mentors and friends at the same time, and without their support I would not have been able to come this far. If not for prof.dr. Giampiero Gerini, this whole project would never have begun. He took the time to convince me that pursuing a PhD was a worthwhile endeavor. He also secured funding for this research at University of Eindhoven (TU/e) with an AiO-grant from TNO. Giampiero provided very helpful feedback and commentary on my work and I greatly appreciate the time and effort he put into reviewing it. Throughout these years I have also had the good fortune to have prof.dr. Andrea Neto as supervisor and mentor. His knowledge and his enthusiastic approach to research, as well as his outstanding personality, have made this experience all the more enjoyable. I thank him for all the support he has given me.

I would like to express my gratitude to prof.dr. Anton Tjihuis, the chief of the Electromagnetic Section at TU/e, for the interesting periodic discussions and his careful review of this dissertation. A special acknowledgement goes to all other members of the Ph.D. committee for their helpful comments that improved the consistency of the manuscript.

I am grateful to prof.dr. Vincenzo Galdi from University of Sannio for providing me with an opportunity to perform an internship at TNO back in 2007. That was a valuable experience and it enabled me to proceed further on my studies. I also would like to thank Frans Nennie and Pascal Aubry for their support in testing and measuring the prototype demonstrators.

This project has been supported by the following master students and post-graduate trainees at TNO: Martina Verdi (University of Florence), Alessandro Micco (University

of Sannio), Davide Morello (University of Sannio), Claudia Casali (Ingegneria dei sistemi (IDS), Pisa), Silvio Savoia (University of Sannio). Thank you for your help with performing simulations and parametric analysis.

It has been a great pleasure working with all the colleagues at TNO during my tenure as a doctoral student. A special thanks to Henk Medenblik, with whom I shared the office for most of my time at TNO. Thanks for the friendship, for your great music, and for teaching me most of the Dutch I know; “jij bent een grappig mannetje”. Thanks to Roland and Henk for the “afgrijselijk sushi eten” evenings and the nice beers.

I will remember with fondness the people I had lunch with for 5 years: Simona, Nuria, my usual conference companion Mauro, the paranympths Francesco and Annalisa, Laura, Daniela, Stefania, Teis, Gabriele, Alessandro, Frans, Dave, Carlo, prof.dr. Angelo Freni, and many others.

I feel really lucky to share my passion for jazz music with some of the colleagues. A heartfelt thank to the members of TNO jazz band: Erik, Duje, Miguette, Henk, Wim, Gijs, Sander and Jos. Erik, playing with you was incredible fun and I hope we can still play together in the future.

I would like to dedicate this thesis to my parents Anna and Enrico and my brother Francesco. I will forever be indebted and grateful to you for your sacrifices and examples that encouraged me to seek a higher education and to pursue a life-long goal of learning. You have also put up with me going away for five years, while always supporting me through this period.

I hope you are proud of me!

Vorrei dedicare questa tesi ai miei genitori Anna ed Enrico e a mio fratello Francesco. Vi sarò per sempre grato e riconoscente per i vostri sacrifici che mi hanno incoraggiato a continuare nei miei studi e intraprendere il mio percorso dedicato alla ricerca. Nonostante sia stato lontano per cinque anni, mi avete sempre supportato e incoraggiato in questo periodo.

Spero siate orgogliosi di me!